Frequency Estimation for Low Earth Orbit Satellites

Elias Aboutanios (BE Hons 1)

A thesis submitted for the degree of
Doctor of Philosophy

University of Technology, Sydney
Faculty of Engineering (Telecommunications Group)
2002

CERTIFICATE

I certify that the work in this thesis has not previously been submitted for a degree nor has it been submitted as part of requirements for a degree except as fully acknowledged within the text.

I also certify that the thesis has been written by me. Any help that I have received in my research work and the preparation of the thesis itself has been acknowledged. In addition, I certify that all information sources and literature used are indicated in the thesis.

Signature of Candidate

_____

ACKNOWLEDGMENTS

This research would not have been possible without the support of a number of people and organisations.

Firstly, I would like to thank my former supervisor, A/Prof. Sam Reisenfeld, for his support and guidance throughout my research work. I would also like to thank my current superviser, Professor Robin Braun, for his valuable support for the past few months.

I would like to acknowledge The *Cooperative Research Centre for Satellite Systems* for the financial support during the course of this work.

I would like to express my appreciation for a number of people at UTS. Firstly Ms Rosa Tay for her kind administrative support, Dr Tim Aubrey and Mr Ray Clout who are part of the CRCSS team and Mr Robert Corran for his assistance in computer related issues.

My friend and colleague Dr Keith Willey for being able to put up with my sense of humour and for the friendship we share. I would also like to express my gratitude to Dr Michael Eckert for his valuable help and advice.

To my friends, at the university and outside, thank you for keeping a sanity check on my life.

My brother, Joseph, and sisters, Souraya and Rita, thank you for your love, support and encouragement, and for putting up with me all these years. I pray that I will always be there for you like you have been for me.

To my parents for all the sacrifices you made in order to give me the opportunity to get this far. I love you with all my heart. You are the shoulders that carried me so that I could see further than you could. It is to you that I dedicate this thesis.

To My Parents

Table of Contents

Certificate ..... **ii**
Acknowledgements ..... **iii**
Table of Contents ..... **iv**
List of Figures ..... **viii**
List of Tables ..... **xiv**
List of Symbols ..... **xvi**
List of Abbreviations ..... **xix**
Abstract ..... **xxi**

Chapter 1 Introduction **1**
1.1 Motivation for thesis 1
1.1.1 Doppler shifts and Local Oscillator Drift 2
1.1.2 The Application of Frequency Information to Spatial Tracking 3
1.2 Research objectives 4
1.3 Thesis structure 4
1.4 Original contributions 8
1.5 Publications 10
Chapter 2 Theory and Background **12**
2.1 Introduction 12
2.2 The Central Limit Theorem and Noise Properties 12
2.3 The Cramer-Rao Lower Bound 14
2.3.1 CRB for the Estimate of the Frequency of a Sinusoid 16
2.4 Kalman Filtering 19
2.4.1 The Kalman Filter – Linear, Time-Invariant Case 19
2.4.2 Non-Linear Case – The EKF 21
2.5 Frequency Estimation 23
2.5.1 Phase-Based Frequency Estimation 25
2.5.2 Correlation Based Frequency Estimation 28
2.5.3 Least Squares Frequency Estimation 29
2.5.4 Frequency Estimation Using ARMA Modeling 31
2.5.5 Kalman Filtering Frequency Tracking 33

2.5.6 Frequency Domain Frequency Estimation 35
2.6 Conclusion 37
Chapter 3 Complete Characterisation of Low Earth Orbits 38
3.1 Introduction 38
3.2 Angular Velocity of Satellite in ECEF Frame 39
3.3 Orbital Propagation 42
3.4 Satellite Velocity Approximations 44
3.5 Spatial Characterisation 46
3.5.1 Satellite Visibility Duration 49
3.5.2 Latitude and Longitude of the Sub-satellite Point S 51
3.5.3 Azimuth and Elevation 54
3.5.4 Azimuth-Elevation to X-Y Transformation 58
3.5.5 Off-Boresight Error 61
3.6 Doppler Shift and Doppler Rate 63
3.7 Conclusion 65
Chapter 4 Frequency Domain Frequency Estimation 67
4.1 Introduction 67
4.2 The DFT and FFT 68
4.3 The Maximum Bin Search 69
4.4 Threshold Effects 71
4.5 Approximate Expression for Threshold Onset 75
4.5.1 Derivation of the Approximate Expression 76
4.5.1.1 Lemma 88
4.5.1.2 Theorem 89
4.5.1.3 Proof 90
4.6 Conclusion 91
Chapter 5 Frequency Estimation by Interpolation on Fourier Coefficients 93
5.1 Introduction 93
5.2 Existing Interpolation on Fourier Coefficients Techniques 94
5.2.1 Theory 96
5.2.1.1 Theorem 98
5.3 Interpolation on Three Fourier Coefficients 100
5.4 Quinn's First Estimator 101
5.4.1 Motivation 102
5.4.2 Analysis 103

5.4.2.1 Theorem 103
5.4.2.2 Derivation of the Asymptotic Variance 103
5.4.3 Quinn's Second Estimator 111
5.4.4 Macleod's Three Coefficients Interpolator 114
5.4.5 Motivation 115
5.5 Interpolation on Five Fourier Coefficients 118
5.6 Interpolation Using the Moduli of Fourier Coefficients– The Rife-Vincent Estimators 121
5.6.1 Rife-Vincent Estimator 122
5.6.2 Motivation 122
5.6.3 Modified Rife-Vincent Estimator 124
5.6.4 Performance of the Rife-Vincent Estimators 124
5.7 Conclusion 126
Chapter 6 Frequency Estimation by Interpolation on Fractional Fourier Coefficients 127
6.1 Introduction 127
6.2 Fractional Fourier Coefficients 128
6.3 Interpolation on Two Fractional Fourier Coefficients 129
6.3.1 Analysis 130
6.3.1.1 Theorem 133
6.4 Interpolation on the Magnitudes of Two Fractional Fourier Coefficients 137
6.4.1 Motivation 137
6.4.2 Analysis 139
6.4.2.1 Theorem 148
6.5 Interpolation on the Magnitudes Squared of Two Fractional Fourier Coefficients 150
6.5.1 Motivation 151
6.6 Modified Interpolation on the Magnitudes Squared of Two Fractional Fourier Coefficients 155
6.6.1 Motivation 156
6.6.2 Analysis 157
6.7 Conclusion 159
Chapter 7 Iterative Frequency Domain Frequency Estimation 160
7.1 Introduction 160
7.2 Dichotomous Search of the Periodogram Peak 161

7.3 Modified Dichotomous Search of the Periodogram peak 168
7.4 Guided Search of the Periodogram Peak Algorithm 172
7.5 Other Hybrid Algorithms 175
7.6 Conclusion 177
Chapter 8 Iterative Interpolation on the Fractional Fourier Coefficients 178
8.1 Introduction 178
8.2 The Fixed Point Theorem and Algorithm Convergence 179
8.2.1 Theorem 179
8.2.2 Proof 179
8.2.3 Definition 180
8.2.4 Fixed Point Theorem 180
8.2.5 Performance of Iterative Estimation and Number of Iterations 181
8.3 Iterative Implementation of Quinn's First Algorithm 182
8.3.1 Theorem 187
8.4 Iterative Fractional Fourier Coefficients Interpolation 189
8.4.1 Theorem 192
8.5 Iterative Magnitudes Only Interpolation 194
8.5.1 Theorem 197
8.6 Iterative Magnitudes Squared Interpolation 199
8.6.1 Theorem 202
8.7 Conclusion 205
Chapter 9 Frequency Assisted Spatial Tracking 206
9.1 Introduction 206
9.2 Doppler Based Position Determination 207
9.3 Satellite Orbit Determination 208
9.4 Frequency Assisted Spatial Tracking 209
9.5 FAST Implementations Based on Simplified Equations 212
9.5.1 One-sided FAST Approach 213
9.5.2 Calculation of the Expected Maximum Elevation Point 215
9.5.3 Extended Kalman Filter for the Simplified Model 221
9.5.3.1 Derivation of the EKF with the Maximum Elevation assumed known 222
9.6 Conclusion 229
Chapter 10 Conclusion 230
10.1 Review of Research Results 230
10.1.1 Orbital Characterisation 231

10.1.2 Frequency Estimation 231
10.1.3 Threshold effects 232
10.1.4 Interpolation on the Fractional Fourier Coefficients 232
10.1.5 Iterative Estimation Using the Dichotomous Search 233
10.1.6 Iterative Interpolation on the Fractional Fourier Coefficients 234
10.1.7 Frequency Assisted Spatial Tracking 235
10.2 Suggestions for Future Work 236
10.2.1 A Study of the Threshold Properties of the Frequency Estimators 236
10.2.2 Implementation of the Algorithms Recursively 237
10.2.3 Extension of the Family of Interpolators on Fractional Fourier Coefficients 237
10.2.4 Rigorous Analysis of the Estimators of Chapter 7 237
10.2.5 Strategies for the Doppler Shift Compensation 238
10.2.6 Development of a More Accurate Orbital Model 238
10.2.7 Implementation of a Two-dimensional Spatial Tracker 239
10.2.8 Frequency Rate Estimation 239
10.3 Conclusion 239
Appendix A. Spherical Geometry 241
Appendix B. Asymptotic Theory 242
B.1 The Notations o_p and O_p 242
B.2 Properties of o_p and O_p sequences 243
B.2.1 Lemma 243
B.2.2 Proof 244
B.2.3 Corollaries 245
B.3 Convergent and Bounded Deterministic Sequences 245
B.4 Properties of Convergent and Bounded Sequences 246
B.4.1 Lemma 246
B.4.2 Proof 247
B.4.3 Corollaries 248
Appendix C. Fourier Coefficients of AWGN 249
C.1 Properties of AWGN Fourier Coefficients 249
C.2 Fractional Fourier Coefficients of AWGN 251
C.3 Fourier Coefficients of Signal plus Noise 253
Appendix D. References 255

List of Figures

Figure 3.1 – *Satellite position in ECI frame of reference.* 40
Figure 3.2 – *Orbit propagation algorithm results.* 44
Figure 3.3 – *Angular velocity of satellite in ECEF frame as observed by an earth station at a longitude of 10º west and latitude 33.5º north. The pass used has a maximum elevation angle of 85.45º and is east of the earth station.* 45
Figure 3.4 - *Orbital Geometry for a LEO with altitude h and inclination i.* 47
Figure 3.5 – *Enlarged view of sub-satellite path.* 48
Figure 3.6 – *Plot of visibility duration as a function of the observed maximum elevation angle.* 50
Figure 3.7 – *Plot of the calculated orbits in Lat-Long coordinates for a pass with maximum elevation 85.45º. The earth station is at 10º west and 33.5º north.* 53
Figure 3.8 – *Plot of the latitude and longitude errors for a pass with a maximum elevation angle of 85.45º.* 54
Figure 3.9 – *Plot of the azimuth (a), azimuth errors (b), elevation (c) and elevation errors (d) as a function of time for a pass with a maximum elevation angle of 85.45º.* 57
Figure 3.10 – *Azimuth-Elevation to X-Y transformation.* 58
Figure 3.11 – *Plot of the X and Y rotations for a pass with a maximum elevation angle of 85.45º.* 60
Figure 3.12 – *Off-boresight error.* 61
Figure 3.13 – *Plot of the off-boresight error curves for a pass with a maximum elevation angle of 85.45º for both ECEF angular velocity approximation strategies.* 62
Figure 3.14 – *Plot of the Doppler shift and Doppler rate for a pass with a maximum elevation angle of 85.* 65
Figure 4.1 – *Outlier probability versus signal to noise ratio for various sample block sizes.* 74
Figure 4.2 – *Frequency RMSE versus signal to noise ratio for various sample block sizes.* 75
Figure 4.3 – *Plot of f(v) Vs v for different values of* ε. *N was set to* 8 *(that is K =* 7*).* .. 81
Figure 4.4 – *Plot Threshold SNRs (defined at the point where the total frequency RMSE equals 2×CRB). The total RMSE is also shown Vs the signal to noise ratio.* 91

Figure 5.1 – *Plot of the amplitude spectrum of a sinusoidal signal with frequency = 0.2137. (a) shows the 0-padded spectrum with N = 128 and L = 1024. A zoomed in version is shown in (b) along with the 128 sample FFT.* 95

Figure 5.2 – *Plot of the ratio of the asymptotic variance of the periodogram maximiser using three coefficients to asymptotic CRB.* 100

Figure 5.3 – *Plot of the theoretical and simulated ratios of the asymptotic variance of Quinn's first algorithm to the asymptotic CRB. 10000 simulation runs were averaged.* 110

Figure 5.4 – *Plot of the standard deviation of the frequency estimates obtained using Quinn's first algorithm Vs the signal to noise ratio. 10000 simulation runs were averaged.* 110

Figure 5.5 – *Plot of the ratio of the asymptotic variance of Quinn's second algorithm to the asymptotic CRB as a function of δ_0 at 0 dB SNR and N = 1024. 10000 simulation runs were averaged.* 113

Figure 5.6 – *Plot of the performance of Quinn's frequency estimation algorithms Vs SNR. N = 1024, f_s = 1MHz. 10000 simulation runs were averaged.* 114

Figure 5.7 – *Plot of the ratio of the variance Macleod's three coefficients interpolator to the asymptotic CRB as a function of δ_0. N was set to 1024 and SNR to 0 dB. 10000 simulation runs were averaged.* 117

Figure 5.8 – *Comparison of the performance of Quinn's second frequency estimation algorithm and Macleod's three coefficients interpolator as a function of SNR. N = 1024, f_s = 1MHz. 10000 simulation runs were averaged.* 118

Figure 5.9 – *Plot of simulation results of the ratio of the variance Macleod's five coefficients interpolator to the asymptotic CRB as a function of δ_0. N was set to 1024 and SNR to 0 dB. 10000 simulation runs were averaged.* 120

Figure 5.10 – *Plot of the performance of Macleod's three and five coefficients interpolators as a function of SNR. N = 1024, f_s = 1MHz. 10000 simulation runs were averaged.* 121

Figure 5.11 – *Plot of simulation results of the ratio of the variance the Rife-Vincent estimators to the asymptotic CRB as a function of δ_0. N was set to 1024 and SNR to 0 dB.* 125

Figure 5.12 – *Plot of the performance of the Rife-Vincent as a function of SNR. N = 1024, f_s = 1MHz. 10000 simulation runs were averaged.* 126

Figure 6.1 – *Plot of the ratio of the asymptotic variance of the interpolation on fractional Fourier Coefficients estimator to the asymptotic CRB versus* δ_0. *10000 simulation runs at 0 dB SNR were averaged.* 134

Figure 6.2 – *Plot of the performance of the interpolation on fractional Fourier coefficients algorithm as a function of SNR. N = 1024,* f_s *= 1MHz. 10000 simulation runs were averaged.* 135

Figure 6.3 – (a) *Plot of the theoretical ratio of the asymptotic variance to the asymptotic CRB. The curves for Quinn's first algorithm and the interpolation on fractional Fourier Coefficients estimator are shown repeated periodically versus* δ_0. (b) *A shifted version.* 136

Figure 6.4 – (a) *Plot of the ratio of the asymptotic variance of the MOI estimator to the asymptotic CRB versus* δ_0. *10000 simulation runs at 0 dB SNR were used in the simulation.* (b) *Zoomed version of (a) on the interval* $[0.4,0.5]$. 149

Figure 6.5 – *Plot of the performance of the MOI algorithm as a function of SNR. N = 1024,* f_s *= 1MHz. 10000 simulation runs were averaged.* 150

Figure 6.6 – *Plot of the estimator mapping function* $\psi(\delta)$ *of the MOI and MSI estimators.* 152

Figure 6.7 – (a) *Plot of the ratio of the asymptotic variance of the MSI estimator to the asymptotic CRB versus* δ_0. *10000 simulation runs at 0 dB SNR and N=1024 were used in the simulation.* (b) *Zoomed in version of (a).* 154

Figure 6.8 – *Plot of the performance of the MSI algorithm as a function of SNR. N = 1024,* f_s *= 1MHz. Note that the above figure shows the square root of the CRB.* 155

Figure 6.9 – *Plot of the ratio of the asymptotic variance of the MMSI estimator to the asymptotic CRB versus* δ_0. *10000 simulation runs at 0 dB SNR and N=1024 were used in the simulation.* 158

Figure 6.10 – *Plot of the performance of the MMSI algorithm as a function of SNR. N = 1024,* f_s *= 1MHz. 10000 simulation runs were averaged.* 158

Figure 7.1 – *Plot of ratio of the variance of the Dichotomous Search algorithm, with L = N = 1024, to the ACRB as a function of* δ_0. (a) *shows the performance for 1, 4 and 10 iterations.* (b) *is a zoomed in version of* (a). *5000 simulation runs were averaged.* 164

Figure 7.2 – *Plot of the performance of the Dichotomous Search algorithm, with L = N = 1024, as a function of SNR. 10000 simulation runs were averaged.* 165

Figure 7.3 – *Plot of ratio of the variance of the Dichotomous Search algorithm to the asymptotic CRB, with L = 1.5N, to the ACRB as a function of* δ_0. (a) *shows the performance for 1, 4 and 10 iterations.* (b) *is a zoomed in version of* (a). *5000 simulation runs were averaged.* 166

Figure 7.4 – *Plot of the standard deviation of the frequency error of the zero-padded dichotomous search algorithm, with L = 1.5N, as a function of SNR. 10000 simulation runs were averaged.* 167

Figure 7.5 – *Plot of rate of change of the differential, D as a function of the offset from the bin centre* δ_0. 169

Figure 7.6 – *Plot of standard deviation of the frequency error of the Modified Dichotomous Search algorithm, with* $\Delta = 0.75$ *and* $\Delta = 0.6$, *as a function of SNR. 10000 simulation runs were averaged.* 172

Figure 7.7 – *Plot of standard deviation of the frequency error of the Guided Search algorithm as a function of SNR. The Guided Search was run for 4 iterations. 10000 simulation runs were averaged.* 174

Figure 8.1 – *Plot of ratio of the variance of the iterative form of Quinn's first algorithm to the asymptotic CRB. 5000 simulation runs were averaged at an SNR = 0dB.* 188

Figure 8.2 – *Plot of Standard Deviation of the Frequency Error of the iterative form of Quinn's first algorithm Vs Signal to Noise Ratio. 10000 simulation runs were averaged.* 188

Figure 8.3 – *Plot of ratio of the variance of the iterative form of the FFCI algorithm to the asymptotic CRB. 5000 simulation runs were averaged at an SNR = 0dB.* ... 193

Figure 8.4 – *Plot of Standard Deviation of the Frequency Error of the iterative form of the FFCI algorithm Vs Signal to Noise Ratio. 10000 simulation runs were averaged.* 193

Figure 8.5 – *Plot of ratio of the variance of the iterative form of the MOI algorithm to the asymptotic CRB. 5000 simulation runs were averaged at a SNR = 0dB.* 198

Figure 8.6 – *Plot of Standard Deviation of the Frequency Error of the iterative form of the MOI algorithm Vs Signal to Noise Ratio. 10000 simulation runs were averaged.* 199

Figure 8.7 – *Plot of ratio of the variance of the iterative form of the MSI algorithm to the asymptotic CRB. 5000 simulation runs were averaged at a SNR = 0dB.* 204

Figure 8.8 – *Plot of Standard Deviation of the Frequency Error of the iterative form of the MSI algorithm Vs Signal to Noise Ratio. 10000 simulation runs were averaged.* 204

Figure 9.1 – *Doppler shift and Doppler rate contours evaluated using the approximate orbital equations developed in chapter 3. The full and dashed lines represent the Doppler shift and Doppler rate respectively. The earth station is marked by the square containing an x and the zenith pass is shown.* 210

Figure 9.2 – *Doppler shift and Doppler rate contours evaluated using the orbit generation algorithm presented in chapter 3. The full lines represent the Doppler shift and the dashed the Doppler rate. The earth station is marked by the square containing an x and the zenith pass is shown.* 211

Figure 9.3 – (a) *Doppler shift and* (b) *Doppler rate curves for passes of maximum elevation 74.6° east and west of the earth station.* 212

Figure 9.4– *A reprint of figure 3.5; enlarged view of sub-satellite path.* 215

Figure 9.5 – *Actual and predicted maximum elevations for passes 1 and 2.* 220

Figure 9.6 – *Errors in the predicted maximum elevations for passes 1 and 2.* 220

Figure 9.7 – *Error in the predicted locations of the maximum elevations for pass 2...* 221

Figure 9.8 – *EKF spatial tracker performance in the noiseless case.* 224

Figure 9.9 – *EKF spatial tracker performance at a SNR of 0dB.* 225

Figure 9.10 – *Off-boresight error for scalar EKF against time for different signal to noise ratios.* 226

Figure 9.11 – *EKF spatial tracker performance at a SNR of 0dB with a 0.3° error in the assumed maximum elevation value.* 226

Figure 9.12 – *EKF spatial tracker performance at a SNR of 0 dB with a 0.3° error in the assumed maximum elevation value.* 227

Figure 9.13 – (a) *EKF spatial tracker performance at a SNR of 0 dB. A zero-mean random (Gaussian distributed) error, with a 5° standard deviation was added to the initial value of* ψ. (b) *Zoomed version of (a).* 228

List of Tables

Table 3.1 – *Orbital Propagation Algorithm.* 43
Table 4.2 – *Outlier probability bounds for threshold calculation.* 85
Table 5.1 – *Quinn's First Algorithm.* 101
Table 5.2 – *Quinn's second algorithm.* 112
Table 5.3 – *Macleod's three coefficients interpolator.* 116
Table 5.4 – *Macleod's five coefficients interpolator.* 119
Table 5.5 – *Rife-Vincent estimator.* 122
Table 5.6 – *Modified Rife-Vincent estimator.* 124
Table 6.1 – *Fractional Fourier Coefficients Interpolation (FFCI) estimator.* 130
Table 6.2 – *Magnitudes Only Interpolation (MOI) on fractional Fourier coefficients estimator.* 137
Table 6.3 – *Magnitudes Squared Interpolation (MSI) on fractional Fourier coefficients estimator.* 151
Table 6.4 – *Modified Magnitudes Squared Interpolation (MMSI) on fractional Fourier coefficients estimator.* 156
Table 7.1 – *Dichotomous Search of the Periodogram Peak frequency estimator.* 162
Table 7.2 – *Modified Dichotomous Search of the Periodogram Peak frequency estimator.* 171
Table 7.3 – *Guided Search of the Periodogram Peak frequency estimator.* 173
Table 8.1 – *Iterative Implementation of Quinn's first algorithm.* 183
Table 8.2 – *Iterative Implementation of the Fractional Fourier Coefficient Interpolation algorithm.* 189

List of Symbols

a	Azimuth
α_x	X-rotation
α_y	Y-rotation
β	Off-boresight error
δ	The offset between true frequency line and the closest bin
$\hat{\delta}$	Estimate of δ
D_r	Normalised Doppler rate
D_s	Normalised Doppler shift
$\Phi(x)$	Standard Normal density function, $= \frac{1}{\sqrt{2\pi}} e^{-\frac{x^2}{2}}$
φ_{ES}	Earth station latitude
φ_s	Satellite latitude
f	Signal frequency
$\hat{f}$	Frequency estimate
f_s	Sampling frequency
γ	Central angle between earth station and satellite
G	Gravitational constant $\approx 6.672 \times 10^{-11}$ $\mathrm{m^3 kg^{-1} s^{-2}}$
GM_e	Earth figure $= 3.986004418 \times 10^{14}$
i	Satellite orbit inclination
$\mathbf{I}$	The identity matrix
$\Im(z)$	Imaginary part of z

$\binom{K}{l}$	Binomial coefficients
λ_{ES}	Earth station longitude
λ_s	Satellite longitude
$\ln(x)$	Natural logarithm of x
$\log(x)$	Logarithm base 10 of x
m	Index of the bin with the highest magnitude
M_e	Mass of the Earth $\approx 5.9736\times10^{24}$ kg
N	Number of samples
ω	Angular frequency of a sinusoidal signal $= 2\pi f$
ω_e	Angular velocity of the Earth
ω_F	Satellite angular velocity in the ECEF frame
ω_I	Satellite angular velocity in the ECI frame
ψ	Angular displacement of the satellite from the point of closest approach
Q	Number of iterations
$Q(x)$	The standard Q-function $= \int_x^\infty \Phi(t)dt$
q	Probability of an outlier
ρ	Signal to Noise Ratio
ρ(dB)	Signal to Noise Ratio in decibels
$\mathbb{R}$	The set of real numbers
$\Re(z)$	Real part of z
σ	Standard deviation of a random variable
$s(k)$	k^{th} sample of sinusoidal signal
$S(n)$	Fourier transform of $s(k)$

$s(t)$	Earth station to satellite slant range at time t
θ	Elevation
θ_v	Minimum elevation for visibility
$\mathbf{v}^T$	Transpose of $\mathbf{v}$
T_s	Sampling time $= 1/f_s$
T_v	Satellite visibility duration
$w(k)$	k^{th} sample of additive white Gaussian noise
$W(n)$	Fourier transform of $w(k)$
x^*	Complex Conjugate of x
$x(k)$	Signal plus noise $= s(k) + w(k)$
$X(n)$	Fourier transform of $x(k)$
$Y(n)$	Magnitude of $X(n)$
N(0,1)	The standard normal distribution, $= \int_{-\infty}^{x} \Phi(x)dx$

List of Abbreviations

ACRB	Asymptotic Cramer Rao Bound
a.s.	Almost Surely
ARMA	Auto-Regressive Moving Average
AWGN	Additive White Gaussian Noise
Az	Azimuth
BPSK	Binary Phase Shift Keying
CLT	Central Limit Theorem
CRB	Cramer Rao Bound
CRCSS	Cooperative Research Centre for Satellite Systems
DFT	Discrete Fourier Transform
DSP	Digital Signal Processing
ECEF	Earth Centred Earth Fixed
ECI	Earth Centred Inertial
EKF	Extended Kalman Filter
El	Elevation
FAST	Frequency Assisted Spatial Tracking
FFCI	Fractional Fourier Coefficients Interpolation
FFT	Fast Fourier Transform
GPS	Geographical Positioning System
IEKF	Iterative Extended Kalman Filter
IFFCI	Iterative Fractional Fourier Coefficients Interpolation
i.i.d.	Independent and Identically Distributed
IMOI	Iterative Magnitudes Only Interpolation
IMSI	Iterative Magnitudes Squared Interpolation

LEO	Low Earth Orbit
LO	Local Oscillator
MBS	Maximum Bin Search
ML	Maximum Likelihood
MOI	Magnitudes Only Interpolation
MSI	Magnitudes Squared Interpolation
MMSI	Modified Magnitudes Squared Interpolation
MSE	Mean Squared Error
NORAD	North American Aerospace Command
pdf	Probability Density Function
PSK	Phase Shift Keying
QAM	Quadrature Amplitude Modulation
QPSK	Quadrature Phase Shift Keying
RMSE	Root Mean Squared Error
SNR	Signal to Noise Ratio
STK™	Satellite Tool Kit
TLEs	Two Line Elements
TT&C	Tracking, Telemetry and Command

Abstract

Low Earth Orbit (LEO) satellites have received increased attention in recent years. They have been proposed as a viable solution for remote sensing, telemedicine, weather monitoring, search and rescue and communications to name a few applications. LEO satellites move with respect to an earth station. Thus, the station must be capable of tracking the satellite both spatially and in frequency. In addition, as the spectrum becomes more congested, links are being designed at higher frequencies such as Ka band. These frequencies experience larger attenuations and therefore the system must be capable of operating at low signal to noise ratios.

In this dissertation we report on the research conducted on the following problems. Firstly, we study the estimation of the frequency of a sinusoid for the purpose of acquiring and tracking the frequency of the received signal. Secondly, we propose the use of the frequency measurements to assist the spatial tracking of the satellite.

The highly dynamic environment of a LEO system, combined with the high Ka band frequencies result in large Doppler rates. This limits the available processing time and, consequently, the fundamental resolution of a frequency estimator. The frequency estimation strategy that is adopted in the thesis consists of a coarse estimator followed by a fine estimation stage. The coarse estimator is implemented using the maximum of the periodogram. The threshold effect is studied and the derivation of an approximate expression of the signal to noise ratio at which the threshold occurs is examined.

The maximum of the periodogram produces a frequency estimate with an accuracy that is $O\left(N^{-1}\right)$, where N is the number of data samples used in the FFT. The lower bound for the estimation of the frequency of a sinusoid, given by the Cramer-Rao bound (CRB), is $O\left(N^{-\frac{3}{2}}\right)$. This motivates the use of a second stage in order to improve the estimation resolution. A family of new frequency estimation algorithms that interpolate on the fractional Fourier coefficients is proposed. The new estimators can be implemented iteratively to give a performance that is uniform in frequency. The iterative algorithms are analysed and their asymptotic properties derived. The

asymptotic variance of the iterative estimators is only 1.0147 times the asymptotic CRB.

Another method of refining the frequency estimate is the Dichotomous search of the periodogram peak. This is essentially a binary search algorithm. However, the estimator must be padded with zeroes in order to achieve a performance that is comparable to the CRB. An insight into this is offered and a modified form that does not require the zero-padding is proposed. The new algorithm is referred to as the modified dichotomous search. A new hybrid technique that combines the dichotomous search with an interpolation technique in order to improve its performance is also suggested.

The second research aim was to study the possibility of applying the frequency measurements to obtain spatial tracking information. This is called the frequency assisted spatial tracking (FAST) concept. A simple orbital model is presented and the resulting equations are used to show that the Doppler shift and rate uniquely specify the satellite's position for the purpose of antenna pointing. Assuming the maximum elevation of the pass is known, the FAST concept is implemented using a scalar Extended Kalman Filter (EKF). The EKF performance was simulated at a signal to noise ratio of 0dB. The off-boresight error was found better than 0.1º for elevations higher than 30º.

Chapter 1

Introduction

This thesis is primarily concerned with the estimation of frequency for the purpose of Doppler shift correction in Low Earth Orbit (LEO) satellite Communications, and the application of the resulting frequency information to assist in the spatial tracking of LEO satellites. In the thesis, unless otherwise specified, the word satellite without qualification refers to a LEO satellite and the terms earth station and terminal are used interchangeably. The purpose of this chapter is to introduce the problem and set it in context. The motivation of the thesis is presented in the next section. The research objectives are stated in section 1.2. Section 1.3 sets out the thesis structure, while section 1.4 details the author's claims of original contributions. Finally, the relevant publications are listed in section 1.5.

1.1 Motivation for thesis

FedSat is a small experimental Low Earth Orbit (LEO) satellite being built by the Cooperative Research Centre for Satellite Systems (CRCSS). It is intended to be launched in 2002 aboard a Japanese HIIA rocket into an 800 km sun-synchronous orbit. For a discussion of satellite orbits refer to [1] chapter 2. Among other experimental payloads, the satellite will carry a Ka Band communications experiment. For Ka Band links, the uplink frequency is in the range 29 to 30 GHz whereas the downlink frequency is between 19 and 20 GHz. Higher frequencies experience larger path losses which would place a larger power burden on the satellite bus. Therefore, the higher frequency band is used on the uplink as it is easier to increase the transmit power of the ground equipment.

The University of Technology, Sydney (UTS) is charged with building a low cost fast tracking Ka Band earth station to communicate with the satellite, [2]. The Ka band earth terminal must be capable of rapidly tracking the satellite both spatially and in frequency. The frequency uncertainties consist of the induced Doppler shifts and the

local oscillator (LO) drifts. For a LEO satellite at Ka band, the total frequency mismatch between the received signal and the receiver reference frequency can be very large, even many times the symbol rate As a result, the main research topic of this thesis involves proposing, analysing and proving new algorithms for the estimation of the frequency of a sinusoidal signal (a complex exponential). It is important to note, however, that although the thesis topic was conceived in the context of satellite systems, the resulting algorithms have applications in any area where the estimation of the frequency of a sinusoid is required. These areas include, to name a few, radar, sonar, biomedicine, radio astronomy, seismology, communications, etc…

1.1.1 Doppler shifts and Local Oscillator Drift

LEO satellites move with respect to an observer on earth. This relative motion introduces Doppler shifts into the communications signal. The Doppler shift is proportional to the satellite – earth station relative velocity and to the carrier frequency of the communications signal. Therefore, a Ka Band communications payload aboard a LEO satellite experiences large Doppler shifts, in the order of hundreds of KHz. These Doppler shifts maybe many times the magnitude of the symbol rate and therefore pose a significant problem for the communications system. For instance for a satellite in an 800 Km orbit, such as FedSat, the maximum normalised Doppler shift is in the order of 2×10^{-5} Hz/Hz. Multiplying that by the uplink carrier frequency at Ka Band, assuming a frequency of 30 GHz, we find that the uplink Doppler shift is about 600 KHz. Similarly the downlink Doppler shift would be, for a downlink frequency of 20 GHz, about 400 KHz.

Local Oscillator (LO) frequencies also drift due to thermal effects. A typical earth terminal – satellite – earth terminal link may contain four LOs, two in the uplink path and two in the downlink. The LOs are necessary for the up-conversion and down-conversion of the communications signal to and from the transmit and receive frequencies. Typical LO stabilities are in the order of 1 to 10 parts per million. At Ka band frequencies, this translates to drifts in the order of tens to hundreds of KHz. For instance, assuming LO stability of 10 parts per million, a Ka band uplink of 30 GHz would experience up to 300 KHz drift for each LO. If the two LOs in the earth station

and on-board the satellite drifted in opposite directions, their drifts would add up and we would have a total drift up to 600 KHz.

As the two LOs aboard the satellite (or in the earth station) are co-located, it is reasonable to expect that would experience similar thermal effects and thus would drift in the same direction by similar amounts. The resulting frequency uncertainty depends on whether an inverting or non-inverting transponder is used aboard the satellite, [3], chapter 8 pp. 4-5. Therefore, if no spectrum inversion is employed aboard the satellite, the Doppler shifts would add up, but the LO drifts would subtract. If on the other hand, spectrum inversion is used, the reverse happens and the Doppler shifts would subtract leaving the LO drifts to accumulate. The combined frequency uncertainty resulting from the Doppler shift and LO drifts would be in the order of a few KHz to a MHz. This would severely degrade the performance of the communications link and might make the demodulation of the signal impossible. Hence, the frequency error must be estimated and compensated for at the receiver prior to the demodulation of the signal.

1.1.2 The Application of Frequency Information to Spatial Tracking

Doppler shift measurements have been used for position determination in radar and search and rescue satellite systems [4], [5], [6] and [7]. Traditionally, the Doppler shift for an entire pass is measured at one or multiple stations and the position of a transmitter aboard the space craft or on the earth is determined knowing precisely the position of the other terminal involved in the communications [8]. In this thesis, we propose the use of the Doppler shift information obtained from the frequency acquisition and tracking process to determine the spatial position of the satellite for the purpose of earth station antenna pointing. As the frequency shift is related to the relative velocity of the satellite with respect to the earth station, knowing the position of the earth station, one can infer some information on the position of the satellite. Adding the Doppler rate, which is related to the satellite acceleration relative to the earth station, introduces another dimension to the problem and allows the satellite position to be determined in two dimensions. Accurate frequency measurements, combined with some restrictions on the satellite orbit allow the use the frequency information to determine the satellite position in real time. A Kalman filtering approach is used to this end.

1.2 Research objectives

The primary research objective of the thesis may now be summarised as follows:

"To develop new fast and efficient frequency estimation strategies for the purpose of the frequency tracking of a LEO satellite and to apply the resulting frequency information in assisting the spatial tracking of the satellite."

From this primary objective, three other key objectives emerge; these are:

- To completely characterise the LEO satellite orbit in a simplified fashion in order to allow for the determination of look-angles (Azimuth-Elevation and X-Y) and of Doppler shift and Doppler rate curves as a function of the observed maximum elevation. This objective involves the collation of some existing work, documenting work that is not easily found in the literature as well as the proposal of some new ideas.
- To develop frequency estimation algorithms for an unmodulated carrier that are computationally efficient and have good performance at low signal to noise ratios (SNR), near the breakdown threshold. The algorithms are analysed and simulated. They are also compared to existing algorithms.
- To study the application of the frequency estimation data to the orbit determination process for the purpose of spatial pointing and to present ways of implementing the Frequency Assisted Spatial Tracking concept. This applies the work of the two previous objectives in determining the position and frequency curves and the relationship between them and also in the gathering of the necessary frequency information.

These research objectives have resulted in some additional results being obtained which will be detailed in the original contributions section. The following section sets the structure of the thesis.

1.3 Thesis structure

The thesis is organised as follows:

Chapter 1 (**Introduction**) provides an overview of the thesis, sets the research problem into context and the contributions that have been made.

Chapter 2 (**Theory and Background**) presents the theory and literature background to the thesis. Firstly, the theory that is necessary to the development and analysis of the proposed ideas is presented. The Central Limit theorem and the assumed noise properties are discussed. These allow for the derivation of the asymptotic performance of the new estimators. The Cramer-Rao lower bound and the Kalman filtering theories are also discussed. The frequency estimation literature is then briefly reviewed. We present and discuss examples of phase based, correlation based, least squares, ARMA modelling and Kalman filtering estimators. These estimators, however, are generally computationally intensive or have high SNR thresholds. Therefore, they are unsuitable for real-time applications where fast, computationally efficient, frequency estimation is a necessity. The frequency domain estimators are computationally simple and suitable for Digital Signal Processor (DSP) implementation as they rely on the Fast Fourier Transform (FFT) algorithm. These estimators usually comprise a coarse estimation stage followed by a fine estimator.

Chapter 3 (**Complete Characterisation of Low Earth Orbits**) In this chapter we completely characterise a LEO satellite's orbit in terms of the maximum elevation that is observed at a particular earth station. A first order orbital model is assumed and no second order perturbations are included. The analysis is done in the Earth Centred Earth Fixed (ECEF) coordinate system. We present a simple orbital propagator in order to assess the results of the rest of the chapter. A number of simplifying assumptions, such as the constancy of the observed satellite velocity and the approximation of the observed satellite path by a great circle arc, are then used to derive simple expressions for the satellite position and Doppler shift and rate that are observed at the earth station. The resulting off-boresight error is used to gauge the accuracy of the derived equations. The validity of the assumptions is asserted by the small off-boresight error and Doppler shift error and rate errors with respect to the orbital propagator.

Chapter 4 (**Frequency Domain Frequency Estimation**) In this chapter we look at the estimation of the frequency of a sinusoidal signal using its Fourier spectrum. The Discrete Fourier Transform (DFT) is easily calculated using the computationally efficient Fast Fourier Transform (FFT) algorithm. We present a brief discussion of the DFT and the FFT. We then discuss the Maximum Bin Search (MBS) algorithm and its

associated frequency resolution. The MBS algorithm returns the frequency corresponding to the bin with the highest amplitude, that is, the bin closest to the signal. For a noisy signal, however, the presence of outliers results in an incorrect frequency estimate. The SNR threshold point where the frequency error rises rapidly due to the rapid increase in the probability of occurrence of outliers is then discussed. Quinn's work, [9], on the derivation of a simple expression for the threshold onset is examined and an error in the derivation is rectified. The practical effect of the error, however, is found to be small and decreasing with increasing number of samples, N, which renders Quinn's expression "valid" for sufficiently large N.

Chapter 5 (**Frequency Estimation by Interpolation on Fourier Coefficients**) This chapter forms a background for chapters 6 and 7 where a number of new frequency estimation algorithms are presented. We review the literature on the frequency estimation by interpolation on the Fourier coefficients of the signal. The bulk of the work was done by Quinn and presented in his book *The Estimation and Tracking of Frequency*. We start by discussing the theory and presenting the bounds on the performance of the estimators. Then we discuss a number of existing estimators, dividing them into interpolation on three and five coefficients. The interpolation on three coefficients category is in turn divided into interpolators on the raw coefficients and interpolators on the magnitudes of the coefficients. The performance of each of the algorithms is presented and discussed. This forms the background against which we assess the performance of the new algorithms presented in the following two chapters.

Chapter 6 (**Frequency Estimation by Interpolation on Fractional Fourier Coefficients**) We present, in this chapter, a number of new frequency estimation algorithms. These algorithms are analysed and their asymptotic performance derived. Simulation results are also presented to verify the theory. The estimators differ from those of the previous chapter in that they perform interpolation on the fractional Fourier coefficients (defined in appendix C). Their performance is shown to be identical to the corresponding standard algorithms. They, however, are shown to possess certain characteristics that make them suitable for iterative implementation in order to obtain some performance improvement at the expense of a slight increase in the computational load. After briefly introducing the fractional Fourier coefficients in section 6.2, we present the first of the algorithms named Fractional Fourier Coefficients Interpolation (FFCI) algorithm. This algorithm is shown to have the same asymptotic error

performance as Quinn's first algorithm but shifted by half a bin. The Magnitudes Only Interpolation (MOI) estimator is then presented and analysed. Its asymptotic performance is shown to be identical to the FFCI algorithm. We then discuss the Magnitudes Squared Interpolation (MSI) algorithm showing that it is severely biased away from zero and therefore is not an efficient estimator. The necessary modifications are then presented in the following section resulting in an unbiased estimator called the Modified MSI (MMSI). This estimator is, however, shown to be a variation on the MOI estimator.

Chapter 7 (**Iterative Frequency Domain Frequency Estimation**) In this chapter we examine iterative techniques for the estimation of frequency using the Fourier coefficients. We present, analyse and simulate a number of new algorithms. We start by discussing the binary search estimator named the dichotomous search of the periodogram peak. This algorithm does not require any non-linear operations on Fourier coefficients and is, therefore, computationally simple. The N data points, however, must be padded with zeroes up to $1.5N$ in order to achieve a performance that is of the same order as the CRB. We provide an explanation for this and consequently propose a new algorithm called the modified dichotomous search algorithm that eliminates the need for padding the data with zeroes. We also propose a new hybrid algorithm that uses an interpolation technique to initialise the search. This new algorithm has a performance that is practically on the CRB curve without zero-padding the data. We also discuss other existing hybrid estimators.

Chapter 8 (**Iterative Interpolation on the Fractional Fourier Coefficients**) The fractional Fourier coefficients interpolators, presented in chapter 6, are implemented iteratively. We start by considering the convergence of an estimator. The fixed point theorem that is used to prove the convergence is stated and discussed. We, then, present the iterative implementation of the algorithms introduced in chapter 6 and prove their convergence. The Iterative Fractional Fourier Coefficients Interpolator (IFFCI) and Iterative Magnitudes Only Interpolator (IMOI) are shown to converge almost surely (a.s.) in two iterations whereas the Iterative Magnitudes Squared Interpolator (IMSI), [10], is shown to require at least three iterations. The ratio of variances of the frequency error of all three algorithms to the asymptotic Cramer-Rao bound converges to a value of 1.0147.

Chapter 9 (**Frequency Assisted Spatial Tracking**) We propose and implement a new method for the application of the Doppler shift information to assist the spatial tracking of the satellite. We call this the FAST concept. We start by briefly reviewing the satellite positioning literature and the use of the Doppler shift for position determination. We then show that the Doppler shift and Doppler rate information completely characterise the look-angles to the satellite. The FAST concept is implemented using the simplified orbital equations presented in chapter 3. Furthermore, assuming that the maximum elevation of the orbit is known, the problem is reduced to tracking the satellite in one dimension. We propagate the longitude of the ascending node of the satellite and use the algorithm of Ali *et al*, [11], to calculate the expected maximum elevation of the orbit. We implement the spatial tracking algorithm using an extended one-dimensional Kalman filter. The filter is simulated at a signal to noise ratio of 0dB. The frequency estimator is assumed to achieve the CRB and a zero-mean Gaussian distributed frequency error with a variance equal to the CRB at a SNR of 0dB is added to the signal frequency prior to EKF spatial tracker.

Chapter 10 (**Conclusion**) reviews the thesis and summarises the main conclusions. Further areas of research are also suggested.

Appendix A (**Spherical Geometry**) Includes spherical trigonometry formulae needed for chapter 3.

Appendix B (**Asymptotic Theory**) This appendix reviews the asymptotic theory for random and deterministic sequences. The order notation is presented and its properties stated. Proofs for some of the properties are included.

Appendix C (**Fourier Coefficients of AWGN**) The properties of the Fourier coefficients of additive white Gaussian noise are discussed. The fractional Fourier coefficients are also presented. Finally, the signal plus noise case is reviewed.

Appendix D (**References**) lists the references cited in the course of the thesis.

1.4 Original contributions

The author believes that the following areas of research outlined in this thesis are original contributions:

1. The complete characterisation of LEO orbits: Assuming the orbit to be a great circle arc and the observed satellite angular velocity to be constant, the orbit of a LEO satellite is completely characterised in the ECEF frame (chapter 3). A new strategy for approximating the satellite's velocity by its value at the maximum elevation point instead of its minimum value is proposed (section 3.4). This is shown to result in lower errors overall by spreading them over the entire visibility period. The expressions for the latitude and longitude of the satellite as well as the transformation from the azimuth-elevation coordinate system to the X-Y coordinate system are derived (sections 3.5.3 and 3.5.4).

2. Approximate expression for threshold onset: In chapter 4 we discuss the SNR threshold for the estimation of frequency of a sinusoid in the frequency domain. We examine Quinn's method for the derivation of an approximate expression for the onset of the threshold (section 4.5). We show that Quinn made an error in the derivation and we rectify this mistake. The new expression is derived and compared to Quinn's and the effect of the error is shown to be very small that Quinn's expression is judged to still be "valid" for large N.

3. The proposal of two new interpolation frequency estimators: The FFCI and MOI frequency estimators are proposed in chapter 6, sections 6.3 and 6.4 respectively. The ratio of an estimator's asymptotic variance to the asymptotic CRB is used to as a performance gauge. Asymptotic analysis is done on both estimators and they are shown to be unbiased and have the same performance as Quinn's first estimator. Simulation results are used to verify the theoretical analysis. The estimators are also shown to have their best error variance at a frequency offset of zero. This fact as we demonstrate in chapter 8, makes them suitable for iterative implementation. A third algorithm, the MSI estimator, is also presented and shown to be severely biased.

4. Iterative frequency domain frequency estimation: (chapter 7). The dichotomous search of the periodogram is discussed in section 7.2. Insight is offered into the necessity to pad the data with zeroes in order to approach the CRB for the estimation of frequency. This insight is then used to propose a new estimator named the modified dichotomous search of the periodogram peak (section 7.3). This new estimator does not require the data to be padded with zeroes thereby reducing the computational load. In section 7.4 we propose the guided search of

the periodogram peak frequency estimation algorithm. This is a hybrid estimator that initialises the dichotomous search method using an interpolation estimator thus removing the need for zero padding the data.

5. Iterative implementation of the new interpolation frequency estimators: In chapter 8, we implement the interpolation algorithms proposed in chapter 6 iteratively. Proof of the convergence of the iterative algorithms is provided and their asymptotic performance obtained. The IFFCI estimator is presented in section 8.4 and the IMOI algorithm in section 8.5. These two algorithms are shown to converge in two iterations. The IMSI algorithm is shown in section 8.6 and is found to require three iterations to converge uniformly in frequency. All three algorithms converge to a ratio of 1.0147 to the asymptotic CRB.
6. Frequency Assisted Spatial Tracking (FAST) concept: The FAST concept is proposed and implemented in chapter 9. The suitability of the frequency information (Doppler shift and Doppler rate) to the spatial tracking of a LEO satellite is discussed and illustrated in section 9.4. The one dimensional FAST concept is implemented in section 9.5 for the simplified orbital model of chapter 3. An extended Kalman filter is used.

1.5 Publications

The following papers, relating directly to the thesis material, have been submitted, published and where appropriate presented by the author.

E. Aboutanios, “A Modified Dichotomous Search Frequency Estimator”, to be published in the IEEE Signal Processing Letters.

E. Aboutanios and S. Reisenfeld, “On the Use of Frequency Information for the Spatial Tracking of Low Earth Orbit Satellites”, submitted to the IEEE Transactions on Aerospace and Electronic Systems.

E. Aboutanios and S. Reisenfeld, "Frequency estimation and tracking for Low Earth Orbit Satellites," *IEEE Vehicular Technology Conference*, vol. 4, pp. 3003-3004, 2001.

E. Aboutanios and S. Reisenfeld, "Analysis of Frequency Assisted Spatial Tracking for Low Earth Orbit Satellites," presented at Sixth Ka Band Utilization Conference, Cleveland, Ohio, USA, 2000.

E. Aboutanios and S. Reisenfeld, "Frequency Acquisition and Tracking for FedSat Low Earth Orbit Satellite," presented at Fifth Ka Band Utilization Conference, Taormina, Sicily, 1999.

Chapter 2

Theory and Background

2.1 Introduction

This chapter aims to review the theory required for the development of the ideas in the thesis as well as set the thesis in the context of the literature. We start by discussing the Central Limit Theorem and the noise model in section 2.2. Section 2.3 deals with the Cramer-Rao inequality and the CRB in the context of frequency estimation. As an example, we derive the CRB of the estimate of the frequency of a sinusoidal signal in additive white noise assuming the phase and amplitude assumed are known. The theory of Kalman filtering is then introduced in section 2.4. The second aim of the chapter is addressed in section 2.5. We review the frequency estimation literature discussing algorithms that are representative of the various approaches. Finally, section 2.6 gives the concluding remarks to the chapter.

2.2 The Central Limit Theorem and Noise Properties

Statistical tools, like the central limit theorem are extremely useful to the analysis of the frequency estimation algorithms we will propose in later chapters. It is also essential that we gain an understanding of the relevant noise models. In this section we present a brief account of the CLT as well as the generalised noise assumptions that are used in [12], [13] and [14].

According to Pollard, [15], the CLT essentially means that "a sum of a large number of small, independent random variables is approximately normally distributed." The CLT, [16], is stated as follows:

Let X be a random variable with mean μ and variance σ^2 (both assumed to be finite). Suppose we have N independent realizations of X, denoted by $X_1, X_2, \cdots, X_N$. Define the random variable Z_N as

$$Z_N = \sum_{n=1}^{N} \frac{X_n - \mu}{\sqrt{N}\sigma}$$

Then the distribution of Z_N converges to the standard normal distribution, N(0,1), as $N \to \infty$.

In fact, a more general statement of the theorem does not require the random variables X_n to be identically distributed, [17]. However, in the context of the estimation of frequency, we usually deal with i.i.d. data samples.

The number of samples, N, that are normally employed in signal processing in general and in the estimation of frequency in particular, is usually "large". For instance, for the rest of the thesis and unless otherwise specified, $N = 1024$. This allows the use of the CLT to obtain the asymptotic properties of an algorithm with a relaxed set of assumptions on the noise.

Hannan, [12], discusses the estimation of the parameters of a sinusoidal model in the presence of noise. He takes the sinusoidal signal model to be

$$x(k) = a\cos(2\pi kf) + b\sin(2\pi kf) + w(k) \tag{2.1}$$

where a and b are the amplitudes of the in-phase and quadrature components and $a^2 + b^2 \neq 0$. The noise, $w(k)$, is assumed to be stationary and ergodic with zero mean and finite variance. Hannan shows that under these conditions, the periodogram maximiser (discussed in section 4.3) has the following property;

$$\lim_{N\to\infty} N\left(\hat{f}_N - f\right) = 0, \text{ a.s.} \tag{2.2}$$

That is, the frequency estimate obtained from the periodogram maximiser converges to the true frequency as the number of samples tends to infinity. Furthermore, the error itself is $o\left(N^{-1}\right)$. For a discussion of the order notation refer to appendix B.

The convergence properties of an estimator are largely dictated by the behaviour of the noise terms. Chen *et al*, in [18], consider the distribution of the periodogram ordinates of a strictly stationary time series, $w(k)$. Let $W(n)$ be the Fourier coefficients of $w(k)$. These are given by

$$W(n) = \frac{1}{N}\sum_{k=0}^{N-1} w(k) e^{-j2\pi\frac{kn}{N}}$$

They prove the convergence, in an almost sure sense, of the distribution of the coefficients y_n, defined as

$$y_n = \frac{N|W(n)|^2}{4\pi f_x(\omega_n)}$$

where $f_x(\omega)$ is the spectral density of $w(k)$ and $\omega = 2\pi f$ is the angular frequency.

An *et al*, in [19], discuss the maximum of the periodogram of a zero mean stationary process. They show that

$$\limsup_{N\to\infty} \sup_{\omega} \frac{N|W(n)|^2}{4\pi f_x(\omega)\ln N} \le 1, \text{ a.s.} \tag{2.3}$$

This ensures the convergence of the distribution of the Fourier coefficients noise terms and that they are $O\left(N^{-\frac{1}{2}}\ln N\right)$.

In the frequency estimation literature, the noise is usually assumed to be zero-mean Gaussian with variance σ^2. We adopt this assumption in our analysis in this thesis. The frequency dependent noise variance given by $4\pi f_x(\omega)$ is then replaced by σ^2. The distribution of the Fourier coefficients is also normal (see appendix C). The results obtained for the estimators of chapters 5, 6 and 8, although derived for the AWGN case, apply for the more general noise assumptions given here. The asymptotic results also continue to hold.

In the following section we discuss the Cramer-Rao lower bound (CRB) theory and give the bound for the estimation of the frequency of a complex sinusoid from N data samples.

2.3 The Cramer-Rao Lower Bound

It is important, when estimating a parameter (or a function of the parameter), to know the theoretical limit on the performance of the estimator. This is given by the lower bound on the variance of the resulting estimates. There are many bounds with differing merits and suitability depending on the application. These are presented in [20], section

3.3. The CRB, however, is the most important and most widely used for the estimation of the frequency of a sinusoid.

Suppose that X is a random variable with probability density function with parameter vector $\boldsymbol{\alpha}$,

$$\boldsymbol{\alpha} = [\alpha_1 \quad \ldots \quad \alpha_M]$$

For instance the parameter $\boldsymbol{\alpha}$ may consist of the amplitude and frequency for a sinusoid in noise. Denote the probability density of x by $f_\alpha(X)$ where the subscript α indicates the dependence of $f(X)$ on $\boldsymbol{\alpha}$. The Fisher information matrix, $\mathbf{J}$, is essentially a measure of the sensitivity (information content) of the distribution of X with respect to the parameter vector $\boldsymbol{\alpha}$. The information matrix must have a number of desirable properties such as the additive property [20]. This simply states that if two independent observations of X are made, say X_1 and X_2, then the information content of the combined observation $[X_1, X_2]^T$ is the sum of the information contents of each observation taken separately. The superscript (^{T}) is the transpose operator. The random variable, X, itself does not need to be a scalar and the notation is easily adapted to vector random variables. The elements of $\mathbf{J}$ are defined as

$$\begin{aligned} J_{k,l}(\boldsymbol{\alpha}) &= E_\alpha\left[\frac{\partial \ln(f_\alpha(Y))}{\partial \alpha_k}\frac{\partial \ln(f_\alpha(Y))}{\partial \alpha_l}\right] \\ &= -E_\alpha\left[\frac{\partial^2 \ln(f_\alpha(Y))}{\partial \alpha_k \partial \alpha_l}\right] \end{aligned} \tag{2.4}$$

for $k = 1 \ldots M$ and $l = 1 \ldots M$.

Now we are ready to present the Cramer-Rao inequality. Suppose that we are estimating a function, in general a K-dimensional vector function, of $\boldsymbol{\alpha}$, say $\mathbf{g}(\boldsymbol{\alpha})$. Then a lower bound on the variance of an unbiased estimator of the $\mathbf{g}(\boldsymbol{\alpha})$, say $\hat{\mathbf{g}}(\boldsymbol{\alpha})$, is

$$E\left[(\hat{\mathbf{g}}(\boldsymbol{\alpha}) - \mathbf{g}(\boldsymbol{\alpha}))(\hat{\mathbf{g}}(\boldsymbol{\alpha}) - \mathbf{g}(\boldsymbol{\alpha}))^T\right] \geq \mathbf{G}(\boldsymbol{\alpha})\mathbf{J}^{-1}(\boldsymbol{\alpha})\mathbf{G}^T(\boldsymbol{\alpha}) \tag{2.5}$$

where $\mathbf{G}(\boldsymbol{\alpha})$ is the Jacobian of the function $\mathbf{g}(\boldsymbol{\alpha})$. The Jacobian matrix is of $K \times M$ dimensions.

$$G_{k,l}(\boldsymbol{\alpha}) = \left[\frac{\partial g_l(\boldsymbol{\alpha})}{\partial \alpha_k} \right]$$

As a special case, suppose that the function is $\mathbf{g}(\boldsymbol{\alpha}) = \boldsymbol{\alpha}$. The Jacobian is then equal to the identity matrix $\mathbf{I}$ and the CRB is given by

$$E\left[(\hat{\boldsymbol{\alpha}} - \boldsymbol{\alpha})(\hat{\boldsymbol{\alpha}} - \boldsymbol{\alpha})^T\right] \geq \mathbf{J}^{-1}(\boldsymbol{\alpha}) \tag{2.6}$$

As a further simplification, consider the case where we are estimating a scalar parameter α. The CRB then becomes

$$\mathrm{var}\left[\hat{\alpha}\right] \geq -\frac{1}{E_\alpha\left[\dfrac{d^2 \ln\left(f_\alpha(Y)\right)}{d\alpha^2}\right]} \tag{2.7}$$

If an estimator achieves the CRB, then that estimator is identical to the ML estimate of the parameter. The ML estimate is simply the value of the parameter that maximises the likelihood of seeing the particular observation it was obtained from. The ML estimator may not exist or maybe prohibitively computationally expensive.

In the following we present the CRB for the estimates of the frequency of a sinusoidal signal. We will, for illustration purposes, derive the CRB for the estimates of the frequency.

2.3.1 CRB for the Estimate of the Frequency of a Sinusoid

The CRB expressions for the estimation of the parameters of a sinusoid were derived by Rife in [21], pp. 26-31. Here, we will assume that the amplitude and phase are known and derive the bound on the estimates of the frequency. Without loss of generality we set the amplitude and the initial phase to 1 and 0 respectively. Consider the following complex signal model

$$x(k) = e^{j2\pi k \frac{f}{f_s}} + w(k)$$

where f_s is the sampling frequency and $w(k)$ are i.i.d. zero mean Gaussian noise with variance σ^2. The signal frequency, f, is to be estimated using N independent observations. Now, the density of the $w(k)$ is given by

$$f_W(w) = \frac{1}{\sqrt{2\pi\sigma^2}} e^{-\frac{u^2+v^2}{2\sigma^2}}$$

where $w(k) = u(k) + jv(k)$. Now writing $w(k)$ as

$$w(k) = x(k) - e^{j2\pi k \frac{f}{f_s}}$$

the pdf of $x(k)$ given f, is

$$f_X(x,f) = \frac{1}{\sqrt{2\pi\sigma^2}} e^{-\frac{\left(x_R(k) - \cos\left(2\pi k \frac{f}{f_s}\right)\right)^2 + \left(x_I(k) - \sin\left(2\pi k \frac{f}{f_s}\right)\right)^2}{2\sigma^2}} \tag{2.8}$$

where the measurements, $x(k)$, are written as $x_R(k) + jx_I(k)$. Since the noise terms are independent, the joint pdf of N samples is the product of the individual pdfs. That is

$$f_X(\mathbf{x},f) = \prod_{k=0}^{N-1} \frac{1}{\sqrt{2\pi\sigma^2}} e^{-\frac{\left(x_R(k) - \cos\left(2\pi k \frac{f}{f_s}\right)\right)^2 + \left(x_I(k) - \sin\left(2\pi k \frac{f}{f_s}\right)\right)^2}{2\sigma^2}}$$

$$= \left(\frac{1}{\sqrt{2\pi\sigma^2}}\right)^N e^{-\frac{\sum_{k=0}^{N-1}\left\{\left(x_R(k) - \cos\left(2\pi k \frac{f}{f_s}\right)\right)^2 + \left(x_I(k) - \sin\left(2\pi k \frac{f}{f_s}\right)\right)^2\right\}}{2\sigma^2}}$$

The log-likelihood function is given by

$$\ln\left(f_X(\mathbf{x},f)\right) = C - \sum_{k=0}^{N-1} \left\{ \frac{\left(x_R(k) - \cos\left(2\pi k \frac{f}{f_s}\right)\right)^2 + \left(x_I(k) - \sin\left(2\pi k \frac{f}{f_s}\right)\right)^2}{2\sigma^2} \right\}$$

where C is a constant. The expectation of the second derivative of the log-likelihood with respect to f, after carrying out the differentiation and necessary simplifications, is

$$E\left[\frac{d^2 \ln\left(f_X(\mathbf{x}),f\right)}{df^2}\right] = -\left(\frac{2\pi}{f_s\sigma}\right)^2 \sum_{k=0}^{N-1} \left\{ k^2 \left(E[x_R(k)] \cos\left(2\pi k \frac{f}{f_s}\right) + E[x_I(k)] \sin\left(2\pi k \frac{f}{f_s}\right) \right) \right\}$$

However, the real and imaginary parts of the noise terms are zero mean. Therefore,

$$E[x_R(k)] = \cos\left(\frac{2\pi kf}{f_s}\right)$$

and

$$E[x_I(k)] = \sin\left(\frac{2\pi kf}{f_s}\right)$$

and consequently the expression above reduces to

$$E\left[\frac{d^2 \ln(f_X(\mathbf{x}), f)}{df^2}\right] = -\left(\frac{2\pi}{f_s \sigma}\right)^2 \sum_{k=0}^{N-1} k^2$$
$$= -\left(\frac{2\pi}{f_s \sigma}\right)^2 \frac{N(N-1)(2N-1)}{6}$$

Thus, using (2.7), the CRB for the estimation of the frequency of a sinusoid assuming the phase is known is given by

$$\text{var}(\hat{f}) \geq -\frac{1}{E\left[\frac{d^2 \ln(f_X(\mathbf{x}), f)}{df^2}\right]}$$
$$= \frac{6 f_s^2}{(2\pi)^2 \rho N(N-1)(2N-1)} \tag{2.9}$$

Here we define the signal to noise ratio (SNR), ρ, as A^2/σ^2, where in our case the amplitude of the sinusoidal signal A is assumed to be 1. The SNR in dB is

$$\rho(\text{dB}) = 10 \log_{10}\left(\frac{A^2}{\sigma^2}\right) \tag{2.10}$$

The expression in (2.9) is identical to that obtained by Rife, [21] pp. 29, for the case where the phase known and the sampling started at $t = 0$. If the phase is unknown, the parameter vector is two dimensional consisting of the frequency and the phase. The resulting CRB for the estimation of the frequency is,

$$\text{CRB} = \frac{6 f_s^2}{(2\pi)^2 \rho N(N^2 - 1)} \tag{2.11}$$

For large N, the term $N^2 - 1 \approx N^2$ and the asymptotic CRB expression becomes

$$\text{AsymptoticCRB} = \frac{6 f_s^2}{(2\pi)^2 \rho N^3} \tag{2.12}$$

2.4 Kalman Filtering

Kalman filtering theory has been well published in the literature, [22] and [23], and has enjoyed application in many areas. For instance, in [24-26], the authors employ Kalman filtering for the purpose of target localisation and radar tracking. In, [27, 28] the Kalman filter is applied to the satellite orbit determination problem. And in [29-31], Extended Kalman Filters (EKF) are used to track the frequency of a signal.

The Kalman filter allows the estimation of the state of the system and the use of the state estimate to predict and filter the output at the next time step. The filter takes the measurement and modelling noise into account. The original Kalman filter was derived for linear systems. In the case of a non-linear system, it is possible to linearise the system equations. The linearised Kalman filter is discussed by Montenbruck in [32] pp. 281. The Kalman filtering equations, however, have been extended to cover non-linear systems. The resulting algorithm is called the Extended Kalman Filter or EKF. In this section we will briefly review both the Kalman filter and the EKF.

2.4.1 The Kalman Filter – Linear, Time-Invariant Case

Consider a system whose state is represented, at time n, by the vector $\mathbf{X}_n$. Let $\mathbf{\Phi}$ be the state transition matrix. The state of the system at time n is, therefore, given by

$$\mathbf{X}_n = \mathbf{\Phi}\mathbf{X}_{n-1} + \mathbf{U}_{n-1} \tag{2.13}$$

where $\mathbf{U}_{n-1}$ is the system model noise vector. For satellite tracking, for instance, it can account for perturbations that are left out of the chosen model, such as atmospheric drag. Let $\mathbf{Y}_n$ be the measurements vector at time n. This is related to the state vector by the observation matrix, $\mathbf{M}$,

$$\mathbf{Y}_n = \mathbf{M}\mathbf{X}_n + \mathbf{V}_n \tag{2.14}$$

$\mathbf{V}_n$ is a vector of measurement noise. In the following, an asterisk (*) over a variable will be used to indicate the predicted value of the variable and the over-hat the filtered value. The state transition matrix is used to propagate the state of the system from time n to time $n+1$. Thus, the predictor equation is

$$\mathbf{X}_n^* = \mathbf{\Phi}\hat{\mathbf{X}}_{n-1} \tag{2.15}$$

The error between the observation and the prediction is then given by

$$\Delta\mathbf{Y}_n = \mathbf{Y}_n - \mathbf{M}\mathbf{X}_n^* \tag{2.16}$$

The filtered state at time n is obtained by adjusting the predicted state by the weighted prediction error. The weight matrix, $\mathbf{K}_n$ is called the Kalman gain, and the Kalman filtering equation is shown below,

$$\hat{\mathbf{X}}_n = \mathbf{X}_n^* + \mathbf{K}_n\left(\mathbf{Y}_n - \mathbf{M}\mathbf{X}_\mathbf{n}^*\right) \tag{2.17}$$

The Kalman filter adjusts the weights based on the quality of the measurements which is indicated by the covariance matrix. The weight update equation is,

$$\mathbf{K}_n = \mathbf{P}_n^*\mathbf{M}^T\left[\mathbf{R}_n + \mathbf{M}\mathbf{P}_n^*\mathbf{M}^T\right]^{-1} \tag{2.18}$$

The predictor covariance matrix, $\mathbf{P}_n^*$, is obtained from

$$\mathbf{P}_n^* = \mathbf{\Phi}\overline{\mathbf{P}}_{n-1}\mathbf{\Phi}^T + \mathbf{Q}_n \tag{2.19}$$

where $\mathbf{Q}_n$ and $\mathbf{R}_\mathbf{n}$ are the covariance matrices of the model noise ($\mathbf{U}_n$) and the measurement vector respectively. That is

$$\mathbf{Q}_n^* = \mathrm{COV}\left(\mathbf{U}_n\right)$$

and

$$\mathbf{R}_n = \mathrm{COV}\left(\mathbf{Y}_n\right)$$

Finally, the covariance matrix of the smoothed estimates, $\overline{\mathbf{P}}_n$, is updated using the following recursion,

$$\overline{\mathbf{P}}_n = \left(\mathbf{I} - \mathbf{K}_n\mathbf{M}_n\right)\mathbf{P}_n^* \tag{2.20}$$

2.4.2 Non-Linear Case – The EKF

Now suppose that we have a non-linear system dynamic model. This, for instance, is the case when tracking the satellite using the measured Doppler shift and rate. The Kalman filter can, as demonstrated by Montenbruck [32], pp. 281, be applied to a linearised form of the equations. However, the time interval for the prediction step must be small enough to allow the non-linearities in the system model to be neglected. The EKF, on the other hand, avoids this restriction by taking full advantage of the sequential estimation process.

Let the observation vector be related to the state vector by,

$$\mathbf{Y}_n = \mathbf{G}(\mathbf{X}_n) + \mathbf{V}_n \tag{2.21}$$

where $\mathbf{G}(\mathbf{X}_n)$ is a vector of non-linear functions of the state variable $\mathbf{X}_n$. That is,

$$\mathbf{G}(\mathbf{X}_n) = \begin{bmatrix} g_1(\mathbf{X}_n) \\ g_2(\mathbf{X}_n) \\ \vdots \\ g_n(\mathbf{X}_n) \end{bmatrix} \tag{2.22}$$

The EKF effectively linearises the model by relating a change in the state variable, $\delta\mathbf{X}_n$, to the corresponding change in the observation, $\delta\mathbf{Y}_n$,

$$\delta\mathbf{Y}_n = \mathbf{M}(\mathbf{X}_n)\delta\mathbf{X}_n + \mathbf{V}_n \tag{2.23}$$

where

$$\left[\mathbf{M}(\mathbf{X}_n)\right]_{i,j} = \left.\frac{\partial g_i(\mathbf{X})}{\partial x_j}\right|_{\mathbf{X}=\mathbf{X}_n} \tag{2.24}$$

Similarly to the original Kalman filter, the EKF adjusts the predicted value at time n by the weighted prediction error to give the filtered state variable at time n.

$$\hat{\mathbf{X}}_n = \mathbf{X}_n^* + \mathbf{K}_n\left[\mathbf{Y}_n - \mathbf{G}(\mathbf{X}_n^*)\right] \tag{2.25}$$

where we see that the last estimate was used in the function $\mathbf{G}(\mathbf{X}_n)$. This effectively amounts to resetting our reference state to the last estimate. The Kalman gain is again given by the weight update equation,

$$\mathbf{K}_n = \mathbf{P}_n^* \mathbf{M}^T \left[\mathbf{R}_n + \mathbf{M} \mathbf{P}_n^* \mathbf{M}^T \right]^{-1} \tag{2.26}$$

Now we address the state transition equation. The state at time n is generally a non-linear function of the state at time $n-1$, say

$$\mathbf{X}_n = \mathbf{H}(\mathbf{X}_{n-1})$$

where

$$\mathbf{H}(\mathbf{X}_n) = \begin{bmatrix} h_1(\mathbf{X}_n) \\ h_2(\mathbf{X}_n) \\ \vdots \\ h_n(\mathbf{X}_n) \end{bmatrix}$$

Employing the same linearisation process used in equation (2.23), we get

$$\delta \mathbf{X}_n = \mathbf{\Phi}_n \delta \mathbf{X}_{n-1} \tag{2.27}$$

where the state transition matrix, $\mathbf{\Phi}_n$, is

$$\left[\mathbf{\Phi}_n \right]_{i,j} = \left. \frac{\partial h_i(\mathbf{X})}{\partial x_j} \right|_{\mathbf{X} = \hat{\mathbf{X}}_{n-1}} \tag{2.28}$$

Thus the prediction equations become

$$\mathbf{X}_n^* = \mathbf{H}\left(\hat{\mathbf{X}}_{n-1} \right) \tag{2.29}$$

and

$$\mathbf{P}_n^* = \mathbf{\Phi}_n \overline{\mathbf{P}}_{n-1} \mathbf{\Phi}_n^T \tag{2.30}$$

Finally, the covariance matrix of the filtered estimates is updated using

$$\overline{\mathbf{P}}_n = (\mathbf{I} - \mathbf{K}_n \mathbf{M}_n) \mathbf{P}_n^* \tag{2.31}$$

The EKF has proven successful in a large number of applications. In chapter 9, the EKF will be used to derive the spatial information of a LEO satellite using the measured Doppler shift. As we will see in the next section, the EKF has also been applied to the problem of frequency estimation and tracking.

2.5 Frequency Estimation

The problem of the estimation of frequency is relevant in a number of areas such as communications, radar, sonar, biomedicine, electrical power generation and distribution, seismology and astronomy. The wealth of literature on the topic testifies to its importance, [12, 21, 33-36]. In this section, we will review the general literature that is relevant to the topic. The published material that is immediately connected with the concepts of the thesis is dealt with in the appropriate chapters. For instance, the interpolation on Fourier coefficients algorithms are reviewed in chapter 5, immediately prior to the proposal of the new algorithms of chapter 6. This helps set the background at a more useful point in the thesis.

Boashash published, in [35, 36], a tutorial on the estimation and interpretation of the "Instantaneous Frequency" (IF) of a signal. While the frequency of a sinusoid is easily defined and intuitively understood, that of a general signal, whose parameters are time-varying, is not. The IF of a signal is defined as the derivative of the phase of its corresponding analytic signal. The analytic signal is obtained from the real signal using the Hilbert transform, [37] pp. 79-83. Boashash states that the IF of a signal is a parameter of practical importance in many situations such as seismology, radar, etc. where it is a good descriptor of some physical phenomena.

In many cases, the signals that are encountered are stationary, or quasi-stationary. That is, the signal parameters are constant or slowly varying that they can be assumed constant over the observation window. This is the case for the Doppler frequency estimation of a LEO satellite, for instance. The Doppler shift and Doppler rate, as is shown in section 3.6, are proportional to the carrier frequency and the relative velocity between the source and the receiver. For a communications link such as the FedSat Ka band link (refer to section 1.1), the maximum Doppler rate for the downlink carrier frequency of 30 GHz is around 6 kHz/s at zenith for an overhead pass. The UTS fast tracking Ka band earth station uses an observation window 1024 samples long at a sampling frequency of 1 MHz. Thus, the maximum frequency drift that might be experienced in one observation window is 6Hz. This validates the assumption that the frequency is essentially constant. The assumption allows for the construction of simple estimation algorithms such as the estimators we propose in this thesis. In fact, a compromise is usually made when setting the observation window length. The longer

the observation window is, the lower the estimation variance. This trend is, however, upset by the drift of the frequency over the observation interval which then invalidates the assumption of a constant signal frequency.

Accurate frequency estimation plays a significant role in power systems both in the protection of power equipment and energy measurements [33]. The authors of [38, 39] evaluate some frequency estimation and tracking methods for the application of power system protection and control. These are used to measure the fundamental frequency of the system. In [40], the estimation of frequency is applied to the speed (and torque) control of induction motors. This method is non-intrusive and eliminates the need for mounting tachometers or position transducers on the motor shaft.

The estimation of the frequency of a received signal is also important in radar technology. The estimation of the Doppler shift of a moving target in the context of a Doppler radar is examined in [41]. A linearly modulated signal (linear chirp) is usually reflected off the target and its frequency estimated. The resulting Doppler shift is used to deduce the speed of the target.

In a mobile or satellite communications system, there is usually a mismatch at the receiver between the reference frequency and the received signal carrier. This mismatch must be removed and the actual carrier frequency recovered in order to demodulate the signal. Significant work research has been done on the estimation of the frequency of a modulated signal [42-48]. In a LEO satellite system, [49], the Doppler shifts can be many times the symbol rate. Many LEO communications links include a beacon frequency that is used to estimate the Doppler shift. In the absence of a beacon, the modulated signal itself must be used to in the synchronisation process. For phase shift keying (PSK) modulation schemes, the modulated signal is passed through a non-linearity, usually an M^{th} power device, to remove the modulation, [47]. Cowley, in [46], examines the estimation of the frequency from PSK packets and derives the CRB for BPSK and QPSK. Rice *et al*, [50], and Steendam *et al*, [48], derive the CRB for Quadrature Amplitude Modulation (QAM) based estimation of the phase and the frequency.

Besides the carrier recovery for the purpose of acquiring and demodulating the signal, the Doppler shifts measurements of a satellite-observer link have been used in the spatial tracking of the satellite, [51, 52]. In the Cospas-Sarsat system, the frequency information is used to locate a beacon on the Earth for search and rescue purposes, [53].

In another application, Ali *et al*, [54], have proposed the use of the measured Doppler shift profile to regulate the multiple access of a LEO satellite. The Doppler profile seen at an earth terminal is used to determine the period of time that the satellite is above a certain elevation. The earth station then communicates to the satellite only above this elevation angle, thereby regulating the access of multiple earth stations.

The application of the estimator usually dictates the specification that the algorithm must satisfy. In the following we look at the some of the methods that have been proposed for the estimation of the frequency of a signal in general and a sinusoidal signal in particular.

2.5.1 Phase-Based Frequency Estimation

As the signal frequency is the rate of change of the phase, it seems natural to use the phases of the data samples to obtain a frequency estimate. There has been considerable work published on the subject, [55-62]. Most of the applications tend to be in burst mode communications where rapid carrier acquisition from a small number of samples is required. Tretter, in [60], suggested a least squares approach to estimate the frequency and initial phase of a sinusoid. The general sinusoidal signal model is

$$x(k) = Ae^{j\left[2\pi k\frac{f}{f_s}+\theta\right]} + w(k),\ k = 0,1,\ldots N-1 \tag{2.32}$$

where A and θ are the amplitude and initial phase of the signal respectively. The noise terms, $w(k)$, are zero-mean AWGN with variance σ^2. Tretter established that, at high SNR ($\rho = \frac{A^2}{\sigma^2}$), the signal model can be re-written as

$$x(k) \approx e^{j\left[2\pi k\frac{f}{f_s}+\theta+u(k)\right]} \tag{2.33}$$

The noise terms $u(k)$ are zero-mean AWGN with variance $\frac{\sigma^2}{2A^2}$. Thus the signal phase is given by

$$\angle x(k) = 2\pi k\frac{f}{f_s} + \theta + u(k) \tag{2.34}$$

Tretter, thus, applied a least squares estimator to the collected phase trajectory given by equation (2.34). He showed that, at high SNR, the estimator is efficient, that is it achieves the CRB. A drawback of his approach, though, is that the phase must be unwrapped prior to the estimation process. Kay, in [59], discussed Tretter's method and suggested a new algorithm that is identical to Tretter's in performance but avoids the phase unwrapping problem. Kay turned his attention to the differential phase data. Let

$$\begin{aligned}\Delta(k) &= \angle x(k) - \angle x(k-1) \\ &= 2\pi\frac{f}{f_s} + u(k) - u(k-1)\end{aligned} \tag{2.35}$$

The problem is now to estimate the mean of the sequence $\Delta(k)$. As the noise is now coloured, Kay takes the covariance matrix, $\mathbf{C}$, of the phase differences into account. Equation (2.35) represents a moving average process with coefficients 1 and -1. Let $\mathbf{\Delta} = [\Delta(0) \quad \Delta(1) \quad \cdots \quad \Delta(N-2)]^T$ (note we obtain $N-1$ differential phase data points from N data samples) and $\mathbf{1} = [1 \quad 1 \quad \cdots \quad 1]^T$. The ML estimate of the frequency is

$$\hat{f} = \frac{f_s}{2\pi}\frac{\mathbf{1}^T\mathbf{C}^{-1}\mathbf{\Delta}}{\mathbf{1}^T\mathbf{C}^{-1}\mathbf{1}} \tag{2.36}$$

And the variance of the estimator is

$$\text{var}\left[\hat{f}\right] = \frac{f_s}{2\pi}\frac{1}{\mathbf{1}^T\mathbf{C}^{-1}\mathbf{1}} \tag{2.37}$$

Going through the algebraic manipulations, Kay finally arrives at the following estimator

$$\hat{f} = \frac{f_s}{2\pi}\sum_{k=1}^{N-1}\alpha(k)\angle x(k)x^*(k-1) \tag{2.38}$$

where $\Delta(k)$ was rewritten as $\angle x(k)x^*(k-1)$ and $\alpha(k)$ are the window weights, computed using the following expression

$$\alpha(k) = \frac{3N}{2\left(N^2-1\right)}\left\{1 - \left[\frac{k - \frac{N}{2} + 1}{\frac{N}{2}}\right]^2\right\} \tag{2.39}$$

The variance, in equation (2.37) is shown to be equal to the CRB. The parabolic window results in the optimality of the estimator at high SNR. Kay points out that replacing the window by a rectangular one, would result in a simpler, but worse performing estimator. This is shown in the following equation.

$$\hat{f} = \frac{f_s}{2\pi(N-1)} \sum_{k=1}^{N-1} \angle x(k) x^*(k-1) \tag{2.40}$$

Although the estimators presented above are computationally simple, they perform well only at high SNR. Kay found that for $N = 24$ the ML estimator (that is the Maximum Likelihood estimator which is equivalent to the periodogram maximiser) has a threshold at SNR = -1dB, whereas the weighted estimator given here has a threshold at 6dB.

Lang and Musicus, in [63], commented on Kay's method and showed that it can be derived from Tretter's formula by employing a summation by parts. They also applied the algorithm to the estimation of the frequency of a chirp signal. They suggested an adaptive formulation of the algorithm that continually updates the frequency estimate with each new phase observation. The adaptive estimator, however, requires the phase unwrapping algorithm. Furthermore, they studied the threshold effect and explained the effect of a phase unwrapping failure on the estimator performance. For high SNR, the unwrapped phases are almost normally distributed and the frequency estimates behave regularly. As the SNR drops, the likelihood of a phase error increases. The phase of a sample might be incorrectly unwrapped resulting in a $\pm 2\pi$ phase error in the phases of all succeeding samples.

Fiore, in [57], looked at simplifying the computational requirements of Kay's estimator for the purpose of high speed applications. He proposed the replacement of the parabolic weighing function of equation (2.39) with a trapezoidal function. This eliminates the need for multiply operations and leads to a simpler recursive implementation of the estimator using finite phase differencing. Inspired by the work of Lang and Musicus, discussed in the previous paragraph, he also extended the recursive implementation to the estimation of chirp rate. The theoretical aspects of Kay's estimator have also been discussed in the literature. Clarkson *et al*, [56], for instance, derived an approximate expression for the variance of Kay's estimator and calculated the SNR threshold. They also optimised the window weights in order to improve the variance threshold. Fowler, [64], suggested lowering the threshold of the phased

estimators by pre-processing the signal by a bank of overlapping filters. This improves the SNR in each of the bands. The band containing the signal is chosen by the pre-processor and Kay's estimator used as a fine frequency estimator.

2.5.2 Correlation Based Frequency Estimation

Autocorrelation based estimators, [58, 62, 65-67], are closely related to the phase based estimation discussed in the previous section. The estimation of the frequency of a sinusoidal signal from arbitrary sets of correlations coefficients is studied by Volker in [68].

The un-normalised autocorrelation of a complex signal $x(k)$ is defined as

$$R(l) = \sum_{k=l+1}^{N} x(k)x^*(N-k),\ l = 0,1,\ldots N-1 \tag{2.41}$$

Whereas the normalised autocorrelation function given by

$$\overline{R}(l) = \frac{1}{N-l} R(l) \tag{2.42}$$

The estimators of equations (2.38) and (2.40) are, at high SNR, equivalent to the autocorrelation function with $l = 1$. Kay, [59], gave two alternate expressions to the two estimators;

$$\hat{f} = \frac{f_s}{2\pi} \angle \sum_{k=1}^{N-1} \alpha(k)x(k)x^*(k-1) \tag{2.43}$$

and

$$\hat{f} = \frac{f_s}{2\pi(N-1)} \angle \sum_{k=1}^{N-1} x(k)x^*(k-1) \tag{2.44}$$

These equations illustrate the relation to the autocorrelation function more clearly. The last expression, in particular, is rewritten in terms of $\overline{R}(1)$ as

$$\hat{f} = \frac{f_s}{2\pi} \angle \overline{R}(1)$$

Fitz, [58], generalised Kay's estimator using the un-normalised autocorrelation function. He argued that higher lags would result in improved frequency estimates as

the autocorrelation function is then less affected by noise. In fact the optimum lag is shown in [69] to be $l = \frac{2N}{3}$. For $M << N$, Fitz' estimator has the form,

$$\hat{f} = \frac{f_s}{2\pi M(M+1)(M+2)} \sum_{l=1}^{M} l \angle R(l) \tag{2.45}$$

While the estimator has improved performance over Kay's algorithm, it only performs well at moderate SNR values.

Employing a similar approach to Fitz, Luise and Reggiannini suggested an estimation algorithm using the sample autocorrelation function of the data, [67]. Their estimator is given by the following expression

$$\hat{f} = \frac{f_s}{\pi(M+1)} \angle \sum_{l=1}^{M} \overline{R}(l) \tag{2.46}$$

The estimator implementation suggested by the authors lends itself to an FIR filtering approach. The estimator has a unambiguous estimation range, Δf, given by

$$\Delta f = \frac{f_s}{M+1}$$

They showed that the optimum value of M is given by $\frac{N}{2}$. Using their suggested implementation, the complexity of the algorithm is $O(NM)$. Thus, the algorithm is $O(N^2)$ the optimal value of M. This is much less efficient than an FFT based algorithm. The authors, however, noted that for the applications of interest, namely burst mode communications, only a small number of samples is available. They also suggested reducing M, for instance to $\frac{N}{4}$, in order to reduce the number of required operations without losing much of the optimality of the algorithm.

2.5.3 Least Squares Frequency Estimation

The papers discussed so far maximise the likelihood function in order to derive a frequency estimator. Another approach is to use a minimization of the sum of the squares to derive a frequency estimator, [70-72]. In [73] a least squares fit of the phase

trajectory for the estimation of the Doppler shift and rate of a LEO satellite communications link.

The continuous-time received signal of a satellite link is given by

$$x(t) = s(t) + w(t)$$

where $s(t) = A\cos(\theta(t))$ and $w(t)$ are i.i.d. Gaussian noise with variance σ^2. Expanding the received signal phase at time $t + \Delta t$ into a Taylor series yields

$$\theta(t + \Delta t) = \theta(t) + \omega(t)\Delta t + \frac{\dot{\omega}(t)}{2!}\Delta t^2 + O(\Delta t^3)$$

where $\omega(t)$ is the Doppler shift and $\dot{\omega}(t)$ the Doppler rate. This suggests that the phase can be approximated by polynomial of order p. The polynomial coefficients are given by the Doppler shift and its derivatives. In [73], first and second order polynomial fit algorithms are implemented. However, only the second order algorithm is presented here. The Doppler shift and rate are then estimated using the least squares fit of a second order polynomial to the received phase trajectory. Let $\tilde{\theta}(k)$ and $\hat{\theta}(k)$ be the phases of the k^{th} received sample and estimate respectively. We have

$$\hat{\theta}(k) = \hat{\theta}_0 + \hat{\omega}T_s + \frac{\hat{\dot{\omega}}}{2}T_s^2 \tag{2.47}$$

T_s being the sampling period and $\hat{\theta}_0 = \hat{\theta}(0)$.

The cost function, given by

$$\sum_{k=1}^{N}\left[\tilde{\theta}(k) - \hat{\theta}(k)\right]^2 \tag{2.48}$$

is minimized to give the estimates $\hat{\theta}_0, \hat{\omega}$ and $\hat{\dot{\omega}}$. The solution for the quantities of interest, namely $\hat{\omega}$ and $\hat{\dot{\omega}}$ is

$$\hat{\omega} = \frac{\alpha_N}{T_s}\sum_{k=1}^{N}\left\{\tilde{\theta}(k)\left[\frac{\beta_N}{15}k - \frac{2N+1}{10}\gamma_N - (N+1)k^2\right]\right\} \tag{2.49}$$

and

$$\hat{\dot{\omega}} = \frac{2\alpha_N}{T_s^2}\sum_{k=1}^{N}\left\{\tilde{\theta}(k)\left[k^2 - (N+1)k + \frac{\gamma_N}{6}\right]\right\} \tag{2.50}$$

where

$$\alpha_N = \frac{180}{N\left(N^2-1\right)\left(N^2-4\right)},$$

$$\beta_N = (2N+1)(8N+11)$$

and $$\gamma_N = (N+1)(N+2)$$

This algorithm requires the unwrapped phase trajectory. To this end, the authors suggest calculating the differential phases of the samples and then integrating up to the current sample. That is

$$\Delta\tilde{\theta}(k) = \cos^{-1}\left[\frac{x_R(k)x_R(k-1)+x_I(k)x_I(k-1)}{\sqrt{x_R^2(k)+x_I^2(k)}\sqrt{x_R^2(k-1)+x_I^2(k-1)}}\right] \tag{2.51}$$

and

$$\tilde{\theta}_k(k) = \sum_{l=0}^{k}\Delta\tilde{\theta}(l)$$

The estimator can be implemented in either a batch mode or recursive form. The batch mode is equivalent to a sliding window algorithm.

2.5.4 Frequency Estimation Using ARMA Modeling

A sinusoidal signal can be modeled as an Autoregressive Moving Average (ARMA) process, allowing the frequency to be estimated, [41, 74, 75]. Quinn and Fernandes, [14], iteratively fit an ARMA(2,2) model to the sinusoidal data. Quinn, [76] showed that the technique can be interpreted as the maximiser of a smoothed periodogram of the signal. He also generalised it to the estimation of the frequencies of multiple sinusoids. The technique is again reviewed in [34], chapter 4.

Consider the real sinusoid

$$x(k) = A\cos\left(2\pi k\frac{f}{f_s}+\theta\right)+w(k),\ k=0,1,\ldots \tag{2.52}$$

It is well known that, in the noiseless case, the second order difference equation

$$x(k)-2\cos\left(2\pi\frac{f}{f_s}\right)x(k-1)+x(k-2)=0 \tag{2.53}$$

holds. This is easily shown by substituting $x(k)$ with the $w(k)$ set to zero into (2.53) and going through the necessary algebraic manipulations. Including the noise terms, the equation becomes,

$$x(k)-2\cos\left(2\pi\frac{f}{f_s}\right)x(k-1)+x(k-2)=w(k)-2\cos\left(2\pi\frac{f}{f_s}\right)w(k-1)+w(k-2) \tag{2.54}$$

Substituting general constants for the coefficients in f in the above equation results in

$$x(k)-\beta x(k-1)+x(k-2)=w(k)-\alpha w(k-1)+w(k-2)$$

The approach of Quinn and Fernandes, then, reduces to the estimation of α and β, subject to the condition $\alpha=\beta$. Suppose we have N samples. This is carried out as follows.

Set $\hat{\alpha}_1=2\cos\left(2\pi\frac{\hat{f}_c}{f_s}\right)$, where $\hat{f}_c$ is a coarse frequency estimate obtained using a coarse estimator such as the maximiser of the periodogram.

Now, for each iteration i do

$$y(k)=x(k)+\hat{\alpha}_i y(k-1)-y(k-2), \qquad k=0,1,\ldots N-1$$

with $y(k)=0, k<0$. $\hat{\beta}_i$ is now calculated using the linear regression of $y(k)+y(k-2)$ on $y(k-1)$. That is

$$\begin{aligned}\hat{\beta}_i &= \frac{\sum_{k=0}^{N-1}[y(k)+y(k-2)]y(k-1)}{\sum_{k=0}^{N-1}y^2(k-1)} \\ &= \alpha_i+\frac{\sum_{k=0}^{N-1}x(k)y(k-1)}{\sum_{k=0}^{N-1}y^2(k-1)}\end{aligned} \tag{2.55}$$

If $\left|\hat{\alpha}_i - \hat{\beta}_i\right| < \delta$, where δ is a set tolerance, then exit the loop and set $\hat{f} = \cos^{-1}\left(\frac{\hat{\beta}_i}{2}\right)$.

Otherwise, put $\hat{\alpha}_{i+1} = \hat{\beta}_i$ and repeat the procedure.

The asymptotic properties of the algorithm are derived in [14]. It is shown that the estimation error is asymptotically normal with variance equal to the asymptotic CRB. If the initialising estimator is $O\left(N^{-\varepsilon}\right)$, the residual in the estimate of α after iteration Q, becomes $o\left(N^{-\frac{3}{2}}\right)$ where

$$Q = \left\lfloor 3 - \frac{\ln(2\varepsilon - 1)}{\ln 2} \right\rfloor$$

and $\lfloor \bullet \rfloor$ is the floor (or integer part of) $\bullet$. Thus, if the periodogram is used to initialise the algorithm, then $\varepsilon = 1$ and the algorithm takes 3 iterations to converge to the CRB. Since the number of iterations for convergence can be pre-determined, the tolerance based stopping criteria can be discarded and the algorithm simply run for Q iterations.

2.5.5 Kalman Filtering Frequency Tracking

Another interpretation of the algorithm of the previous section is in terms of the existence of a second order filter that suppresses a particular sinusoidal component, that is, a very narrow notch filter. Therefore, the estimator, in effect, tunes the coefficients of the filter to get the best possible suppression using the available data. Other adaptive filtering techniques have been proposed for the purpose of frequency estimation [77-79]. Kalman filter frequency tracking algorithms have also received significant attention, [30, 31, 40, 80]. In this section, we briefly review a Kalman filter frequency tracking algorithm.

Consider the real sinusoidal model of equation (2.52). The signal at $k+1$ can be expanded in terms of $x(k)$,

$$\begin{aligned} x(k+1) &= A\cos\left(2\pi(k+1)\frac{f}{f_s} + \theta\right) + w(k) \\ &= \cos\left(2\pi\frac{f}{f_s}\right)x(k) - \sin\left(2\pi\frac{f}{f_s}\right)A\sin\left(2\pi k\frac{f}{f_s} + \theta\right) + w(k) \end{aligned}$$

Now putting $z_1(k) = A\cos\left(2\pi k\frac{f}{f_s} + \theta\right)$, $z_2(k) = A\sin\left(2\pi k\frac{f}{f_s} + \theta\right)$, and $z_3(k) = 2\pi\frac{f}{f_s}$, we can split the expression for $x(k+1)$ into the following system of equation (referred to as a third order state space model),

$$\begin{cases} z_1(k+1) = \cos(z_3(k))z_1(k) - \sin(z_3(k))z_2(k) \\ z_2(k+1) = \sin(z_3(k))z_1(k) + \cos(z_3(k))z_2(k) \\ z_3(k+1) = z_3(k) + \nu(k) \\ x(k+1) = z_1(k+1) + \eta(k) \end{cases} \tag{2.56}$$

The noise terms, $\nu(k)$ and $\eta(k)$ are zero-mean uncorrelated white noise with variances σ_ν^2 and σ_η^2 respectively. The frequency is given by the state variable z_3.

Now applying the EKF theory of section 2.4, we see that the state vector is given by

$$\mathbf{Z}_k = \begin{bmatrix} z_1(k) \\ z_2(k) \\ z_3(k) \end{bmatrix}$$

The equation is consequently given by,

$$\hat{\mathbf{Z}}_{k+1} = \mathbf{H}\left(\hat{\mathbf{Z}}_k\right) + \mathbf{K}_k\left(x_{k+1} - \mathbf{M}\mathbf{H}\left(\hat{\mathbf{Z}}_k\right)\right) \tag{2.57}$$

where

$$\mathbf{H}(\mathbf{Z}_k) = \begin{bmatrix} \cos(z_3(k))z_1(k) - \sin(z_3(k))z_2(k) \\ \sin(z_3(k))z_1(k) + \cos(z_3(k))z_2(k) \\ z_3(k) \end{bmatrix} \tag{2.58}$$

and

$$\mathbf{M} = \begin{bmatrix} 1 & 0 & 0 \end{bmatrix} \tag{2.59}$$

The Kalman gain update equation is

$$\mathbf{K}_{k+1} = \mathbf{P}_{k+1}\mathbf{M}^T\left(\mathbf{M}\mathbf{P}_{k+1}\mathbf{M}^T + \sigma_\eta^2\right)^{-1} \tag{2.60}$$

The predictor covariance matrix is obtained from

$$\mathbf{P}_{k+1}^* = \mathbf{\Phi}_k\left[\mathbf{I} - \mathbf{K}_k\mathbf{M}\right]\mathbf{P}_k^*\mathbf{\Phi}_k^T + \sigma_\nu^2\mathbf{1}_3 \tag{2.61}$$

$\mathbf{I}$ is the identity matrix. The quantities $\mathbf{\Phi}_k$ and $\mathbf{1}_3$ are defined as

$$[\mathbf{\Phi}_k]_{i,j} = \left.\frac{\partial \mathbf{H}_i(\mathbf{Z})}{\partial z_j}\right|_{\mathbf{Z}=\hat{\mathbf{Z}}_{k-1}}$$

and

$$\mathbf{1}_3 = \begin{bmatrix} 0 & 0 & 0 \\ 0 & 0 & 0 \\ 0 & 0 & 1 \end{bmatrix}$$

Notice that equation (2.61) is a combination of equations (2.31) and (2.30). Bittanti and Savaresi, [30], studied the Kalman filter presented here and showed that it is unbiased in its steady state response to a sinusoidal signal with a fixed frequency. Furthermore they proved that the performance is dependent only on the ratio $\frac{\sigma_\eta^2}{\sigma_v^2}$. This greatly simplifies the design of the filter parameters.

2.5.6 Frequency Domain Frequency Estimation

Rife showed that that the ML frequency estimator is given by the maximiser of the periodogram, [21]. The advent of digital signal processors and the efficiency of the FFT algorithm have contributed to the popularity of the frequency domain frequency estimation algorithms. Unlike the phase and correlator-based estimators, the FFT based algorithms exhibit excellent performance at low SNR. They have a much lower SNR threshold. Boashash, in [81], explains this as follows: "The Fourier Transform peak is that value of f (the frequency) for which there is maximum correlation between the complex phase sequence, $e^{j2\pi\frac{kn}{N}}$, and the (complex) phase of the observed signal. That is, the peak of the Fourier Transform is the frequency which results in the best achievable smoothing of the complex phase, subject to the constraint that the frequency is constant… Because this type of smoothing completely avoids the phase unwrapping problem it yields IF (Instantaneous Frequency) estimates which are low in variance at much lower SNR thresholds than the methods based on smoothing of the phase." By the methods based on the smoothing of the phase he implies the time-domain methods, and in particular the phase based methods.

FFT-based algorithms usually consist of a coarse frequency search followed by a fine estimation algorithm. Rife in [21], studied the digital estimation of the frequency of a sinusoidal signal from N data samples in the presence of AWGN. He suggested a coarse frequency estimator given by the index corresponding to the maximum Fourier coefficient of the signal followed by a fine estimation stage. He also examined low complexity fine frequency estimation methods, such as the secant method and the Newton method. Quinn, [82, 83], Macleod, [84] and Zakharov et al, [85, 86], among others, have also proposed interpolation methods that improve the resolution of the coarse frequency estimator. These will be discussed in detail in chapters 5 and 7. In this dissertation, a two stage estimation technique is adopted. The periodogram maximiser, referred to as the Maximum Bin Search (MBS) algorithm, is used as the coarse estimation stage.

Although the methods mentioned so far are mostly suitable for stationary or quasi-stationary signals, Boashash, [81], points out that they can be extended to polynomial phase signals. Assume the signal can be written as

$$s(k) = e^{j\left(a_0 + a_1 k + a_2 k^2 + \cdots + a_p k^p\right)} \tag{2.62}$$

where, without loss of generality, the amplitude is set to 1. Then the estimate of the vector $\mathbf{A} = \left[a_0, a_1 \ldots, a_p\right]$ is the maximiser of the likelihood function

$$\mathrm{L}(\mathbf{A}) = \left| \frac{1}{N} \sum_{n=0}^{N-1} x(k) e^{-j\left(a_1 n + a_2 n^2 + \cdots + a_p n^p\right)} \right|^2 \tag{2.63}$$

Notice that coefficient a_0 is not present in the likelihood function as it is a constant phase which is removed by the modulus operator. This technique is simply a p-dimensional peak search of a generalised Fourier transform. Thus, this method is inefficient and is computationally intensive. Many other techniques have been proposed for this purpose. The Short Time Fourier Transform (STFT) has been well studied in connection with non-stationary signals, [87, 88]. Time-frequency distributions, especially the Wigner-Ville distribution (WVD), have also been considered in the context of estimating the frequency of non-stationary signals, [89-92]. The authors of [93] apply the Wavelet transform to the Doppler shift estimation problem for LEO satellites. The Wavelet transform differs from the STFT in that it

employs a kernel consisting of wavelets. A wavelet is a wave that is restricted to a specified length of time.

2.6 Conclusion

This chapter was intended to provide the theoretical background on which the thesis is built and to set it in the context of the literature. The properties of the noise and the central limit theorem were discussed in section 2.2, section 2.3 presented the Cramer-Rao inequality and the CRB for frequency estimation while Section 2.4 dealt with the theory of Kalman filtering both in the linear time-invariant and the nonlinear cases.

The frequency estimation literature is reviewed in section 2.5. There is an enormous amount of work published on the topic. This review was only intended to be a general summary of the methodologies that are relevant in the context of a LEO satellite communications link. In highly dynamic environments, the computational efficiency of an estimator plays an important characteristic as the available processing time is limited. At Ka band, the signal experiences large attenuations, due to atmospheric effects, rain fade as well as antenna pointing error. This dictates that the estimators have a good performance at low signal to noise ratios. Although the phase based estimators are computationally simple, they have a high SNR threshold. The filtering techniques, on the other hand, are more computationally intensive but tend to have a slightly better performance. With the advent of digital signal processors, FFT based methods have become real contenders for real time frequency estimation. They are computationally simple and perform very well at low SNR values.

Many other techniques, not reviewed due to the lack of space, have been applied to the estimation of the frequency. These are generally more computationally intensive. Examples include MUSIC, [94, 95], subspace rotation techniques, [96, 97], and Prony's method, [98, 99], to name a few.

The orbital mechanics of a satellite in a low earth orbit will be examined in the next chapter. The theory developed will be useful in the application of the frequency measurements to the spatial tracking of the satellite.

Chapter 3

Complete Characterisation of Low Earth Orbits

3.1 Introduction

Satellite orbit determination has been dealt with extensively in the literature, [32], [100], [101] and [102]. These books generally start with a simplified orbital model obtained by solving the Keplerian equations of motion. They, then, incorporate perturbations of first, second and higher orders to get a more accurate model. These perturbations include the non-sphericity of the earth, the pull of the sun and moon, atmospheric drag and relativistic effects. This chapter, however, is not concerned with accurate orbital determination but rather with a simplified orbital model. The chapter aims at presenting a simplified orbital model that will be useful in developing the ideas of chapter 9. The orbital model also serves in the derivation of the Doppler shift and Doppler rate equations. The Doppler shift curves are useful in implementing the frequency compensation in the communications link prior to the demodulation of the received signal.

In [103] and [104], the authors present a simplified characterisation of the Doppler shift of a LEO satellite. They assume the earth to be spherical and ignore all perturbations and second order effects. Their analysis is done in the Earth-Centred, Earth-Fixed (ECEF) frame of reference. The observed satellite orbit in the ECEF frame is assumed to be a great circle arc. This is in actual fact not the case due to the earth's motion. The authors also calculate the satellite orbital velocity in the ECEF frame and they show the validity of approximating it by a constant.

In this chapter we develop a simple iterative implementation of the two-body model in the latitude-longitude coordinate system. We derive expressions for the position, look angles and the Doppler shift and Doppler rate for a LEO satellite in the ECEF frame. We then use the assumptions stated above to simplify the equations obtained. We also

present another strategy of approximating the angular velocity of the satellite in the ECEF frame by a constant value obtained at the maximum elevation point. An expression for the off-boresight pointing error is also derived and used to assess the performance of the derived model.

The chapter is organised as follows. In section 3.2 we derive the angular position of the satellite in the ECEF frame. We use this in section 3.3 to present a simple iterative orbit propagation algorithm. In section 3.4 we present the strategy of Ali *et al.*, as well as our own, for approximating the ECEF angular velocity of the satellite by a constant. The complete spatial characterisation of a LEO satellite is presented in section 3.5, and the Doppler characterisation in section 3.6. Finally, section 3.7 concludes the chapter.

3.2 Angular Velocity of Satellite in ECEF Frame

In order to carry out the analysis in the ECEF frame, we must calculate the satellite orbit in that frame. For a treatment of the different frames of reference refer to [101]. As the earth is fixed in the ECEF frame, this involves taking into account the earth rotation in the orbital calculations. The satellite orbit in the ECEF frame is no longer circular and its observed angular velocity depends on its latitude.

Consider a satellite in an Earth-Centred Inertial frame (ECI). We assume the satellite orbit is circular and the spherical earth model is used. The angular velocity of the satellite is given by

$$\omega_I = \sqrt{\frac{GM_e}{r^3}} \text{rad.s}^{-1} \tag{3.1}$$

where G is the gravitational constant ($\approx 6.672 \times 10^{-11}$ $\text{m}^3\text{kg}^{-1}\text{s}^{-2}$)

M_e is the mass of the earth ($\approx 5.9736 \times 10^{24}$ kg)

And r is the radius of the satellite orbit ($= r_e + h$, where $r_e \approx 6378.15$ km, is the radius of the earth and h is the satellite altitude)

The gravitational constant is usually determined directly from torsional experiments involving two bodies, [32]. Due to the small size of the gravitational force, however, it is hard to determine G accurately. The term GM_e, on the other hand, has been

determined with significant precision using orbital tracking data of artificial Earth satellites. Therefore the value of GM_e or earth figure, is usually specified.

In [104], the satellite velocity in the ECEF frame was derived. We will repeat some of the analysis here for the purpose of completeness. Let the subscript *I* stand for the ECI and *F* for the ECEF frames respectively. The symbols λ and φ stand for longitude and latitude respectively.

Figure 3.1 shows the satellite orbit in the ECI frame. The satellite ascending node is S_i' and the node at maximum latitude is S_m'. The satellite angular velocity is given by ω_I and the satellite position is denoted by $(r, \varphi_s, \lambda_s)$. ω_F denotes the satellite velocity in the ECEF frame.

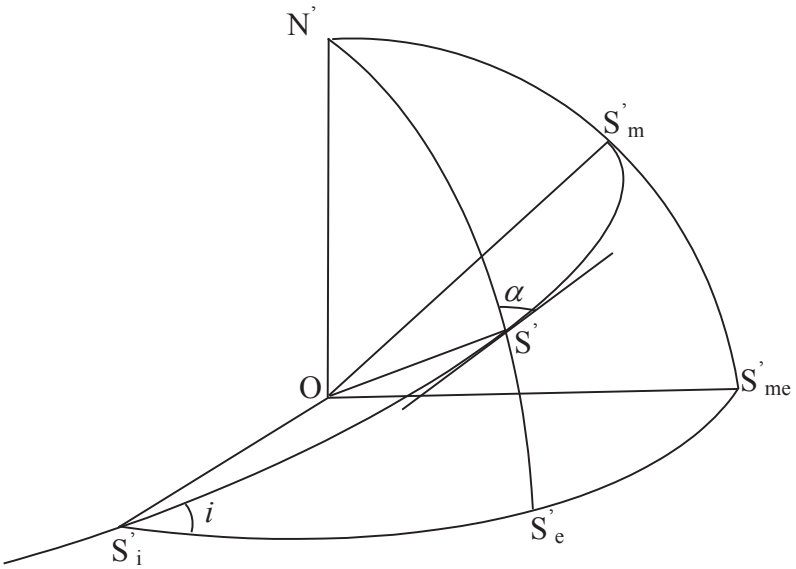

Figure 3.1 – *Satellite position in ECI frame of reference.*

Since the earth is fixed in the ECEF frame, the earth rotation must be taken into account in ω_F. To this end, we need to decompose the satellite angular velocity into its latitude and longitude components. Denote angle $S_i'S'S_e'$ by α. The north and east components of the satellite velocity at time *t*, denoted by v_N and v_E, are

$$\begin{aligned} v_N &= v_I \cos(\alpha) \\ &\text{and} \\ v_E &= v_I \sin(\alpha) \end{aligned} \tag{3.2}$$

The satellite velocity in the ECI frame, v_I, is related to the angular velocity by $r\omega_I$ where ω_I is given by equation (3.1). As the earth's rotation affects only the longitude, v_N and v_E in the ECEF frame become

$$\begin{aligned} v_N &= r\omega_I \cos(\alpha) \\ &\text{and} \\ v_E &= r\omega_I \sin(\alpha) - r\omega_e \cos(\varphi_s) \end{aligned} \tag{3.3}$$

The velocity of the satellite in the ECEF frame, v_F, is found by combining v_N and v_E

$$\begin{aligned} v_F &= \sqrt{v_N^2 + v_E^2} \\ &= \sqrt{(r\omega_I \cos(\alpha))^2 + (r\omega_I \sin(\alpha) - r\omega_e \cos(\varphi_s))^2} \end{aligned} \tag{3.4}$$

Expanding (3.4) and simplifying we get,

$$v_F = r\sqrt{\omega_I^2 + \omega_e^2 \cos^2(\varphi_s) - \omega_I \omega_e \sin(\alpha)\cos(\varphi_s)} \tag{3.5}$$

Spherical trigonometry identity (A.6) applied to triangle $S_i'S'S_e'$ results in the following expressions for cos(α) and sin(α)

$$\begin{aligned} &\cos(\alpha) = \cos(\lambda_s - \lambda_i)\sin(i) \\ &\text{and} \\ &\sin(\alpha) = \frac{\cos(i)}{\cos(\varphi_s)} \end{aligned} \tag{3.6}$$

Substituting sin(α) into (3.5) and then dividing by *r* we obtain the following expression for the angular velocity of the satellite, ω_F, in the ECEF frame,

$$\omega_F = \sqrt{\omega_I^2 + \omega_e^2 \cos^2(\varphi_s) - 2\omega_I \omega_e \cos(i)} \tag{3.7}$$

Equation (3.7) clearly shows that the satellite angular velocity in the ECEF frame for an orbit with inclination *i* depends solely on the latitude of the satellite.

The expressions for the sine and cosine of α are also substituted into equation (3.3) to give

$$\begin{aligned} v_N &= r\omega_I \cos(\lambda_s - \lambda_i)\sin(i) \\ &\text{and} \\ v_E &= r\omega_I \frac{\cos(i)}{\cos(\varphi_s)} - r\omega_e \cos(\varphi_s) \end{aligned} \tag{3.8}$$

The satellite velocity in the north direction, v_N, is related to the satellite latitude rate of change, ω_L, through the orbit radius r. The east-west component, v_E, on the other hand is related to the longitude rate of change, ω_l, through the projection of the orbit radius onto the equatorial plane, that is $r\cos(\varphi_s)$. Hence the satellite latitude and longitude rates of change are given by respectively

$$\begin{aligned} &\omega_L = \dot{\varphi}_s = \omega_I \cos(\lambda_s - \lambda_i)\sin(i) \\ &\text{and} \\ &\omega_l = \dot{\lambda}_s = \omega_I \frac{\cos(i)}{\cos^2(\varphi_s)} - \omega_e \end{aligned} \tag{3.9}$$

Equation (3.9) gives us some insight into the behaviour of the satellite in the ECEF frame. As expected, as the satellite moves in its orbit away from the equatorial plane, the latitude rate of change decreases while that of the longitude increases. The earth's rotation affects the longitude rate of change only and hence is of differing magnitude depending on the latitude of the satellite. For inclined orbits, this implies that the satellite pass as observed from a ground station is not symmetrical about the zenith or maximum elevation point. The other implication is that equal maximum elevation passes east and west of the ground station have different Doppler and spatial characteristics as they would occur at different latitudes. These effects will be discussed in greater detail in later sections and in chapter 9.

3.3 Orbital Propagation

The satellite latitude and longitude rates of change, shown in equation (3.9), can be implemented iteratively in order to obtain the satellite orbit. Specifying the longitude of the ascending node λ_i is sufficient to calculate the satellite orbit. Let the orbit sampling time be T_s. We start the algorithm by setting the satellite longitude to λ_i and the latitude to 0. During iteration *n*, the latitude and longitude are propagated from time $(n-1)T_s$ to time nT_s using the following equations:

$$\begin{aligned} &\lambda_s(n) = \lambda_s(n-1) + \dot{\lambda}_s(n-1)T_s \\ &\text{and} \\ &\varphi_s(n) = \varphi_s(n-1) + \dot{\varphi}_s(n-1)T_s \end{aligned} \tag{3.10}$$

Since we are interested in the satellite orbit in the ECEF frame, the effect of the earth's rotation on the longitude of the satellite ascending node must be accounted for. Therefore, λ_i at time nT_s is given by,

$$\lambda_i(n) = \lambda_i(n-1) - \omega_e T_s \tag{3.11}$$

The latitude and longitude rates of change at time nT_s can now be updated using equation (3.9) and the values for λ_s, φ_s and λ_i given above. The algorithm steps are summarised in table 1 below.

Inititialisation:

$$\lambda_s = \lambda_i$$
$$\varphi_s = 0$$

Propagation: for $n = 1$ to N

$$\dot{\lambda}_s = \omega_I \frac{\cos(i)}{\cos^2(\varphi_s)} - \omega_e$$
$$\dot{\varphi}_s = \omega_I \cos(\lambda_s - \lambda_i)\sin(i)$$
$$\lambda_s = \lambda_s + \dot{\lambda}_s T_s$$
$$\varphi_s = \varphi_s + \dot{\varphi}_s T_s$$
$$\lambda_i = \lambda_i - \omega_e T_s$$

Table 3.1 – *Orbital Propagation Algorithm.*

The performance of the orbital propagation algorithm of table 3.1 was evaluated with respect to a simulation done using the package Satellite Toolkit (STK). The orbital propagator chosen for comparison purposes is the Two-Body model that assumes the earth is spherical and ignores any second order effects. A more elaborate orbital model is beyond the scope of this work. However, the non-sphericity of the earth can be taken into account by replacing the earth radius by the actual earth radius obtained from the reference ellipsoid and using the geodetic latitude instead of its geocentric equivalent, [102] pp 268. A scenario was created with a satellite having an orbital altitude of 800 km and an inclination of 81°. STK uses an earth radius of 6378.137 km and an earth figure of $3.986004418 \times 10^{14}$.

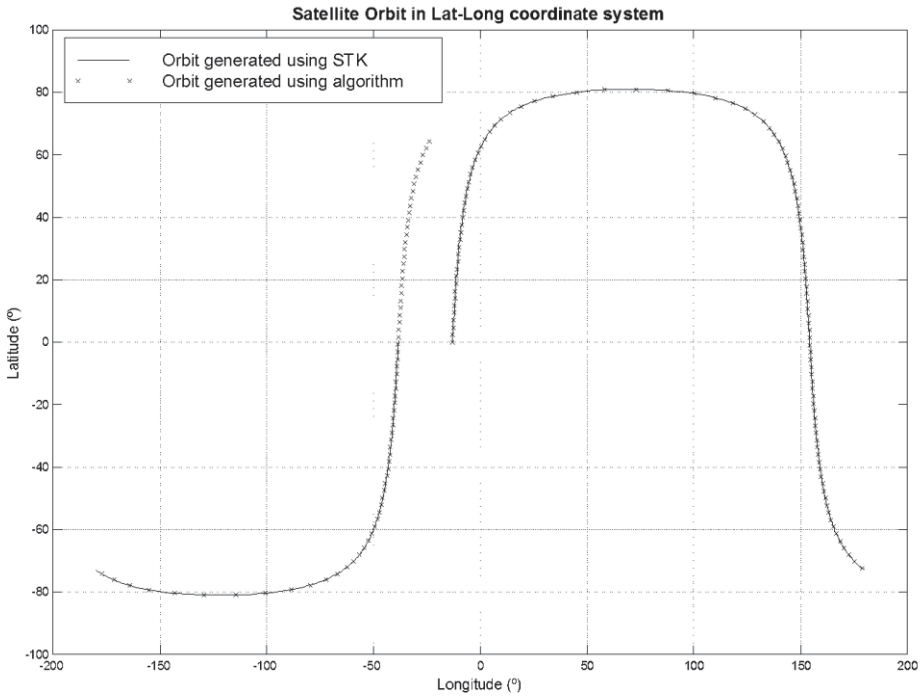

Figure 3.2 – *Orbit propagation algorithm results.*

Figure 3.2 above shows the results obtained from STK and the orbit propagation algorithm. We can see very good agreement between the two. In fact the orbit propagation algorithm presented in this section is based on the two-body model used in STK. In the following section we present an approximation of the ECEF angular velocity of the satellite that was developed in [104]. This leads to a simplified set of equations for calculating the satellite orbit based on the maximum elevation angle.

3.4 Satellite Velocity Approximations

For a low earth orbit satellite, the angular velocity of the satellite is much larger than that of the earth. Therefore the second term under the square root sign in equation (3.7), that is $\omega_e^2 \cos(\varphi)$, is much smaller than the difference of the other two terms. This implies that the velocity variation induced by the earth's rotation is very small and hence the satellite velocity can be approximated by a constant. In [104], Ali *et al.* approximate the satellite velocity by its lowest magnitude, that is its magnitude at latitude i. For an orbit at an altitude of 800 km and inclination 81°, the ECI angular

velocity ω_I is 0.00104 rad/s, that is equivalent to a velocity of 7.4518 km.s^{-1}. The corresponding satellite velocity in the ECEF frame varies between 7.3881 km.s^{-1} and 7.3699 km.s^{-1}. This results in a percentage variation in the velocity with respect to v_I of about 0.25%. This variation is an order of magnitude smaller than the earth angular velocity.

Another strategy for approximating the angular velocity of the satellite in the ECEF frame would be to take its value at the moment of maximum elevation. This requires the determination of the maximum elevation latitude, φ_{s0}. However, this gives a value that is closer to that observed by the earth station during the visible pass duration. In the following section we will derive the spatial and Doppler characterisation of the LEO satellite. We will then examine the effect of the approximation on the derived formulae.

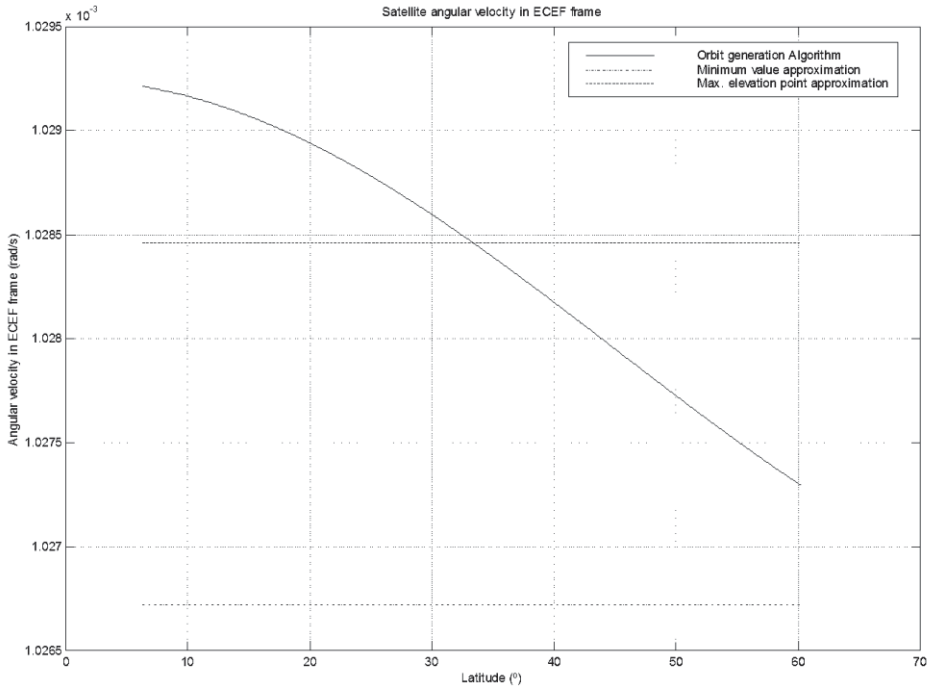

Figure 3.3 – *Angular velocity of satellite in ECEF frame as observed by an earth station at a longitude of 10º west and latitude 33.5º north. The pass used has a maximum elevation angle of 85.45º and is east of the earth station.*

Figure 3.3 shows a comparison between the two approximation strategies and the actual observed angular velocity. The earth station was placed at 10º west and 33.5º north.

The pass has a maximum elevation of 85.45º. The approximation suggested here results in a value closer to the mean of the observed angular velocity in the ECEF frame. This reduces the mean error over the entire visible duration of the pass.

3.5 Spatial Characterisation

In this section we complete the spatial characterisation of the satellite orbit. This involves the derivation of the satellite position and Doppler shift and rate with respect to time. The satellite position will be derived in both an Azimuth-Elevation coordinate system in section 3.5.3 and X-Y coordinate system in section 3.5.4. We will start, however, by deriving the longitude and latitude of the satellite at time *t* in order to be able to derive the other quantities. Let the earth station have a longitude λ_{ES} and latitude φ_{ES}.

Denote by $\gamma(t)$ the angle that the earth station and the satellite subtend at the centre of the earth at time *t*. The time reference is taken to be the moment of closest approach between the satellite, S, and the earth station, P. That is t_0 is the moment where the satellite is at the maximum elevation θ_0. $\gamma(t)$ is given by POS in figure 3.4(a).

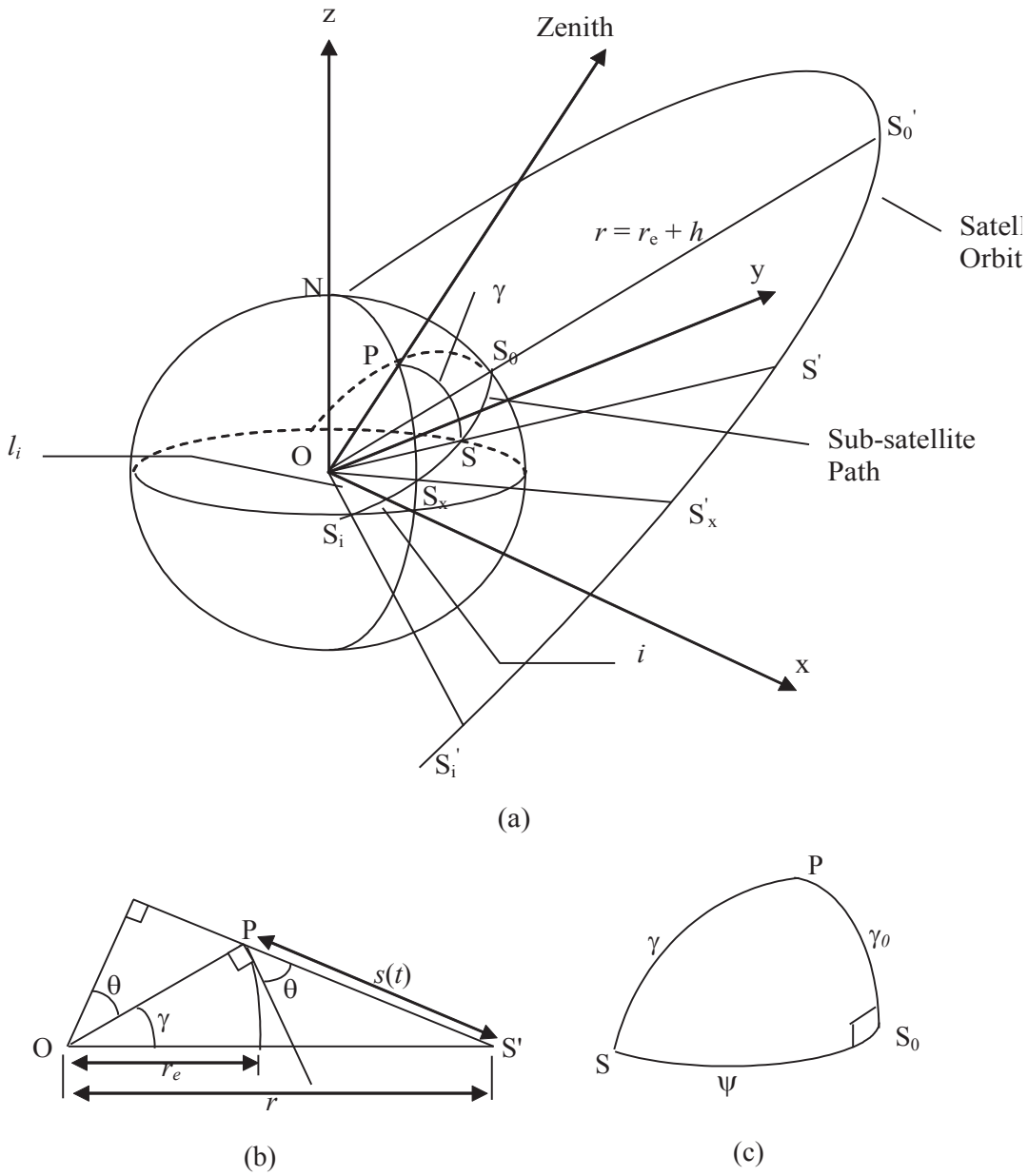

Figure 3.4 - *Orbital Geometry for a LEO with altitude h and inclination i.*

Figure 3.4(b) gives

$$r_e \cos(\theta) = r \cos(\gamma + \theta) \tag{3.12}$$

Hence, angle $\gamma(t)$ at maximum elevation θ_0, denoted as γ_0, is given by, [104],

$$\gamma_0 = \cos^{-1}\left(\frac{r_e}{r}\cos(\theta_0)\right) - \theta_0 \tag{3.13}$$

Due to the symmetry of the spatial dynamics about the zenith or overhead pass, we assign to γ_0 a positive sign for passes to the east of zenith and negative sign for those to the west.

From figure 3.4(b), the earth station to satellite slant, $s(t)$, is given by the cosine rule,

$$s(t) = \sqrt{r_e^2 + r^2 - 2r_e r\cos(\gamma(t))} \tag{3.14}$$

Figure 3.5 shows the sub-satellite path between the ascending node S_i and the maximum elevation point S_0. Note that this is a snapshot at the moment of maximum elevation. φ_{s0} is the latitude of the sub-satellite point at maximum elevation θ_0, that is point S_0. Angles PS_0S_i and $PS_{xe}S_i$ are right angles, and side PS_0 is equal to γ_0. Here the subscript e refers to points in the equatorial plane.

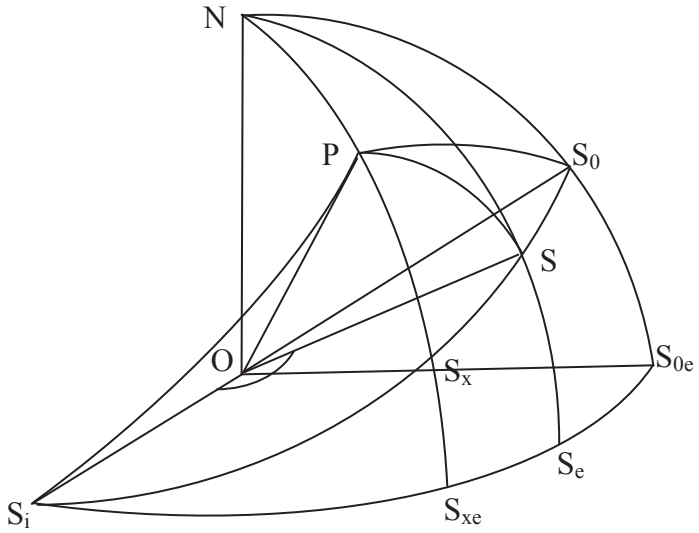

Figure 3.5 – *Enlarged view of sub-satellite path.*

Consider the spherical triangle NPS_0. Arc NP is equal to $90-\varphi_{ES}$ and NS_0 to $90-\varphi_{S0}$. Applying the cosine rule, given in (A.1), we have,

$$\cos(90-\varphi_{ES}) = \cos(90-\varphi_{s0})\cos(\gamma_0) + \sin(90-\varphi_{s0})\sin(\gamma_0)\cos(NS_0P) \tag{3.15}$$

Triangle $S_iS_0S_{0e}$ is a right angle spherical triangle. Using identity (A.6) we write angle $S_iS_0S_{0e}$ in terms of the orbit inclination, i, and φ_{s0},

$$\sin(S_i S_0 S_{0e}) = \frac{\cos(i)}{\cos(\varphi_{s0})} \tag{3.16}$$

Since PS_0S_i is a right angle, we have that $NS_0P + S_iS_0S_{0e} = 90º$. Combining equations (3.15) and (3.16) and solving for φ_{s0}, we get,

$$\varphi_{s0} = \sin^{-1}\left(\frac{\sin(\varphi_{ES}) \mp \sin(\gamma_0)\cos(i)}{\cos(\gamma_0)}\right) \tag{3.17}$$

The negative sign is used for orbits east of the zenith pass and the positive sign for those west of it.

The longitude of the maximum elevation point, λ_{s0}, is obtained using identity (A.1) on triangle NPS_0,

$$\lambda_{s0} = \lambda_{ES} \pm \cos^{-1}\left(\frac{\cos(\gamma_0) - \sin(\varphi_{ES})\sin(\varphi_{s0})}{\cos(\varphi_{ES})\cos(\varphi_{S0})}\right) \tag{3.18}$$

with the positive sign for orbits east of the zenith pass and negative for those west of the zenith pass.

3.5.1 Satellite Visibility Duration

A minimum elevation angle is normally set for communications with a Low Earth Orbit satellite. Let this minimum visibility angle be denoted by θ_v. The total visibility duration T_v for a particular earth station is the time the satellite spends above elevation θ_v. For the case where the satellite velocity is approximated by a constant value, T_v was derived in [104] as

$$T_v = \frac{2}{\omega_F} \cdot \cos^{-1}\left(\frac{\cos\left(\cos^{-1}\left(\frac{r_e}{r}\cos(\theta_v)\right) - \theta_v\right)}{\cos(\gamma_0)}\right) \tag{3.19}$$

The visibility duration was calculated for the LEO satellite at 800 km altitude and inclination of 81º. The results are shown in the figure below.

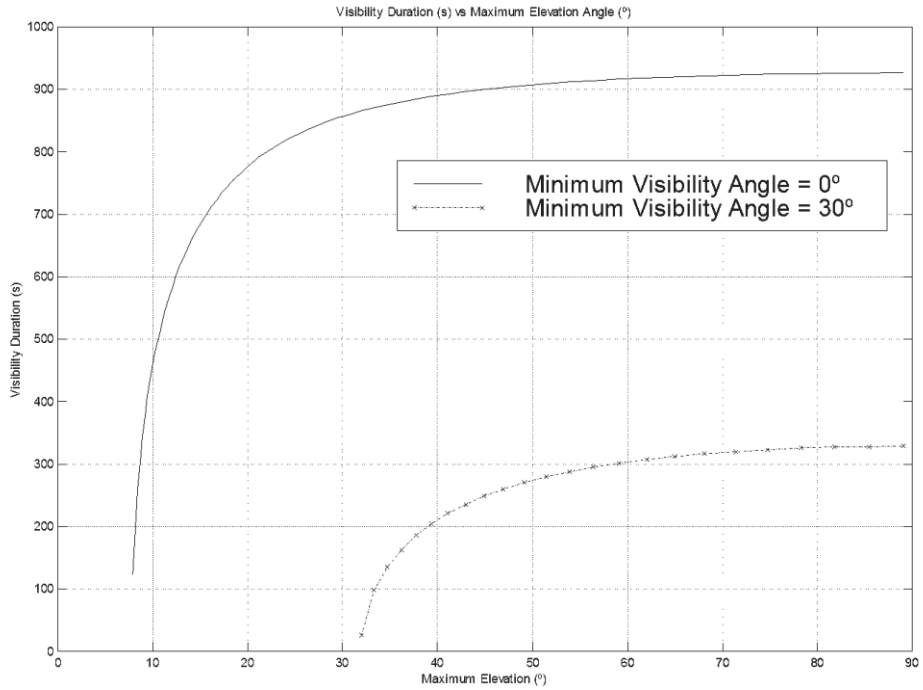

Figure 3.6 – *Plot of visibility duration as a function of the observed maximum elevation angle.*

The visibility time for the pass with maximum elevation of 85.45º is 926.6 s. Equation (3.19) gives a value of 928.3 s with ω_F approximated by its minimum value and 926.8 s with ω_F approximated by its value at the maximum elevation point. The error arises from the approximation of the satellite velocity in the ECEF frame by a constant. A closer examination of the visibility duration calculations reveals another difference. Equation (3.19) assumes a visibility window that is symmetrical about the maximum elevation point. This in reality is not the case due to the earth's rotation and the satellite orbit inclination. At lower latitudes, the satellite velocity translates mostly into a latitude component. As the latitude increases, however, the longitude component of the angular velocity increases and the latitude rate of change decreases. The total observed angular velocity of the satellite also decreases. Thus, the visible portion of the satellite orbit appears asymmetrical to the earth station.

Figure 3.6 shows the visibility duration as a function of the maximum elevation of the pass for different minimum visibility angles. The curves demonstrate that the satellite spends most of the visibility time at low elevation angles. For example, the visibility duration of a zenith pass for minimum visibility angle of 30º is a little over 300 s.

Taking the minimum visibility angle to be 0º, on the other hand, we find that the visibility duration of a zenith pass is a more than 900 s. This indicates that, for a zenith pass, the satellite spends about 600 s between the 0º and 30º. Therefore, it is essential to maximise the probability of closure of a communications link at high elevations to efficiently utilise the satellite resources during visibility.

3.5.2 Latitude and Longitude of the Sub-satellite Point S

In order to calculate the relative position of the satellite to the earth station at a time *t*, we must determine the latitude and longitude of the sub-satellite point at that time instant. The angular displacement of the sub-satellite point S, at time *t*, from the point of maximum elevation S_0 is given by $\psi(t)$, refer to figure 3.5.

Let ψ_i be the angular displacement of the ascending node S_i from point S_0. From the spherical triangle $S_iS_0S_{0e}$ and identity (A.5) we have

$$\sin(\varphi_{s0}) = \sin(\psi_i)\sin(i) \tag{3.20}$$

Solving for ψ_i and replacing $\sin(\varphi_{s0})$ by the expression in equation (3.17), we get

$$\psi_i = \sin^{-1}\left(\frac{\sin(\varphi_{ES}) - \sin(\gamma_0)\cos(i)}{\sin(i)\cos(\gamma_0)}\right) \tag{3.21}$$

On the ascending part of an orbit, ψ_i has the opposite sign to the earth station latitude while on the descending part of the orbit, the reverse is true.

Next we consider triangle S_iSS_e. The latitude of the sub-satellite point at time *t* is denoted by $\varphi_s(t)$ (equal to arc SS_e). Identity (A.5) results in

$$\sin(\varphi_s) = \sin(i)\sin(S_iS) \tag{3.22}$$

However $S_iS = S_0S - S_0S_i = \psi(t) - \psi_i = \Delta\psi(t)$, hence

$$\varphi_s(t) = \sin^{-1}(\sin(i)\sin(\Delta\psi(t))) \tag{3.23}$$

The longitude of the satellite can be found using the spherical triangle NSS_0. Using the sine rule, identity (A.3), we can calculate the difference in longitude from the maximum elevation point S_0.

$$\sin(\psi)\sin(\lambda_s - \lambda_{s0}) = \sin(90 - \varphi_s)\sin(\mathrm{NS_0S}) \tag{3.24}$$

Angle NS_0S is equal to 180-SS_0S_{0e}. Hence, using identity (A.6), $\sin(NS_0S)$ is found to be,

$$\sin(\mathrm{NS_0S}) = \sin(\mathrm{SS_0S_{0e}}) = \frac{\cos(i)}{\cos(\varphi_{s0})} \tag{3.25}$$

Combining equations (3.24) and (3.25), the satellite longitude is found to be,

$$\lambda_s = \lambda_{s0} + \sin^{-1}\left(\frac{\sin(\psi)\cos(i)}{\cos(\varphi_{s0})\cos(\varphi_s)}\right) \tag{3.26}$$

The above expression for λ_s must be modified to take into account the rotation of the earth in the time t from the maximum elevation point. The earth in that time rotates through an angle $\Delta\lambda$ given by $\omega_e t$. Therefore the actual longitude of the satellite must be adjusted by $-\Delta\lambda$ and is given by,

$$\lambda_s = \lambda_{s0} + \sin^{-1}\left(\frac{\sin(\psi)\cos(i)}{\cos(\varphi_{s0})\cos(\varphi_s)}\right) - \Delta\lambda \tag{3.27}$$

The equations derived above were assessed against results obtained from the orbit propagation algorithm presented in section 3.3. A pass with a maximum elevation of 85.45º was chosen, with the earth station at 10º west and 33.5º north. The latitude, longitude and range were obtained as a function of time. The pass was calculated using the above equations and both angular velocity approximation strategies presented in section 3.4. Figure 3.7 shows the simulated and calculated passes in the latitude-longitude coordinate system. We can see close agreement between the all three curves.

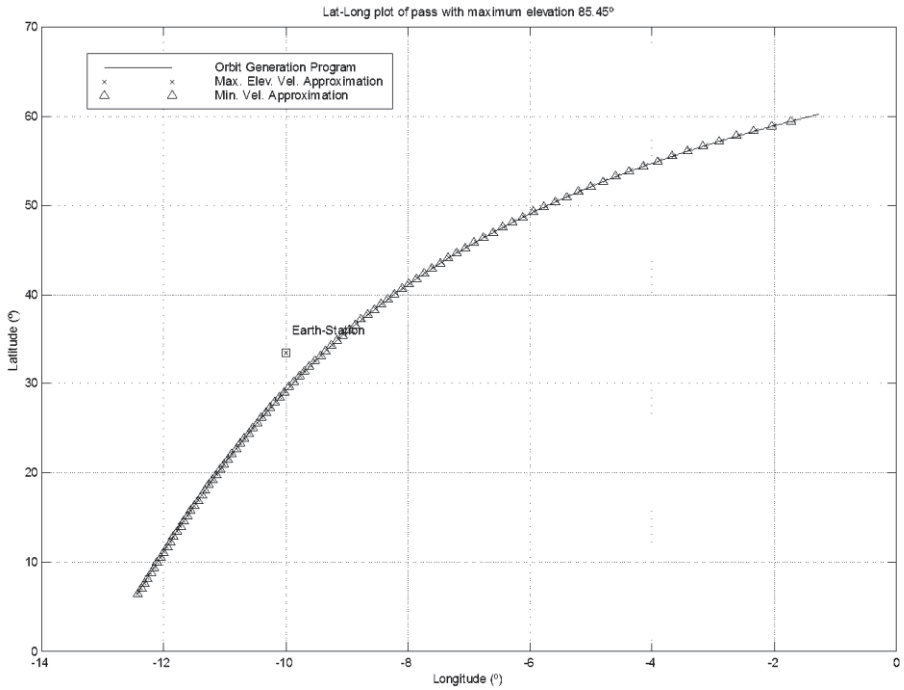

Figure 3.7 – *Plot of the calculated orbits in Lat-Long coordinates for a pass with maximum elevation 85.45°. The earth station is at 10° west and 33.5° north.*

Figure 3.8, below, shows the errors in latitude and longitude as a function of time. The latitude error is within ±0.3° and the longitude error is less than 0.2°. We can see that the results obtained from approximating the ECEF angular velocity of the satellite by its value at the maximum elevation point have a smaller error than those obtained from the minimum value approximation.

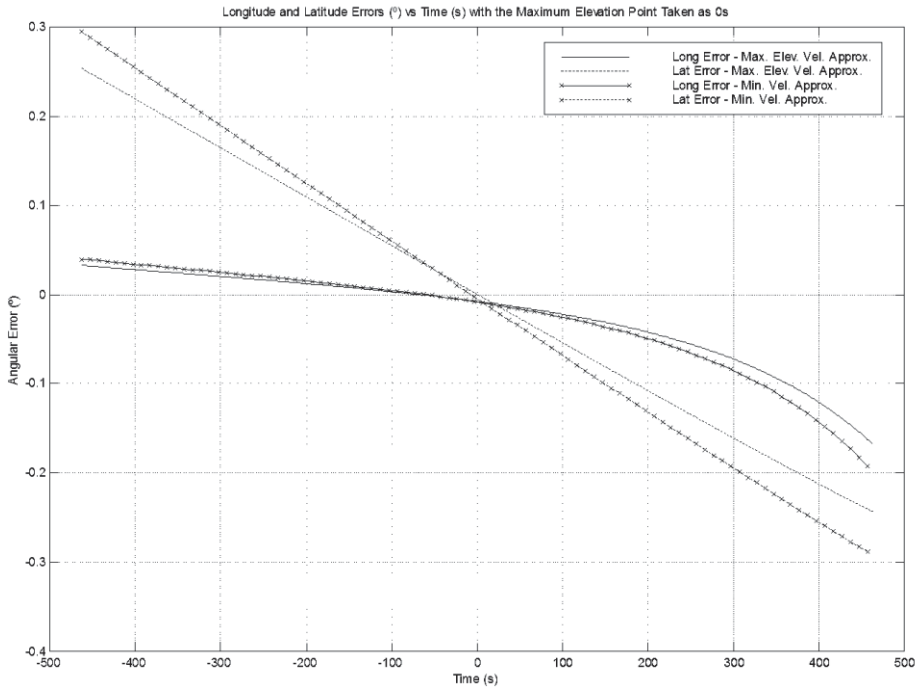

Figure 3.8 – *Plot of the latitude and longitude errors for a pass with a maximum elevation angle of 85.45º.*

3.5.3 Azimuth and Elevation

The position of a satellite with respect to an earth-bound observer is usually given in an Azimuth-Elevation (or topocentric) coordinate system, [100] and [1] pp. 55. The elevation of the satellite is the angle its line of sight makes with the horizontal of the earth station (that is θ in figure 3.4(b)). The azimuth is the angle that the arc from the earth station to the sub-satellite point makes with the north direction at the earth station with the easterly direction being positive. Therefore the azimuth is angle NPS in figure 3.4(a).

Using the cosine rule in triangle OPS' in figure 3.4(b), the elevation of the satellite, $\theta(t)$, is found to be

$$\theta(t) = \sin^{-1}\left(\frac{r^2 - r_e^2 - s^2(t)}{2r_e s(t)}\right) \tag{3.28}$$

Maral, in [102] pp. 268-270, derives the transformation from the Latitude-longitude (topocentric-Horizon) coordinate system to the Azimuth-Elevation coordinate system giving another form for the elevation of the satellite.

$$\theta = \tan^{-1}\left(\frac{\cos(\gamma) - r_e/r}{\sin(\gamma)}\right) \tag{3.29}$$

The azimuth, A, is obtained from triangle NPS in figure 3.5. Let angle NPS be denoted by a. Angle PNS is equal to the difference in longitudes between the satellite and the earth station. Using spherical geometry, a is found to be,

$$a = \sin^{-1}\left(\frac{\sin(\lambda_s - \lambda_{ES})\cos(\varphi_s)}{\sin(\gamma)}\right) \tag{3.30}$$

The azimuth of the sub-satellite point, A, is related to a as follows,

$$A = \begin{cases} a, & \text{satellite north - east of earth - station} \\ \pi - a, & \text{satellite south - east of earth - station} \\ 2\pi + a, & \text{satellite north - west of earth - station} \\ \pi - a, & \text{satellite south - west of earth - station} \end{cases} \tag{3.31}$$

We must note that care must be taken when determining the quadrant of the azimuth based on equation (3.31). The difficulty is that we cannot rely on the relationship between the latitudes to determine the north-south relative position, [105]. In the algorithm implementation, we have adopted the method of Kelso, [106]. The Cartesian coordinates of the satellite and earth station are calculated. These are then transformed to the topocentric (Cartesian) coordinate system using two successive rotations. The azimuth is finally calculated. The quadrant is then determined by looking at the sign of the north-south coordinate.

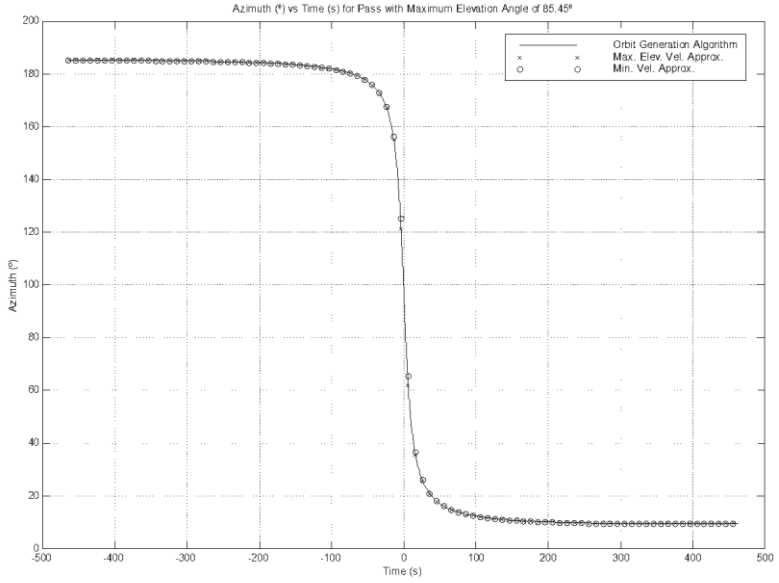
Azimuth (°) vs Time (s) for Pass with Maximum Elevation Angle of 85.45°
Orbit Generation Algorithm
Max. Elev. Vel. Approx.
Min. Vel. Approx.
Azimuth (°)
Time (s)

(a)

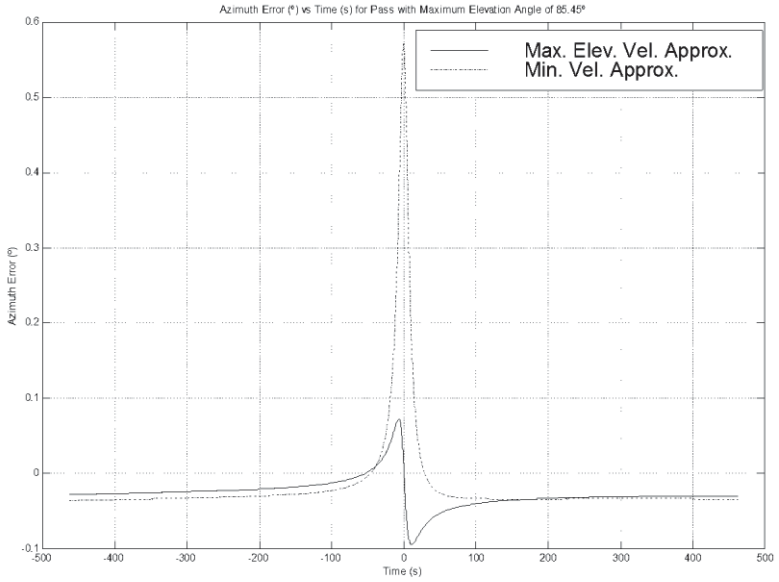
Azimuth Error (°) vs Time (s) for Pass with Maximum Elevation Angle of 85.45°
Max. Elev. Vel. Approx.
Min. Vel. Approx.
Azimuth Error (°)
Time (s)

(b)

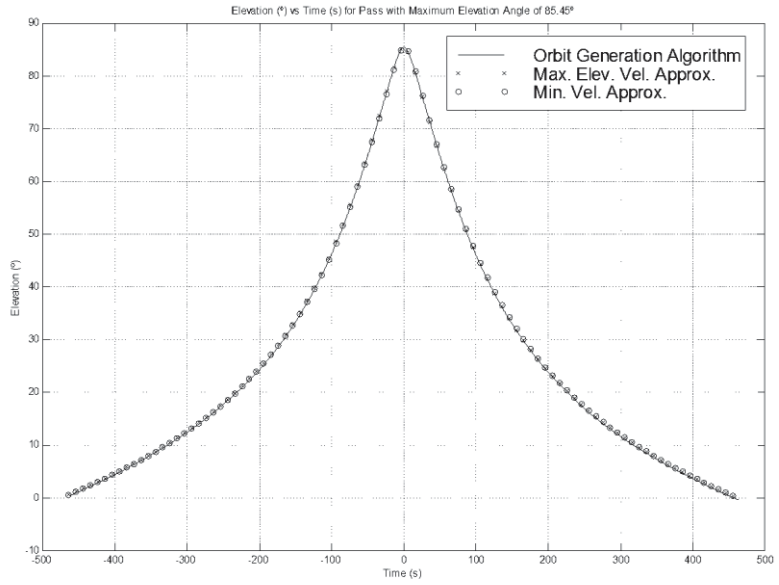

(c)

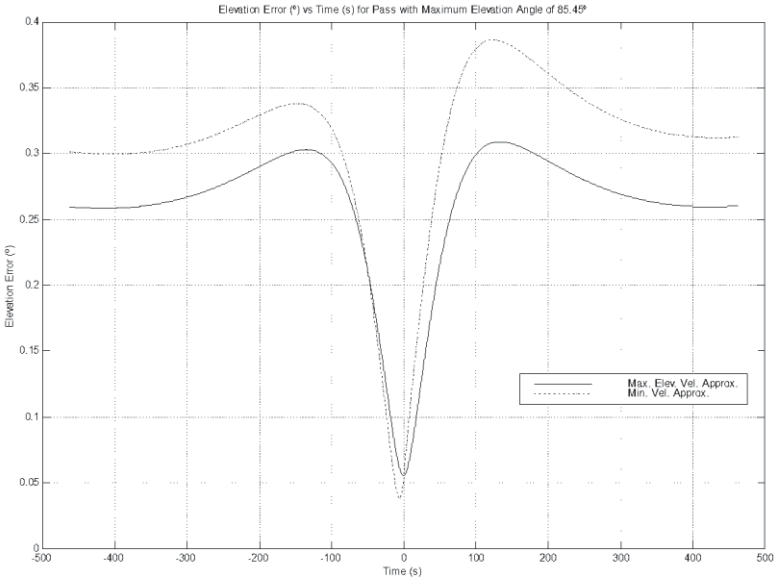

(d)

Figure 3.9 – *Plot of the azimuth (a), azimuth errors (b), elevation (c) and elevation errors (d) as a function of time for a pass with a maximum elevation angle of 85.45º.*

The figures above show the azimuth and elevation as well as the error curves as a function of time. We can see that as in the latitude and longitude cases, we have good agreement between the curves generated using the orbit generation algorithm and those

obtained using the approximated equations. Furthermore, upon examination of the errors, we see that the approximation of the angular velocity by its value at maximum elevation point gives a slightly better performance than the minimum value approximation.

3.5.4 Azimuth-Elevation to X-Y Transformation

In the case of high elevation passes, the rate of change of the azimuth increases as the satellite reaches its maximum elevation. For a zenith pass, the azimuth curve has a discontinuity at the maximum elevation point, [102] pp. 366-368. To avoid this problem, an X-Y coordinate system can be used, figure 3.10. The relative merits of using an X-Y pedestal as opposed to an azimuth elevation pedestal are discussed by Willey in [107] pp. 84-87.

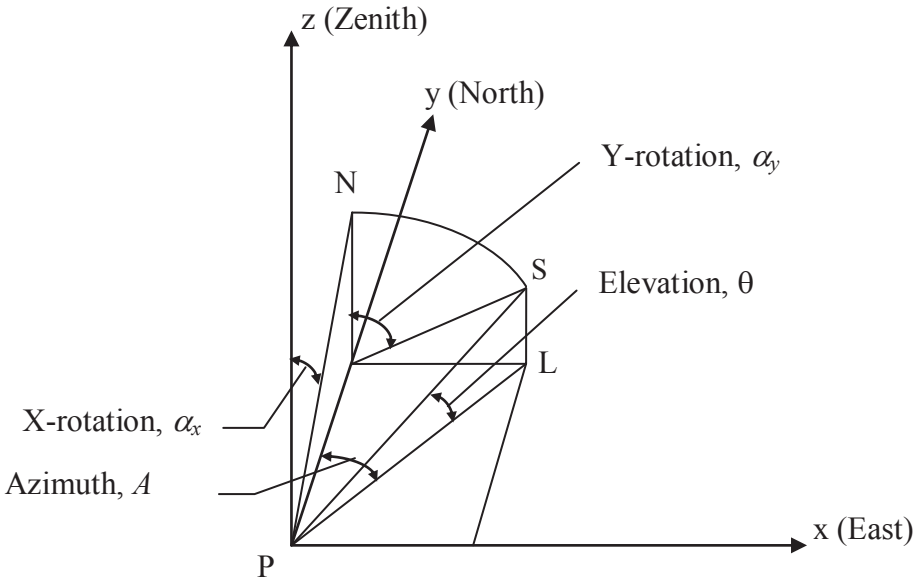

Figure 3.10 – *Azimuth-Elevation to X-Y transformation.*

The X and Y-axes are in the local horizontal plane with the x-axis pointed due East and the y-axis due North. The z-axis is pointed in the zenith direction. Specifying the satellite position requires a rotation, α_x, about the x-axis followed by a rotation, α_y, about the y-axis. In order to preserve the right hand rule, the positive x-rotation is taken to be from zenith towards south and the positive y-rotation from zenith towards east. In the scheme shown in figure 3.10, the x-rotation always follows a great circle arc while

the y-rotation forms a cone depending on the position of the x-axis. The resulting pedestal is termed X/Y (read "X over Y" pedestal). This means that the y-axis is the bottom axis and is fixed, whereas the x-axis is mounted on top of the y-axis and is therefore mobile. Again for a detailed discussion of X-Y pedestals refer to [107]. The X and Y-rotations can be derived from the azimuth and elevation as follows;

Since point P In figure 3.10 above is at the earth station location, line segments PS and PN are equal to $s(t)$ in figure 3.4(b). Line segments PL, LS and ML are given by

$$\mathrm{PL} = s(t)\cos(\theta) \tag{3.32}$$

$$\mathrm{LS} = s(t)\sin(\theta) \tag{3.33}$$

and

$$\begin{aligned} \mathrm{ML} &= \mathrm{PL}\sin(A) \\ &= s(t)\cos(\theta)\sin(A) \end{aligned} \tag{3.34}$$

Therefore from triangle MLS, and using the expressions for ML and LS, we have,

$$\begin{aligned} \tan(\alpha_y) &= \frac{\mathrm{ML}}{\mathrm{LS}} \\ &= \frac{s(t)\cos(\theta)\sin(A)}{s(t)\sin(\theta)} \\ &= \frac{\sin(A)}{\tan(\theta)} \end{aligned}$$

Side PM in triangle PML is given by

$$\begin{aligned} \mathrm{PM} &= \mathrm{PL}\cos(A) \\ &= s(t)\cos(A)\sin(\theta) \end{aligned} \tag{3.35}$$

The X-rotation, α_x, is found from triangle PMN,

$$\begin{aligned} \sin(-\alpha_x) &= \frac{\mathrm{PM}}{\mathrm{PN}} \\ &= \frac{s(t)\cos(\theta)\cos(A)}{s(t)} = \cos(\theta)\cos(A) \end{aligned}$$

Summarising we have,

$$\alpha_x = -\sin^{-1}(\cos(\theta)\cos(A)) \tag{3.36}$$

and

$$\alpha_y = \tan^{-1}\left(\frac{\sin(A)}{\tan(\theta)}\right) \tag{3.37}$$

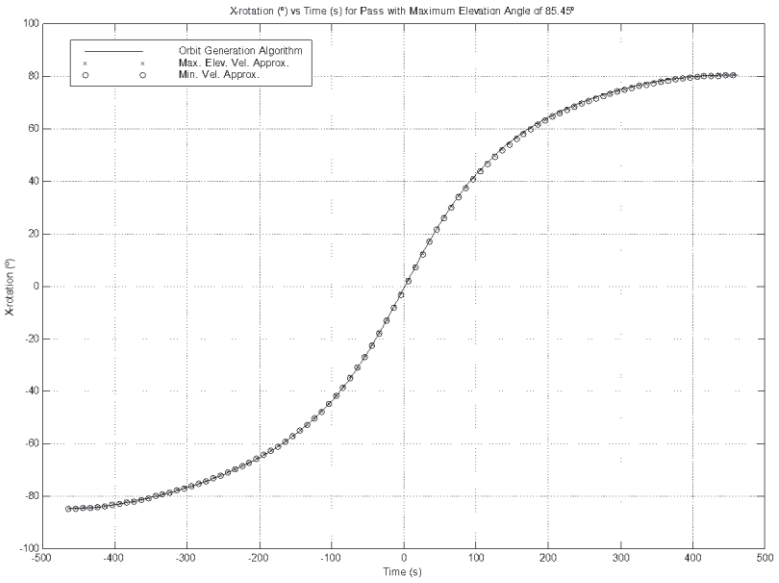

(a)

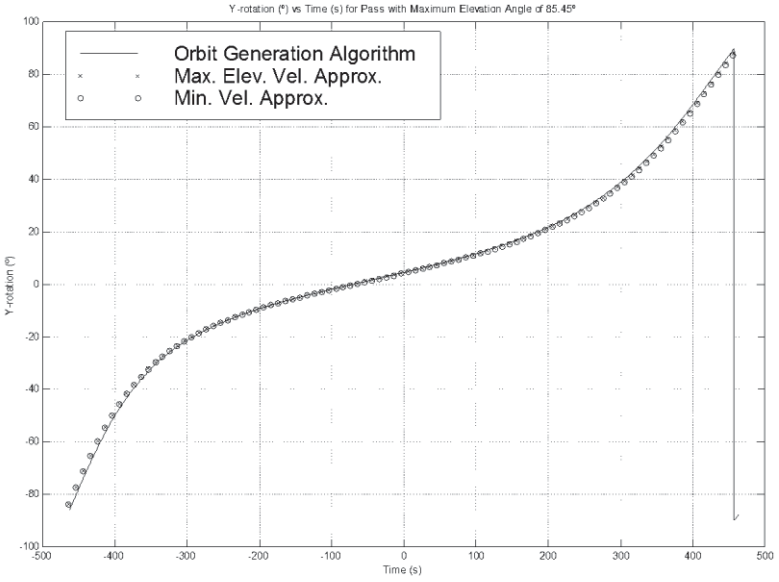

(b)

Figure 3.11 – *Plot of the X and Y rotations for a pass with a maximum elevation angle of 85.45°.*

Figures 3.11(a) and (b) show the X and Y rotations respectively. The curves obtained using the approximated equations agree very well with those from the orbit generation algorithm. The key-hole effect seen in figure 3.9(a) near zenith due to the high azimuth rate of change is transferred in the X-Y coordinate system to a point near the horizon. This is convenient since high elevation passes are far more important than low-elevation ones.

3.5.5 Off-Boresight Error

In order to assess the accuracy of an orbital model for the purpose of antenna spatial pointing, we need to calculate the off-boresight error (or pointing error), [108]. This is the error in degrees resulting from incorrectly pointing the antenna due to satellite position inaccuracy. Let the true satellite position in the topocentric-horizontal coordinate system be (A, θ) and the calculated position (A', θ'). This is shown in the figure below,

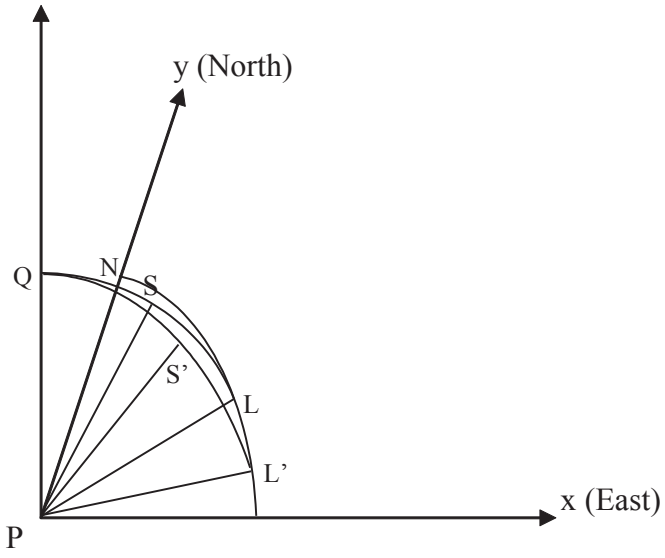

Figure 3.12 – *Off-boresight error.*

The off-boresight pointing error is given by angle SPS' in the figure above. Angles NPL and NPL′ are equal to A and A' respectively. Also SPL and S′PL′ give the elevations of S and S' respectively. Denote the off-boresight angular error, SPS', by β. Using the spherical identity (A.1) β is given by

$$\cos(\beta) = \cos(90-\theta)\cos(90-\theta') + \sin(90-\theta)\sin(90-\theta')\cos(A-A') \quad (3.38)$$

Simplifying equation (3.38) we obtain the following expression for β

$$\beta = \cos^{-1}\left(\sin(\theta)\sin(\theta') + \cos(\theta)\cos(\theta')\cos(A-A')\right) \quad (3.39)$$

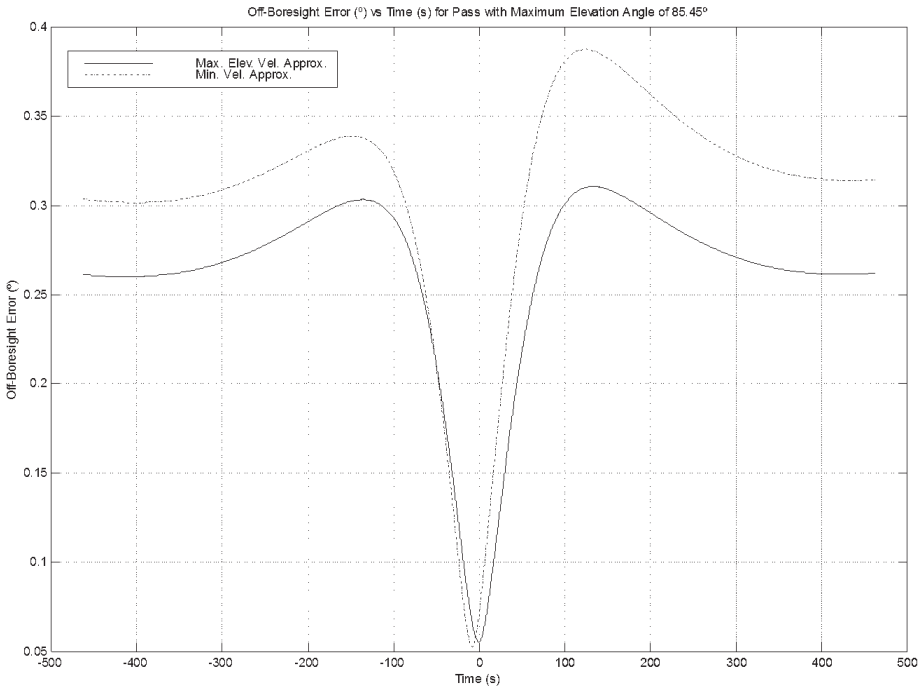

Figure 3.13 – *Plot of the off-boresight error curves for a pass with a maximum elevation angle of 85.45° for both ECEF angular velocity approximation strategies.*

Figure 3.13 shows the off-boresight error for the two angular velocity approximation strategies with respect to the orbit generation algorithm results. We can clearly see that the approximation of the ECEF angular velocity by its value at the maximum elevation point results in a smaller off-boresight error profile. The graph also shows that the off-boresight error is smallest at the time of closest approach. This is due to the fact that the pass approximation is parameterised on the maximum elevation point. Hence, we expect the approximation to be closest to the true pass at the maximum elevation point. The other interesting fact to notice is the much nearer symmetry of the curve.

3.6 Doppler Shift and Doppler Rate

When a source moves with respect to a receiver, a Doppler shift is observed on the received signal, [102]. The amount of Doppler shift is proportional to the relative velocity between the emitter and receiver. The observed normalised Doppler shift, D_s, is the amount of Doppler shift divided by the carrier frequency, f.

The normalised Doppler shift is therefore related to the rate of change of the earth station to satellite slant, $s(t)$, by

$$\begin{aligned} D_s &= \frac{\Delta f}{f} \\ &= -\frac{1}{c}\frac{ds(t)}{dt} \end{aligned} \tag{3.40}$$

where c is the speed of light

Using the expression for $s(t)$ given in equation (3.14) and carrying out the differentiation, we obtain the following expression for D_s,

$$D_s(t) = -\frac{1}{c}\frac{r_e r\dot{\gamma}(t)\sin(\gamma(t))}{\sqrt{r_e^2 + r^2 - 2r_e r\cos(\gamma(t))}} \tag{3.41}$$

The normalised Doppler rate is obtained by differentiating the above equation with respect to time.

$$D_r(t) = -\frac{1}{c}r_e r\left\{\frac{\left(\ddot{\gamma}\sin(\gamma)+\dot{\gamma}^2\cos(\gamma)\right)s^2 - r_e r\dot{\gamma}^2\sin^2(\gamma)}{s^3}\right\} \tag{3.42}$$

where s denotes the earth station to satellite slant range, given in equation (3.14) and the time index has been dropped for conciseness.

Equations (3.41) and (3.42) can be simplified using the assumptions stated in the introduction. Consider the right-angle spherical triangle MNP in figure 3.4(c). Using identity (A.4) we can write $\gamma(t)$ in terms of γ_0 and $\psi(t)$. Therefore

$$\cos(\gamma) = \cos(\psi)\cos(\gamma_0) \tag{3.43}$$

The range expression given in (3.14) becomes,

$$s(t) = \sqrt{r_e^2 + r^2 - 2r_e r\cos(\psi)\cos(\gamma_0)} \tag{3.44}$$

Combining equations (3.41) and (3.43) and remembering that $\dot{\psi} = \omega_F(t)$, we get the following expression for the normalised Doppler shift of the satellite at time *t*

$$D_s(t) = -\frac{1}{c}\frac{r_e r \sin(\psi(t))\cos(\gamma_0)\omega_F(t)}{\sqrt{r_e^2 + r^2 - 2r_e r\cos(\psi(t))\cos(\gamma_0)}} \tag{3.45}$$

The Doppler rate expression also becomes,

$$D_r = -\frac{1}{c} r_e r \omega_F \cos(\gamma_0)\left\{\frac{\omega_F \cos(\psi)s^2 - r_e r\omega_F \cos(\gamma_0)\sin^2(\psi)}{s^3}\right\} \tag{3.46}$$

As was done with the spatial characterisation equations, the approximated equations derived above were compared to Doppler shift and rate curves obtained using the orbit propagation algorithm. The results are shown in figure 3.14 below.

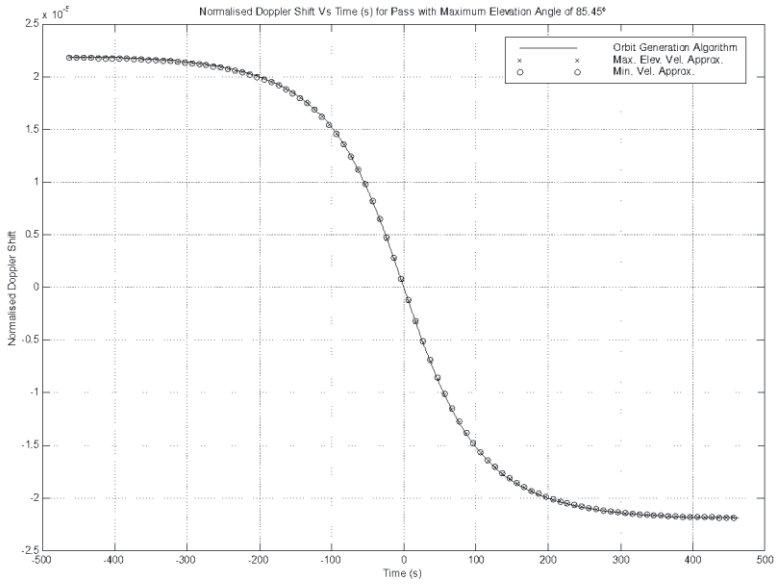

(a)

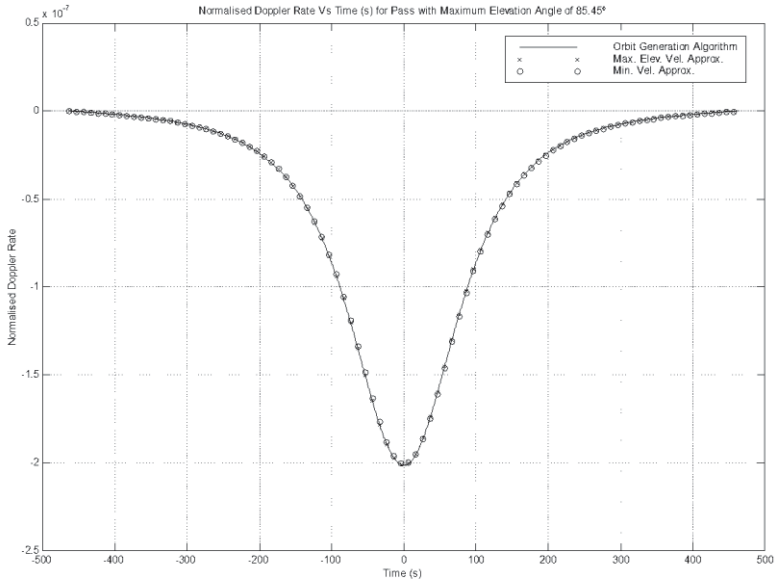

(b)

Figure 3.14 – *Plot of the Doppler shift and Doppler rate for a pass with a maximum elevation angle of 85.*

3.7 Conclusion

In this chapter we have presented a simplified orbital model for the determination of the orbit of a LEO satellite. This model set the thesis in context as it allows for the calculation of the Doppler shift. It is necessary for the development of many of the ideas in the thesis especially the FAST concept of chapter 9. The LEO satellite orbit is parameterised on the maximum elevation angle observed at the earth station. The analysis was done in the ECEF frame and the two body model was used. The earth was assumed to be spherical and lower order perturbations were ignored. In section 3.3 we presented an orbital propagation algorithm. Starting with an initial longitude of the ascending node, the algorithm propagates the orbit in time at the specified sampling rate.

We adopted the strategy of [103] and proceeded to fully characterise the orbit in terms of the maximum elevation angle observed at the earth station. The satellite orbit in the ECEF frame was assumed to be a great circle arc and the observed satellite angular velocity was taken to be constant. In section 3.4 we discussed the second assumption

and suggested approximating the angular velocity by its value at the maximum elevation point rather than its minimum value. We showed that this results in a more even spread of the errors and therefore in a smaller maximum absolute off-boresight error over the visible part of the orbit. We then proceeded in the rest of the chapter to derive simplified equations for the satellite's position as well as the observed Doppler shift and Doppler rate.

In the next chapter we look at the frequency domain frequency estimation problem. We examine the threshold effects and provide the context for the development of the novel frequency estimation algorithms to be presented in chapters 6, 7 and 8.

Chapter 4

Frequency Domain Frequency Estimation

4.1 Introduction

In this chapter we consider the problem of estimating the frequency using the Fourier coefficients of the gathered data. Due to the advent of digital signal processors, the Fourier coefficients are available very cheaply using the Fast Fourier Transform (FFT) algorithm. In the FedSat Ka band earth station, for instance, the Blue Wave Systems PCI/C6600 board, [109], is used to perform the signal processing functions. The board is based on two TMS320C67 floating point processors each capable of up to 1Gflops, [110]. A 1024 size FFT using the optimised algorithm obtained from Texas Instruments, [111], was found to take less than 200 μs. In contrast, at a sampling rate of 1 MHz, the data collection for 1024 samples takes 1.024 ms.

The estimation of frequency using Fourier coefficients has been dealt with extensively in the literature. It is well known that the Maximum Likelihood Estimate (MLE) of the frequency is given by the DFT maximiser, [112]. However performing this maximization numerically is not a trivial task. The DFT is commonly implemented using the FFT algorithm. The MLE of the frequency can be approximated by the FFT bin with the highest magnitude. This is termed the Maximum Bin Search (MBS) algorithm. The MBS algorithm, however, suffers from limited resolution since the FFT samples the DFT at N equally spaced points, where N is the number of data points used in the FFT. As a result, the MBS algorithm is often referred to as a coarse frequency estimator. One method to improve the resolution might be constructed by zero-padding the data before obtaining the FFT. This results in "sampling" the DFT more densely and hence improves the resolution. This rudimentary method, however, suffers from degradation due to noise and does not result in significant gain in resolution. It is also computationally costly. Therefore, in order to achieve a higher resolution, a fine frequency estimator is usually employed following the coarse search stage. In

subsequent chapters, we look at interpolation as well as search methods that are computationally efficient and result in a significant gain in resolution.

In this chapter we provide some preliminary theory on the estimation of the frequency of a sinusoid in the frequency domain. We start with a brief discussion on the Discrete Fourier Transform and the Fast Fourier Transform algorithm in section 4.2. In 4.3 we examine the MBS algorithm. We look at the SNR threshold effect in section 4.4. We then proceed to discuss and correct Quinn's derivation of an approximate expression for the onset of the threshold. Finally, the conclusion is presented in section 4.6.

4.2 The DFT and FFT

In this section we discuss the DFT and its implementation using the FFT. As there is an enormous amount of material on the subject, the discussion will be brief. Consider a complex sampled signal $s(k)$ consisting of a pure sinusoid. The signal is given by

$$s(k) = Ae^{j2\pi k\frac{f}{f_s}+\phi}, \qquad k = 0,1,\ldots,N-1 \tag{4.1}$$

where as defined earlier, N is the number of samples, A is the amplitude, f the signal frequency, ϕ the initial phase and f_s the sampling frequency. The Discrete Fourier Transform of s is defined by,

$$S(n) = \frac{1}{N}\sum_{k=0}^{N-1} s(k)e^{-j2\pi kn/N}, \text{ for } n = 0,1, \ldots, N\text{-}1 \tag{4.2}$$

where the normalising factor $1/N$ is intended to simplify many of the expressions to be derived. Some authors, like Haykin, [37], prefer to include the $1/N$ in the expression for the inverse DFT (IDFT) while others like Quinn, [34], split it into two $\frac{1}{\sqrt{N}}$ factors that are included in both the DFT and the IDFT expressions. The IDFT, which allows the original time-domain signal to be retrieved is, in our case, given by,

$$s(k) = \sum_{n=0}^{N-1} S(n)e^{j2\pi kn/N}, \text{ for } k = 0,1, \ldots, N\text{-}1 \tag{4.3}$$

For the sinusoidal signal defined in equation (4.1) above, the DFT is given by,

$$
\begin{aligned}
S(n) &= \frac{1}{N}\sum_{k=0}^{N-1} A e^{j2\pi k\frac{f}{f_s}+\phi} e^{-j2\pi k\frac{n}{N}} \\
&= \frac{Ae^{j\phi}}{N}\sum_{k=0}^{N-1}\left[e^{j2\pi\left(\frac{f}{f_s}-\frac{n}{N}\right)} \right]^k \\
&= \frac{Ae^{j\phi}}{N}\frac{e^{j2\pi N\frac{f}{f_s}}-1}{e^{j2\pi\left(\frac{f}{f_s}-\frac{n}{N}\right)}-1}
\end{aligned}
\tag{4.4}
$$

For a noisy signal $x(k) = s(k) + w(k)$ where the $w(k)$ is complex noise, the linearity property of the DFT implies that,

$$X(n) = S(n) + W(n) \tag{4.5}$$

With $S(n)$ being the DFT of the signal and $W(n)$ that of the noise. In this thesis, unless stated otherwise, it is assumed that the noise is Additive White Gaussian Noise (AWGN). The properties of the Fourier coefficients of AWGN are discussed in appendix C.

As mentioned in the introduction, the DFT is generally implemented in digital signal processors using the Fast Fourier Transform algorithm. Haykin, [37] pp. 102-108, presents a thorough discussion of the decimation-in-time and decimation-in-frequency FFT algorithms. Whereas a straightforward implementation of an N point DFT requires N^2 complex multiplications, the FFT algorithm reduces that to $\frac{N}{2}\log_2 N$.

4.3 The Maximum Bin Search

For a sinusoidal signal, the amplitude spectrum or periodogram is given by the magnitude of the expression given in (4.4). It can be shown that this magnitude is

$$
\begin{aligned}
|S(n)|^2 &= \frac{A^2}{N^2}\left|\frac{e^{j2\pi N\frac{f}{f_s}}-1}{e^{j2\pi\left(\frac{f}{f_s}-\frac{n}{N}\right)}-1}\right|^2 \\
&= \frac{A^2}{N^2}\frac{\sin^2\left(\pi N\frac{f}{f_s}\right)}{\sin^2\left(\pi\left(\frac{f}{f_s}-\frac{n}{N}\right)\right)}
\end{aligned}
\tag{4.6}
$$

It is well known, [21], that the periodogram is maximised if $n = {Nf}/{f_s}$. For n integer, this occurs at the index closest to the true frequency of the signal, that is for $n = \left[{Nf}/{f_s}\right]$ with $[\bullet]$ meaning rounding $\bullet$ to the nearest integer. Therefore, a coarse estimate of the frequency can be obtained using the index of the periodogram maximum. This is the Maximum Bin Search (MBS). Let the index corresponding to the maximum be denoted by m. Given that the correct maximum is chosen, the resolution of the Maximum Bin Search algorithm is

$$
|\Delta f| = \left|f - m\frac{f_s}{N}\right| \le \frac{f_s}{2N} \tag{4.7}
$$

If the signal frequency is uniformly distributed over the entire bandwidth (as may reasonably be assumed if the frequency is unknown), the error in frequency is also uniformly distributed over the frequency bin. This implies that the resulting MSE of the frequency estimate $\hat{f}$ is given by

$$
\begin{aligned}
\sigma_f^2 &= \mathrm{var}\left[\hat{f}\right] \\
&= \frac{f_s^2}{12N^2}
\end{aligned}
\tag{4.8}
$$

We see that the resolution of the MBS is $O(N^{-1})$ whereas the ACRB is $O(N^{-3/2})$. Therefore, there is significant scope for improvement in the resolution. This room for improvement motivates the research into higher resolution techniques such as the interpolation algorithm which build on the MBS to improve its resolution.

4.4 Threshold Effects

The analysis of the previous section assumes that the bin closest to the true frequency was chosen. In [19] and [34] pp.54-61, the properties of the periodogram maximiser were discussed under general assumptions on the noise model (refer to section 2.2). The noise was assumed to be generated by a zero-mean stationary, ergodic process. Their analysis shows that, provided we are above the SNR threshold, the frequency estimate of a sinusoidal signal plus noise is, almost surely, given by the maximum periodogram. That is

$$\left|\hat{f} - f\right| \leq \frac{f_s}{2N}, \text{a.s.} \tag{4.9}$$

This certainly holds under the stricter assumption of AWGN. As the signal to noise ratio deteriorates, however, the likelihood of making an incorrect choice increases. This incorrect bin is called an outlier and it occurs when the magnitude of at least one of the Fourier coefficients corresponding to the noise exceeds that of the coefficient corresponding to the signal. When the SNR threshold is reached, a rapid rise in the frequency error is observed. This is due to the increase in the probability of an outlier.

Let the probability that at least one of the noise terms exceeds the signal coefficient be denoted by q. We will proceed to calculate q and the total MSE. For large N, it is simpler to calculate the probability (1-q) that the correct bin is chosen, [21]. This is equivalent to the probability that the magnitudes of all bins are less than that of the index corresponding to the frequency closest to the signal. If the signal frequency is $f = \frac{m+\delta}{N} f_s$, where $|\delta| \leq 1/2$, the correct bin is that at index m. (1-q) is then expressed as,

$$1 - q = \int_0^\infty \mathrm{P}\{R_n < r, \forall n \neq m\} \mathrm{P}\{R_m = r\} dr \tag{4.10}$$

where R_n is the amplitude of the n^{th} Fourier coefficient.

The first factor in the integral consists of the conditional probabilities that the magnitude of all bins other than that closest to the signal are less than r, while the second factor is the probability that the magnitude of the correct bin is equal to r. Given that the Fourier coefficients are independent, the first factor can be written as the product of the individual probabilities. That is

$$\mathrm{P}\{R_n < r \mid R_m = r, \forall n \neq m\} = \prod_{\substack{n=0 \\ n \neq m}}^{N-1} P\{R_n < r \mid R_m = r\} \tag{4.11}$$

In the general case, where δ is not necessarily 0, the individual probabilities, given in equation (C.24), are Ricean. Hence,

$$\mathrm{P}\{R_n < r \mid R_m = r, \forall n \neq m\} = \prod_{\substack{n=0 \\ n \neq m}}^{N-1} \int_0^r \frac{Nx}{\sigma^2} e^{-N\frac{x^2+B_n^2}{2\sigma^2}} I_0\left(\frac{NB_n x}{\sigma^2}\right) dx \tag{4.12}$$

where B_n is the magnitude of the n^{th} Fourier coefficient of the sinusoidal signal at index n. B_n is given by the square root of expression (4.6).

The total probability that the correct bin is chosen, assuming that bin m is closest to the true frequency, is

$$1 - q = \int_0^\infty \left[\prod_{\substack{n=0 \\ n \neq m}}^{N-1} \int_0^r \frac{Nx}{\sigma^2} e^{-N\frac{x^2+B_n^2}{2\sigma^2}} I_0\left(\frac{NB_n x}{\sigma^2}\right) dx \right] \frac{Nr}{\sigma^2} e^{-N\frac{r^2+B_m^2}{2\sigma^2}} I_0\left(\frac{NB_m r}{\sigma^2}\right) dr \tag{4.13}$$

In the general case, the MSE can be derived as a function of f. We can write it in the form,

$$MSE\left(\hat{f}\right) = \sum_{m=-N/2}^{N/2-1} \left(\frac{m}{N} f_s - f\right)^2 . P\{R_n < R_m, \forall n \neq m\} \tag{4.14}$$

The probabilities in the above expression can be obtained using equation (4.13). In the general case where the sinusoid is not on the bin centre, all of the bins will contain a signal component as well as a noise component. The resulting distributions are all Ricean and the MSE expression is somewhat complicated. However, for large N, the leakage of the sinusoidal signal to other bins is small compared to the "main lobe". In fact the signal coefficients B_n are $O\left(N^{-1}\right)$ unless

$$\frac{f}{f_s} - \frac{n}{N} = 0$$

or equivalently, from (C.23), $m - n + \delta = 0$ (which is only satisfied if $m = n$ and $\delta = 0$). In that case, the resulting coefficient is $O(1)$ and the rest of the B_n are all zero and we can, consequently simplify the MSE expression considerably. It is clear that if the

signal frequency corresponds to a bin centre, that is $\delta = 0$, the "effective" SNR of the bin containing the signal is highest at $\frac{A^2}{\sigma^2}$. If on the other hand, the signal frequency falls halfway between two bin centres, the effective SNR is $\frac{A^2}{2\sigma^2}$, and the threshold is highest.

The outlier probability, q_N, where the subscript N indicates the dependence of q on N, was derived for the best case ($\delta = 0$) by Rife and Boorstyn in [21]. It is given by

$$q_N = 1 - \int_0^\infty \left[1 - e^{-N\frac{r^2}{2\sigma^2}}\right]^{N-1} \frac{Nr}{\sigma^2} e^{-N\frac{r^2+A^2}{2\sigma^2}} I_0\left(\frac{NAr}{\sigma^2}\right) dr \tag{4.15}$$

This simplifies to

$$q_N = \frac{1}{N} \sum_{k=2}^{N} \frac{N!(-1)^m}{(N-m)!m!} e^{-N\rho\frac{m-1}{m}} \tag{4.16}$$

The total MSE is then composed of the CRB and the error due to the occurrence of outliers. Since Rife has assumed that the signal is contained in one bin only, the rest of the bins are equally likely outlier candidates. Hence the MSE due to the outliers is simply the variance of a uniform distribution over the range $-f_s/2$ to $f_s/2$. This is given by $f_s^2/12$. Hence the total MSE is given by,

$$\sigma_{\hat{f}}^2 = q_N \frac{f_s^2}{12} + (1 - q_N) \frac{6 f_s^2}{(2\pi)^2 \rho N (N^2 - 1)} \tag{4.17}$$

As the terms in the summation in (4.16) become very large and alternate in sign, the expression becomes difficult to evaluate on a computer for any reasonably large N. Therefore equation (4.15) must be integrated numerically. The plot in figure 4.1 below shows the outlier probability versus SNR in dB for various values of N. As the number of samples increases, the outlier probability decreases as a function of the SNR. Therefore we expect that the MSE threshold decreases with respect to N.

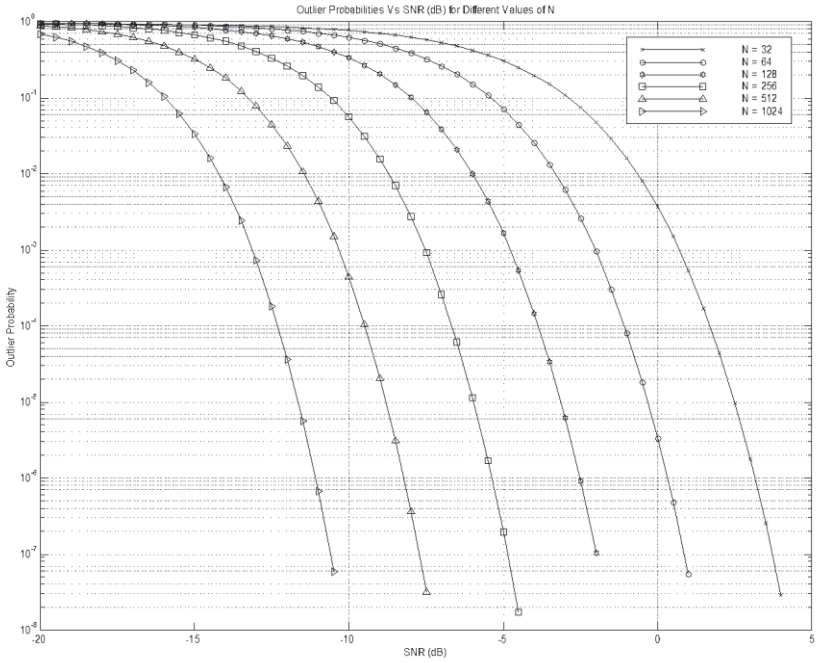

Figure 4.1 – *Outlier probability versus signal to noise ratio for various sample block sizes.*

The theoretical frequency RMSE was calculated using equation (4.17) for different values of N and with the sampling frequency set to 1. The results are shown in figure 4.2 below. The onset of the threshold is clearly visible. We also remark that the threshold decreases by about 3 dB for each doubling of N.

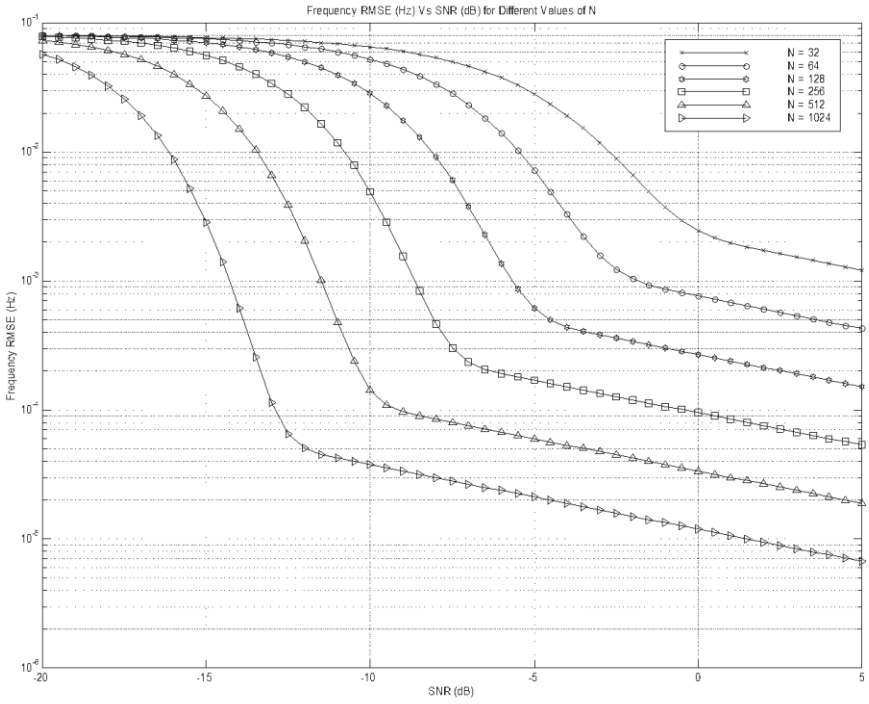

Figure 4.2 – *Frequency RMSE versus signal to noise ratio for various sample block sizes.*

4.5 Approximate Expression for Threshold Onset

While equations (4.15) - (4.17) account for the threshold behaviour, they are complicated and must be evaluated numerically. It is, thus, advantageous to obtain an approximate expression for the SNR at which the threshold occurs. In [113], the authors attempt to understand and characterise the threshold behaviour using known results from phase locked loops. They define the threshold for each N as the knee of the frequency RMSE curves as is seen in figure 4.2. They show that the threshold can be characterised by a single parameter, γ_N, given by

$$\gamma_N = \frac{3}{\rho N}$$

where ρ is the SNR. This parameter is related to the phase error of the estimator by

$$\gamma_N = \frac{3}{4} \times \text{phase MSE}$$

The value of the phase mean square error at the threshold is shown to be approximately constant, equal to 0.0625 rad^2. The threshold, then, occurs when the value of ρ for which the Mean Square (MS) phase error is roughly 0.0625 rad^2. Solving for ρ in dB we get,

$$\rho(\text{dB}) \approx 10\log\left(\frac{32}{N}\right) \tag{4.18}$$

In [114], the author attempts to provide a "more fundamental" approach to the understanding of the onset threshold effect. We should note here that he seems to have made a mistake in defining the signal to noise ratio. He takes the complex noise to have a variance σ^2 and then defines the SNR as $\frac{A^2}{2\sigma^2}$. According to his SNR definition, the real and imaginary parts of the noise each have variance σ^2. The Barankin bound (BRB) is deemed to be a tighter lower bound than the CRB for nonlinear estimation problems. The approach to establishing the threshold SNR, then, consists of determining the point where the two bounds depart from each other. The indicator quantity is taken to be the ratio of the BRB to the CRB. When this becomes larger than unity, the threshold effect is said to have occurred. This is shown to be equivalent to the inequality,

$$\frac{\rho N}{\ln N} < 1 \tag{4.19}$$

Whereas the above expressions provide indicator quantities, Quinn, in [9], derives an approximate expression for the threshold SNR. He starts by discussing the Rife and Boorstyn result. He then, stipulates that the onset of the threshold occurs when the total MSE is twice to the CRB. He only considers the case where $\delta = 0$. Furthermore, in order to simplify the analysis, he sets the signal frequency to $\frac{f_s}{2}$. In the following section, we examine Quinn's approach and correct an error in the derivation. The mistake was found, however, to have a small effect that diminishes with increasing N.

4.5.1 Derivation of the Approximate Expression

The total frequency estimation MSE was given in equation (4.17). Normalising the MSE expression by the CRB we get,

$$\overline{MSE}\left(\hat{f}\right)-1 = q_N \frac{\pi^2 \rho N\left(N^2-1\right)}{18} - q_N \tag{4.20}$$

Quinn argued that the threshold is reached when the term on the right hand side of (4.20) is "substantially" different from zero. He defines the threshold to occur when the total MSE is twice the CRB. Here, we adopt this definition. Therefore, the strategy consists of obtaining an expression for the SNR at which the total MSE is exactly twice the CRB.

Recall that the index of the bin containing the signal is denoted by *m*. The outlier probability, q_N, is equivalent to the probability that the maximum of all bins excluding bin *m* exceeds the magnitude of bin *m*. In order to simplify the analysis we set $m = \frac{N}{2}$. Therefore q_N is

$$\begin{aligned} q_N &= P\left\{ \max_{\substack{0\le n\le N-1 \\ n\ne m}} \left|X(n)\right|^2 > \left|X(m)\right|^2 \right\} \\ &= P\left\{ \max_{\substack{0\le n\le N-1 \\ n\ne N/2}} \left|X(n)\right|^2 > \left|X\left(\tfrac{N}{2}\right)\right|^2 \right\} \end{aligned} \tag{4.21}$$

Let $Z(n) = \frac{2N\left|X(n)\right|^2}{\sigma^2}$. $Z\left(N/2\right)$ is evaluated as follows,

$$\begin{aligned} Z\left(\tfrac{N}{2}\right) &= \frac{2N}{\sigma^2}\left|\frac{1}{N}\sum_{k=0}^{N-1}\left(Ae^{j\phi}e^{jk\pi} + w(k)\right)e^{-jk\pi}\right|^2 \\ &= \left|\frac{\sqrt{2}}{\sqrt{N}\sigma}\sum_{k=0}^{N-1}\left(Ae^{j\phi} + w(k)e^{-jk\pi}\right)\right|^2 \\ &= \left|\sqrt{\frac{2}{N}}e^{-j\phi}\sum_{k=0}^{N-1}(-1)^k\frac{w(k)}{\sigma} + \sqrt{2N}\frac{A}{\sigma}\right|^2 \\ &= \left(U+\sqrt{2N\rho}\right)^2 + V^2 \end{aligned} \tag{4.22}$$

where U and V are the real and imaginary parts of

$$\sqrt{\frac{2}{N}}e^{-j\phi}\sum_{k=0}^{N-1}(-1)^k\frac{w(k)}{\sigma}$$

Since the noise terms $w(k)$ Gaussian i.i.d. with mean 0 and variance σ^2, it follows that U and V are independent Gaussian with mean 0 and variance 1.

Let $\hat{Z}_N$ be the maximum of $Z(n)$ over the set of all Fourier coefficients excluding that at index $N/2$. Substituting into equation (4.21) yields,

$$\begin{aligned} q_N &= P\left\{\hat{Z}_N > \left(U+\sqrt{2N\rho}\right)^2 + V^2\right\} \\ &= \int_{-\infty}^{\infty}\int_{-\infty}^{\infty}\left\{1-\left[1-e^{-\frac{1}{2}\left(u^2+v^2\right)}\right]^{N-1}\right\}\Phi(v)\Phi\left(u-\sqrt{2N\rho}\right)dvdu \end{aligned} \tag{4.23}$$

where $\Phi(x)$ is the standard normal density function, given by

$$\Phi(x) = \frac{1}{\sqrt{2\pi}}e^{-\frac{x^2}{2}}$$

Consider the probability that the envelope squared is less than a positive constant *z*. The square of the envelope follows an exponential distribution, [115] pp. 108-109. In order to simplify the notation let $K = N-1$. In the following analysis we will implicitly use the fact that, [116] pp. 284,

$$\text{if } f(x) \le g(x)\ \forall x \in [a,b], \text{ then } \int_a^b f(x)dx \le \int_a^b g(x)dx$$

Now we have that,

$$\begin{aligned} P\left\{\hat{Z}_N - 2\ln K \le z\right\} &= \left[1-e^{-\frac{1}{2}(z-2\ln K)}\right]^K \\ &= \left[1-\frac{1}{K}e^{-\frac{1}{2}z}\right]^K \to e^{-e^{-\frac{1}{2}z}}, \text{ as } K\to\infty \end{aligned} \tag{4.24}$$

Hence $\hat{Z}_N - 2\ln K$ converges in distribution. Next, we break the integral in (4.23) into three parts, I_1, I_2 and I_3 defined over the intervals $\left(-\infty,-\sqrt{2\ln K}\right)$, $\left(-\sqrt{2\ln K},\sqrt{2\ln K}\right)$ and $\left(\sqrt{2\ln K},\infty\right)$ respectively. Considering each integral separately, we have

$$\begin{aligned} I_1 &= \int_{-\infty}^{-\sqrt{2\ln K}}\int_{-\infty}^{\infty}\left\{1-\left[1-e^{-\frac{1}{2}\left(u^2+v^2\right)}\right]^K\right\}\Phi(v)\Phi\left(u-\sqrt{2N\rho}\right)dvdu \\ &= \int_{-\infty}^{-\sqrt{2\ln K}}\Phi\left(u-\sqrt{2N\rho}\right)\int_{-\infty}^{\infty}\left\{1-\left[1-e^{-\frac{1}{2}\left(u^2+v^2\right)}\right]^K\right\}\Phi(v)dvdu \end{aligned}$$

Now for $u < -\sqrt{2\ln K}$ the inequality $e^{-\frac{u^2}{2}} < K^{-1}$ holds and the inner integral becomes,

$$\int_{-\infty}^{\infty}\left\{1-\left[1-e^{-\frac{1}{2}\left(u^2+v^2\right)}\right]^K\right\}\Phi(v)dv < \int_{-\infty}^{\infty}\left\{1-\left[1-K^{-1}e^{-\frac{1}{2}v^2}\right]^K\right\}\Phi(v)dv \qquad (4.25)$$

Here Quinn asserts that the term $\left(1-K^{-1}e^{-\frac{1}{2}v^2}\right)^K$ converges to $e^{-e^{-\frac{1}{2}v}}$ from above and the expression in (4.25) becomes

$$\int_{-\infty}^{\infty}\left\{1-\left[1-e^{-\frac{1}{2}\left(u^2+v^2\right)}\right]^K\right\}\Phi(v)dv < \int_{-\infty}^{\infty}\left(1-e^{-e^{-\frac{1}{2}v^2}}\right)\Phi(v)dv \qquad (4.26)$$

$$\approx 0.4860709$$

This, however, is not correct since $\left(1-K^{-1}e^{-\frac{1}{2}v^2}\right)^K$ converges to $e^{-e^{-\frac{1}{2}v}}$ from below and we have that,

$$\left(1-\frac{e^{-\frac{v^2}{2}}}{K}\right)^K \le e^{-e^{-\frac{v^2}{2}}} \Rightarrow$$

$$\left[1-\left(1-\frac{e^{-\frac{v^2}{2}}}{K}\right)^K\right]\Phi(v) \ge \left(1-e^{-e^{-\frac{v^2}{2}}}\right)\Phi(v)$$

Thus the inequality of equation (4.26) cannot be asserted. Furthermore, one can show that there is no value for K, say K_0, above which the inequality holds. Hence we have to adopt another strategy of partitioning the integral in (4.23).

Let $u = -\sqrt{2\ln K} - \varepsilon$ for some ε>0. Substituting into the binomial expression yields,

$$\left(1-e^{-\frac{u^2+v^2}{2}}\right)^K = \left(1-\frac{1}{K}e^{-\frac{\varepsilon^2+2\varepsilon\sqrt{2\ln K}+v^2}{2}}\right)^K$$

We attempt to find the value of ε corresponding to K, denoted by ε_N (since $K = N$-1), for which the inequality

$$\left(1-\frac{1}{K}e^{-\frac{\varepsilon^2+2\varepsilon\sqrt{2\ln K}+v^2}{2}}\right)^K > e^{-e^{-\frac{v^2}{2}}}$$

holds for all v. Now we use the fact that the logarithm function is monotonically increasing and consequently if $x > y$ then $\ln(x) > \ln(y)$ and $\ln(x) - \ln(y) > 0$. Hence, the above is equivalent to finding ε such that the function

$$f(v) = K\ln\left(1-\frac{1}{K}e^{-\frac{\varepsilon^2+2\varepsilon\sqrt{2\ln K}+v^2}{2}}\right)+e^{-\frac{v^2}{2}} > 0, \forall v \tag{4.27}$$

We firstly note that $f(v)$ is even in v. Now looking for turning points, we have

$$f'(v) = \frac{ve^{-\frac{v^2}{2}}}{1-\frac{1}{K}e^{-\frac{\varepsilon^2+2\varepsilon\sqrt{2\ln K}+v^2}{2}}}\left\{e^{-\frac{\varepsilon^2+2\varepsilon\sqrt{2\ln K}}{2}}\left(1+\frac{e^{-\frac{v^2}{2}}}{K}\right)-1\right\}$$

Now $f'(v) = 0$ for $v = 0, \pm\infty$. Furthermore, as v tends to ∞, $f(v)$ tends to zero from above. This is concluded from the fact that for v large, $f'(v)$ is negative since the numerator tends to $e^{-\frac{\varepsilon^2+2\varepsilon\sqrt{2\ln K}}{2}}-1$ which is negative. Hence as v approaches ∞, $f(v)$ is asymptotically decreasing to zero. This implies that $f(v)$ has either three or five turning points depending on the value of ε. Also only in the case where $f(v)$ has five turning points that it can have negative values and $f(0)$ becomes a global minimum. This is illustrated in the plot below.

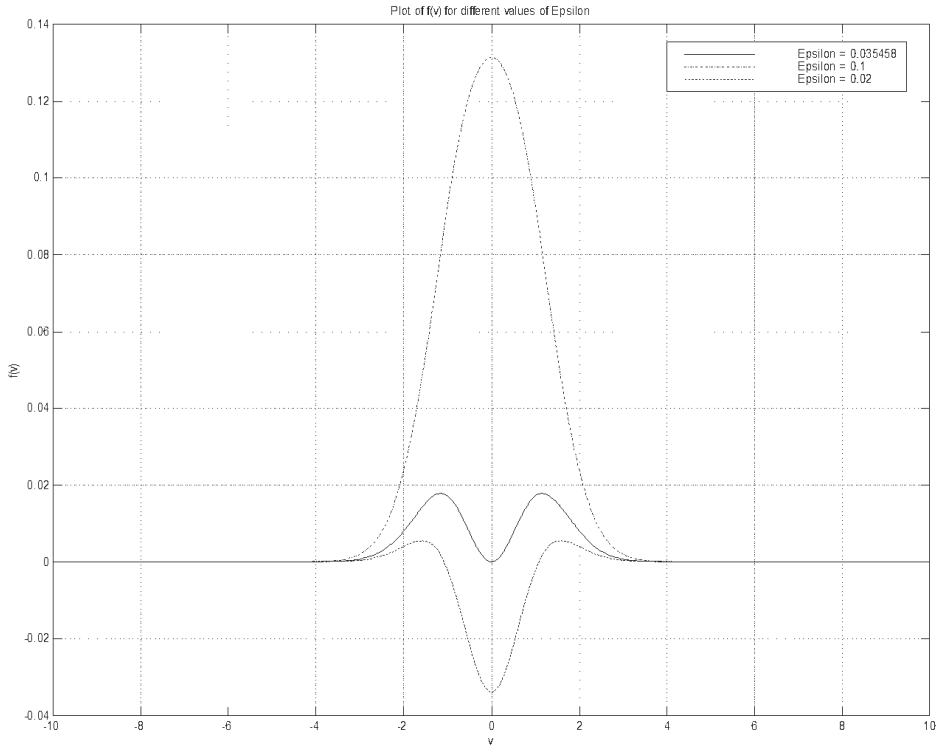

Figure 4.3 – *Plot of f(v) Vs v for different values of* ε. *N was set to* 8 *(that is K = 7).*

The plot shows that there is a value of ε, ε_N, above which $f(v)$ is strictly positive. Therefore ε_N can easily be calculated by solving $f(0)=0$ for ε. Thus,

$$f(0) = K\ln\left(1-\frac{1}{K}e^{-\frac{\varepsilon^2+2\varepsilon\sqrt{2\ln K}}{2}}\right)+1$$
$$= 0$$

Carrying out the necessary algebra we obtain

$$\varepsilon_N = -\sqrt{2\ln K} \pm \sqrt{2\ln K - 2\ln\left[K\left(1-e^{-\frac{1}{K}}\right)\right]}$$

Since ε>0, we must take the positive solution and ε_N becomes

$$\varepsilon_N = -\sqrt{2\ln K} + \sqrt{2\ln K - 2\ln\left[K\left(1-e^{-\frac{1}{K}}\right)\right]} \qquad (4.28)$$

For example for $K = 7$ (that is $N = 8$), ε_N is found to be 0.035458. This agrees with figure 4.3 since the curve corresponding the this value of ε is positive with $f(0) = 0$, whereas the curve corresponding to $\varepsilon = 0.1$ is strictly positive. Therefore,

$$\left(1-e^{-\frac{u^2+v^2}{2}}\right)^K > e^{-e^{-\frac{v^2}{2}}}$$

holds for all v for $u < -\sqrt{2\ln K} - \varepsilon_N$. Guided by this knowledge, we continue with Quinn's analysis but with the modified interval boundaries for the three integrals and with two additional integrals for the problem regions of $\left(\pm\sqrt{2\ln K} \pm \varepsilon_N, \pm\sqrt{2\ln K}\right)$. We will keep the rest of the chapter brief by not including the detailed algebraic derivations. Let $u_N = \sqrt{2\ln K} + \varepsilon_N$ and break the integral in (4.23) into I_1, I_{12}, I_2, I_{23} and I_3 defined over $(-\infty, -u_N)$, $\left(-u_N, -\sqrt{2\ln K}\right)$, $\left(-\sqrt{2\ln K}, \sqrt{2\ln K}\right)$, $\left(\sqrt{2\ln K}, u_N\right)$ and (u_N, ∞) respectively. Now for $u < -u_N$ the first integral, I_1 becomes,

$$\begin{aligned} I_1 &= \int_{-\infty}^{-u_N}\int_{-\infty}^{\infty}\left\{1-\left(\left[1-e^{-\frac{1}{2}\left(u^2+v^2\right)}\right]^K\right)\right\}\Phi(v)\Phi\left(u-\sqrt{2N\rho}\right)dvdu \\ &< \int_{-\infty}^{-u_N}\Phi\left(u-\sqrt{2N\rho}\right)\int_{-\infty}^{\infty}\left(1-e^{-e^{-\frac{1}{2}v^2}}\right)\Phi(v)dvdu \qquad (4.29) \\ &= 0.4860709Q\left(u_N+\sqrt{2N\rho}\right) \\ &= cQ\left(u_N+\sqrt{2N\rho}\right) \end{aligned}$$

where $c = 0.4860709$ and $Q(x)$ is the standard Q function defined as

$$Q(x) = \int_z^{\infty}\Phi(t)dt$$

Now for $|u| < -\sqrt{2\ln K}$,

$$\left(1-e^{-\frac{u^2+v^2}{2}}\right)^K < e^{-e^{-v^2}}$$

Therefore I_2 becomes,

$$
\begin{aligned}
I_2 &= \int_{-\sqrt{2\ln K}}^{\sqrt{2\ln K}} \int_{-\infty}^{\infty} \left\{ 1 - \left[1 - e^{-\frac{1}{2}\left(u^2+v^2\right)} \right]^K \right\} \Phi(v)\Phi\left(u - \sqrt{2N\rho}\right) dv\,du \\
&> \int_{-\sqrt{2\ln K}}^{\sqrt{2\ln K}} \Phi\left(u - \sqrt{2N\rho}\right) \int_{-\infty}^{\infty} \left(1 - e^{-e^{-\frac{1}{2}v^2}} \right) \Phi(v)\,dv\,du \\
&= c\left\{ Q\left(\sqrt{2N\rho} - \sqrt{2\ln K}\right) - Q\left(\sqrt{2N\rho} + \sqrt{2\ln K}\right) \right\}
\end{aligned}
\tag{4.30}
$$

An upper bound for I_2 is obtained as follows. Setting $\left\{ 1 - \left(\left[1 - e^{-\frac{1}{2}\left(u^2+v^2\right)} \right]^K \right) \right\}$ to its maximum value which occurs for u=v=0, we get,

$$
\begin{aligned}
I_2 &< \int_{-\sqrt{2\ln K}}^{\sqrt{2\ln K}} \Phi\left(u - \sqrt{2N\rho}\right) \int_{-\infty}^{\infty} \Phi(v)\,dv\,du \\
&= Q\left(\sqrt{2N\rho} - \sqrt{2\ln K}\right) - Q\left(\sqrt{2N\rho} + \sqrt{2\ln K}\right)
\end{aligned}
\tag{4.31}
$$

Quinn then calculates I_3 directly using the binomial approach. Expanding the Kth power term into a binomial series we get,

$$
I_3 = \sum_{l=1}^{K} (-1)^{l-1} \binom{K}{l} \int_{-\infty}^{\infty} e^{-\frac{lv^2}{2}} \Phi(v)\,dv \int_{u_N}^{\infty} e^{-\frac{lu^2}{2}} \Phi\left(u - \sqrt{2N\rho}\right) du
$$

where $\binom{K}{l}$ are the binomial coefficients. Changing variables and integrating we get,

$$
\int_{-\infty}^{\infty} e^{-\frac{lv^2}{2}} \Phi(v)\,dv = \frac{1}{\sqrt{l+1}}
$$

and

$$
\int_{u_0}^{\infty} e^{-\frac{lu^2}{2}} \Phi\left(u - \sqrt{2N\rho}\right) du = \frac{e^{-\frac{lN\rho}{l+1}}}{\sqrt{l+1}} Q\left[\sqrt{l+1} \left(u_N - \frac{\sqrt{2N\rho}}{l+1} \right) \right]
$$

Substituting the above expressions into I_3,

$$
I_3 = \sum_{l=1}^{K} (-1)^{l-1} \binom{K}{l} \frac{e^{-\frac{lN\rho}{l+1}}}{l+1} Q\left[\sqrt{l+1} \left(u_N - \frac{\sqrt{2N\rho}}{l+1} \right) \right] \tag{4.32}
$$

This expression for I_3 is realisable numerically since the Q terms decay fast enough to compensate for the growth in the factorial terms of the binomial coefficients.

Now considering the two remaining integrals,

$$
\begin{aligned}
I_{12} &= \int_{-u_N}^{-\sqrt{2\ln K}} \int_{-\infty}^{\infty} \left\{ 1 - \left[1 - e^{-\frac{1}{2}\left(u^2+v^2\right)} \right]^K \right\} \Phi(v)\Phi\left(u - \sqrt{2N\rho}\right) dv du \\
&< \int_{-u_N}^{-\sqrt{2\ln K}} \Phi\left(u - \sqrt{2N\rho}\right) \int_{-\infty}^{\infty} \left(1 - \left[1 - \frac{1}{K} e^{-\frac{1}{2}v^2} \right]^K \right) \Phi(v) dv du \\
&= \int_{-u_N}^{-\sqrt{2\ln K}} \Phi\left(u - \sqrt{2N\rho}\right) du \int_{-\infty}^{\infty} \left\{ e^{-\frac{1}{2}v^2} - \sum_{l=2}^{K} (-1)^l \binom{K}{l} \frac{1}{K^l} e^{-\frac{l}{2}v^2} \right\} \Phi(v) dv
\end{aligned}
$$

In the above, the binomial series expansion was employed. Looking at the difference between successive even and odd coefficients under the summation we see that it is can be written as

$$
\frac{K(K-1)\cdots(K-l)}{l!} \frac{1}{K^l} e^{-\frac{l}{2}v^2} \left\{ \frac{1}{K-l} - \frac{e^{-\frac{1}{2}v^2}}{K(l+1)} \right\}
$$

We see that as l increases, the difference is positive and decreasing and therefore the summation result is positive. Hence we can place a lower bound on the integral by making the summation result zero. That is

$$
\begin{aligned}
I_{12} &< \int_{-u_N}^{-\sqrt{2\ln K}} \Phi\left(u - \sqrt{2N\rho}\right) du \int_{-\infty}^{\infty} e^{-\frac{1}{2}v^2} \Phi(v) dv \\
&= \frac{1}{\sqrt{2}} \left\{ Q\left(\sqrt{2\ln K} + \sqrt{2N\rho}\right) - Q\left(u_N + \sqrt{2N\rho}\right) \right\}
\end{aligned}
\tag{4.33}
$$

Similarly, I_{23} can be shown to be bounded by,

$$
\begin{aligned}
I_{23} &< \int_{\sqrt{2\ln K}}^{u_N} \Phi\left(u - \sqrt{2N\rho}\right) du \int_{-\infty}^{\infty} e^{-\frac{1}{2}v^2} \Phi(v) dv \\
&= \frac{1}{\sqrt{2}} \left\{ Q\left(\sqrt{2N\rho} - u_N\right) - Q\left(\sqrt{2N\rho} - \sqrt{2\ln K}\right) \right\}
\end{aligned}
\tag{4.34}
$$

In order to summarise the above results, we define the following terms

$$
\begin{aligned}
\alpha_1 &= Q\left(u_N + \sqrt{2N\rho}\right) \\
\alpha_2 &= Q\left(\sqrt{2N\rho} + \sqrt{2\ln K}\right) \\
\alpha_3 &= Q\left(\sqrt{2N\rho} - \sqrt{2\ln K}\right) \\
\alpha_4 &= Q\left(\sqrt{2N\rho} - u_N\right)
\end{aligned}
$$

The table below shows the resulting bounds. Note that for I_3 we calculated an exact result and therefore it is included in the table as I_3 in both the upper and lower bound cells.

Lower Bound	Integral	Upper Bound
0	I_1	$c\alpha_1$
0	I_{12}	$\frac{1}{\sqrt{2}}(\alpha_2 - \alpha_1)$
$c(\alpha_3 - \alpha_2)$	I_2	$(\alpha_3 - \alpha_2)$
0	I_{23}	$\frac{1}{\sqrt{2}}(\alpha_4 - \alpha_3)$
I_3	I_3	I_3

Table 4.2 – *Outlier probability bounds for threshold calculation.*

Now using the above results, the outlier probability is bounded by

$$c(\alpha_3 - \alpha_2) + I_3 < q_N < \left(c - \frac{1}{\sqrt{2}}\right)\alpha_1 + \left(\frac{1}{\sqrt{2}} - 1\right)\alpha_2 + \left(1 - \frac{1}{\sqrt{2}}\right)\alpha_3 + I_3 \qquad (4.35)$$

This expression differs from that given in [9] due to the terms from the two additional integrals. The right hand side in equation (4.20) converges to zero when all of the Q expressions in the bounds above converge to zero individually. We first rewrite $Q(x)$ as follows:

$$\begin{aligned} Q(x) &= \frac{1}{\sqrt{2\pi}} \int_x^\infty e^{-\frac{t^2}{2}} dt \\ &= \frac{e^{-\frac{x^2}{2}}}{x\sqrt{2\pi}} - \frac{1}{\sqrt{2\pi}} \int_x^\infty \frac{e^{-\frac{t^2}{2}}}{t^2} dt \end{aligned}$$

Now let $N\rho = \gamma \ln K$. As the constants do not affect the convergence properties of the integral, we will ignore them in the following. Substituting into equation (4.20) and considering the term in α_1,

$$N\rho\left(N^2-1\right)\alpha_1 = N\rho\left(N^2-1\right)\frac{e^{-\frac{\left(\sqrt{2\ln K}+\varepsilon_N+\sqrt{2\gamma\ln K}\right)^2}{2}}}{\sqrt{2\ln K}+\varepsilon_N+\sqrt{2\gamma\ln K}}\left[1+o(1)\right]$$

where the term $o(1)$ converges to zero as N goes to infinity (see appendix B). Using identity 3.a in lemma B.4.1,

$$N\rho\left(N^2-1\right)\alpha_1 = \left(N^2-1\right)\gamma\ln K\frac{e^{-\frac{\left(\sqrt{2}+\frac{\varepsilon_N}{\sqrt{\ln K}}+\sqrt{2\gamma}\right)^2\ln K}{2}}}{\sqrt{2\ln K}+\varepsilon_N+\sqrt{2\gamma\ln K}}\left[1+o(1)\right]$$

$$= \gamma\sqrt{\ln K}\frac{K^{2-\frac{\left(\sqrt{2}+\frac{\varepsilon_N}{\sqrt{\ln K}}+\sqrt{2\gamma}\right)^2}{2}}}{\sqrt{2}+\frac{\varepsilon_N}{\sqrt{\ln K}}+\sqrt{2\gamma}}\left[1+o(1)\right]$$

The above converges to zero if the exponent of K is negative, that is

$$2-\frac{1}{2}\left(\sqrt{2}+\frac{\varepsilon_N}{\sqrt{\ln K}}+\sqrt{2\gamma}\right)^2 < 0$$

which results in

$$\gamma > \frac{1}{2}\left(2-\sqrt{2}-\frac{\varepsilon_N}{\sqrt{\ln K}}\right)^2 \tag{4.36}$$

Similarly for α_2, we have

$$N\rho\left(N^2-1\right)\alpha_2 = \gamma\sqrt{\ln K}\frac{K^{2-\frac{\left(\sqrt{2}+\sqrt{2\gamma}\right)^2}{2}}}{\sqrt{2}+\sqrt{2\gamma}}\left[1+o(1)\right]$$

which converges to 0 if

$$\gamma > 3-2\sqrt{2} \tag{4.37}$$

Now α_3 gives

$$N\rho\left(N^2-1\right)\alpha_3 = \gamma\sqrt{\ln K}\frac{K^{2-\frac{\left(-\sqrt{2}+\sqrt{2\gamma}\right)^2}{2}}}{-\sqrt{2}+\sqrt{2\gamma}}\left[1+o(1)\right]$$

This converges if

$$\gamma > 3 + 2\sqrt{2} \tag{4.38}$$

And finally for α_4 we have

$$N\rho\left(N^2-1\right)\alpha_4 = \gamma\sqrt{\ln K}\,\frac{K^{2-\frac{\left(-\sqrt{2}-\frac{\varepsilon_N}{\sqrt{\ln K}}+\sqrt{2\gamma}\right)^2}{2}}}{-\sqrt{2}-\frac{\varepsilon_N}{\sqrt{\ln K}}+\sqrt{2\gamma}}\left[1+o(1)\right]$$

which converges if γ satisfies

$$\gamma > \frac{1}{2}\left(2+\sqrt{2}+\frac{\varepsilon_N}{\sqrt{\ln K}}\right)^2 \tag{4.39}$$

It is left to examine the convergence of I_3. We consider two cases; first, if $\frac{\sqrt{2\gamma}}{l+1} > \sqrt{2}+\frac{\varepsilon_N}{\sqrt{\ln K}}$, then the argument of Q in (4.32) is negative and we have that the lth term is given by

$$\begin{aligned}&(-1)^{l-1}\binom{K}{l}\frac{e^{-\frac{l\gamma\ln K}{l+1}}}{l+1}\left\{1-Q\left[\sqrt{l+1}\ln K\left(\frac{\sqrt{2\gamma}}{l+1}-\frac{\varepsilon_N}{\sqrt{\ln K}}-\sqrt{2}\right)\right]\right\}\\&=(-1)^{l-1}\binom{K}{l}\frac{K^{-\frac{l\gamma}{l+1}}}{l+1}\left[1+o(1)\right]\end{aligned} \tag{4.40}$$

Now the binomial term is of order K^l, i.e. $O(K^l)$, since

$$\lim_{K\to\infty}\frac{K!}{l!(K-l)!K^l} = \frac{1}{l!}$$

Therefore, the product of $N\rho\left(N^2-1\right)$ and the l^{th} term, shown above, is of order $K^{2+l-\frac{l\gamma}{l+1}}\ln K$ and consequently converges to zero if

$$2+l-\frac{l\gamma}{l+1} < 0$$

Now for $\gamma > 6+\frac{\varepsilon_0^2}{\ln K}$, only $l=1$ satisfies $\frac{\sqrt{2\gamma}}{l+1} > \sqrt{2}+\frac{\varepsilon_N}{\sqrt{\ln K}}$ and we have the following,

$$\left(2+l-\frac{l\gamma}{l+1}\right)\Bigg|_{l=1} = 3-\frac{\gamma}{2}$$
$$< -\frac{\varepsilon_N^2}{\ln K} < 0$$

The terms with $\frac{\sqrt{2\gamma}}{l+1} \le \sqrt{2}+\frac{\varepsilon_N}{\sqrt{\ln K}}$, i.e. $l \ge 2$, the product of the l^{th} term with $N\rho\left(N^2-1\right)$ can be shown to be

$$(-1)^{l-1}\gamma\sqrt{\ln K}\,\frac{K^{2+l-\frac{l\gamma}{l+1}-\frac{(l+1)}{2}\left(\sqrt{2}+\frac{\varepsilon_N}{\sqrt{\ln K}}-\frac{\sqrt{2\gamma}}{l+1}\right)^2}}{(l+1)^{3/2}\left(\sqrt{2}+\frac{\varepsilon_N}{\sqrt{\ln K}}-\frac{\sqrt{2\gamma}}{l+1}\right)}\left[1+o(1)\right]$$

Examination of the above shows that it converges for γ satisfying the condition set for $l=1$, and I_3 converges for

$$\gamma > 6+\frac{\varepsilon_N^2}{\ln K} \tag{4.41}$$

Hence we arrive at the following result.

4.5.1.1 Lemma

Let $\rho = {(\gamma \ln K)}/{N}$, then for γ satisfying (4.41) we have

$$\overline{MSE}\left(\hat{f}\right)-1 \to 0 \tag{4.42}$$

This establishes the fact that condition (4.39) marks the onset of the threshold. We then set $N\rho = \gamma \ln K + \upsilon_N + \beta$ where υ_N is a sequence dependent on N and β is a constant. Now we look at the behaviour of the above bounds. We see that $N\rho\left(N^2-1\right)$ times α_1 is

$$\left(N^2-1\right)\left(\gamma \ln K+\upsilon_N+\beta\right)\frac{e^{-\frac{\left(\sqrt{2\ln K}+\varepsilon_N+\sqrt{2(\gamma \ln K+\upsilon_N+\beta)}\right)^2}{2}}}{\sqrt{2\ln K}+\varepsilon_N+\sqrt{2\left(\gamma \ln K+\upsilon_N+\beta\right)}}\left[1+o(1)\right]$$

Hence, if we let $\frac{\upsilon_N}{\ln K} \to 0$, simplifying and ignoring the terms in $\varepsilon_N / \sqrt{\ln K}$, the above is of order at least lower than

$$K^{-5-2\sqrt{6}} \sqrt{\ln K}$$

similarly we find that α_2 is of order lower than

$$K^{-5-2\sqrt{6}} \sqrt{\ln K}$$

whereas α_3 is of order lower than

$$K^{-5+2\sqrt{6}} \sqrt{\ln K}$$

and α_4 is of order lower than

$$K^{-5+2\sqrt{6}} \sqrt{\ln K}$$

Finally, in the expression for I_3 the first term is dominant and therefore I_3 is of order lower than,

$$K^{-\frac{\varepsilon_N^2}{2\ln K}} \ln K$$

Looking at the orders of the individual terms we see that I_3 is the dominant integral and the convergence of the bounds on q_N is dictated by that of I_3. As the sequence $\upsilon_N = 2\ln(\ln K)$ (the factor 2 is needed to cancel the $1/2$ in the exponent) satisfies $\frac{\upsilon_N}{\ln K} \to 0$, we can put

$$N\rho = \gamma \ln K + 2\ln(\ln K) + \beta$$

and we have the following theorem.

4.5.1.2 Theorem

Let $\rho = \frac{1}{N}[\gamma \ln K + 2\ln(\ln K) + \beta]$ then

$$\overline{MSE}(\hat{f}) - 1 \to \frac{\pi^2}{6} e^{-\frac{\beta+\varepsilon_N^2}{2}} \tag{4.43}$$

4.5.1.3 Proof

The convergence of the normalised MSE is dictated by the first term of I_3. Now this is given by

$$\binom{K}{1}\frac{e^{-\frac{N\rho}{2}}}{2}\left\{1-Q\left[\sqrt{2}\ln K\left(\frac{\sqrt{2N\rho}}{2}-\frac{\varepsilon_N}{\sqrt{\ln K}}-\sqrt{2}\right)\right]\right\}$$

Substituting the expressions for $N\rho$ and for γ and simplifying we see that q_N is given by

$$\begin{aligned}&K\frac{e^{-\frac{3\ln K+\varepsilon_N^2+2\ln(\ln K)+\beta}{2}}}{2}\left[1+o(1)\right]\\&=\frac{1}{2\ln K}K^{-2}e^{-\frac{\beta+\varepsilon_N^2}{2}}\left[1+o(1)\right]\end{aligned}$$

Hence the expression for $\overline{MSE}\left(\hat{f}\right)-1$ converges to

$$\begin{aligned}\overline{MSE}\left(\hat{f}\right)-1&=q\frac{\pi^2N\rho\left(N^2-1\right)}{18}+q\\&\approx\frac{\gamma}{36}e^{-\frac{\beta+\varepsilon_N^2}{2}}\left[1+o(1)\right]\\&\to\frac{\pi^2}{6}e^{-\frac{\beta+\varepsilon_N^2}{2}}\end{aligned}$$

We see that the above result differs from that of Quinn, [9], by the factor $e^{-\varepsilon_N^2/2}$ which is necessary to account for the boundary region where one of his assumptions does not hold.

As a corollary we see that the point where the total MSE is twice the CRB occurs when the right hand side of (4.43) is exactly 1. Solving for β and substituting into the expression for the SNR, we have that the SNR in dB is given by

$$\rho_T(\mathrm{dB})=10\log\left\{\frac{1}{N}\left[6\ln(N-1)+2\ln(\ln(N-1))+4\ln\pi-2\ln 6+2\varepsilon_N^2\right]\right\} \quad (4.44)$$

Compare this with Quinn's expression,

$$\rho_{T-Quinn}(\mathrm{dB})=10\log\left\{\frac{1}{N}\left[6\ln(N-1)+2\ln(\ln(N-1))+4\ln\pi-2\ln 6\right]\right\} \quad (4.45)$$

Note that as N increases the above expression approaches that of Quinn. Furthermore, the value of ε decreases rapidly, making the difference between the two expressions negligible. For instance for $N = 32$, $\varepsilon_N = 6.13\times10^{-3}$. As a matter of interest we note that Quinn, in [9], derives a "more accurate" approximation than the expression in (4.45). This expression is, however, more complicated and does not give us any further insight. The threshold SNRs were calculated for N ranging from 32 to 1024 (only powers of 2 were used) according to equation (4.44). These are shown in the figure below.

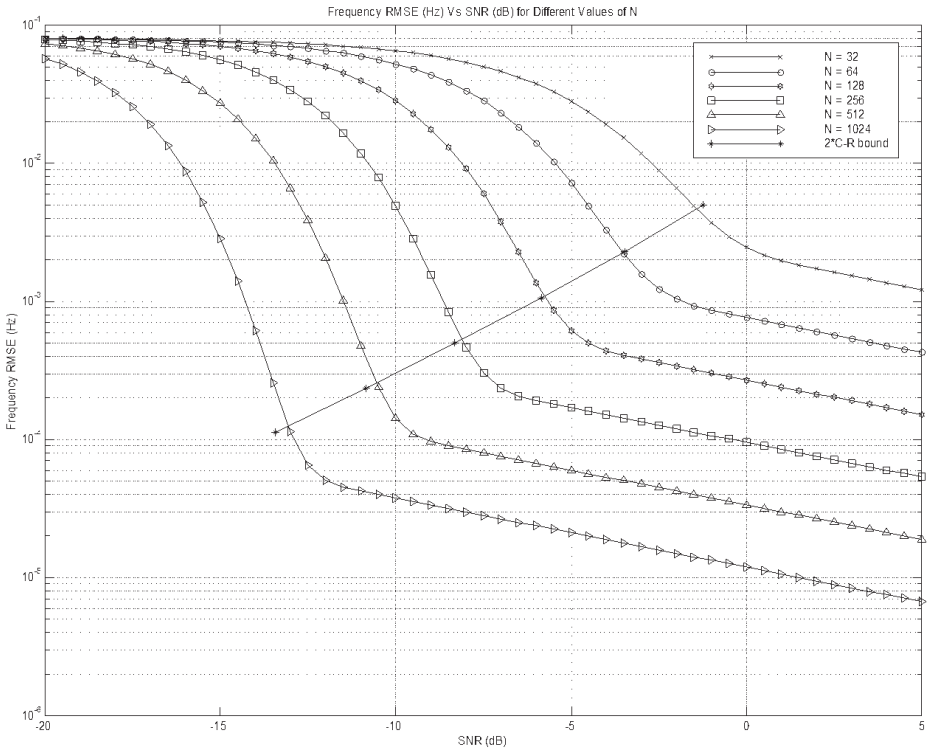

Figure 4.4 – *Plot Threshold SNRs (defined at the point where the total frequency RMSE equals 2×CRB). The total RMSE is also shown Vs the signal to noise ratio.*

4.6 Conclusion

In this chapter we have introduced the topic of frequency domain frequency estimation. We looked at the DFT and FFT algorithms and the Maximum Bin Search estimator. We then discussed the threshold effect that is seen as the signal to noise ratio decreases. We examined Quinn's derivation of an approximate expression for the SNR at the onset

of the threshold as a function of the number of data samples. We corrected an error that Quinn made in his analysis. Although this error was found to have a negligible impact on the expression, it was deemed important for the sake of theoretical correctness and completeness to derive the correct expression.

In the following chapters we look at a number of existing fine frequency estimators that improve on the resolution of the MBS algorithm. We also present a number of new algorithms and derive their performance. The MBS algorithm is assumed as the coarse estimation stage that precedes the fine frequency estimators.

Chapter 5

Frequency Estimation by Interpolation on Fourier Coefficients

5.1 Introduction

In this chapter we review existing methods of estimating the frequency of a sinusoid using the periodogram of the signal. In section 4.3, we showed that, above the SNR threshold, the MBS algorithm has a resolution of order N^{-1}. At the onset of the threshold, the MSE of the frequency increases very rapidly due to the increased likelihood of outliers. Therefore, when the operating point is above the threshold, we can significantly improve over the MBS frequency estimate using interpolation techniques. The algorithms we present in this chapter are all frequency domain estimators that rely on the MBS for initialization. A fine estimator is then used to refine the frequency estimate.

Quinn, in [82], proposed an algorithm that uses three Fourier coefficients, centered on the maximum bin, to improve the frequency estimate. He calls the algorithm "Interpolation on Fourier Coefficients". In this thesis, however, we use this terminology to refer to the family of algorithms that use any number of Fourier coefficients to improve the resolution of the frequency estimate. Quinn's algorithm, on the other hand, is referred to as Quinn's first algorithm. In [34] chapter 6, Quinn discusses a number of estimation techniques that are essentially interpolators on Fourier coefficients.

The chapter is organised as follows. In the following section we will provide an overview of the interpolation techniques that have been proposed. In section 5.3 we present and discuss the existing interpolation on three Fourier coefficients which rely on the raw coefficients themselves. As an illustrative example, the complete analysis of Quinn's first estimator is presented in 5.4.2. Section 5.5 looks at the interpolation on five Fourier coefficients in general and Macleod's method in particular. The

interpolation on the moduli of the Fourier coefficients is then discussed in section 5.6 with particular reference to the Rife-Vincent algorithms. Finally, the conclusion is presented in 5.7.

5.2 Existing Interpolation on Fourier Coefficients Techniques

Rife, [21], proposed the use of a coarse search followed by a fine search for estimating the frequency of a sinusoid. The coarse search consisted of the Maximum Bin Search (MBS) algorithm while the fine search was used to locate the turning point (or true peak) of the periodogram. As can be seen from equation (4.6), the amplitude spectrum of a sinusoid is a sinc function. This function has a maximum at the true frequency of the sinusoid. Padding the signal, of length N samples, with L-N zeros prior to taking the FFT is equivalent to sampling the length N Fourier transform more densely, namely at f_s/L intervals. To illustrate the point, figure 5.1 below shows the standard and zero-padded amplitude spectra of a sinusoidal signal with amplitude 1 and frequency $\frac{m+0.35}{N} f_s$ so that the frequency does not coincide with a bin centre. In this instance, N was taken to be 128, while f_s was set to 1 and m to 27. The corresponding sinusoidal frequency is 0.2137. The signal vector was padded with 896 zeros to obtain a vector of 1024 samples.

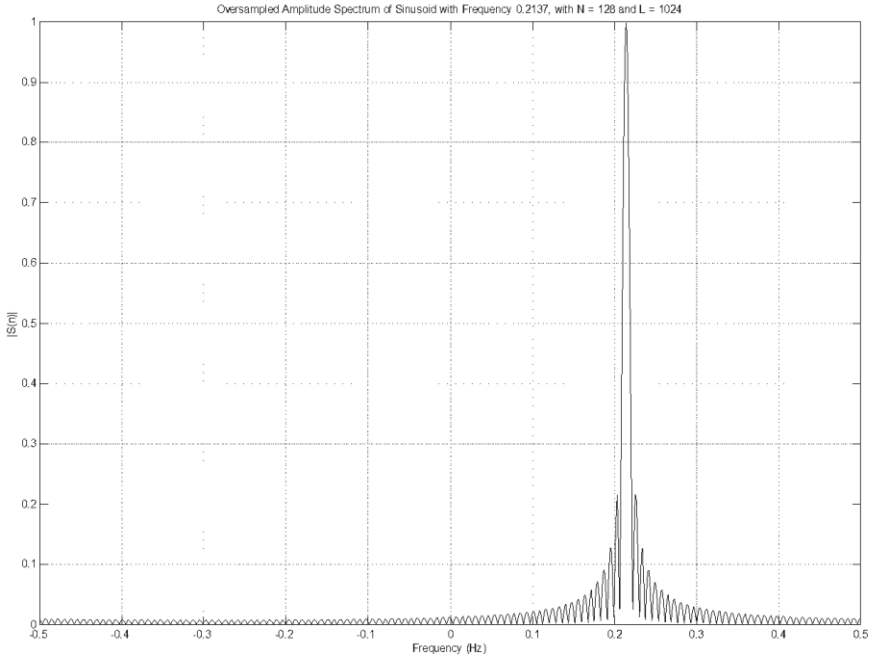

(a)

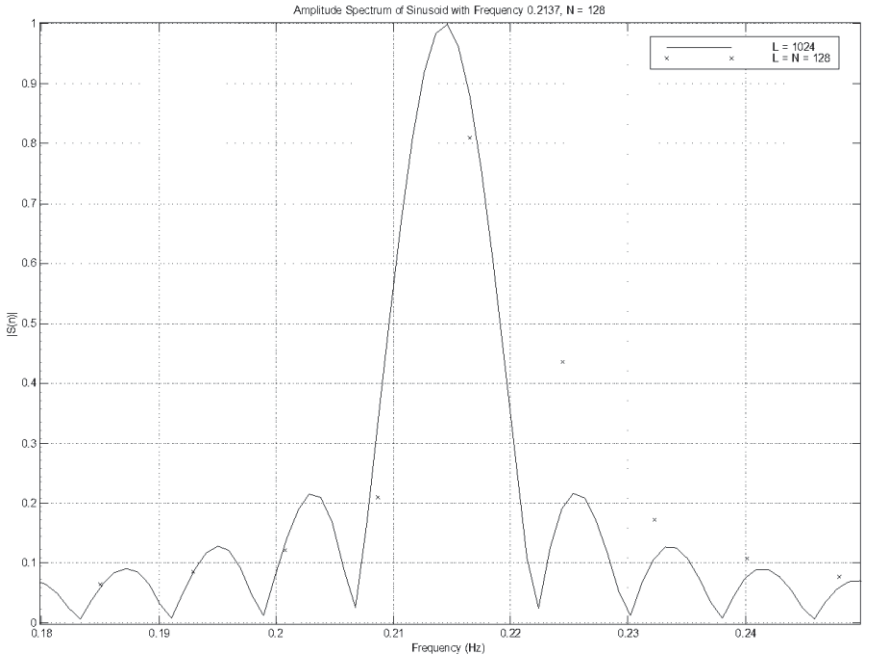

(b)

Figure 5.1 – *Plot of the amplitude spectrum of a sinusoidal signal with frequency = 0.2137. (a) shows the 0-padded spectrum with N = 128 and L = 1024. A zoomed in version is shown in (b) along with the 128 sample FFT.*

The sinc character of the amplitude spectrum is visible in the figure above. This allows for a fine search of the periodogram peak to be used to improve the frequency resolution. Quinn, in [34], attributes two such interpolation algorithms to Rife and Vincent. In the next section we establish the theory and notation necessary for presenting the interpolation algorithms.

5.2.1 Theory

In this section we present the theory to be used in establishing the motivation and analysis of the fine frequency estimators. The MBS algorithm, as seen in equation (4.9), is $O\left(N^{-1}\right)$. Therefore, we write the frequency of the signal as

$$f = \frac{m + \delta_0}{N} f_s \tag{5.1}$$

where m is the index of the bin closest to the true frequency (that is the argument of the periodogram maximiser), N the number of samples and δ_0 is the offset from the bin centre, restricted to the range $-1/2$ to $1/2$. In the context of FedSat, the total frequency uncertainty is in the order of 1MHz (see section 1.1.1). Therefore, the required sampling frequency, f_s, is in the order of 1MHz. Thus, f_s is set to 1MHz for the remainder of the thesis.

The general form of a sinusoidal signal is shown in equation (4.1). In the rest of the thesis, we assume without loss of generality that $A = 1$. Furthermore we take the initial phase to be zero. The Fourier coefficients of the signal given in equation (4.4) are

$$S(n) = \frac{1}{N} \frac{1 - e^{j2\pi N\left(\frac{f}{f_s} - \frac{n}{N}\right)}}{1 - e^{j2\pi\left(\frac{f}{f_s} - \frac{n}{N}\right)}} \tag{5.2}$$

In a practical system, the above signal will be "diluted" by noise. As we mentioned earlier, the noise in this thesis is assumed to be AWGN. The sampled signal is therefore

$$x(k) = s(k) + w(k) \tag{5.3}$$

The noise terms $w(k)$ are complex, having real and imaginary parts with mean zero and variance $\sigma^2/2$. The resulting signal to noise ratio in dB is

$$\rho_{\mathrm{dB}} = -10\log_{10}\sigma^2 \tag{5.4}$$

Let the Fourier transform of the signal x be denoted by X. Due to the linear property of the Fourier transform we have,

$$X(n) = S(n) + W(n) \tag{5.5}$$

where the Fourier coefficients are shown in appendix C to be independent and identically Gaussian distributed with zero mean and variance $\frac{\sigma^2}{N}$. Substituting the expression for $S(n)$ into (5.5) we obtain

$$\begin{aligned} X(n) &= \frac{1}{N}\left(\frac{1-e^{j2\pi N\left(\frac{m+\delta_0}{N}-\frac{n}{N}\right)}}{1-e^{j2\pi\left(\frac{m+\delta_0}{N}-\frac{n}{N}\right)}}\right) + W(n) \\ &= \frac{1}{N}\left(\frac{1-e^{j2\pi\delta_0}}{1-e^{j2\pi\left(\frac{m-n+\delta_0}{N}\right)}}\right) + W(n) \end{aligned}$$

Now using the index m as the reference we can write $n = m + l$ and the above expression becomes

$$X(m+l) = \frac{1}{N}\left(\frac{1-e^{j2\pi\delta_0}}{1-e^{j2\pi\left(\frac{\delta_0-l}{N}\right)}}\right) + W(n)$$

Using the series expansion of e^x,

$$\begin{aligned} e^x &= 1 + x + \frac{x^2}{2!} + \frac{x^3}{3!} + \cdots + \frac{x^n}{n!} + \cdots \\ &\approx 1 + x, \qquad\qquad \text{for } x \text{ small} \end{aligned}$$

we have for $\delta_0 - l << N$,

$$X(m+l) = \frac{1}{N}\left(\frac{1-e^{j2\pi\delta_0}}{1-1-j2\pi\left(\frac{\delta_0 - l}{N}\right)}\right) + W(n)$$
$$= c_0 \frac{\delta_0}{\delta_0 - l} + W(n) \tag{5.6}$$

where

$$c_0 = \frac{e^{j2\pi\delta_0} - 1}{j2\pi\delta_0} \tag{5.7}$$

Knowing that the true frequency of the signal lies in a range specified by some integers M_L and M_U, Bartlett, [117], suggested the minimisation the sum of the squares of the errors to estimate δ_0. This was followed up by Quinn, [34] , in his book. Therefore, knowing that $f \in \left(\frac{m-M_L}{N} f_s, \frac{m+M_U}{N} f_s\right)$, the aim is to minimise

$$\sum_{l=-M_L}^{M_U} \left| X(m+l) - c\frac{\delta}{\delta - l} \right|^2 \tag{5.8}$$

with respect to c and δ. Quinn, pp. 180-185, establishes the CLT of the above procedure under the more general assumptions on the noise terms discussed in 2.2. Here, we only state the relevant theorem under the assumption of AWGN. Taking the AWGN properties into account, the expressions of Quinn and those shown here become equivalent. The noise energy distribution used by Quinn, and given by $4\pi f_x(\lambda)$ where λ is angular frequency ($= 2\pi f$), is replaced by $\sigma^2/2$ in the limiting Gaussian case. The ratio of the asymptotic variance of an estimator to the asymptotic CRB will be used throughout the thesis as an indicator of its performance.

5.2.1.1 Theorem

Let $\hat{\delta}$ be the estimator of δ_0 that maximizes (5.8) and $\hat{f}$ be defined by

$$\hat{f} = \frac{m + \hat{\delta}}{N} f_s$$

then the distribution of $\sigma_{MLE}^{-1}\left(\hat{f}-f_0\right)$ tends toward the standard normal with σ_{MLE} given by

$$\sigma_{MLE}^2=\frac{f_s^2}{2N^3\rho\sin^2(\pi\delta_0)}\left\{\sum_{l=-M_L}^{M_U}\frac{l^2}{(\delta_0-l)^4}-\frac{\left[\sum_{l=-M_L}^{M_U}\frac{l\delta_0}{(\delta_0-l)^3}\right]^2}{\sum_{l=-M_L}^{M_U}\left(\frac{\delta_0}{\delta_0-l}\right)^2}\right\}^{-1} \tag{5.9}$$

The theorem essentially states that as the number of samples is increased to ∞, the distribution of the estimates obtained from the Bartlett method of maximising equation (5.8) is asymptotically standard normal. The asymptotic performance of the estimator is given by the asymptotic variance shown above. In fact, it is the asymptotic performance that will be considered for all of the interpolation based estimators. The ratio of the asymptotic variance to the asymptotic CRB is

$$R_{ACRB}^{MLE}=\frac{\pi^4}{3}\frac{\delta_0^2}{\sin^2(\pi\delta_0)}\left\{\sum_{l=-M_L}^{M_U}\frac{l^2}{(\delta_0-l)^4}-\frac{\left[\sum_{l=-M_L}^{M_U}\frac{l\delta_0}{(\delta_0-l)^3}\right]^2}{\sum_{l=-M_L}^{M_U}\left(\frac{\delta_0}{\delta_0-l}\right)^2}\right\}^{-1} \tag{5.10}$$

As M_L and M_U increase and we use all of the available samples, we expect that the asymptotic variance will approach that of the ACRB. In fact the above ratio can be shown to be 1 for $M_L=M_U=\infty$.

As it will be seen in the following sections, most of the interpolators that have been proposed use three coefficients to obtain an estimate of the frequency. Evaluating the ratio in equation (5.10) for the three coefficients case, that is for $M_L=M_U=1$, we get,

$$R_{ACRB}^{3\,Coeffs}=\frac{\pi^4}{6}\frac{\delta_0^2}{\sin^2(\pi\delta_0)}\left\{\frac{\left(3\delta_0^4+1\right)\left(\delta_0^2-1\right)^2}{3\delta_0^4+6\delta_0^2+1}\right\} \tag{5.11}$$

The figure below shows a plot of the ratio above versus δ_0. We see that the ratio has its minimum at $\pm 1/2$ and its maximum at 0. These values are 1.009 and 1.645 respectively.

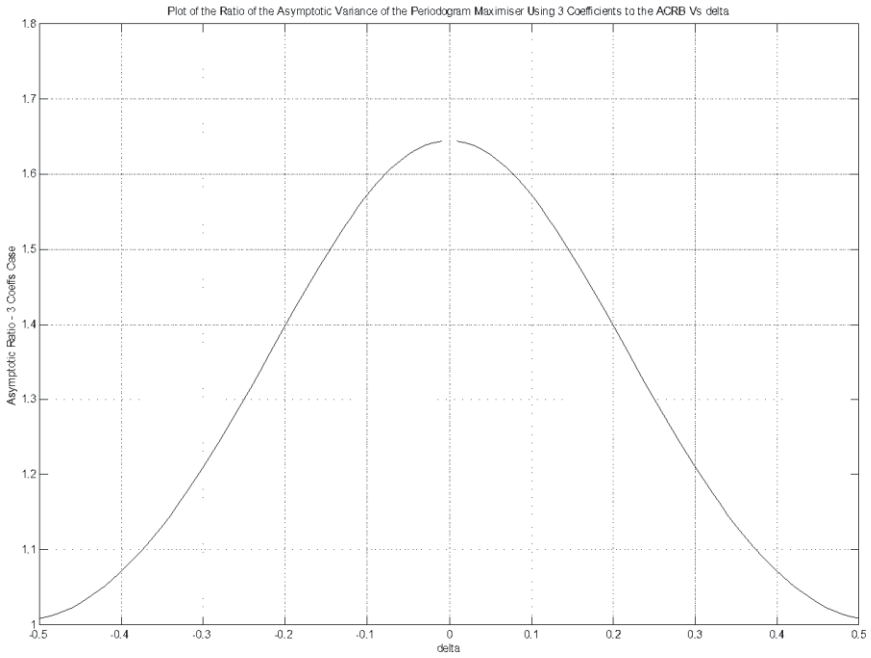

Figure 5.2 – *Plot of the ratio of the asymptotic variance of the periodogram maximiser using three coefficients to asymptotic CRB.*

5.3 Interpolation on Three Fourier Coefficients

The maximisation of (5.8) while numerically possible is computationally intensive and may be sensitive to rounding errors. Quinn, in [82], proposed instead the use of the Fourier coefficients corresponding to l = -1, 0 and 1 to obtain an estimate of δ_0. He followed this by an improved algorithm which he presented in [83]. In this same publication, he showed the method proposed by Rife and Vincent in [118] to be inefficient when δ_0 is in the immediate vicinity of 0. This, as we will explain in section 5.6.4, is due to the comparison between the two Fourier coefficients that are either side of the maximum bin. We will provide an intuitive explanation to supplement Quinn's analysis. In fact, any method involving a straight comparison between the magnitudes of the Fourier coefficients where the resolution is $O(N^{-1})$ will have the same problem. Kitchen and Howard, in [119], generalised Quinn's first algorithm by deriving the exact expression for δ_0 in terms of the Fourier coefficients. This makes the algorithm applicable for short data records. We will not review their expression here as we are only interested in large N, and it will suffice to examine Quinn's original algorithm.

Macleod, in [84], also suggested another interpolator that performs better than Quinn's first algorithm and worse than Quinn's second. Macleod's algorithm is computationally simpler to Quinn's second estimator.

5.4 Quinn's First Estimator

We will now examine Quinn's first algorithm. The method we will adopt consists of first presenting the algorithm, then establishing the motivation behind it and finally presenting the asymptotic analysis and performance, including simulation results.

Let us denote the maximum bin and those either side of it by X_0, X_{-1} and X_1 respectively. We estimate the frequency using the method shown in the table below.

Set	$\alpha_l = \Re\left\{\frac{X_l}{X_0}\right\}$, for $l = \pm 1$
Then Calculate	$\hat{\delta}_l = \frac{l\alpha_l}{\alpha_l - 1}$
If $\hat{\delta}_{-1} > 0$ *and* $\hat{\delta}_1 > 0$ *then set*	
	$\hat{\delta} = \hat{\delta}_1$
otherwise	
	$\hat{\delta} = \hat{\delta}_{-1}$
The frequency estimate is then given by	
	$\hat{f} = \left(m + \hat{\delta}\right)\frac{f_s}{N}$

Table 5.1 – *Quinn's First Algorithm.*

The reader should keep in mind that the index notation of the Fourier coefficient is relative to the maximum bin since the MBS algorithm is used to initialise all of the interpolation estimators. That is to say that for example X_{-1} refers to X_{m-1}. In the following section we will establish the motivation of and derive the above algorithm.

5.4.1 Motivation

Using equation (5.6) and ignoring the noise terms, we can write the three Fourier coefficient corresponding to l = -1, 0 and 1 as

$$X_{-1} = c_0 \frac{\delta_0}{\delta_0 + 1}$$

$$X_0 = c_0$$

and

$$X_1 = c_0 \frac{\delta_0}{\delta_0 - 1}$$

Now substituting for X_{-1} and X_0 in the in the expression for α_{-1},

$$\begin{aligned} \alpha_{-1} &= \Re\left\{\frac{X_{m-1}}{X_m}\right\} \\ &= \Re\left\{\frac{c_0\delta_0}{\delta_0 + 1} \cdot \frac{1}{c_0}\right\} \\ &= \frac{\delta_0}{\delta_0 + 1} \end{aligned}$$

Similarly, the expression for α_1 can be shown to be

$$\alpha_1 = \frac{\delta_0}{\delta_0 - 1}$$

Solving for δ_0 in terms of α_{-1} and α_1 yields,

$$\delta_0 = \pm\frac{\alpha_l}{\alpha_l - 1} \text{ for } l = \pm 1$$

This can be written as

$$\delta_0 = \frac{l\alpha_l}{\alpha_l - 1} \text{ for } l = \pm 1 \tag{5.12}$$

When δ_0 is positive, both $\hat{\delta}_{-1}$ and $\hat{\delta}_1$ would in the noiseless case result in a positive estimate. However, when the signal is affected by noise, X_1 would have a higher effective SNR than X_{-1} and $\hat{\delta}_1$ would be expected to be a better estimator than $\hat{\delta}_{-1}$.

Therefore, we choose $\hat{\delta}_1$ when both $\hat{\delta}_{-1}$ and $\hat{\delta}_1$ are positive. A similar argument shows that it this is equivalent to selecting $\hat{\delta}_{-1}$ if both $\hat{\delta}_{-1}$ and $\hat{\delta}_1$ are negative. This reasoning also suggests that the algorithm performance suffers for δ_0 close to zero where it is more likely to have $\hat{\delta}_{-1}$ and $\hat{\delta}_1$ of different signs. This is clarified in the next section where we derive the asymptotic variance of the algorithm.

5.4.2 Analysis

Quinn, [82] and [34] pp.188-195, proves the central limit theorem (CLT) for the estimator. In this section we will state the theorem and derive the asymptotic variance. We will not explicitly repeat the proof of the CLT. The derivation of the asymptotic variance will be repeated to establish the methodology that will be used to analyse the new estimators presented in chapters 6 to 8.

5.4.2.1 Theorem

Let $\hat{\delta}$ be the estimator of δ_0 according to Quinn's first algorithm and $\hat{f}$ be defined by

$$\hat{f} = \frac{m + \hat{\delta}}{N} f_s$$

then we have almost surely and for all $\nu > 0$,

$$P\left\{\sigma_{Quinn}^{-1}\left(\hat{f} - f\right) \le x\right\} \to \mathrm{N}(0,1)$$

where σ_f is given by

$$\sigma_{Quinn}^2 = \frac{f_s^2}{N^3 \rho \sin^2(\pi\delta_0)} \frac{\pi^2 \delta_0^2}{(1-|\delta_0|)^2} \left\{\delta_0^2 + (1-|\delta_0|)^2\right\} \tag{5.13}$$

and N(0,1) is the standard normal distribution.

5.4.2.2 Derivation of the Asymptotic Variance

In section 5.4.1, we derived expressions for X_l in the noiseless case for $l = 0, \pm 1$. Adding the noise terms, we have the following,

$$X_{-1} = c_0 \frac{\delta_0}{\delta_0 + 1} + W_{-1}$$

$$X_0 = c_0 + W_0$$

and

$$X_1 = c_0 \frac{\delta_0}{\delta_0 - 1} + W_1$$

With c_0 as in equation (5.7).

Let r_l denote the ratio of X_l to X_0. Substituting and simplifying we have

$$\begin{aligned} r_l &= \frac{X_l}{X_0} \\ &= \frac{c_0 \dfrac{\delta_0}{\delta_0 - l} + W_l}{c_0 + W_0} \\ &= \frac{\dfrac{\delta_0}{\delta_0 - l} + \dfrac{W_l}{c_0}}{1 + \dfrac{W_0}{c_0}} \end{aligned}$$

Now from appendix C we have that $W_l = O\left(N^{-\frac{1}{2}} \sqrt{\ln N} \right)$, therefore for large N we have

$$\begin{aligned} \frac{1}{1 + \dfrac{W_0}{c_0}} &= 1 - \frac{W_0}{c_0} + O\left(N^{-1} \ln N\right) \\ &= 1 - \frac{W_0}{c_0} + o(1) \end{aligned}$$

Hence

$$\begin{aligned} r_l &= \frac{\delta_0}{\delta_0 - l}\left(1 + \frac{\delta_0 - l}{\delta_0}\frac{W_l}{c_0}\right)\left\{\left(1 - \frac{W_0}{c_0}\right) + o(1)\right\} \\ &= \frac{\delta_0}{\delta_0 - l} + \frac{W_l}{c_0} - \frac{\delta_0}{\delta_0 - l}\frac{W_0}{c_0} - \frac{W_l W_0}{c_0^2} + o(1) \end{aligned}$$

Using corollary 3 from appendix B section B.2.3, we also get,

$$W_l W_0 = O\left(N^{-1} \log N\right)$$

This term is of lower order than the rest of the expression and hence we ignore it. Furthermore, since the rest of the error term is $O\left(N^{-\frac{1}{2}}\sqrt{\ln N}\right)$, we use the real part of the above ratio r_l as an estimator of α_l.

Let ξ_l be the difference between α_l and $\frac{\delta_0}{\delta_0 - l}$, ignoring the lower order terms, that is those of order $N^{-1}\log N$,

$$\begin{aligned}\xi_l &= \alpha_l - \frac{\delta_0}{\delta_0 - l} \\ &= \Re\left\{\frac{X(l)}{X(0)} - \frac{\delta_0}{\delta_0 - l}\right\} \\ &= \Re\left\{\frac{W_l}{c_0} - \frac{\delta_0}{\delta_0 - l}\frac{W_0}{c_0}\right\}\end{aligned} \tag{5.14}$$

Since W_l are independently Gaussian with mean zero and variance σ^2/N, the real part of their linear combination is also zero mean Gaussian. Hence the ξ_l have zero mean and the elements of the covariance matrix of ξ_l (with $l = \pm 1$) are

$$\begin{aligned}E(\xi_k\xi_l) &= E\left[\Re\left\{\frac{W_k}{c_0} - \frac{\delta_0}{\delta_0 - k}\frac{W_0}{c_0}\right\}\Re\left\{\frac{W_l}{c_0} - \frac{\delta_0}{\delta_0 - l}\frac{W_0}{c_0}\right\}\right] \\ &= \frac{1}{4|c_0|^2}E\left[\left\{W_k - \frac{\delta_0}{\delta_0 - k}W_0 + W_k^* - \frac{\delta_0}{\delta_0 - k}W_0^*\right\}\right. \\ &\qquad \left.\left\{W_l - \frac{\delta_0}{\delta_0 - l}W_0 + W_l^* - \frac{\delta_0}{\delta_0 - l}W_0^*\right\}\right]\end{aligned}$$

Expanding the expression inside the expectation and noting that, since W_k and W_l are independent, we have that

$$E[W_k W_l] = 0$$

and

$$E\left[W_k W_l^*\right] = \begin{cases}\frac{\sigma^2}{N} & \text{if } k = l \\ 0 & \text{otherwise}\end{cases}$$

Thus, the elements of the covariance matrix become

$$E(\xi_{-1}\xi_{-1}) = \frac{1}{2|c_0|^2}\left\{E\left[|W_{-1}|^2\right] + \frac{\delta_0^2}{(\delta_0+1)^2}E\left[|W_0|^2\right]\right\}$$
$$= \frac{1}{2|c_0|^2}\left\{\frac{\sigma^2}{N} + \frac{\delta_0^2}{(\delta_0+1)^2}\frac{\sigma^2}{N}\right\}$$
$$= \frac{\sigma^2}{2N|c_0|^2}\left\{1 + \frac{\delta_0^2}{(\delta_0+1)^2}\right\}$$

Similarly, we can show that

$$E(\xi_1\xi_1) = \frac{\sigma^2}{2N|c_0|^2}\left\{1 + \frac{\delta_0^2}{(\delta_0-1)^2}\right\}$$

and

$$E(\xi_1\xi_{-1}) = E(\xi_{-1}\xi_1)$$
$$= \frac{1}{4|c_0|^2}\left\{2\frac{\delta^2}{\delta^2-1}E\left[|W_0|^2\right]\right\}$$
$$= \frac{\sigma^2}{2N|c_0|^2}\frac{\delta_0^2}{\delta_0^2-1}$$

Thus, the covariance matrix, Σ_ξ is given by

$$\Sigma_\xi = \frac{\sigma^2}{2N|c_0|^2}\begin{bmatrix} 1+\frac{\delta_0^2}{(\delta_0+1)^2} & \frac{\delta_0^2}{\delta_0^2-1} \\ \frac{\delta_0^2}{\delta_0^2-1} & 1+\frac{\delta_0^2}{(\delta_0-1)^2} \end{bmatrix}$$

In order to obtain the asymptotic variance of the estimator, we need to get the variance of the error in frequency, or equivalently, the error in the estimate of δ_0. Now equation (5.12) gives the following,

$$\begin{aligned}\hat{\delta}_l - \delta_0 &= \frac{l\alpha_l}{\alpha_l - 1} - \delta_0 \\ &= \frac{l\left(\dfrac{\delta_0}{\delta_0 - l} + \xi_l\right)}{\dfrac{\delta_0}{\delta_0 - l} + \xi_l - 1} - \delta_0 \\ &= \frac{-(\delta_0 - l)^2 \xi_l}{l + (\delta_0 - l)\xi_l} \\ &= -\frac{(\delta_0 - l)^2}{l} \xi_l \{1 + o_p(1)\}\end{aligned} \tag{5.15}$$

This implies that, as ξ_l has mean zero, $\hat{\delta}_l - \delta_0$ has and asymptotically zero mean. That is the estimator is asymptotically unbiased. In fact, for moderately sized *N* we find that the bias is small enough to be taken as negligible. The covariance matrix for the estimator, denoted by Σ_δ is

$$\Sigma_\delta = \frac{\sigma^2}{2N|c_0|^2}\begin{bmatrix} (\delta_0+1)^4\left\{1+\dfrac{\delta_0^2}{(\delta_0+1)^2}\right\} & -\delta_0^2(\delta_0^2-1) \\ -\delta_0^2(\delta_0^2-1) & (\delta_0-1)^4\left\{1+\dfrac{\delta_0^2}{(\delta_0-1)^2}\right\} \end{bmatrix} \tag{5.16}$$

Now $\hat{\delta}_{-1}$ and $\hat{\delta}_1$ are asymptotically independent with the same distribution. As *N* increases we, almost surely, choose $\hat{\delta}_1$ when δ_0 is positive and $\hat{\delta}_{-1}$ when it is negative. The asymptotic performance of the estimator is therefore obtained by "patching" the asymptotic variances of the two estimators with the precondition that $\hat{\delta}_{-1}$ or $\hat{\delta}_1$ is chosen. Hence the asymptotic variance of the error is

$$\begin{aligned}\mathrm{var}\left[\hat{\delta} - \delta\right] &= \begin{cases} \Sigma_\delta(1,1), & -\tfrac{1}{2} \le \delta < 0 \\ \Sigma_\delta(2,2), & 0 \le \delta \le \tfrac{1}{2} \end{cases} \\ &= \frac{\pi^2 \delta_0^2 \sigma^2}{2N \sin^2(\pi\delta_0)} (1 - |\delta_0|)^2 \left\{\delta_0^2 + (1 - |\delta_0|)^2\right\}\end{aligned}$$

where the expression for $|c_0|^2$ shown below was substituted into the expression for the variance.

$$|c_0|^2 = \left| \frac{e^{j2\pi\delta_0} - 1}{j2\pi\delta_0} \right|^2$$
$$= \frac{\sin^2(\pi\delta)}{\pi^2\delta_0^2}$$

The asymptotic variance of the frequency can be obtained from that of δ_0 by multiplying it by the factor $\left(f_s / N \right)^2$. Hence

$$\sigma^2_{Quinn} = \mathrm{var}\left[\hat{f} - f \right]$$
$$= \frac{\pi^2\delta_0^2 f_s^2}{2N^3\rho\sin^2(\pi\delta_0)} \left(1 - |\delta_0|\right)^2 \left\{ \delta_0^2 + \left(1 - |\delta_0|\right)^2 \right\} \tag{5.17}$$

This completes the derivation of the asymptotic variance of Quinn's first estimator. As stated earlier, an important indicator of the performance is the ratio of the asymptotic variance to the asymptotic CRB. For Quinn's first estimator this is

$$R^{Quinn}_{ACRB} = \frac{\pi^4\delta_0^2}{3\sin^2(\pi\delta_0)} \left(1 - |\delta_0|\right)^2 \left\{ \delta_0^2 + \left(1 - |\delta_0|\right)^2 \right\} \tag{5.18}$$

Figure 5.3 below shows a plot of the theoretical and simulated ratios of σ^2_{Quinn} to the asymptotic CRB. We see close agreement between the two curves. The curves also show that the variance is worst for $\delta_0 = 0$. This validates the argument of section 5.4.1. This problem region results from the comparison used to choose between $\hat{\delta}_{-1}$ and $\hat{\delta}_1$. Kitchen and Howard, in [119], compared two methods for making this choice. The first is given by

$$\hat{\delta} = \begin{cases} \hat{\delta}_{-1} & \dfrac{|X_1|}{|X_{-1}|} < 1 \\ \hat{\delta}_1 & otherwise \end{cases}$$

and the second by

$$\hat{\delta} = \begin{cases} \hat{\delta}_{-1} & \dfrac{\partial |X_0|^2}{\partial f} < 1 \\ \hat{\delta}_1 & otherwise \end{cases}$$

with

$$\frac{\partial |X_0|^2}{\partial f} = -4\pi \Im\left\{ X_0 \sum_{k=0}^{N-1} n x_k^* e^{j2\pi \frac{mk}{N}} \right\}$$

and *m* being the maximum bin index.

They found that the second method performs much better than the first. The first method is amplitude based and is the same as that used in the R-V estimator as we will see in section 5.6.1. Quinn, [34] pp. 201 to 205, showed that this method performs poorly in the presence of noise. Macleod, [84], has suggested an alternative test to this by setting $\hat{\delta}$ to $\hat{\delta}_1$ if $\alpha_{-1} > \alpha_1$ and to $\hat{\delta}_{-1}$ otherwise.

The theoretical expression of the variance shows a minimum of 1.0147 at $\delta_0 = \pm\frac{1}{2}$ and a maximum of 3.2899. Assuming that δ_0 is uniformly distributed over the interval $[-0.5,0.5]$, we can get the average ratio of the asymptotic variance to the asymptotic CRB. Performing this integration numerically we obtain an average ratio of 1.656. The performance of the algorithm was simulated for $N = 1024$ and $f_s = 1\,\mathrm{MHz}$ over the range of signal to noise ratios from 0 to -20 dB. 10000 simulation runs were done at each SNR. The results are shown, along with the CRB and the modified version according to Macleod's suggestion, in figure 5.4. The average ratio of the frequency MSE of the first algorithm to the CRB was found to be between 1.65 and 1.9. This agrees very well with the theoretical results. The small difference can be accounted for by the effect of lower order terms which become more pronounced at low signal to noise ratios. Also we can see that at low signal to noise ratios, Macleod's test is better than Quinn's. The modified estimator performs slightly better near the threshold.

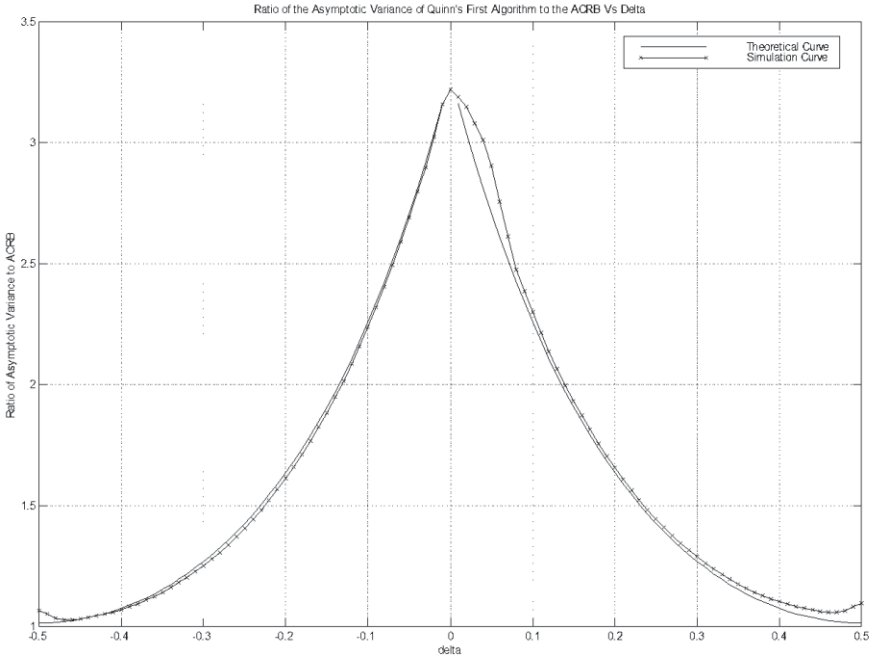

Figure 5.3 – *Plot of the theoretical and simulated ratios of the asymptotic variance of Quinn's first algorithm to the asymptotic CRB. 10000 simulation runs were averaged.*

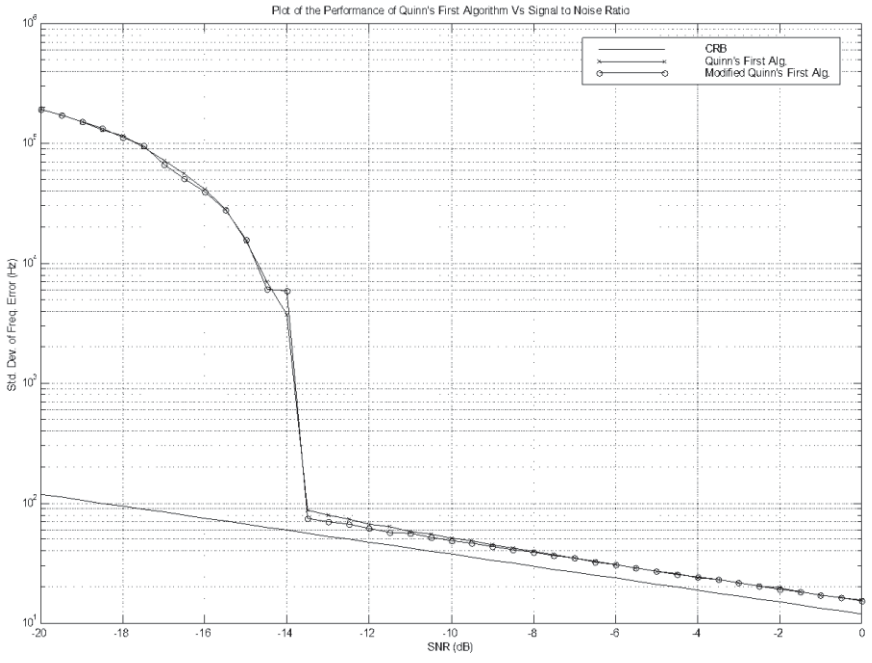

Figure 5.4 – *Plot of the standard deviation of the frequency estimates obtained using Quinn's first algorithm Vs the signal to noise ratio. 10000 simulation runs were averaged.*

5.4.3 Quinn's Second Estimator

In this section we present Quinn's second algorithm. We will not analyse it but, rather simply, state the relevant results that were derived by Quinn in [34] pp.195-198.

Driven by the insight gained from the analysis of the first estimator, Quinn sets to find a form of the interpolator that would give the minimum asymptotic variance uniformly in δ_0.

Since the two estimates, $\hat{\delta}_{-1}$ and $\hat{\delta}_1$ are asymptotically independent, it seems that averaging them would improve the estimator performance. However, the resulting ratio of the asymptotic variance of the averaged estimate to the asymptotic CRB is found to be

$$R_{ACRB}^{Quinn\ Av} = \frac{\pi^4 \delta_0^2}{12 \sin^2(\pi\delta_0)} \left\{4\delta_0^4 + 14\delta_0^2 + 1\right\}$$

This expression has a minimum of 1.645 at $\delta_0 = 0$ and a maximum of 11.669 at $\pm\frac{1}{2}$.

Therefore, although the averaging improves the performance of the estimator at zero, the resulting performance away from zero is significantly worsened.

Thus, we must look for a nonlinear estimator in order to approach the performance of the periodogram maximiser using three coefficients, given in equation (5.11). Writing $\hat{\delta}$ as a generic function of $\hat{\delta}_{-1}$ and $\hat{\delta}_1$, say $g\left(\hat{\delta}_{-1}, \hat{\delta}_1\right)$ and solving for g to minimise the resulting asymptotic variance Quinn found it to be given by

$$\begin{aligned}\hat{\delta} &= g\left(\hat{\delta}_{-1}, \hat{\delta}_1\right) \\ &= g_{-1}\left(\hat{\delta}_{-1}\right) + g_1\left(\hat{\delta}_1\right)\end{aligned}$$

where g_1 and g_2 are given by

$$g_{-1}(x) = \frac{x}{2} - \frac{1}{4}\ln\left(3x^4 + 6x^2 + 1\right) + \frac{\sqrt{6}}{24}\ln\left(\frac{x^2 + 1 - \sqrt{\frac{2}{3}}}{x^2 + 1 + \sqrt{\frac{2}{3}}}\right)$$

and

$$g_1(x) = \frac{x}{2} + \frac{1}{4}\ln\left(3x^4 + 6x^2 + 1\right) - \frac{\sqrt{6}}{24}\ln\left(\frac{x^2 + 1 - \sqrt{\frac{2}{3}}}{x^2 + 1 + \sqrt{\frac{2}{3}}}\right)$$

The resulting algorithm, shown in the table below, is the same as the first estimator with a step added after the calculation of $\hat{\delta}_{-1}$ and $\hat{\delta}_1$ combining them to obtain a value for $\hat{\delta}$.

Set	$\alpha_l = \Re\left\{\frac{X_l}{X_0}\right\}$, for $l = \pm 1$
Then Calculate	$\hat{\delta}_l = \frac{l\alpha_l}{\alpha_l - 1}$
Let	$\hat{\delta} = \frac{\hat{\delta}_{-1} + \hat{\delta}_1}{2} + h\left(\delta_1^2\right) - h\left(\delta_{-1}^2\right)$
Where	
	$h(x) = \frac{1}{4}\ln\left(3x^4 + 6x^2 + 1\right) - \frac{\sqrt{6}}{24}\ln\left(\frac{x^2 + 1 - \sqrt{\frac{2}{3}}}{x^2 + 1 + \sqrt{\frac{2}{3}}}\right)$
The frequency estimate is then given by	
	$\hat{f} = \left(m + \hat{\delta}\right)\frac{f_s}{N}$

Table 5.2 – *Quinn's second algorithm.*

The algorithm in the table above will be called Quinn's second algorithm. Its asymptotic variance is the same as that of the periodogram maximiser using three coefficients. The ratio of its asymptotic variance to the asymptotic CRB is given in equation (5.11).

As a matter of interest, and for the sake of completeness, we mention that in order to avoid the logarithms, Quinn suggested a modification, replacing the term $h\left(\delta_1^2\right) - h\left(\delta_{-1}^2\right)$ by $2\left(\delta_1 - \delta_{-1}\right)\bar{\delta}h'\left(\bar{\delta}^2\right)$ with $\bar{\delta}$ given by $\hat{\delta}_1$ if both $\hat{\delta}_{-1}$ and $\hat{\delta}_1$ are positive and $\hat{\delta}_{-1}$ otherwise.

The figure below shows the simulation results of the ratio of the asymptotic variance of the algorithm to the asymptotic CRB. 10000 simulation runs were averaged. We see

that there is close agreement between the two curves and consequently the optimality of the algorithm is verified.

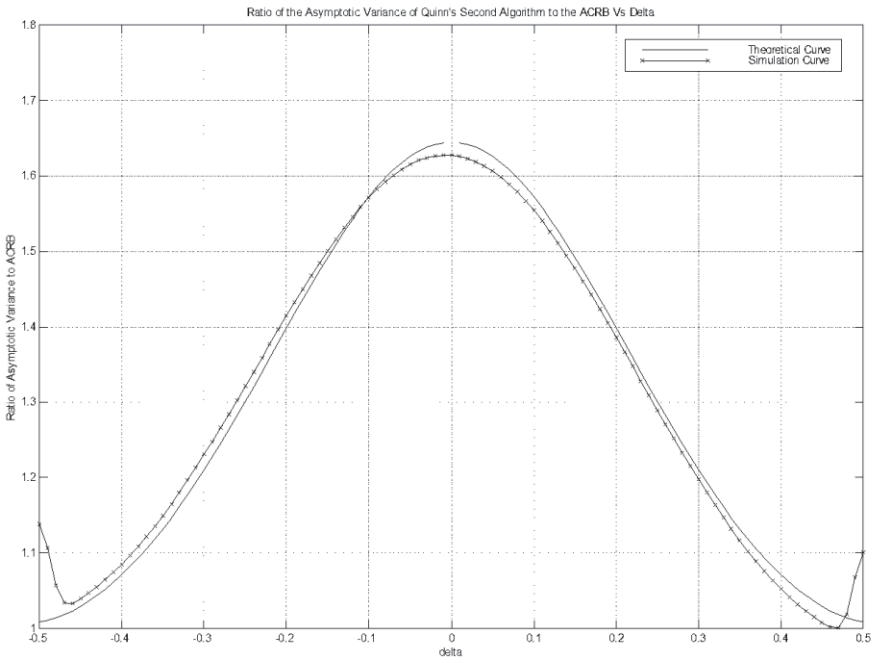

Figure 5.5 – *Plot of the ratio of the asymptotic variance of Quinn's second algorithm to the asymptotic CRB as a function of δ_0 at 0 dB SNR and N = 1024. 10000 simulation runs were averaged.*

Figure 5.6 shows the performance results of Quinn's second algorithm. We see a clear improvement of performance over the first algorithm. The average ratio of the frequency MSE was found through simulation to be between 1.3 and 1.5, whereas the theoretical value obtained from averaging the variance expression of equation (5.11) over the range $[-0.5,0.5]$ is 1.316. It is interesting to note that the optimum estimator has a higher threshold than the first estimator.

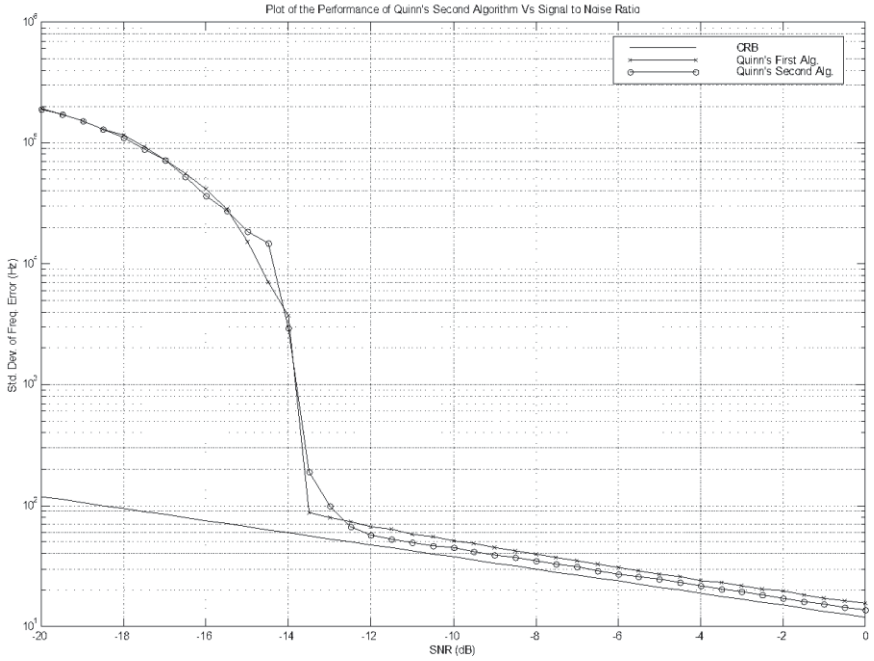

Figure 5.6 – *Plot of the performance of Quinn's frequency estimation algorithms Vs SNR. N = 1024, f_s = 1MHz. 10000 simulation runs were averaged.*

5.4.4 Macleod's Three Coefficients Interpolator

Macleod, in [84], also adopted the approach of combining $\hat{\delta}_{-1}$ and $\hat{\delta}_1$ in order to obtain an improved estimate of δ_0. Unlike Quinn, however, Macleod presented a computationally simple alternative that is nearly optimum. Interestingly, Quinn does not mention Macleod's algorithm in his book. In this section we will present and analyse the algorithm.

We will first present the algorithm in the notation adopted by Macleod and then re-write it in the notation of this thesis.

Let r_l be given by

$$r_l = \Re\left\{X_l X_0^*\right\}, l = -1, 0 \text{ and } 1$$

Then the estimator is given by the following two equations

$$\gamma = \frac{r_{-1} - r_1}{2r_0 + r_{-1} + r_1} \tag{5.19}$$

and

$$\hat{\delta} = \frac{\sqrt{1+8\gamma^2}-1}{4\gamma} \tag{5.20}$$

5.4.5 Motivation

Re-writing the expressions for r_l we get

$$\begin{aligned} r_l &= \Re\left\{X_l X_0^*\right\} \\ &= |X_0|^2 \Re\left\{\frac{X_l}{X_0}\right\} \\ &= |X_0|^2 \alpha_l \end{aligned}$$

where of α_l is shown in table 5.1.

We see that the above expression differs from α_l by a constant that is common to all values of l. Substituting into the expression for γ it becomes

$$\begin{aligned} \gamma &= \frac{r_{-1}-r_1}{2r_0+r_{-1}+r_1} \\ &= \frac{|X_0|^2\alpha_{-1}-|X_0|^2\alpha_1}{2|X_0|^2+|X_0|^2\alpha_{-1}+|X_0|^2\alpha_1} \end{aligned}$$

Putting $\alpha_l = \frac{\delta_0}{\delta_0 - l}$ in the above and simplifying we arrive at

$$\begin{aligned} \gamma &= \frac{\alpha_{-1}-\alpha_1}{2+\alpha_{-1}+\alpha_1} \\ &= \frac{-\delta_0}{2\delta_0^2-1} \end{aligned} \tag{5.21}$$

Now solving for δ_0 in terms of γ we find that the estimator is given by equation (5.20).

The estimator is summarised in the table below.

Set

$$\alpha_l = \Re\left\{\frac{X_l}{X_0}\right\}, \text{ for } l = \pm 1$$

Then Calculate

$$\gamma = \frac{\alpha_{-1} - \alpha_1}{2 + \alpha_{-1} + \alpha_1}$$

Let

$$\hat{\delta} = \frac{\sqrt{1 + 8\gamma^2} - 1}{4\gamma}$$

The frequency estimate is then given by

$$\hat{f} = \left(m + \hat{\delta}\right)\frac{f_s}{N}$$

Table 5.3 – *Macleod's three coefficients interpolator.*

The variance of the estimator was obtained as a function of δ_0 through simulations. The resulting ratio to the asymptotic CRB, shown in figure 5.7, is for $N = 1024$. We clearly see the sacrifice in performance with respect to the optimum estimator incurred in order to obtain a computationally simpler estimator.

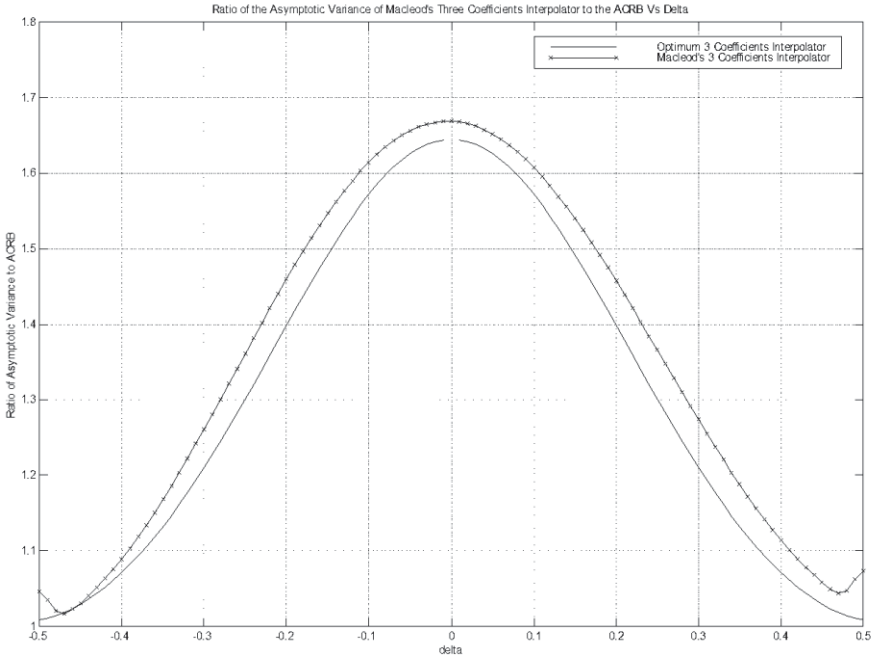

Figure 5.7 – *Plot of the ratio of the variance Macleod's three coefficients interpolator to the asymptotic CRB as a function of δ_0. N was set to 1024 and SNR to 0 dB. 10000 simulation runs were averaged.*

The algorithm was also simulated as a function of SNR over the range of values from 0 to -20 dB. 10000 simulation runs were averaged. The results are shown along with Quinn's second estimator and the CRB in figure 5.8. While being computationally simpler than Quinn's second estimator it still has comparable performance to the latter.

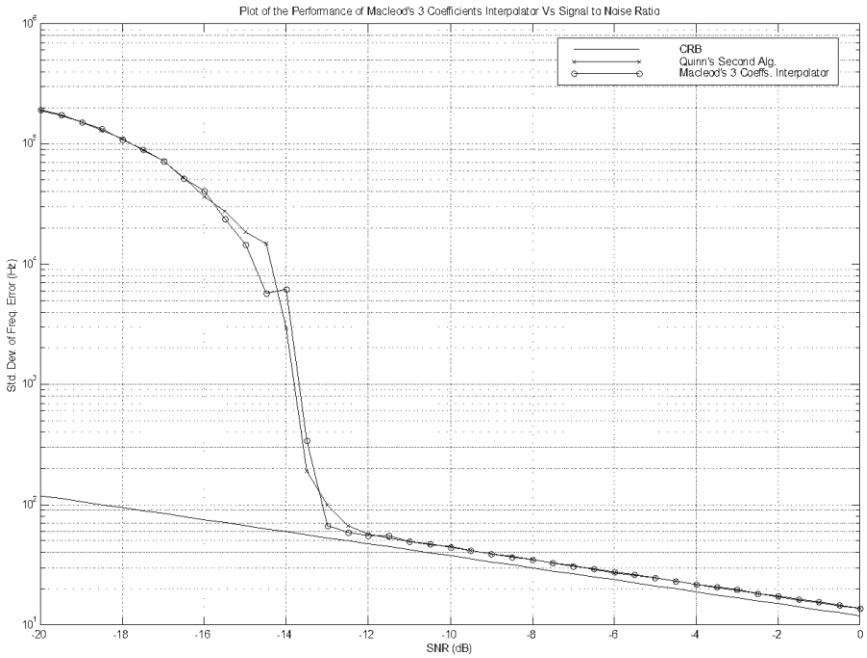

Figure 5.8 – *Comparison of the performance of Quinn's second frequency estimation algorithm and Macleod's three coefficients interpolator as a function of SNR. N = 1024, f_s = 1MHz. 10000 simulation runs were averaged.*

5.5 Interpolation on Five Fourier Coefficients

As we stated earlier in section 5.2.1, the ratio of the resulting asymptotic variance to the ACRB goes to 1 as the number of samples used in the interpolation goes to infinity, that is as M_L and M_U go to infinity. To take advantage of this fact, Macleod, [84], proposed a five sample estimator. The optimum ratio for the five sample interpolator can be found by putting $M_L = M_U = 2$ in equation (5.10).

$$R_{ACRB}^{5\,Coeffs} = \frac{\pi^4}{30}\frac{\delta_0^2}{\sin^2(\pi\delta_0)}\left\{\frac{\left(5\delta_0^8 - 20\delta_0^6 + 45\delta_0^4 + 16\right)\left(\delta_0^2 - 1\right)^2\left(\delta_0^2 - 4\right)^2}{5\delta_0^{12} + 10\delta_0^{10} + 55\delta_0^8 + 48\delta_0^6 - 100\delta_0^4 + 224\delta_0^2 + 64}\right\} \qquad (5.22)$$

Using the notation of the previous section, we have that

$$r_l = \Re\left\{X_l X_0^*\right\}, l = -2\ldots 2$$

and the estimator is given by the following two equations

$$\gamma = \frac{4(r_{-1} - r_1) + 2(r_{-2} - r_2)}{12r_0 + 8(r_{-1} + r_1) + (r_{-2} - r_2)} \tag{5.23}$$

and

$$\hat{\delta} = 0.4041 \tan^{-1}(2.93\gamma) \tag{5.24}$$

Note that equation (5.23) can be re-written in terms of the ratios α_l as

$$\gamma = \frac{4(\alpha_{-1} - \alpha_1) + 2(\alpha_{-2} - \alpha_2)}{12 + 8(\alpha_{-1} + \alpha_1) + (\alpha_{-2} - \alpha_2)}$$

The algorithm is summarised the table below

Set $\alpha_l = \Re\left\{\frac{X_l}{X_0}\right\}$, for $l = 0, \pm 1, \pm 2$
Then Calculate $\gamma = \frac{4(\alpha_{-1} - \alpha_1) + 2(\alpha_{-2} - \alpha_2)}{12 + 8(\alpha_{-1} + \alpha_1) + (\alpha_{-2} - \alpha_2)}$
Let $\hat{\delta} = 0.4041 \tan^{-1}(2.93\gamma)$
The frequency estimate is then given by $\hat{f} = (m + \hat{\delta})\frac{f_s}{N}$

Table 5.4 – *Macleod's five coefficients interpolator.*

The ratio of the asymptotic variance of the five sample interpolator to the asymptotic CRB was obtained by averaging 10000 simulation runs at 0dB SNR. The results are plotted versus δ_0 in figure 5.9 below. The curves for the three sample interpolator and the theoretical ratio of the asymptotic variance to the asymptotic CRB are also shown. There is clear improvement over Macleod's three sample interpolator. Figure 5.10 shows the standard deviation of the frequency error for the three and five coefficient interpolators as a function of signal to noise ratio. The plot also includes the CRB curve for the purpose of comparison. We see that the five sample interpolator is slightly closer to the CRB curve than the three sample interpolator. In fact the average ratio of

the asymptotic variance of the five sample interpolator was found to be about 1.2 compared to 1.35 for the three sample interpolator.

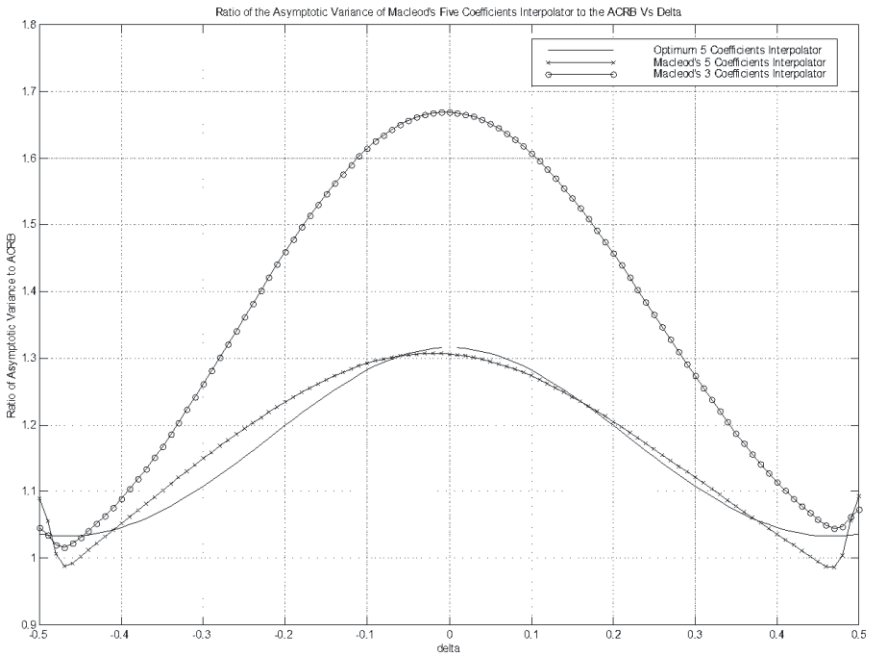

Figure 5.9 – *Plot of simulation results of the ratio of the variance Macleod's five coefficients interpolator to the asymptotic CRB as a function of* δ_0. *N was set to 1024 and SNR to 0 dB. 10000 simulation runs were averaged.*

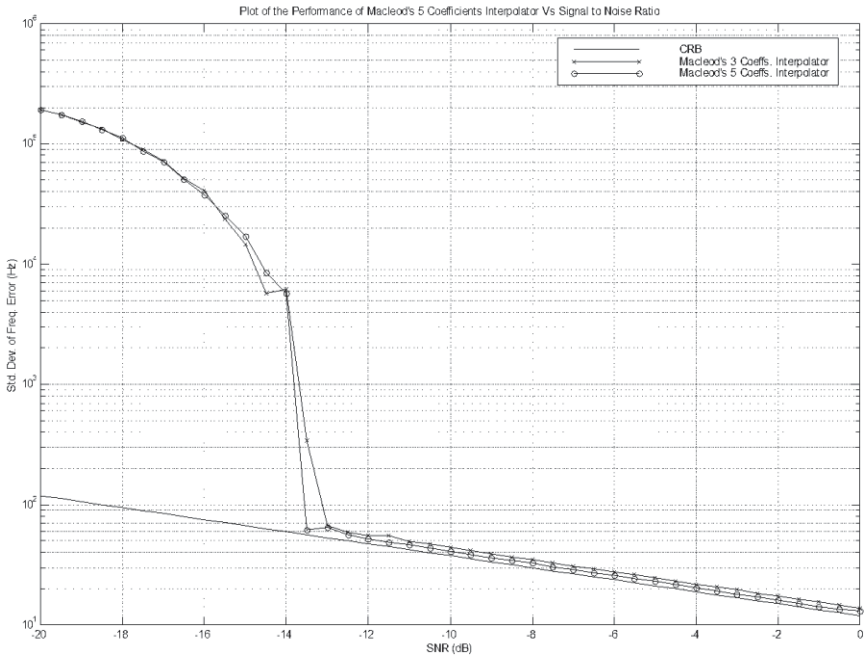

Figure 5.10 – *Plot of the performance of Macleod's three and five coefficients interpolators as a function of SNR. N = 1024, f_s = 1MHz. 10000 simulation runs were averaged.*

5.6 Interpolation Using the Moduli of Fourier Coefficients– The Rife-Vincent Estimators

Most of the energy of a sinusoidal signal is concentrated in the few bins around the maximum (see figure 5.1). Therefore, it is possible to construct frequency estimators that only use the moduli of the Fourier coefficients. In this section we examine two such interpolators. We refer to this group as interpolators on the moduli of Fourier coefficients. These two techniques were attributed by Quinn, [34] pp.199-206, to Rife and Vincent and are therefore called the Rife-Vincent (R-V) estimators. Quinn, however, shows that they do not work as well as the interpolators on Fourier coefficients discussed so far.

5.6.1 Rife-Vincent Estimator

Rife and Vincent, in [118], proposed the use of the magnitudes of the Fourier coefficients for the purpose of digital frequency estimation. In the usual notation, let the maximum bin and those either side of it be X_0, X_{-1} and X_1 respectively. Denote the magnitude of X_l by Y_l. The R-V estimator, [34] pp. 201, is shown in the table below,

Let $$p = \begin{cases} 1 & if\ Y_1 > Y_{-1} \\ -1 & otherwise \end{cases}$$

Then Calculate

$$\hat{\delta} = p\frac{Y_p}{Y_0 + Y_p}$$

The frequency estimate is then given by

$$\hat{f} = \left(m + \hat{\delta}\right)\frac{f_s}{N}$$

Table 5.5 – *Rife-Vincent estimator.*

5.6.2 Motivation

It is quite easy to see the reasoning behind the R-V estimator. Given the expression for X_l from section 5.4.1, Y_l becomes,

$$Y_l = \left|\frac{c_0\delta_0}{\delta_0 - l}\right|$$

Denote the ratio in the expression of $\hat{\delta}$ by β_p, then

$$\begin{aligned}\beta_p &= \frac{Y_p}{Y_0 + Y_p} \\ &= \frac{\left|\frac{c_0\delta_0}{\delta_0 - p}\right|}{|c_0| + \left|\frac{c_0\delta_0}{\delta_0 - p}\right|} \\ &= \frac{|\delta_0|}{|\delta_0 - p| + |\delta_0|}\end{aligned}$$

Now if $\delta_0 < 0$, we would expect Y_{-1} to be larger than Y_1. Therefore the first step in the table above would result in p being set to -1. Furthermore, since $\delta_0 < 0$, $|\delta_0| = -\delta_0$. This implies that

$$\begin{aligned}\beta_{-1} &= \frac{-\delta_0}{\delta_0 + 1 - \delta_0} \\ &= -\delta_0\end{aligned}$$

Following a similar argument, we see that for $\delta_0 > 0$, we use β_1,

$$\begin{aligned}\beta_1 &= \frac{\delta_0}{-\delta_0 + 1 + \delta_0} \\ &= \delta_0\end{aligned}$$

Hence, we find that, provided that the comparison step yields the correct choice for p, β_p equals $p\delta_0$. Since $p = 1/p$, the estimator for δ_0 is given by $p\beta_p$. In the case that the choice is incorrect we find that

$$\beta_p = \frac{\delta_0}{2\delta_0 - p}$$

This is a nonlinear function of δ_0.

This analysis suggests that the R-V algorithm has a problem for δ_0 close to 0 as an incorrect decision in the choice of the p is quite probable. We will now present the modified R-V algorithm proposed by Quinn in order to alleviate this problem.

5.6.3 Modified Rife-Vincent Estimator

In order to alleviate the problem of the R-V estimator in the region close to zero, Quinn suggested replacing the comparison step with an alternative inspired from his first algorithm. The modified R-V algorithm is shown in the table below.

Let

$$\alpha_l = \Re\left\{\frac{X_l}{X_0}\right\}, \text{for } l = \pm 1$$

And

$$s_l = \text{sgn}(\alpha_l)$$

Now put

$$p = \begin{cases} 1 & \text{if } \alpha_{-1} = 1 \text{ and } \alpha_1 = -1 \\ -1 & \text{otherwise} \end{cases}$$

Then Calculate

$$\hat{\delta} = -ps_p \frac{Y_p}{Y_0 - s_p Y_p}$$

The frequency estimate is then given by

$$\hat{f} = \left(m + \hat{\delta}\right)\frac{f_s}{N}$$

Table 5.6 – *Modified Rife-Vincent estimator.*

5.6.4 Performance of the Rife-Vincent Estimators

The ratio of the frequency variance to the asymptotic CRB was obtained for each of the R-V estimators through simulations. The signal to noise ratio was set to 0dB and 1024 samples were used. 10000 simulation runs were averaged and the results are shown in figure 5.11 below. The original and modified estimators have almost identical performances in the regions $[-0.5,-0.25]$ and $[0.25,0.5]$. However, we see that the original algorithm has a significantly worse performance in the interval $[-0.25,0.25]$ compared to the modified algorithm. It is interesting to note that, as δ_0 gets closer to zero, the performance of the original algorithm improves. The reason is that, although the probability of an incorrect decision worsens, the net loss is reduced owing to the decreasing size of δ_0.

Figure 5.12 shows the standard deviation of the frequency error versus signal to noise ratio for both the R-V and the modified R-V estimators. Also shown, for the purpose of comparison are the CRB curve and the standard deviation of the frequency error of Quinn's first algorithm. The performance of the R-V algorithm is clearly inferior to both the modified R-V algorithm and Quinn's first algorithm. In fact Quinn shows that the original R-V algorithm is only $O\left(N^{-\frac{3}{2}}\right)$ if δ_0 is rational and is not even $O\left(N^{-\frac{5}{4}}\right)$ otherwise. This explains the poor performance compared to the other estimators. The modified R-V algorithm, on the other hand, is $O\left(N^{-\frac{3}{2}}\right)$ and has a performance that is comparable to Quinn's first algorithm.

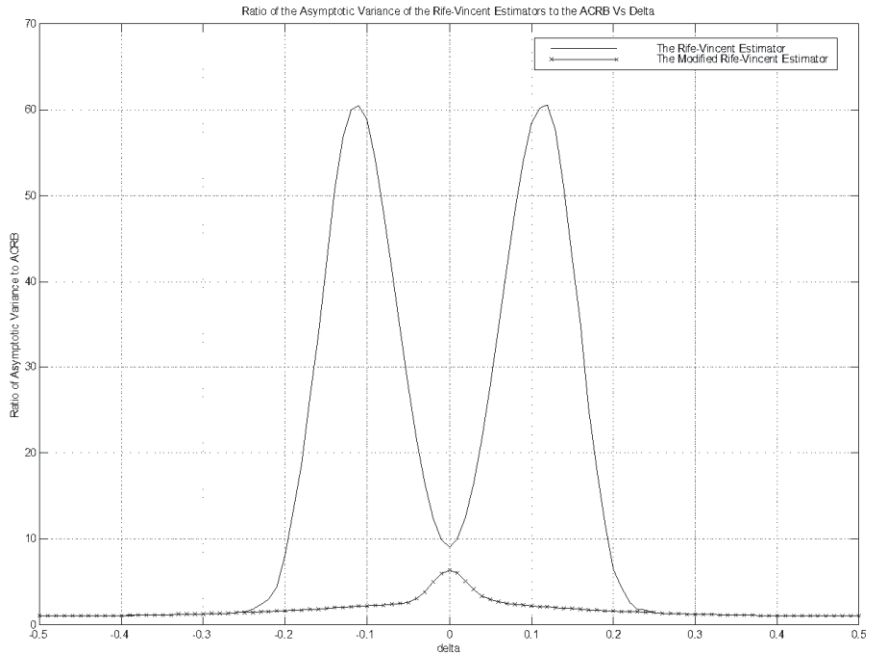

Figure 5.11 – *Plot of simulation results of the ratio of the variance the Rife-Vincent estimators to the asymptotic CRB as a function of δ_0. N was set to 1024 and SNR to 0 dB.*

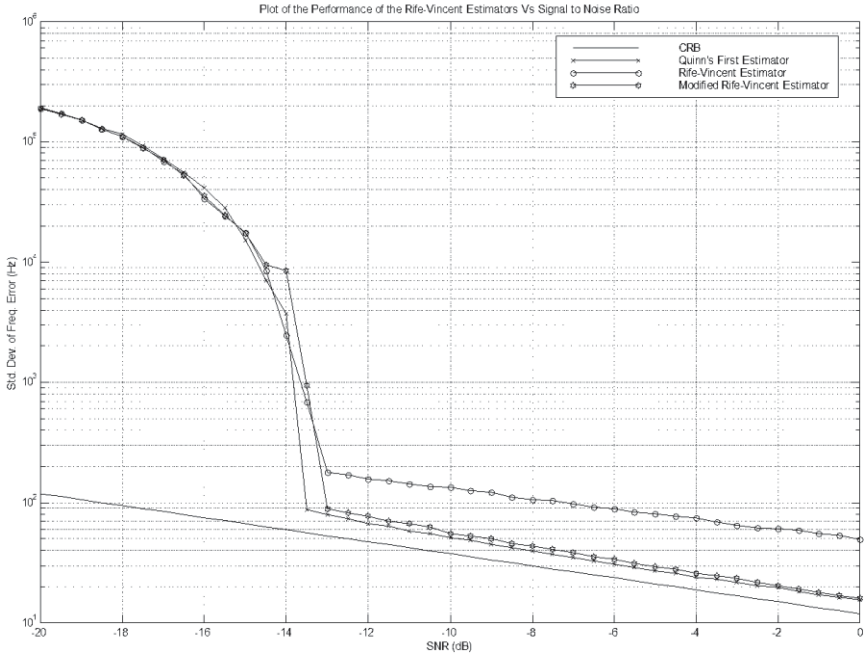

Figure 5.12 – *Plot of the performance of the Rife-Vincent as a function of SNR. N = 1024, f_s = 1MHz. 10000 simulation runs were averaged.*

5.7 Conclusion

In this chapter we examined a number of existing algorithms for the estimation of the frequency of a sinusoidal signal. Although all of the techniques that were presented interpolate on the Fourier coefficients, they vary depending on the number of coefficients used and the method used to combine them. The Quinn and Macleod estimators, for instance, use the raw coefficients and therefore work on complex numbers. Other estimators like the Rife-Vincent algorithms use the moduli of Fourier coefficients. It is accepted that the moduli based algorithms do not perform as well as the first type of estimators. In the next chapter, however, we propose a new class of algorithms that work on two Fourier coefficients computed on a fractional grid. We call these estimators "interpolators on fractional Fourier coefficients" and show that they are suitable for iterative implementation. The resulting iterative algorithms are shown in chapter 8 to have an improved performance over the existing interpolation algorithms.

Chapter 6

Frequency Estimation by Interpolation on Fractional Fourier Coefficients

6.1 Introduction

The algorithms presented in the previous chapter almost invariably exhibit a degraded performance around $\delta_0 = 0$. In this chapter, we present a class of algorithms we call the interpolators on fractional Fourier coefficients. These algorithms have the desirable property of exhibiting the best performance at $\delta_0 = 0$. This, as we demonstrate in chapter 8, results in performance improvement when they are implemented iteratively. The methods of this chapter use two coefficients to give estimators with performances approaching the CRB. The techniques of the previous chapter, on the other hand, require at least three coefficients to obtain a finer estimate of the frequency.

We remind the reader that throughout the thesis, it is assumed that the first step is a coarse frequency estimate given by the MBS algorithm. The techniques of this chapter are then used to refine the frequency estimate.

The chapter is organised as follows; first we introduce the fractional Fourier coefficients in section 6.2. We then proceed to propose the new algorithms in sequence. Section 6.3 presents and analyses the interpolation on two fractional Fourier coefficients (FFCI) algorithm. In section 6.4 we propose the interpolation on the magnitudes of two fractional Fourier coefficients, or MOI algorithm. The MOI algorithm is analysed and compared to the FFCI estimator. Finally the Magnitudes Squared Interpolation (MSI) and Modified Magnitude Squared Interpolation (MMSI) algorithms are presented and discussed in sections 6.5 and 6.6. Section 6.7 contains the concluding remarks of the chapter.

6.2 Fractional Fourier Coefficients

For a signal x, the fractional Fourier coefficients are calculated midway between two bins as shown

$$X_{n+p} = \frac{1}{N}\sum_{k=0}^{N-1} x(k) e^{-j2\pi k\frac{n+p}{N}} \tag{6.1}$$

where p is set to either $1/2$ or $-1/2$. The fractional coefficients can also be obtained by shifting the signal x by half a bin and then taking FFT algorithm. As a result, we showed in appendix C that the resulting Fourier coefficients are independent and identically distributed with zero mean and variance σ^2/N.

Following the notation of section 5.2.1, let m be the index of the maximum of the normal periodogram, that is the index returned by MBS algorithm. The signal frequency is then given by

$$f = \frac{m+\delta_0}{N} f_s$$

The fractional Fourier coefficient X_{n+p} is

$$\begin{aligned} X_{n+p} &= S_{n+p} + W_{n+p} \\ &= \frac{1}{N}\left(\frac{1-e^{j2\pi N\left(\frac{m+\delta_0}{N}-\frac{n+p}{N}\right)}}{1-e^{j2\pi\left(\frac{m+\delta_0}{N}-\frac{n+p}{N}\right)}} \right) + W_{n+p} \\ &= \frac{1}{N}\left(\frac{1+e^{j2\pi\delta_0}}{1-e^{j2\pi\left(\frac{m-n+\delta_0-p}{N}\right)}} \right) + W_{n+p} \end{aligned}$$

Putting $n = m+l$, the above expression becomes

$$X_{m+l+p} = \frac{1}{N}\left(\frac{1+e^{j2\pi\delta_0}}{1-e^{j2\pi\left(\frac{\delta_0-l-p}{N}\right)}} \right) + W_{n+p}$$

For x small, we have

$$e^x \approx 1+x$$

Dropping the index m in order to simplify the notation, we get

$$X_{l+p} = \frac{1}{N}\left(\frac{1+e^{j2\pi\delta_0}}{1-1-j2\pi\left(\frac{\delta_0-l-p}{N}\right)}\right)+W_{n+p} \qquad (6.2)$$
$$= b_0\frac{\delta_0}{\delta_0-l-p}+W_{n+p}$$

where

$$b_0 = -\frac{1+e^{j2\pi\delta_0}}{j2\pi\delta_0} \qquad (6.3)$$

In the following section, we present a new algorithm that efficiently uses the fractional Fourier coefficients to interpolate the frequency of a sinusoidal signal.

6.3 Interpolation on Two Fractional Fourier Coefficients

We saw in section 5.3 of the previous chapter that it is possible to use the complex Fourier coefficients to interpolate the true value of the frequency. We now propose a new technique of interpolating on the fractional Fourier coefficients in order to obtain a fine estimator of the frequency of the sinusoidal signal.

In the noiseless case, according to equation (6.2) and with l set to zero, we have

$$X_{-0.5} = b_0\frac{\delta_0}{\delta_0+0.5}$$

and

$$X_{0.5} = b_0\frac{\delta_0}{\delta_0-0.5}$$

Consider the following ratio,

$$\begin{aligned}\psi &= \frac{1}{2}\frac{X_{0.5}+X_{-0.5}}{X_{0.5}-X_{-0.5}} \\ &= \frac{1}{2}\frac{\dfrac{b_0\delta_0}{\delta_0-0.5}+\dfrac{b_0\delta_0}{\delta_0+0.5}}{\dfrac{b_0\delta_0}{\delta_0-0.5}-\dfrac{b_0\delta_0}{\delta_0+0.5}} \\ &= \delta_0\end{aligned}$$

Therefore we see that the real part of ψ forms an estimate of the offset δ_0 from the maximum bin m. The real part is taken to remove the imaginary component that is purely due to the noise. We now have the following algorithm,

Let $X_p = \sum_{k=0}^{N-1} x(k) e^{-j2\pi\frac{k(m+p)}{N}}$, $p = \pm 0.5$

Then Calculate

$$\hat{\delta} = \frac{1}{2}\Re\left\{\frac{X_{0.5}+X_{-0.5}}{X_{0.5}-X_{-0.5}}\right\}$$

The frequency estimate is then given by

$$\hat{f} = \left(m+\hat{\delta}\right)\frac{f_s}{N}$$

Table 6.1 – *Fractional Fourier Coefficients Interpolation (FFCI) estimator.*

6.3.1 Analysis

We will now analyse the algorithm of table 6.1. We will establish its central limit theorem and derive its asymptotic variance.

Including the noise terms in the expression for ψ gives

$$\begin{aligned}\psi &= \frac{1}{2}\frac{X_{0.5}+X_{-0.5}}{X_{0.5}-X_{-0.5}} \\ &= \frac{1}{2}\frac{\dfrac{b_0\delta_0}{\delta_0-0.5}+W_{0.5}+\dfrac{b_0\delta_0}{\delta_0+0.5}+W_{-0.5}}{\dfrac{b_0\delta_0}{\delta_0-0.5}+W_{0.5}-\dfrac{b_0\delta_0}{\delta_0+0.5}-W_{-0.5}} \\ &= \frac{1}{2}\frac{2\delta_0+\dfrac{\delta_0^2-0.25}{b_0\delta_0}\left(W_{0.5}+W_{-0.5}\right)}{1+\dfrac{\delta_0^2-0.25}{b_0\delta_0}\left(W_{0.5}-W_{-0.5}\right)}\end{aligned}$$

The factor $\dfrac{\delta_0^2-0.25}{b_0\delta_0}$ has a removable singularity at $\delta_0=\pm 0.5$ and

$$\lim_{\delta_0\to\pm 0.5}\frac{\delta_0^2-0.25}{b_0\delta_0}=\mp 1$$

The fractional Fourier coefficients of the noise are $O_p\left(N^{-1/2}\sqrt{\ln N}\right)$ (see appendix C, section C.2). Using the fact that for small x,

$$\begin{aligned}\frac{1}{1+x} &= 1-x+O\left(x^2\right) \\ &\approx 1-x\end{aligned} \tag{6.4}$$

we find that

$$\begin{aligned}\frac{1}{1+\dfrac{\delta_0^2-0.25}{b_0\delta_0}\left(W_{0.5}-W_{-0.5}\right)} &= 1-\frac{\delta_0^2-0.25}{b_0\delta_0}\left(W_{0.5}-W_{-0.5}\right)+O\left(N^{-1}\ln N\right) \\ &\approx 1-\frac{\delta_0^2-0.25}{b_0\delta_0}\left(W_{0.5}-W_{-0.5}\right)\end{aligned}$$

and consequently ψ is given by

$$\begin{aligned}\psi &= \frac{1}{2}\left[2\delta_0+\frac{\delta_0^2-0.25}{b_0\delta_0}\left(W_{0.5}+W_{-0.5}\right)\right]\left[1-\frac{\delta_0^2-0.25}{b_0\delta_0}\left(W_{0.5}-W_{-0.5}\right)+o(1)\right] \\ &= \delta_0+\frac{1}{2}\frac{\delta_0^2-0.25}{b_0\delta_0}\left\{\left(1-2\delta_0\right)W_{0.5}+\left(1+2\delta_0\right)W_{-0.5}\right\}+O\left(N^{-1}\ln N\right)\end{aligned}$$

We see that, as the fractional Fourier coefficients are independent and identically distributed, with a Gaussian distribution, ψ itself is asymptotically unbiased and Gaussian. The estimate of δ_0, denoted by $\hat{\delta}$ is given by the real part of ψ. Therefore, $\hat{\delta}$ is itself asymptotically unbiased and Gaussian distributed. This allows for the CLT of the estimator to be established. The estimate of δ_0 is given by the real part of ψ;

$$\begin{aligned}\hat{\delta} &= \Re\{\psi\} \\ &= \delta_0 + \frac{1}{2}\frac{\delta_0^2 - 0.25}{b_0\delta_0}\{(1-2\delta_0)\Re\{W_{0.5}\} + (1+2\delta_0)\Re\{W_{-0.5}\}\} + O\left(N^{-1}\ln N\right)\end{aligned}$$

The error in $\hat{\delta}$ is

$$\hat{\delta} - \delta_0 = \frac{1}{2}\frac{\delta_0^2 - 0.25}{b_0\delta_0}\{(1-2\delta_0)\Re\{W_{0.5}\} + (1+2\delta_0)\Re\{W_{-0.5}\}\} + O\left(N^{-1}\ln N\right)$$

and consequently the variance of the error is

$$\begin{aligned}\mathrm{var}\left[\hat{\delta} - \delta_0\right] &= \mathrm{var}\left[\frac{1}{2}\frac{\delta_0^2 - 0.25}{b_0\delta_0}\{(1-2\delta_0)\Re\{W_{0.5}\} + (1+2\delta_0)\Re\{W_{-0.5}\}\}\right] \\ &= \frac{1}{4}\frac{\left(\delta_0^2 - 0.25\right)^2}{|b_0|^2\,\delta_0^2}\left\{(1-2\delta_0)^2\,\mathrm{var}\left[\Re\{W_{0.5}\}\right] + (1+2\delta_0)^2\,\mathrm{var}\left[\Re\{W_{-0.5}\}\right]\right\}\end{aligned}$$

From section C.2 we have that

$$\begin{aligned}\mathrm{var}\left[\Re\{W_{0.5}\}\right] &= \mathrm{var}\left[\Re\{W_{-0.5}\}\right] \\ &= \frac{\sigma^2}{2N}\end{aligned}$$

Substituting this into the expression of the variance yields

$$\begin{aligned}\mathrm{var}\left[\hat{\delta} - \delta_0\right] &= \frac{1}{4}\frac{\left(\delta_0^2 - 0.25\right)^2}{|b_0|^2\,\delta_0^2}\left\{(1-2\delta_0)^2\,\frac{\sigma^2}{2N} + (1+2\delta_0)^2\,\frac{\sigma^2}{2N}\right\} \\ &= \frac{1}{8}\frac{\sigma^2}{N}\frac{\left(\delta_0^2 - 0.25\right)^2}{|b_0|^2\,\delta_0^2}\left\{(1-2\delta_0)^2 + (1+2\delta_0)^2\right\} \\ &= \frac{1}{4}\frac{\sigma^2}{N}\frac{\left(\delta_0^2 - 0.25\right)^2\left(4\delta_0^2 + 1\right)}{|b_0|^2\,\delta_0^2}\end{aligned}$$

However from equation (6.3), we obtain

$$|b_0|^2 = \left| -\frac{e^{j2\pi\delta_0}+1}{j2\pi\delta_0} \right|^2$$
$$= \frac{\cos^2(\pi\delta_0)}{(\pi\delta_0)^2}$$

Substituting $|b_0|^2$ into the expression for the variance we get,

$$\text{var}\left[\hat{\delta}-\delta_0\right] = \frac{1}{4}\frac{\sigma^2}{N}\frac{\pi^2\left(\delta_0^2-0.25\right)^2\left(4\delta_0^2+1\right)}{\cos^2(\pi\delta_0)}$$

Finally we have the following theorem,

6.3.1.1 Theorem

Let $\hat{\delta}$ be the estimator of δ_0 as shown in table 6.1 and $\hat{f}$ be defined by

$$\hat{f} = \frac{m+\hat{\delta}}{N} f_s$$

then $\sigma_{FFCI}^{-1}\left(\hat{f}-f_0\right)$ asymptotically follows the standard normal distribution with σ_{FFCI} given by

$$\sigma_{FFCI}^2 = \frac{f_s^2}{4N^3\rho}\frac{\pi^2\left(\delta_0^2-0.25\right)^2\left(4\delta_0^2+1\right)}{\cos^2(\pi\delta_0)} \tag{6.5}$$

The variance of $\hat{\delta}$ was multiplied by f_s^2/N^2 to give that of the frequency. The ratio of the asymptotic variance of the estimator to the asymptotic CRB is given below

$$R_{ACRB}^{IFFC} = \frac{\pi^2}{6}\frac{\pi^2\left(\delta_0^2-0.25\right)^2\left(4\delta_0^2+1\right)}{\cos^2(\pi\delta_0)} \tag{6.6}$$

The figure below shows the theoretical as well as simulation results of the ratio of the asymptotic variance to the asymptotic CRB as a function of δ_0. The results were obtained at a signal to noise ratio of 0dB and 10000 runs were averaged. We see very close agreement between the two curves. The ratio of the asymptotic variance to the

asymptotic CRB has a minimum of 1.0147 at $\delta_0 = 0$. The difference between the simulation and the theoretical curves at the edges of the interval, that is at ±0.5 is due to the removable singularity of the factor $\frac{\left(\delta_0^2 - 0.25\right)^2}{\cos^2(\pi\delta_0)}$. In fact taking the limit of the ratio we have

$$\lim_{\delta_0 \to \pm 0.5} R_{ACRB}^{IFFC} = \lim_{\delta_0 \to \pm 0.5} \frac{\pi^2}{6} \frac{\pi^2 \left(\delta_0^2 - 0.25\right)^2 \left(4\delta_0^2 + 1\right)}{\cos^2(\pi\delta_0)}$$
$$= 3.29$$

The theoretical and simulation curves agree very closely.

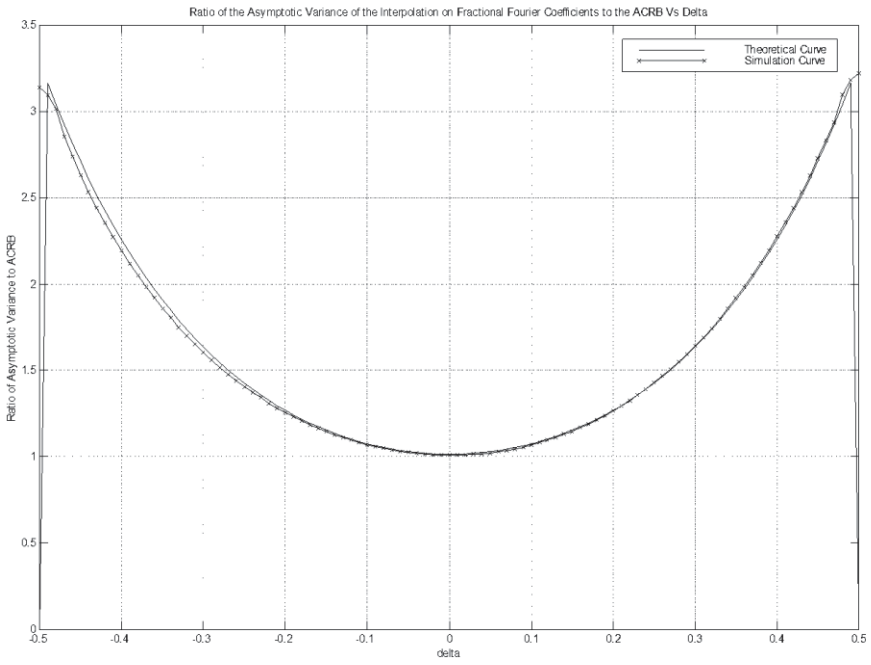

Figure 6.1 – *Plot of the ratio of the asymptotic variance of the interpolation on fractional Fourier Coefficients estimator to the asymptotic CRB versus δ_0. 10000 simulation runs at 0 dB SNR were averaged.*

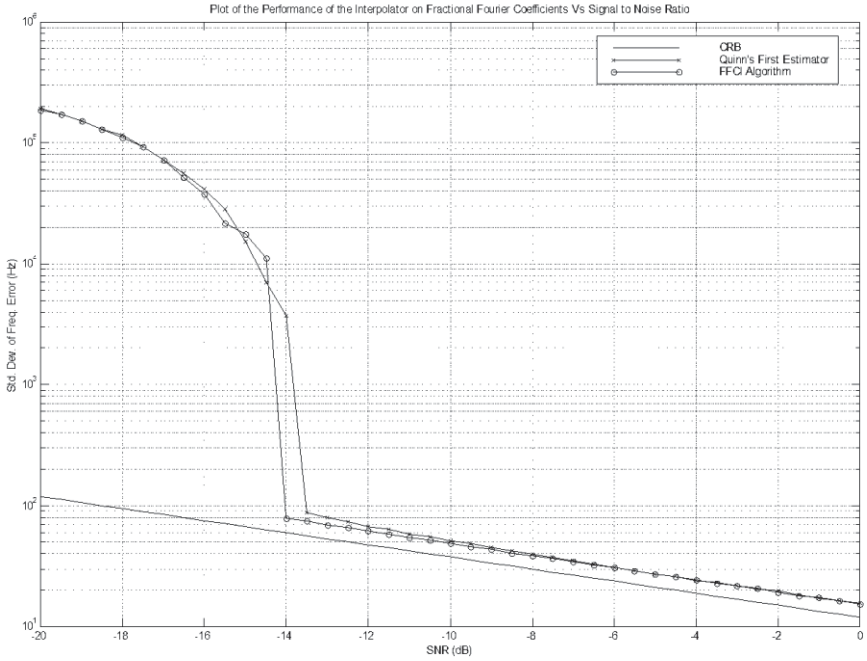

Figure 6.2 – *Plot of the performance of the interpolation on fractional Fourier coefficients algorithm as a function of SNR. N = 1024, f_s = 1MHz. 10000 simulation runs were averaged.*

Figure 6.2 above shows the performance of the estimator along with that of Quinn's first algorithm for the purpose of comparison. The two algorithms have almost identical performance. This is to be expected as the two utilise the same amount of information to derive the estimate of δ_0. In fact, the theoretical curve of figure 6.1 is identical to that of figure 5.3 but with the δ-axis relabelled (that is shifted by 0.5). Figure 6.3(a) shows the theoretical ratio of the asymptotic variance of Quinn's first algorithm and the interpolator on fractional Fourier coefficients repeated periodically. Plot (b) displays that of Quinn's first algorithm on a δ_0 shifted by 0.5 whereas that of the new algorithm is unchanged. We see that the two curves in figure 6.3(b) coincide. This illustrates the important characteristic of the new class of algorithms. As the new algorithms exhibit their lowest variance at $\delta_0 = 0$, we will show in chapter 8 that their performance improves when implemented iteratively. This is in contrast to the algorithms of the previous chapter. We note here that figure 6.2 shows a slightly better performance of the FFCI estimator compared to Quinn's first algorithm near the SNR threshold. This is

due to the absence of the decision making step in the FFCI algorithm. As the noise floor becomes more prominent, the decision step of Quinn's algorithm fails more often. This results in a slightly degraded performance at low SNR.

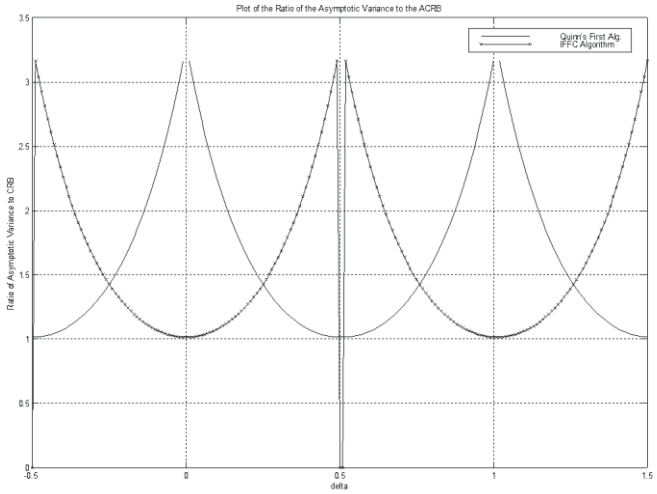

(a)

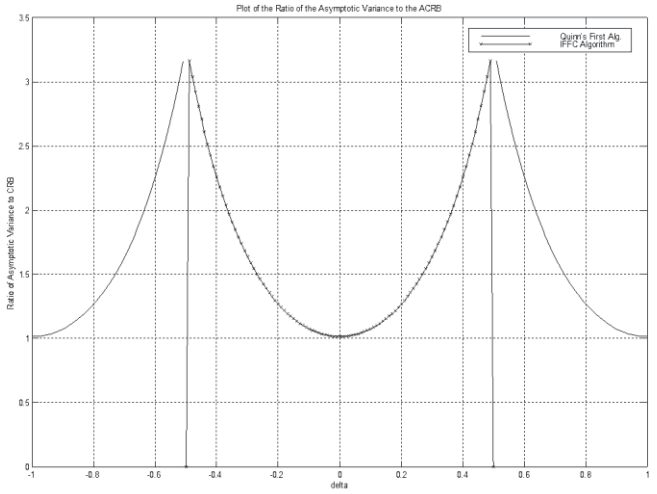

(b)

Figure 6.3 – (a) *Plot of the theoretical ratio of the asymptotic variance to the asymptotic CRB. The curves for Quinn's first algorithm and the interpolation on fractional Fourier Coefficients estimator are shown repeated periodically versus* δ_0. (b) *A shifted version.*

6.4 Interpolation on the Magnitudes of Two Fractional Fourier Coefficients

The algorithm presented in the previous section uses the fractional Fourier coefficients to obtain a fine frequency estimate. In this section we propose and analyse a new estimator that operates on the magnitudes of the fractional Fourier coefficients. We call the algorithm the Magnitudes Only Interpolation (MOI) estimator.

Let Y_p be the magnitudes of the fractional Fourier coefficient X_p. That is $Y_p = \left|X_p\right|$. The estimate of δ_0 is then given by

$$\hat{\delta} = \frac{1}{2}\frac{Y_{0.5} - Y_{-0.5}}{Y_{0.5} + Y_{-0.5}} \tag{6.7}$$

The algorithm is summarised in the table below.

Let $X_p = \sum_{k=0}^{N-1} x(k) e^{-j2\pi\frac{k(m+p)}{N}}$, $p = \pm 0.5$

And

$$Y_p = \left|X_p\right|$$

Calculate

$$\hat{\delta} = \frac{1}{2}\frac{Y_{0.5} + Y_{-0.5}}{Y_{0.5} - Y_{-0.5}}$$

The frequency estimate is then given by

$$\hat{f} = \left(m + \hat{\delta}\right)\frac{f_s}{N}$$

Table 6.2 – *Magnitudes Only Interpolation (MOI) on fractional Fourier coefficients estimator.*

6.4.1 Motivation

Ignoring the noise terms, Y_p is,

$$\begin{aligned} Y_p &= \left| X_p \right| \\ &= \left| \frac{b_0 \delta_0}{\delta_0 - p} \right| \end{aligned}$$

Now looking at the two cases for $p = \pm 0.5$ we have,

$$Y_{0.5} = \left| b_0 \delta_0 \right| \frac{1}{\left| \delta_0 - 0.5 \right|}$$

and

$$Y_{-0.5} = \left| b_0 \delta_0 \right| \frac{1}{\left| \delta_0 + 0.5 \right|}$$

For $\left| \delta_0 \right| \leq 0.5$ we find that

$$\left| \delta_0 - 0.5 \right| = 0.5 - \delta_0$$

and

$$\left| \delta_0 + 0.5 \right| = \delta_0 + 0.5$$

Therefore the expressions for $Y_{0.5}$ and $Y_{-0.5}$ become

$$Y_{-0.5} = \left| b_0 \delta_0 \right| \frac{1}{0.5 + \delta_0}$$

and

$$Y_{0.5} = \left| b_0 \delta_0 \right| \frac{1}{0.5 - \delta_0}$$

Forming the ratio in equation (6.7),

$$\begin{aligned} \psi &= \frac{Y_{0.5} - Y_{-0.5}}{Y_{0.5} + Y_{-0.5}} \\ &= \frac{\left| b_0 \delta_0 \right| \frac{1}{0.5 - \delta_0} - \left| b_0 \delta_0 \right| \frac{1}{0.5 + \delta_0}}{\left| b_0 \delta_0 \right| \frac{1}{0.5 - \delta_0} + \left| b_0 \delta_0 \right| \frac{1}{0.5 + \delta_0}} \\ &= \frac{0.5 + \delta_0 - 0.5 + \delta_0}{0.5 + \delta_0 + 0.5 - \delta_0} \\ &= 2\delta_0 \end{aligned}$$

Thus, we see that an estimator for δ_0 is given by $\Psi/2$.

6.4.2 Analysis

The asymptotic performance of the MOI algorithm of table 6.2 will be obtained in this section. Including the noise term in the expression for Y_p ,

$$\begin{aligned} Y_p &= \left| \frac{b_0\delta_0}{\delta_0 - p} + W_p \right| \\ &= \left| \frac{b_0\delta_0}{\delta_0 - p} \right| \left| 1 + \frac{\delta_0 - p}{b_0\delta_0} W_p \right| \end{aligned} \tag{6.8}$$

The second factor is expanded as follows

$$\begin{aligned} \left| 1 + \frac{\delta_0 - p}{b_0\delta_0} W_p \right| &= \sqrt{\left\{ 1 + \frac{\delta_0 - p}{b_0\delta_0} W_p \right\} \left\{ 1 + \frac{\delta_0 - p}{b_0\delta_0} W_p \right\}^*} \\ &= \sqrt{1 + \frac{(\delta_0 - p)^2}{|b_0|^2 \delta_0^2} |W_p|^2 - 2\frac{\delta_0 - p}{\delta_0} \Re\left\{ \frac{W_p}{b_0} \right\}} \end{aligned} \tag{6.9}$$

Upon examination of this expression we find that we must divide the range of δ_0 into two regions, Δ_1 and Δ_2, defined as

$$\Delta_1 = \left\{ \delta_0 ; |\delta_0| \le \frac{1}{2} - aN^{-\nu} \right\}$$

and

$$\Delta_2 = \left\{ \delta_0 ; \frac{1}{2} - aN^{-\nu} < |\delta_0| \le \frac{1}{2} \right\}$$

for some $a > 0$ and $\nu > 0$.

We will now restrict δ_0 to region Δ_1. The other case will be examined later on. Referring to appendix C we have that

$$\Re\left\{ \frac{W_p}{b_0} \right\} = O\left(N^{-\frac{1}{2}} \sqrt{\ln N} \right) \tag{6.10}$$

Whereas

$$\left|\frac{W_p}{b_0}\right|^2 = O\left(N^{-1}\ln N\right)$$

Therefore we can ignore the lower order terms, that is the terms in $\left|W_p\right|^2$. Substituting into (6.8) we get

$$Y_p = \left|\frac{b_0\delta_0}{\delta_0 - p}\right|\sqrt{1 - 2\frac{\delta_0 - p}{\delta_0}\Re\left\{\frac{W_p}{b_0}\right\}}$$

Now for $x << 1$ we have

$$\sqrt{1+x} = 1 + \frac{x}{2} + O\left(x^2\right)$$

Thus the expressions for Y_p becomes

$$Y_p = \left|\frac{b_0\delta_0}{\delta_0 - p}\right|\left[1 - \frac{\delta_0 - p}{\delta_0}\Re\left\{\frac{W_p}{b_0}\right\}\right] + o(1)$$

Substituting this into (6.7) yields

$$\begin{aligned}\hat{\delta} &= \frac{1}{2}\frac{Y_{0.5} - Y_{-0.5}}{Y_{0.5} + Y_{-0.5}} \\ &= \frac{1}{2}\frac{\left|\frac{b_0\delta_0}{\delta_0 - 0.5}\right|\left\{1 - \frac{\delta_0 - 0.5}{\delta_0}\Re\left(\frac{W_{0.5}}{b_0}\right)\right\} - \left|\frac{b_0\delta_0}{\delta_0 + 0.5}\right|\left\{1 - \frac{\delta_0 + 0.5}{\delta_0}\Re\left(\frac{W_{-0.5}}{b_0}\right)\right\}}{\left|\frac{b_0\delta_0}{\delta_0 - 0.5}\right|\left\{1 - \frac{\delta_0 - 0.5}{\delta_0}\Re\left(\frac{W_{0.5}}{b_0}\right)\right\} + \left|\frac{b_0\delta_0}{\delta_0 + 0.5}\right|\left\{1 - \frac{\delta_0 + 0.5}{\delta_0}\Re\left(\frac{W_{-0.5}}{b_0}\right)\right\}}\end{aligned} \quad (6.11)$$

Simplifying the above equation we get

$$\hat{\delta} = \frac{1}{2}\frac{2\delta_0 - \frac{\delta_0^2 - 0.25}{\delta_0}\left\{\Re\left(\frac{W_{0.5}}{b_0}\right) + \Re\left(\frac{W_{-0.5}}{b_0}\right)\right\}}{1 - \frac{\delta_0^2 - 0.25}{\delta_0}\left\{\Re\left(\frac{W_{0.5}}{b_0}\right) - \Re\left(\frac{W_{-0.5}}{b_0}\right)\right\}}$$

Using identity (6.4) we find

$$\hat{\delta} = \frac{1}{2}\left[2\delta_0 - \frac{\delta_0^2 - 0.25}{\delta_0}\left\{\Re\left(\frac{W_{0.5}}{b_0}\right) + \Re\left(\frac{W_{-0.5}}{b_0}\right)\right\}\right]\left[1 + \frac{\delta_0^2 - 0.25}{\delta_0}\left\{\Re\left(\frac{W_{0.5}}{b_0}\right) - \Re\left(\frac{W_{-0.5}}{b_0}\right)\right\}\right]$$

Expanding and simplifying gives

$$\hat{\delta} = \delta_0 + \frac{1}{2}\frac{\delta_0^2 - 0.25}{\delta_0}\left[(2\delta_0 - 1)\Re\left(\frac{W_{0.5}}{b_0}\right) - (2\delta_0 + 1)\Re\left(\frac{W_{-0.5}}{b_0}\right)\right]$$

The error is given by,

$$\hat{\delta} - \delta_0 = \frac{1}{2}\frac{\delta_0^2 - 0.25}{\delta_0}\left[(2\delta_0 - 1)\Re\left(\frac{W_{0.5}}{b_0}\right) - (2\delta_0 + 1)\Re\left(\frac{W_{-0.5}}{b_0}\right)\right]$$

Thus for $\delta_0 \in \Delta_1$, the estimator is asymptotically unbiased and has a CLT. From section C.2, we see that the noise terms are independent and identically distributed with mean

$$\begin{aligned} E\left[\Re\left\{\frac{W_p}{b_0}\right\}\right] &= \Re\left\{\frac{E[W_p]}{b_0}\right\} \\ &= 0 \end{aligned}$$

and variance

$$\begin{aligned} \mathrm{var}\left[\Re\left\{\frac{W_p}{b_0}\right\}\right] &= E\left[\left(\Re\left\{\frac{W_p}{b_0}\right\}\right)^2\right] \\ &= \frac{1}{|b_0|^4}\left\{b_{0r}^2 E\left[(\Re(W_p))^2\right] + b_{0I}^2 E\left[(\Im(W_p))^2\right]\right\} \end{aligned}$$

where $b_0 = b_{0r} + jb_{0I}$ and we have used the fact that the noise terms have independent real and imaginary parts. Now we have

$$\begin{aligned} E\left[(\Re(W_p))^2\right] &= E\left[(\Im(W_p))^2\right] \\ &= \frac{\sigma^2}{2N} \end{aligned}$$

Therefore

$$\begin{aligned} \mathrm{var}\left[\Re\left\{\frac{W_p}{b_0}\right\}\right] &= \frac{1}{|b_0|^4}\left\{b_{0r}^2\frac{\sigma^2}{2N} + b_{0I}^2\frac{\sigma^2}{2N}\right\} \\ &= \frac{\sigma^2}{2N|b_0|^2} \end{aligned}$$

and finally the variance of the estimator is

$$\begin{aligned}
\mathrm{var}\left[\hat{\delta}-\delta\right] &= \mathrm{var}\left[\frac{1}{2}\frac{\delta_0^2-0.25}{\delta_0}\left\{(2\delta_0-1)\Re\left(\frac{W_{0.5}}{b_0}\right)-(2\delta_0+1)\Re\left(\frac{W_{-0.5}}{b_0}\right)\right\}\right] \\
&= \left\{\frac{\delta_0^2-0.25}{\delta_0}\right\}^2\left\{(2\delta_0-1)^2\,\mathrm{var}\left[\Re\left(\frac{W_{0.5}}{b_0}\right)\right]+(2\delta_0+1)^2\,\mathrm{var}\left[\Re\left(\frac{W_{-0.5}}{b_0}\right)\right]\right\} \\
&= \left\{\frac{\delta_0^2-0.25}{\delta_0}\right\}^2\left\{(2\delta_0-1)^2\frac{\sigma^2}{2N|b_0|^2}+(2\delta_0+1)^2\frac{\sigma^2}{2N|b_0|^2}\right\} \\
&= \frac{\sigma^2\left(\delta_0^2-0.25\right)^2\left(4\delta_0^2+1\right)}{4N\delta_0^2|b_0|^2}
\end{aligned}$$

Substituting $|b_0|^2 = \dfrac{\cos^2(\pi\delta_0)}{(\pi\delta_0)^2}$, we get

$$\begin{aligned}
\mathrm{var}\left[\hat{\delta}-\delta\right] &= \frac{\pi^2\sigma^2\left(\delta_0^2-0.25\right)^2\left(4\delta_0^2+1\right)}{4N\delta_0^2\cos^2(\pi\delta_0)} \\
&= \frac{\pi^2\left(\delta_0^2-0.25\right)^2\left(4\delta_0^2+1\right)}{4\rho N\cos^2(\pi\delta_0)}
\end{aligned}$$

Multiplying the asymptotic variance of $\hat{\delta}$ by $\left(f_s/N\right)^2$ gives the asymptotic variance of the frequency estimates. Hence

$$\mathrm{var}\left[\hat{f}-f\right] = \frac{\pi^2\left(\delta_0^2-0.25\right)^2\left(4\delta_0^2+1\right)f_s^2}{4\rho N^3\cos^2(\pi\delta_0)}$$

The ratio of the algorithm variance to the asymptotic CRB is

$$R_{ACRB}^{MOI} = \frac{\pi^4\left(\delta_0^2-0.25\right)^2\left(4\delta_0^2+1\right)}{6\cos^2(\pi\delta_0)} \tag{6.12}$$

The ratio of the variance to the asymptotic CRB is identical to that of the FFCI algorithm. This is the case for region Δ_1 only.

We will now consider the case where $\delta_0 \in \Delta_2$, that is the case where δ_0 is near ±0.5. Restricting δ_0 to Δ_1 we were able to make use of the fact that $|W_p|^2$ in equation (6.9) is of lower order than $\Re\left\{\dfrac{W_p}{b_0}\right\}$. As δ_0 approaches ±0.5, however, that is no longer true.

We now look at the case where δ_0 is tending towards 0.5. The other case is similar. Let us first examine the expression of $Y_{0.5}$,

$$\begin{aligned} Y_{0.5} &= \left| \frac{b_0 \delta_0}{\delta_0 - 0.5} + W_{0.5} \right| \\ &= \left| \frac{b_0 \delta_0}{\delta_0 - 0.5} \right| \sqrt{1 + \frac{(\delta_0 - 0.5)^2}{|b_0|^2 \delta_0^2} |W_{0.5}|^2 - 2 \frac{\delta_0 - 0.5}{\delta_0} \Re\left\{ \frac{W_{0.5}}{b_0} \right\}} \end{aligned}$$

Considering each of the two terms containing $W_{0.5}$ separately, we have

$$\begin{aligned} \lim_{\delta_0 \to 0.5} \frac{(\delta_0 - 0.5)^2}{|b_0|^2 \delta_0^2} |W_{0.5}|^2 &= \lim_{\delta_0 \to 0.5} \frac{\pi^2 (\delta_0 - 0.5)^2}{\cos^2(\pi \delta_0)} |W_{0.5}|^2 \\ &= |W_{0.5}|^2 \\ &= O\left(N^{-1} \ln N\right) \end{aligned}$$

Whereas

$$\begin{aligned} \lim_{\delta_0 \to 0.5} \frac{\delta_0 - 0.5}{\delta_0} \Re\left\{ \frac{W_{0.5}}{b_0} \right\} &= \lim_{\delta_0 \to 0.5} \frac{\delta_0 - 0.5}{|b_0|^2 \delta_0} \Re\left\{ W_{0.5} b_0^* \right\} \\ &= \lim_{\delta_0 \to 0.5} \frac{\pi^2 \delta_0 (\delta_0 - 0.5)}{\cos^2(\pi \delta_0)} \left\{ b_{0r} \Re(W_{0.5}) + b_{0I} \Im(W_{0.5}) \right\} \end{aligned}$$

Equation (6.3) results in

$$b_{0r} = -\frac{\sin(2\pi \delta_0)}{2\pi \delta_0}$$

and

$$b_{0I} = \frac{1 + \cos(2\pi \delta_0)}{2\pi \delta_0},$$

Therefore the limit becomes

$$\lim_{\delta_0\to 0.5}\frac{\delta_0-0.5}{\delta_0}\Re\left\{\frac{W_{0.5}}{b_0}\right\}=\lim_{\delta_0\to 0.5}\frac{\pi^2\delta_0(\delta_0-0.5)}{\cos^2(\pi\delta_0)}\left\{-\frac{\sin(2\pi\delta_0)}{2\pi\delta_0}\Re(W_{0.5})+\frac{1+\cos(2\pi\delta_0)}{2\pi\delta_0}\Im(W_{0.5})\right\}$$

$$=-\lim_{\delta_0\to 0.5}\frac{\pi^2\delta_0(\delta_0-0.5)}{\cos^2(\pi\delta_0)}\frac{\sin(2\pi\delta_0)}{2\pi\delta_0}\Re(W_{0.5})$$

$$+\lim_{\delta_0\to 0.5}\frac{\pi^2\delta_0(\delta_0-0.5)}{\cos^2(\pi\delta_0)}\frac{1+\cos(2\pi\delta_0)}{2\pi\delta_0}\Im(W_{0.5})$$

$$=\Re(W_{0.5})$$

$$=O\left(N^{-\frac{1}{2}}\sqrt{\ln N}\right)$$

Consequently we see that the orders of the terms for $Y_{0.5}$ are preserved and it is still given by

$$Y_{0.5}=\left|\frac{b_0\delta_0}{\delta_0-0.5}\right|\left[1-\frac{\delta_0-0.5}{\delta_0}\Re\left\{\frac{W_{0.5}}{b_0}\right\}\right]+o(1)$$

And now looking at $Y_{-0.5}$, we have

$$Y_{-0.5}=\left|\frac{b_0\delta_0}{\delta_0+0.5}+W_{-0.5}\right|$$

$$=\left|\frac{b_0\delta_0}{\delta_0+0.5}\right|\sqrt{1+\frac{(\delta_0+0.5)^2}{|b_0|^2\delta_0^2}|W_{-0.5}|^2-2\frac{\delta_0+0.5}{\delta_0}\Re\left\{\frac{W_{-0.5}}{b_0}\right\}}$$

Again considering each of the two terms containing the noise separately, we have

$$\frac{(\delta_0+0.5)^2}{|b_0|^2\delta_0^2}|W_{-0.5}|^2=\frac{\pi^2(\delta_0+0.5)^2}{\cos^2(\pi\delta_0)}|W_{-0.5}|^2$$

and

$$\frac{\delta_0+0.5}{\delta_0}\Re\left\{\frac{W_{-0.5}}{b_0}\right\}=\frac{\delta_0+0.5}{|b_0|^2\delta_0}\Re\left\{W_{-0.5}b_0^*\right\}$$

$$=\frac{\pi^2\delta_0(\delta_0+0.5)}{\cos^2(\pi\delta_0)}\frac{\sin(2\pi\delta_0)}{2\pi\delta_0}\Re(W_{-0.5})$$

$$+\frac{\pi^2\delta_0(\delta_0+0.5)}{\cos^2(\pi\delta_0)}\frac{1+\cos(2\pi\delta_0)}{2\pi\delta_0}\Im(W_{-0.5})$$

Let $\zeta = 0.5 - \delta_0$. In order to compare their magnitudes, we need to establish their orders in terms of ζ. Expanding the sine and cosine terms into their Taylor series and using the multiplicative properties of the order notation of (section B.4), we find that

$$\begin{aligned}\frac{(\delta_0 + 0.5)^2}{|b_0|^2 \delta_0^2} |W_{-0.5}|^2 &= \frac{O(1)}{O(\zeta^2)} |W_{-0.5}|^2 \\ &= O(\zeta^{-2}) |W_{-0.5}|^2 \\ &= O(\zeta^{-2} N^{-1} \ln N)\end{aligned}$$

and

$$\begin{aligned}\frac{\delta_0 + 0.5}{\delta_0} \Re\left\{\frac{W_{-0.5}}{b_0}\right\} &= \frac{O(\zeta)}{O(\zeta^2)} \Re(W_{-0.5}) + \frac{O(\zeta)}{O(\zeta^2)} \Im(W_{-0.5}) \\ &= O\left(\zeta^{-1} N^{-\frac{1}{2}} \sqrt{\ln N}\right)\end{aligned}$$

The above indicates that, for a fixed N, as $\delta_0 \to 0.5$ (that is as $\zeta \to 0$), there will be a threshold point where the relative size of the orders is exchanged. We take this threshold point as the boundary between Δ_1 and Δ_2. The threshold can be calculated as follows; we take the term in $|W_p|^2$ to become dominant when it is of "slightly" larger order than the other term. As a definition, we consider a quantity Q_1 to be dominant with respect to a quantity Q_2 if

$$\frac{Q_2}{Q_1} \propto g(N)$$

where $g(N) \to 0$ as $N \to \infty$. We set $g(N) = \frac{1}{\sqrt{\ln N}}$. Applying this to the terms in the expression of $Y_{-0.5}$,

$$\begin{aligned}\frac{O\left(\zeta^{-1} N^{-\frac{1}{2}} \sqrt{\ln N}\right)}{O(\zeta^{-2} N^{-1} \ln N)} &= o(1) \\ &= O\left(\frac{1}{\sqrt{\ln N}}\right)\end{aligned}$$

That is

$$O\left(\frac{\zeta^{-1}N^{-\frac{1}{2}}\sqrt{\ln N}\zeta^{2}N}{\ln N}\right)=O\left(\frac{1}{\sqrt{\ln N}}\right)$$

This implies that

$$\frac{\zeta N^{\frac{1}{2}}}{\sqrt{\ln N}}=\frac{1}{\sqrt{\ln N}}$$

Solving for ζ we get

$$\zeta=N^{-\frac{1}{2}}$$

And the threshold point δ_{0T} is given by

$$\delta_{0T}=0.5-N^{-\frac{1}{2}}$$

For $N=1024$, for instance, the threshold point is 0.469. The definition of the two regions, Δ_1 and Δ_2, is therefore restated as

$$\Delta_1=\left\{\delta_0;\left|\delta_0\right|\le 0.5-N^{-\frac{1}{2}}\right\}$$

and

$$\Delta_2=\left\{\delta_0;0.5-N^{-\frac{1}{2}}<\left|\delta_0\right|\le\frac{1}{2}\right\}$$

Now for δ_0 close to 0.5 (that is $\delta_0\in\Delta_2$), the orders of the terms in $Y_{-0.5}$ are swapped and it is given by

$$Y_{-0.5}=\left|\frac{b_0\delta_0}{\delta_0+0.5}\right|\left[1+\frac{1}{2}\frac{(\delta_0+0.5)^2}{|b_0|^2\delta_0^2}|W_{-0.5}|^2\right]+o(1)$$

We now substitute the expressions of $Y_{0.5}$ and $Y_{-0.5}$ into $\hat{\delta}$ and follow a similar analysis to the case where $\delta_0\in\Delta_1$.

$$\hat{\delta} = \frac{1}{2}\frac{Y_{0.5} - Y_{-0.5}}{Y_{0.5} + Y_{-0.5}}$$

$$= \frac{1}{2}\frac{\left|\frac{b_0\delta_0}{\delta_0 - 0.5}\right|\left\{1 - \frac{\delta_0 - 0.5}{\delta_0}\Re\left(\frac{W_{0.5}}{b_0}\right)\right\} - \left|\frac{b_0\delta_0}{\delta_0 + 0.5}\right|\left\{1 + \frac{1}{2}\frac{(\delta_0 + 0.5)^2}{|b_0|^2\delta_0^2}|W_{-0.5}|^2\right\}}{\left|\frac{b_0\delta_0}{\delta_0 - 0.5}\right|\left\{1 - \frac{\delta_0 - 0.5}{\delta_0}\Re\left(\frac{W_{0.5}}{b_0}\right)\right\} + \left|\frac{b_0\delta_0}{\delta_0 + 0.5}\right|\left\{1 + \frac{1}{2}\frac{(\delta_0 + 0.5)^2}{|b_0|^2\delta_0^2}|W_{-0.5}|^2\right\}} \quad (6.13)$$

Again keeping in mind that $|\delta_0| \le 0.5$, equation (6.11) simplifies to

$$\hat{\delta} = \frac{1}{2}\frac{2\delta_0 - \frac{\delta_0^2 - 0.25}{\delta_0}\left\{\Re\left(\frac{W_{0.5}}{b_0}\right) + \frac{1}{2}\frac{\delta_0 + 0.5}{|b_0|^2\delta_0}|W_{-0.5}|^2\right\}}{1 - \frac{\delta_0^2 - 0.25}{\delta_0}\left\{\Re\left(\frac{W_{0.5}}{b_0}\right) - \frac{1}{2}\frac{\delta_0 + 0.5}{|b_0|^2\delta_0}|W_{-0.5}|^2\right\}}$$

Using identity (6.4) we obtain

$$\hat{\delta} = \frac{1}{2}\left[2\delta_0 - \frac{\delta_0^2 - 0.25}{\delta_0}\left\{\Re\left(\frac{W_{0.5}}{b_0}\right) + \frac{1}{2}\frac{\delta_0 + 0.5}{|b_0|^2\delta_0}|W_{-0.5}|^2\right\}\right]$$

$$\left[1 + \frac{\delta_0^2 - 0.25}{\delta_0}\left\{\Re\left(\frac{W_{0.5}}{b_0}\right) - \frac{1}{2}\frac{\delta_0 + 0.5}{|b_0|^2\delta_0}|W_{-0.5}|^2\right\}\right]$$

$$= \delta_0 + \frac{1}{2}\frac{\delta_0^2 - 0.25}{\delta_0}\left[(2\delta_0 - 1)\Re\left(\frac{W_{0.5}}{b_0}\right) - \frac{1}{2}\frac{(\delta_0 + 0.5)(2\delta_0 + 1)}{|b_0|^2\delta_0}|W_{-0.5}|^2\right]$$

This implies that the estimator is now biased and that the CLT is not easily established. The bias, however, is

$$O\left(\zeta^{-2}N^{-1}\ln N\right) = O\left(\left(N^{-\frac{1}{2}}\right)^{-2}N^{-1}\ln N\right)$$

$$= O(\ln N)$$

whereas the width of the region Δ_2 is $o\left(N^{-\frac{1}{2}}\right)$. Therefore the width of Δ_2 decreases faster than rate of increase of the bias. This ensures validity of the conclusions of the asymptotic analysis for region Δ_1. Finally we have the following theorem,

6.4.2.1 Theorem

Let $\hat{\delta}$ be the estimator of δ_0 as shown in table 6.2 with $\delta_0 \in \Delta_1$ and $\hat{f}$ be defined by

$$\hat{f} = \frac{m + \hat{\delta}}{N} f_s$$

then $\sigma_{MOI}^{-1}\left(\hat{f} - f_0\right)$ is asymptotically standard normal with σ_{MOI} given by

$$\sigma_{MOI}^2 = \frac{f_s^2}{4N^3\rho} \frac{\pi^2\left(\delta_0^2 - 0.25\right)^2\left(4\delta_0^2 + 1\right)}{\cos^2\left(\pi\delta_0\right)}$$

The ratio of the asymptotic variance of the estimator to the asymptotic CRB is identical to the FFCI algorithm and is shown in equation (6.12).

The algorithm was simulated and the ratio of the asymptotic variance to the asymptotic CRB was plotted. Figure 6.4(a) shows the theoretical and simulation curves. The simulation curve clearly exhibits the threshold point where the term in $\left|W_p\right|^2$ becomes dominant. The simulation results were obtained at δ_0 intervals of 0.01 and 10000 runs were averaged at a SNR of 0 dB. The threshold points were found to be around ±0.47 thus closely agreeing with the theoretical value of 0.469. A finer simulation comprising 10000 runs was performed on the interval $[0.4,0.5]$ at a resolution of 0.001. The results are shown in figure 6.4(b). As expected, we see that the transition region is not an abrupt one. The value for the threshold we calculated was based on the assumption of ratio of the orders of the terms being $\frac{1}{\sqrt{\ln N}}$. There are of course infinitely many functions, $g(N)$, satisfying $\lim_{N\to\infty} g(N) = 0$. The lower the order of $g(N)$ is, the closer the threshold point is to the point where the theoretical and simulation curves depart. The choice we made is simply a convenient and logical one.

The performance of the algorithm was also simulated as a function of signal to noise ratio. The results are shown in figure 6.5 along with the performance of the FFCI algorithm of section 6.3 for the purpose of comparison. The results show that the two algorithms perform almost identically. This is expected as the region where the MOI algorithm performs worse, that is region Δ_2, asymptotically vanishes. The FFCI

algorithm has a slightly lower SNR threshold which might be attributed to the worse performance of the MOI algorithm near ±0.5.

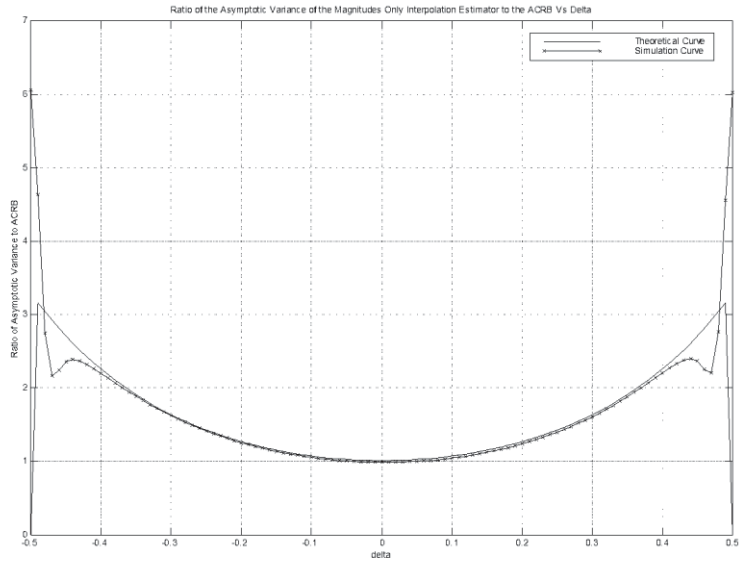

(a)

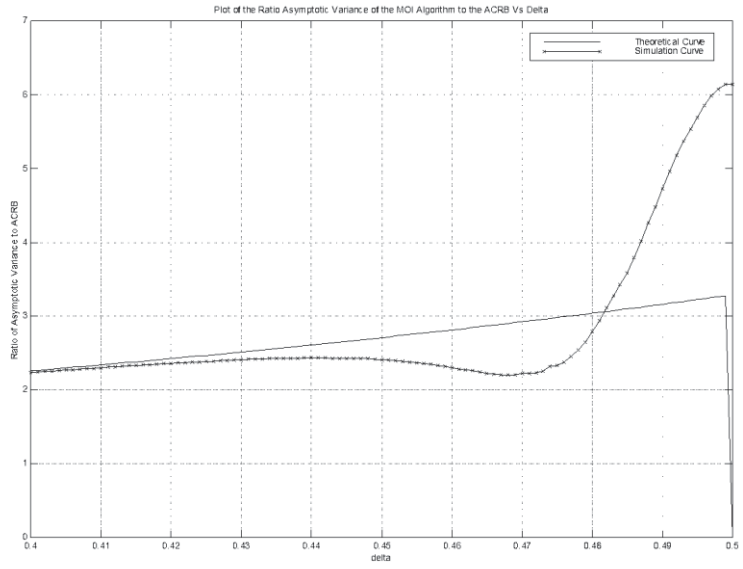

(b)

Figure 6.4 – (a) *Plot of the ratio of the asymptotic variance of the MOI estimator to the asymptotic CRB versus* δ_0. *10000 simulation runs at 0 dB SNR were used in the simulation.* (b) *Zoomed version of (a) on the interval* $[0.4,0.5]$.

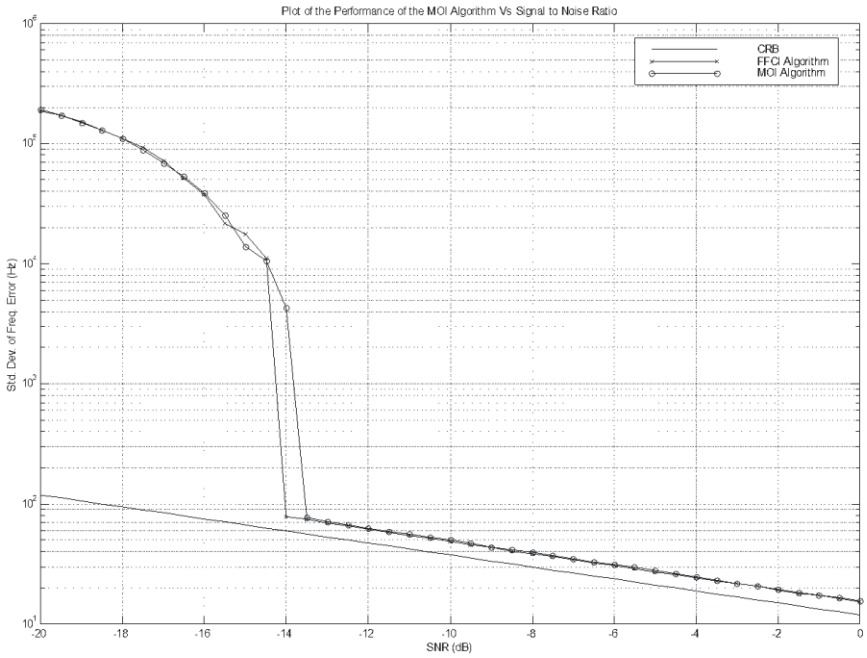

Figure 6.5 – *Plot of the performance of the MOI algorithm as a function of SNR. N = 1024, f_s = 1MHz. 10000 simulation runs were averaged.*

6.5 Interpolation on the Magnitudes Squared of Two Fractional Fourier Coefficients

In this section we look at the possibility of replacing Y_p in the MOI estimator with Y_p^2, [10]. We show that the resulting estimator which we designate as the Magnitude Squared Interpolation (MSI) algorithm is severely biased for δ far from zero. Therefore the MSI algorithm does not significantly improve on the coarse estimation stage. In the next section, however, we propose a modified MSI (MMSI) algorithm that has $O\left(N^{-\frac{3}{2}}\right)$ frequency RMSE.

The MSI algorithm is summarised in the table below

Let $X_p = \sum_{k=0}^{N-1} x(k) e^{-j2\pi \frac{k(m+p)}{N}}$, $p = \pm 0.5$

And

$$Y_p = \left| X_p \right|$$

Calculate

$$\hat{\delta} = \frac{1}{4} \frac{Y_{0.5}^2 - Y_{-0.5}^2}{Y_{0.5}^2 + Y_{-0.5}^2}$$

The frequency estimate is then given by

$$\hat{f} = \left(m + \hat{\delta}\right) \frac{f_s}{N}$$

Table 6.3 – *Magnitudes Squared Interpolation (MSI) on fractional Fourier coefficients estimator.*

6.5.1 Motivation

In order to establish the motivation behind the MSI estimator, we consider $\left|Y_p\right|^2$, in the noiseless case, for $p = \pm 0.5$,

$$\begin{aligned} Y_p^2 &= \left|X_p\right|^2 \\ &= \left| \frac{b_0 \delta_0}{\delta_0 - p} \right|^2 \\ &= \left|b_0\right|^2 \frac{\delta_0^2}{(\delta_0 - p)^2} \end{aligned}$$

Therefore, the ratio in the expression of $\hat{\delta}$ becomes

$$\begin{aligned} \psi &= \frac{Y_{0.5}^2 - Y_{-0.5}^2}{Y_{0.5}^2 + Y_{-0.5}^2} \\ &= \frac{\left|b_0\right|^2 \frac{\delta_0^2}{(\delta_0 - 0.5)^2} - \left|b_0\right|^2 \frac{\delta_0^2}{(\delta_0 + 0.5)^2}}{\left|b_0\right|^2 \frac{\delta_0^2}{(\delta_0 - 0.5)^2} + \left|b_0\right|^2 \frac{\delta_0^2}{(\delta_0 + 0.5)^2}} \\ &= \frac{2\delta_0}{2\delta_0^2 + 0.5} \end{aligned} \tag{6.14}$$

For δ_0 much smaller than ±0.5, we can ignore the term in δ_0^2 in the denominator and ψ becomes equal to $4\delta_0$. However, we see that this is only valid for $|\delta_0| << 0.5$. As we move away from zero, the quotient of (6.14) becomes heavily biased and therefore the algorithm does not constitute an efficient estimator. Figure 6.6 below shows the estimator mapping functions $\psi(\delta)$ for both the MOI and MSI algorithms. We clearly see that the estimator function for the MSI algorithm is non-linear as we move away from zero.

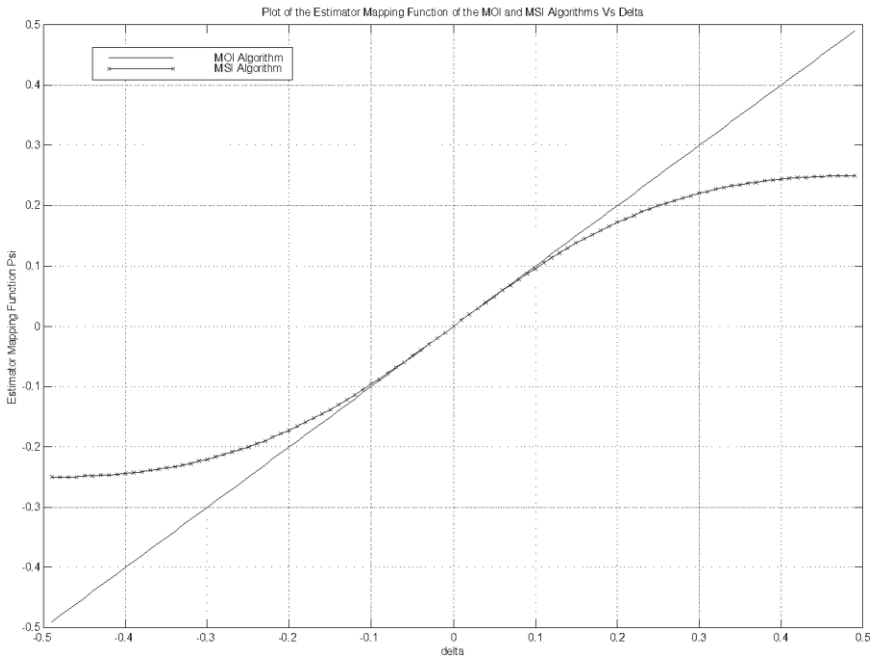

Figure 6.6 – *Plot of the estimator mapping function $\psi(\delta)$ of the MOI and MSI estimators.*

The performance of the algorithm was simulated and the results are presented in figures 6.7 and 6.8 below. Figure 6.7(a) shows the ratio of the variance of the algorithm to the asymptotic CRB. We find that the problem region is about the same width as region Δ_2 of the MOI algorithm but the performance of the MSI algorithm is severely worse there. In fact it can be shown that it is not $O\left(N^{-\frac{3}{2}}\right)$ as the previous algorithms of this chapter

are. Figure 6.7(b) shows a close up of the performance in region Δ_1 (defined in section 6.4.2) along with the ratio of the MOI algorithm. It is interesting to note that the performance of the MSI algorithm seems better than the CRB. However, this is of course not actually the case as the standard deviation of the error does not include the estimator bias. Incorporating the bias we would see that the performance is actually much worse than the MOI algorithm.

Figure 6.8 shows the performance as a function of signal to noise ratio. The plot confirms the results obtained above.

Despite the fact that the performance of the MSI estimator is severly degraded compared to the previous two algorithms, its characteristic of the mapping function does show that the estimator possesses the important property of having a "fixed point" at $\delta_0 = 0$. Furthermore, its variance is comparable to the CRB there. Hence, as we will see in chapter 8, these facts imply that the estimator lends itself to an iterative implementation.

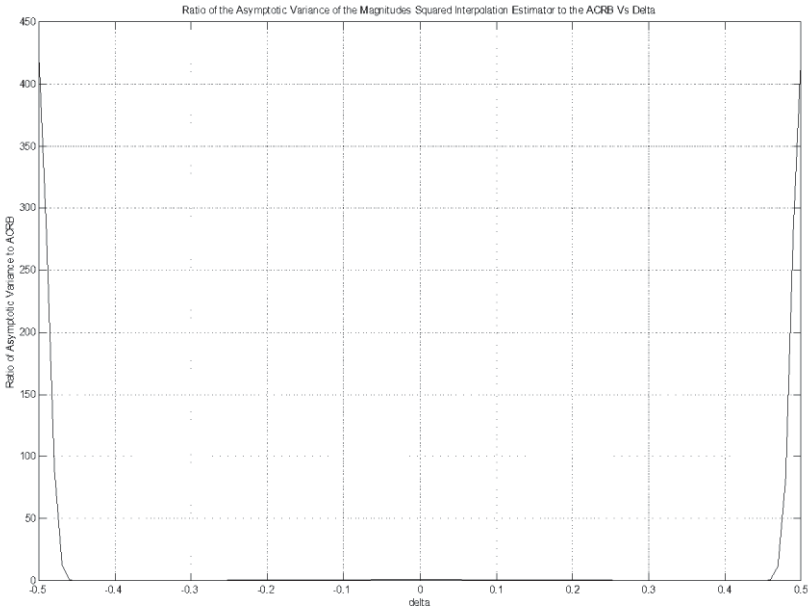

(a)

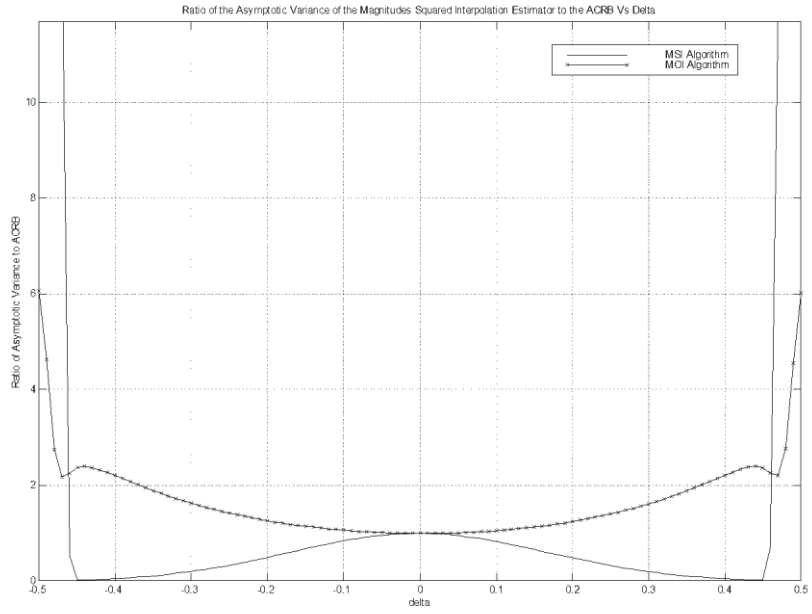

(b)

Figure 6.7 – (a) *Plot of the ratio of the asymptotic variance of the MSI estimator to the asymptotic CRB versus* δ_0. *10000 simulation runs at 0 dB SNR and N=1024 were used in the simulation.* (b) *Zoomed in version of (a).*

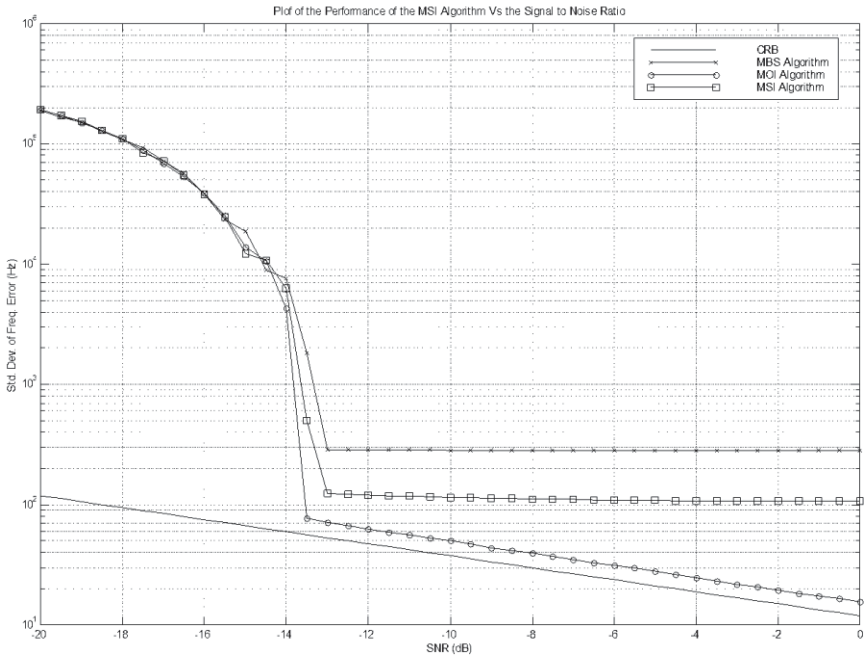

Figure 6.8 – *Plot of the performance of the MSI algorithm as a function of SNR. N = 1024, f_s = 1MHz. Note that the above figure shows the square root of the CRB.*

6.6 Modified Interpolation on the Magnitudes Squared of Two Fractional Fourier Coefficients

In this section, we set out to rectify the problem of the MSI algorithm. The resulting estimator, shown in the table below, will be named the Modified Magnitudes Squared Interpolation (MMSI) algorithm.

Let $X_p = \sum_{k=0}^{N-1} x(k) e^{-j2\pi \frac{k(m+p)}{N}}$, $p = \pm 0.5$

And

$$Y_p = \left| X_p \right|$$

Then Calculate

$$\hat{\delta} = \frac{1}{2} \frac{Y_{0.5}^2 + Y_{-0.5}^2 - 2Y_{0.5}Y_{-0.5}}{Y_{0.5}^2 - Y_{-0.5}^2}$$

The frequency estimate is then given by

$$\hat{f} = \left(m + \hat{\delta}\right) \frac{f_s}{N}$$

Table 6.4 – *Modified Magnitudes Squared Interpolation (MMSI) on fractional Fourier coefficients estimator.*

6.6.1 Motivation

The motivation behind the MMSI algorithm is straightforward and is deduced from equation (6.14) which gives

$$\psi = \frac{Y_{0.5}^2 - Y_{-0.5}^2}{Y_{0.5}^2 + Y_{-0.5}^2} = \frac{2\delta_0}{2\delta_0^2 + 0.5}$$

This can be re-written as

$$\psi \delta_0^2 - \delta_0 + 0.25\psi = 0$$

This is a quadratic in δ_0 which can be solved to give and estimator for δ_0

$$\hat{\delta} = \frac{1 \pm \sqrt{1 - \psi^2}}{2\psi}$$

where careful examination reveals that we need to take the negative sign since $\delta_0 \in [-0.5, 0.5]$. Now substituting the expression for ψ back into that of $\hat{\delta}$, we can express it in terms of the fractional Fourier coefficients, Y_p^2. Therefore,

$$\hat{\delta} = \frac{1-\sqrt{1-\left\{\frac{Y_{0.5}^2 - Y_{-0.5}^2}{Y_{0.5}^2 + Y_{-0.5}^2}\right\}^2}}{2\frac{Y_{0.5}^2 - Y_{-0.5}^2}{Y_{0.5}^2 + Y_{-0.5}^2}} \qquad (6.15)$$
$$= \frac{1}{2}\frac{Y_{0.5}^2 + Y_{-0.5}^2 - 2Y_{0.5}Y_{-0.5}}{Y_{0.5}^2 - Y_{-0.5}^2}$$

as required.

6.6.2 Analysis

The algorithm presented above is in fact equivalent to the MOI algorithm of section 6.4. We will show that expression for $\hat{\delta}$ as shown in equation (6.15) simplifies to equation (6.7).

Consider now equation (6.15), the numerator on the right is a square term while the denominator can be factorised to give

$$\hat{\delta} = \frac{1}{2}\frac{Y_{0.5}^2 + Y_{-0.5}^2 - 2Y_{0.5}Y_{-0.5}}{Y_{0.5}^2 - Y_{-0.5}^2}$$
$$= \frac{1}{2}\frac{(Y_{0.5} - Y_{-0.5})^2}{(Y_{0.5} - Y_{-0.5})(Y_{0.5} + Y_{-0.5})}$$
$$= \frac{1}{2}\frac{Y_{0.5} - Y_{-0.5}}{Y_{0.5} + Y_{-0.5}}$$

The performance of the MMSI estimator is, therefore, identical to that of the MOI estimator and is governed by theorem 6.4.2.1. This was verified by simulations. Figure 6.9 shows the resulting ratio of the asymptotic variance to the asymptotic CRB. A Monte Carlo simulation of 10000 runs at a signal to noise ratio of 0dB was performed. The figure also shows the performance of the MOI algorithm for comparison purposes. We see that the two curves are almost identical, taking into account the statistical variances between the runs. Figure 6.10 shows the performance of the algorithm as a function of the SNR. The standard deviation of the frequency error of the MOI estimator is also shown. The two curves coincide, indicating identical performances of the two algorithms.

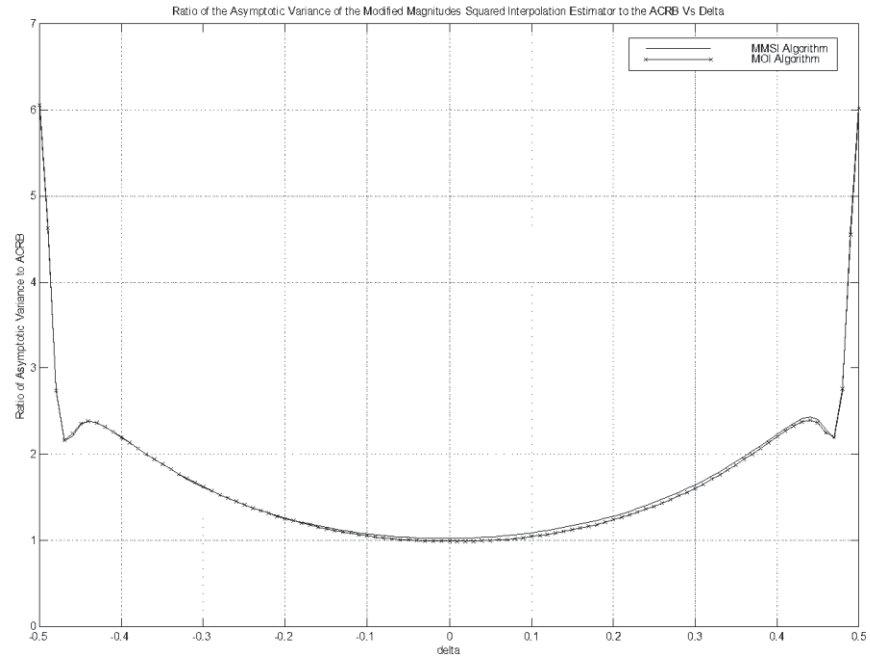

Figure 6.9 – *Plot of the ratio of the asymptotic variance of the MMSI estimator to the asymptotic CRB versus δ_0. 10000 simulation runs at 0 dB SNR and N=1024 were used in the simulation.*

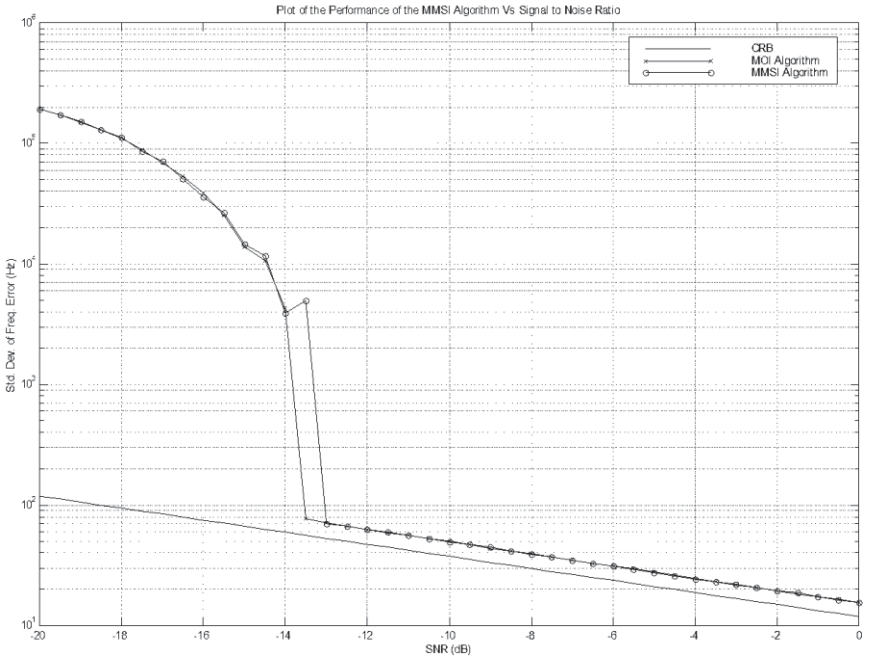

Figure 6.10 – *Plot of the performance of the MMSI algorithm as a function of SNR. N = 1024, f_s = 1MHz. 10000 simulation runs were averaged.*

6.7 Conclusion

We have in this chapter introduced a new class of frequency estimators that interpolate on the fractional Fourier coefficients of the sinusoidal signal. The new estimators were analysed and their performances confirmed using simulations. The FFCI algorithm has the best performance among the new estimators due to its regular behaviour near ±0.5. The new estimators were also shown to have similar average variances to the known estimators of chapter 5. However, unlike those estimators, the new algorithms exhibit their best performance at $\delta_0 = 0$ which will be shown in chapter 8 to be a fixed point. An estimator with a mapping function, $\hat{\delta} = \psi(\delta)$, has a fixed point $\tilde{\delta}$ if $\psi(\tilde{\delta}) = \tilde{\delta}$. This enables the iterative implementation of the algorithms to result in an improvement in their performance. The result is that the iterative estimators almost attain the Cramer-Rao lower bound of the frequency estimation from N samples. In fact the asymptotic variance of the iterative estimates will be shown to be only 1.0147 times the CRB.

Chapter 7

Iterative Frequency Domain Frequency Estimation

7.1 Introduction

We saw in chapter 5 that the resolution of the MBS algorithm can be improved by padding the data samples with zeroes. This, however, is a costly way of refining the frequency estimate. In chapters 5 and 6 we discussed fine frequency estimators that interpolate on the Fourier coefficients. In this chapter as well as in chapter 8, we examine iterative methods for refining the frequency estimate. The estimators we consider iterate on each block of data samples to give a frequency estimate. Frequency estimates obtained from successive data blocks remain independent.

Quinn and Fernandes, in [14], proposed an iterative time domain method to estimate the frequency of a sinusoidal signal in noise. Their technique, discussed in section 2.5.4 iteratively fits an ARMA(2,2) model to the available data.

In this thesis we are mainly concerned with frequency domain methods. Zakharov and Tozer, in [86], suggested a method of iteratively refining the frequency estimate using a binary search on the Fourier coefficients. Their technique is simple and does not need any non-linear operations. The entire algorithm relies only on multiply, add and compare operations. This makes the algorithm suitable for real time DSP implementation. However, the data samples must be padded with zeroes to give a performance that approaches the CRB.

The chapter is organised as follows; in the next section, we present the dichotomous search algorithm giving an explanation for the need to pad the data with zeroes. Guided by the insight of section 7.2 we propose a modified algorithm in section 7.3 that does away with the zero-padding requirement. In 7.4 we discuss a hybrid algorithm, [120], that combines an interpolation algorithm with the dichotomous search. In section 7.5

we review other variants of the dichotomous search. Finally section 7.6 concludes the chapter.

7.2 Dichotomous Search of the Periodogram Peak

In chapter 4 we explained that the size N DFT samples the Fourier transform at N equally spaced points. Therefore, a natural method to improve the MBS resolution is to sample the DFT at finer intervals and choose the maximum. This, as explained in section 5.2, can be implemented by padding the available data samples with enough zeroes to obtain a resolution comparable to the CRB. The number of zeroes required to approach the CRB depends the SNR. However, the FFT requires $\frac{N}{2}\log_2 N$ operations, a number that quickly becomes large as N increases. For instance, for 1024 data samples and a sampling frequency $f_s = 1\,\text{MHz}$, the CRB is approximately 11.82 Hz at a SNR of 0dB. Thus, to obtain this resolution, the number of sampling points of the spectrum needs to be

$$\frac{1\times 10^6}{11.82} = 84603$$

and the data must be padded with $84603 - 1024 = 83579$ zeroes. The resulting number of operations is 692410 operations compared to 5120 for a 1024-FFT.

Another possible implementation of the peak location strategy was proposed by Zakharov and Tozer in [86]. A binary search method is employed. Denote the index of the periodogram maximiser by m. Let the magnitude of bin m be Y_0 and those of the bins either side of it be Y_{-1} and Y_1. We deduce from the sinc nature of the periodogram of a sinusoid (refer to section 5.2) that $Y_{-1} > Y_1$ if the true frequency lies in the interval $\left[\left(m-\frac{1}{2}\right)\frac{f_s}{N}, m\frac{f_s}{N}\right]$, $Y_1 > Y_{-1}$ otherwise. Therefore, comparing Y_{-1} and Y_1 we can select the half bin that the true frequency lies in. Having narrowed the search region by half, we can repeat the procedure, until the required resolution is reached. The resolution after the i^{th} iteration is $\frac{f_s}{N2^{i-1}}$. Zakharov and Tozer found, however, that it is necessary to pad the data with zeros in order to achieve a performance comparable to

the CRB. Let L denote the data length after zero-padding. They showed through simulation that L needed to be equal to $1.5N$. The algorithm is summarized in the table below:

Let	$L = \gamma N$
Calculate	$\mathbf{X} = FFT(\mathbf{x}, L)$
And	$Y(n) = \lvert X(n) \rvert$
Find	$m = \arg\max_n \{Y(n)\}$
Set	$\Delta = 1$ $Y_{-1} = Y(m-1),\ Y_0 = Y(m)$ *and* $Y_1 = Y(m+1)$
for Q iterations do	
	$\Delta = \Delta/2$
	if $Y_1 > Y_{-1}$
	then $Y_{-1} = Y_0$ *and* $m = m + \Delta$
	else $Y_1 = Y_0$ *and* $m = m - \Delta$
	$Y_0 = \left\lvert \sum_{k=0}^{N-1} x(k) e^{-j2\pi \frac{km}{L}} \right\rvert$
Finally calculate	
	$\hat{f} = 2\pi \frac{m}{L} f_s$

Table 7.1 – *Dichotomous Search of the Periodogram Peak frequency estimator.*

Simulation results with $\gamma = 1$ and $\gamma = 1.5$ were obtained. Figure 7.1 shows the ratio of the algorithm variance to the asymptotic CRB for $\gamma = 1$. We see that, after one iteration, the error variance is quite large around $\delta_0 = 0$. This is easily explained by considering that the estimate is set to $\left(m + \frac{1}{2}\right)\frac{f_s}{N}$ if $Y_1 > Y_{-1}$ and $\left(m - \frac{1}{2}\right)\frac{f_s}{N}$ otherwise. For δ_0 near 0, both Y_{-1} and Y_1 are very small and therefore dominated by noise. Therefore, the

decision is almost purely driven by noise and is therefore almost random. That is the two possibilities are practically equally likely. The resulting error is then

$$\hat{\delta} - \delta_0 = \begin{cases} 0.5 - \delta_0 & \textit{if } Y_1 > Y_{-1} \\ -0.5 - \delta_0 & \textit{otherwise} \end{cases}$$

Therefore the variance is

$$\begin{aligned} \mathrm{var}\left[\hat{\delta} - \delta_0\right] &= \frac{1}{2}\left\{(0.5 - \delta_0)^2 + (-0.5 - \delta_0)^2\right\} \\ &= 0.25 + \delta_0^2 \end{aligned}$$

The ratio of the variance to the asymptotic CRB is

$$\frac{0.25(2\pi)^2 N\rho}{6} \tag{7.1}$$

At a SNR of 0dB, the variance is about 1685 times larger than the asymptotic CRB. This agrees very well with the simulation results in figure 7.1(a), the simulation value being 1684 at $\delta_0 = 0$. Figure 7.1(b) displays a zoomed version of 7.1(a). This shows more clearly the simulation results for 4 and 10 iterations. The curve obtained after 4 iterations shows as expected a number of peaks, in fact exactly 8. Note that a peak occurs at $\delta_0 = 0$ whereas the eighth is divided in half between $\delta_0 = 0.5$ and $\delta_0 = -0.5$. This is due to the circular nature of the FFT. The "peak" at zero is almost flat and stretched between the two adjacent peaks. This is due to the wide peak of the first iteration. The curve resulting from 10 iterations, gives us some insight into the poor performance of the search algorithm with no zero padding. The multiple peaks seen after four iterations disappear and are replaced by two peaks symmetrically positioned about zero. In section 7.3 we use this observation to offer an explanation for the need to pad the data with zeroes.

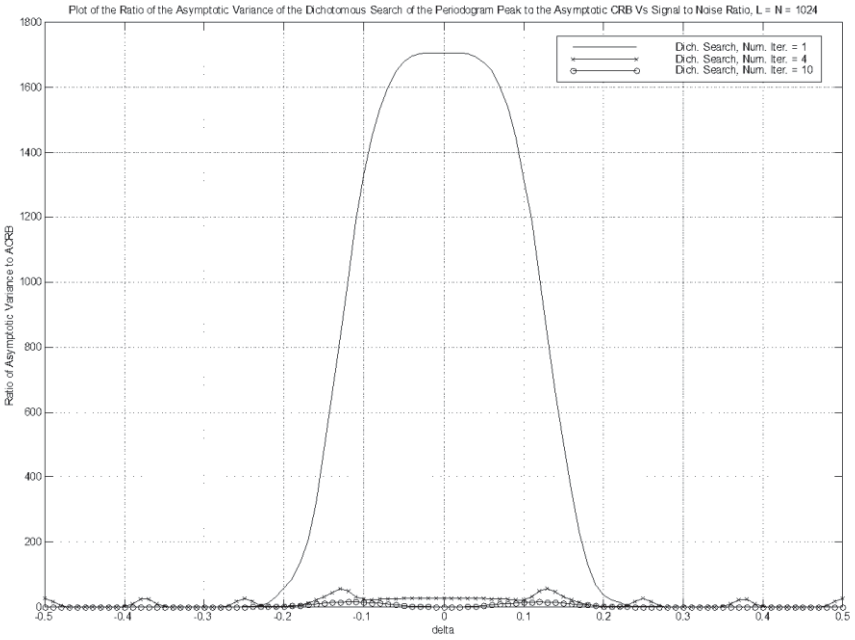

(a)

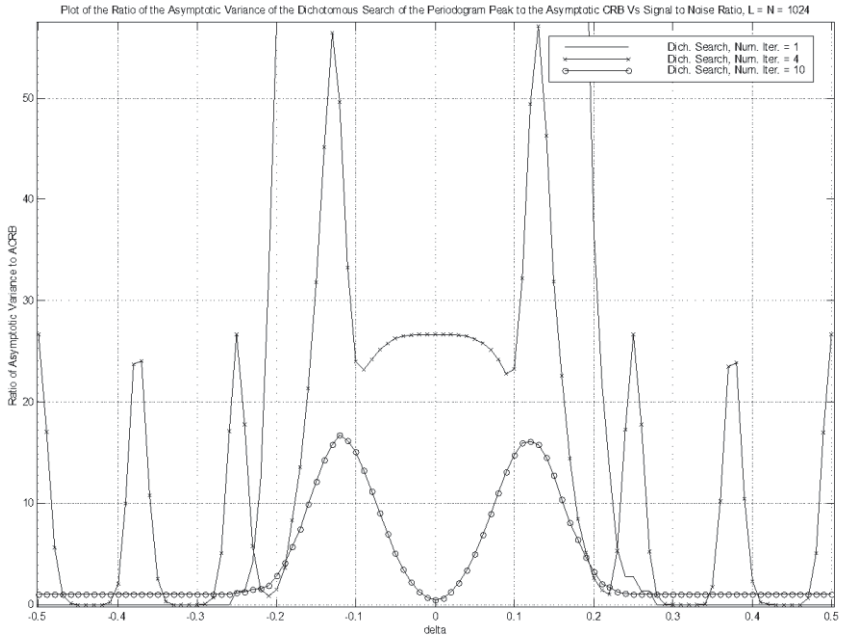

(b)

Figure 7.1 – *Plot of ratio of the variance of the Dichotomous Search algorithm, with L = N = 1024, to the ACRB as a function of* δ_0. (a) *shows the performance for 1, 4 and 10 iterations.* (b) *is a zoomed in version of* (a). *5000 simulation runs were averaged.*

Figure 7.2 shows the performance of the algorithm as a function of signal to noise ratio. We see that, although the algorithm improves on the performance of the Maximum Bin Search, it does not achieve the CRB. In fact we see that as the signal to noise ratio increases the simulation and CRB curves depart. This is in part due to the remaining bias. Also, the number iterations required to reach the CRB increases with increasing SNR.

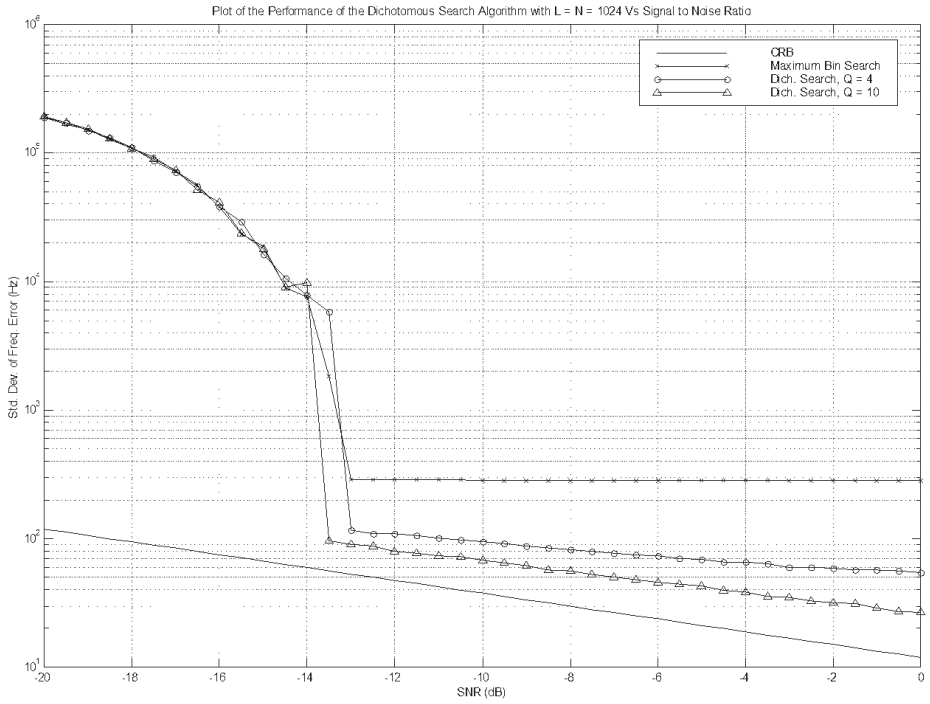

Figure 7.2 – *Plot of the performance of the Dichotomous Search algorithm, with L = N = 1024, as a function of SNR. 10000 simulation runs were averaged.*

Figures 7.3 and 7.4 below present the performance of the dichotomous search algorithm with $\gamma = 1.5$, that is with the zero-padded data sequence having a length $L = 1.5N$. The resulting performance shows an obvious improvement over the case where $L = N$. This is due to the fact that the padded algorithm overcomes the problem encountered around zero.

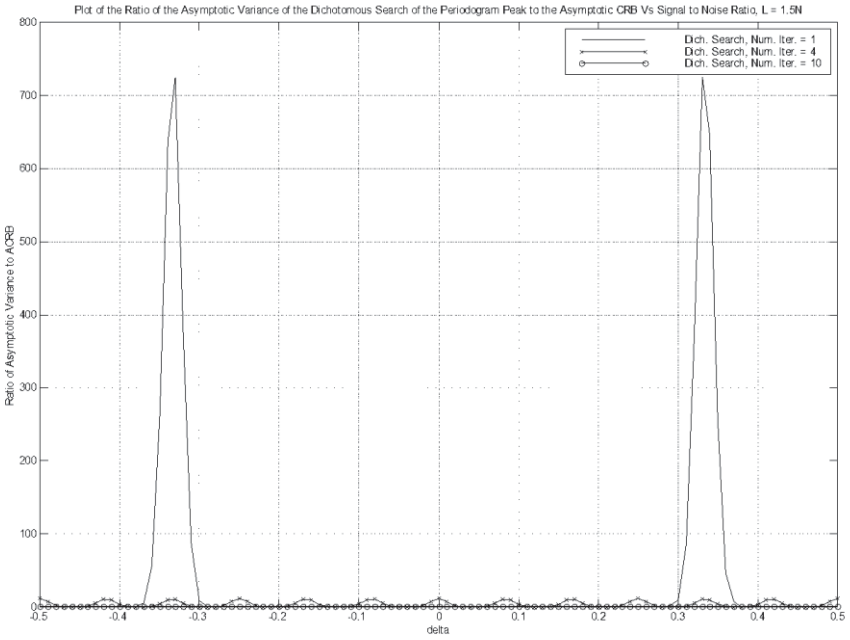

(a)

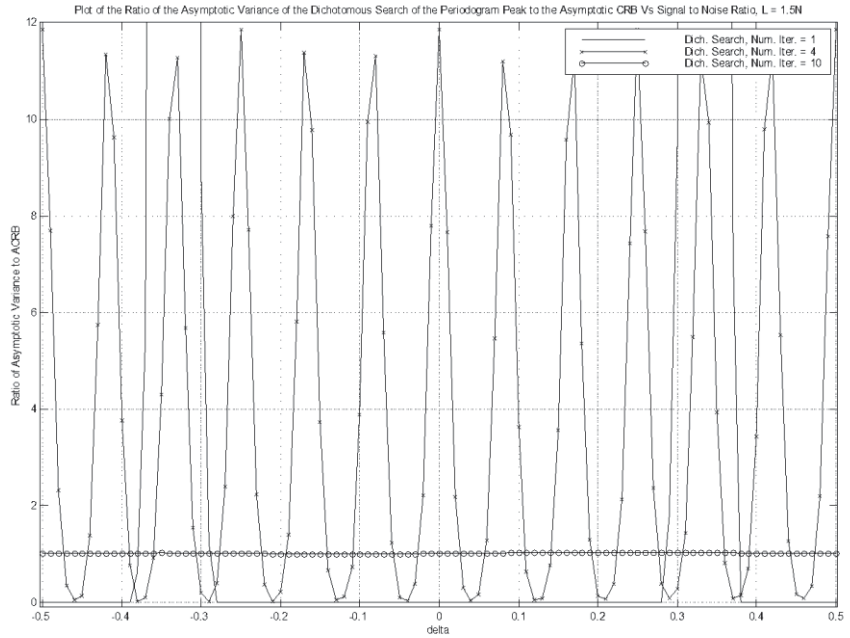

(b)

Figure 7.3 – *Plot of ratio of the variance of the Dichotomous Search algorithm to the asymptotic CRB, with L = 1.5N, to the ACRB as a function of* δ_0. (a) *shows the performance for 1, 4 and 10 iterations.* (b) *is a zoomed in version of* (a). *5000 simulation runs were averaged.*

Figure 7.4 below shows the performance of the padded dichotomous search as a function of the SNR. We see that, for the range of SNR used in the simulation, 10 iterations are sufficient for the simulation curve to virtually lie on the CRB. However, as the SNR increases, the resolution after Q iterations asymptotes to $\frac{f_s}{\sqrt{12}L2^{Q-1}}$. For $Q=4$, this is equal to a standard deviation of the frequency error equal to 23.4924 Hz. This is confirmed by the simulation results. This also implies that the curve corresponding to $Q=10$ will eventually diverge from the CRB curve. The point where the two curves diverge is itself dependent on the number of iterations. As the number of iterations approaches infinity so does the divergence point and therefore the two curves practically coincide above the breakdown threshold.

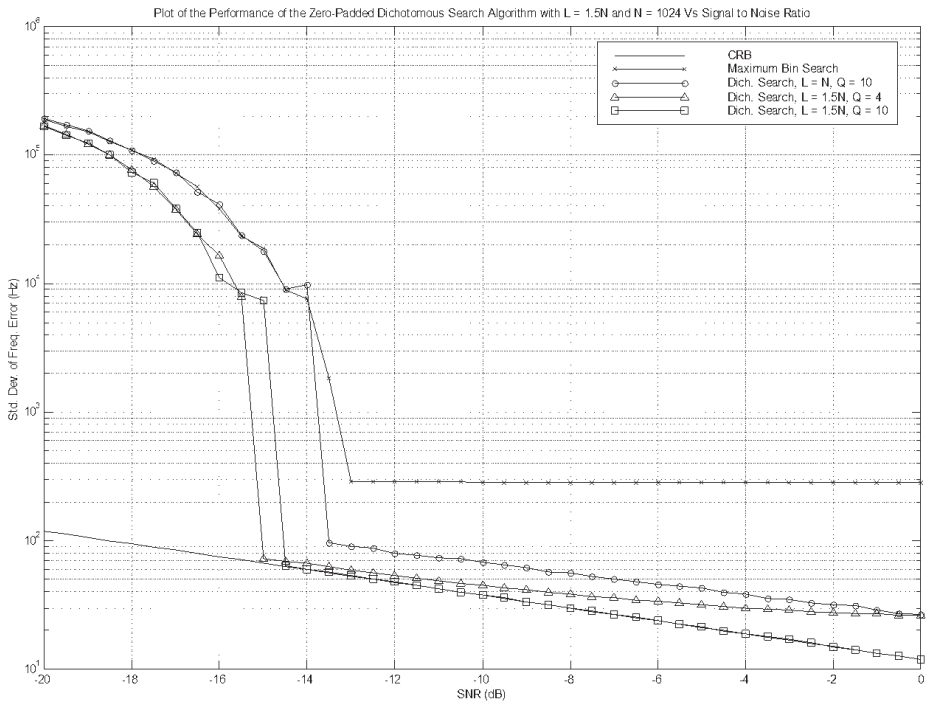

Figure 7.4 – *Plot of the standard deviation of the frequency error of the zero-padded dichotomous search algorithm, with L = 1.5N, as a function of SNR. 10000 simulation runs were averaged.*

7.3 Modified Dichotomous Search of the Periodogram peak

The plot of the ratio of the variance of the non-padded dichotomous search to the asymptotic CRB, shown figure 7.1, provides us with clues to the poor performance of the estimator in the case of no zero padding. The performance is, as discussed in the previous section, worst for δ_0 near zero due to the degraded effective signal to noise ratio of Y_1 and Y_{-1}. This severely affects the performance of the algorithm after the first iteration. The width of the lobe, D, in the characteristic curve is dependent on the rate of change of the differential between Y_1 and Y_{-1} as a function of δ_0. The smaller the rate of change is, the larger the width of the lobe. Two equidistant bins from the true frequency are equal and their differential is zero. This produces the worst case performance. The quicker the differential moves away from zero as we move away from the true frequency of the signal, the narrower the lobe is. Hence we can write,

$$D \propto \left[\frac{d}{d\delta_0} \left(Y_1 - Y_{-1} \right) \right]^{-1} \tag{7.2}$$

A plot of D as a function of δ_0 for both the non-padded ($L = N = 1024$) and padded ($L = 1.5N$) cases is shown below.

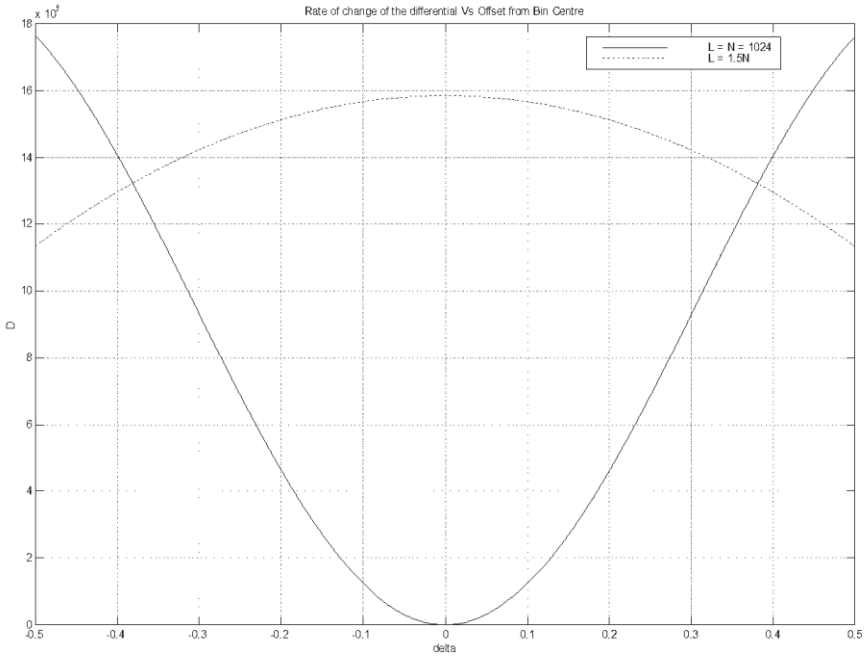

Figure 7.5 – *Plot of rate of change of the differential, D as a function of the offset from the bin centre* δ_0.

For the non-padded case, the derivative shown above is lowest at $\delta_0 = 0$ whereas for the padded case it has a maximum there. It must be noted, however, that $\delta_0 = 0$ does not coincide for both cases as the frequency axis is divided differently in each case.

This also explains why the padded algorithm works better. The zero padded periodogram effectively samples the spectrum more densely. The bin width is thus reduced to $\frac{f_s}{L}$ instead of $\frac{f_s}{N}$ which prevents two bins either side of the maximum being equal and very close to zero as this only occurs at a separation of $2\frac{f_s}{N}$.

The poor performance near zero after the first iteration in the non-padded case is carried through the following iterations and eventually gives the characteristic curve seen after 10 iteration, (figure 7.1(b)). The problem arises from the fact that the choice at the first iteration is made between two intervals with only one point in common. This implies that, although the performance is very poor for $\delta_0 = 0$, the resulting error is reduced in subsequent iterations since $\delta_0 = 0$ belongs to both sub-intervals. Therefore, if $\delta_0 = 0$,

the same error is incurred after the first iteration regardless of which sub-interval is chosen. However, this is not the case for points removed from zero but still close enough to it that they lie in the central lobe of the curve corresponding to one iteration in figure 7.1(a). These points suffer from a degraded performance due to the high probability of choosing the incorrect interval at the first iteration. As these points are removed from the chosen interval in the event of an incorrect decision, the resulting error is not recoverable in subsequent iterations. As we move away from zero, the size of the error increases due to the increasing distance from the complementary interval. The probability of an error on the other hand, decreases with the distance of the true frequency from zero. Therefore the combined effect is to see the error increasing until it reaches a maximum, then decreasing as the probability the error occurring decreases.

Guided by this insight we propose a method of improving the performance of the dichotomous search algorithm without resorting to padding the data with zeroes. We achieve this by using overlapping intervals for the first iteration. This effectively gives the algorithm another chance to recover the erroneous choice that might have been made during the first iteration. The degree of the overlap must at least account for the width of the peaks seen in figure 7.1(b) in the curve corresponding to 10 iterations. Using an overlap of half a bin width, for instance, we set Y_{-1} to $Y_{-0.25}$ if $Y_1 > Y_{-1}$, and Y_1 to $Y_{0.25}$ otherwise. The reader should always keep in mind that the index notation is relative to the maximum bin m. The resulting algorithm, called modified dichotomous search, is shown in the table below.

Calculate $\mathbf{X} = FFT(\mathbf{x}, N)$

And $Y(n) = |X(n)|$

Find $m = \arg\max_n \{Y(n)\}$

Set $\Delta = 0.75$
$Y_{-1} = Y(m-1),\ Y_0 = Y(m)$ *and* $Y_1 = Y(m+1)$

if $Y_1 > Y_{-1}$

then $Y_{-1} = \left| \sum_{k=0}^{N-1} x(k) e^{-j2\pi \frac{k(m+1-2\Delta)}{N}} \right|$ *and* $m = m + 1 - \Delta$

else $Y_1 = \left| \sum_{k=0}^{N-1} x(k) e^{-j2\pi \frac{k(m-1+2\Delta)}{N}} \right|$ *and* $m = m - 1 + \Delta$

for Q iterations do

$$Y_0 = \left| \sum_{k=0}^{N-1} x(k) e^{-j2\pi \frac{km}{L}} \right|$$

$\Delta = \Delta / 2$

if $Y_1 > Y_{-1}$

then $Y_{-1} = Y_0$ *and* $m = m + \Delta$

else $Y_1 = Y_0$ *and* $m = m - \Delta$

Finally calculate

$$\hat{f} = 2\pi \frac{m}{L} f_s$$

Table 7.2 – *Modified Dichotomous Search of the Periodogram Peak frequency estimator.*

Setting Δ to 0.75 produces an overlap of half a bin between the two sub-intervals. The overlap is in fact given by 2Δ-1. If Δ is set to 1 we see that there is no change from the original algorithm as the "if" statement outside the loop does not have any effect. It simply retains things as they are set. This implies that the original algorithm is a special case of the implementation shown in the table above. The performance of the modified dichotomous search algorithm was simulated and is shown in the figure below. Two

cases are shown, the first referred to by Alg1 was obtained with Δ set to 0.75 whereas the second, Alg2, had Δ = 0.6. 10000 simulation runs were averaged. The simulation results show that the new algorithm has a performance comparable to the CRB without the need for 0-padding the data. The case with Δ = 0.6 shows a slightly better threshold performance than the other case.

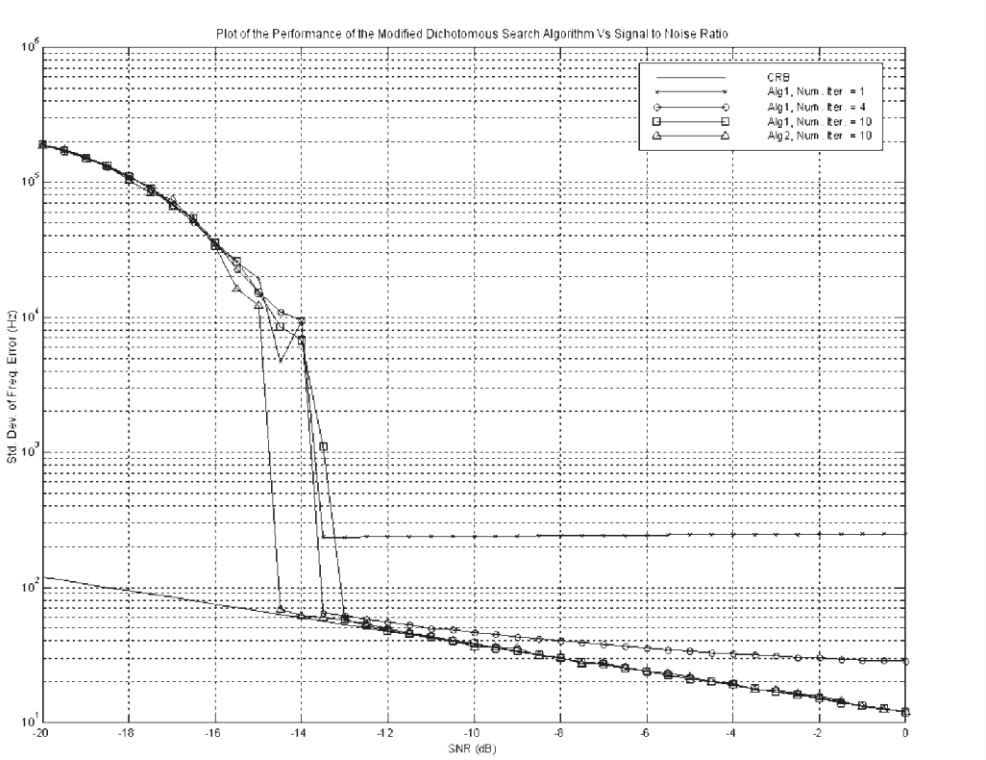

Figure 7.6 – *Plot of standard deviation of the frequency error of the Modified Dichotomous Search algorithm, with Δ = 0.75 and Δ = 0.6, as a function of SNR. 10000 simulation runs were averaged.*

7.4 Guided Search of the Periodogram Peak Algorithm

In this section we briefly present and discuss the Guided Search algorithm which we proposed in [120]. In the previous section we implemented and simulated a strategy for overcoming the problem of the dichotomous search algorithm near the bin centre. The large variance of the error in the estimates in this area prevents the algorithm from being of order $N^{-\frac{3}{2}}$ and reaching the CRB. An algorithm such as Quinn's first or second

estimator, however, is already $O\left(N^{-\frac{3}{2}}\right)$, but does not quite reach the CRB either. Therefore, it seems logical to use Quinn's algorithm (or any other algorithm that is $O\left(N^{-\frac{3}{2}}\right)$) to initialise the dichotomous search in order to speed it up and improve its performance. In [120], Quinn's first algorithm was used. This eliminates the need to pad the data with zeroes.

The Guided Search algorithm, as given in the paper, is shown in the table below.

Calculate $\mathbf{X} = FFT(\mathbf{x}, N)$ *And* $Y(n) = |X(n)|$

Find $m = \arg\max_n \{Y(n)\}$

Set $\alpha_l = \Re\left\{\frac{X_l}{X_0}\right\}$, for $l = \pm 1$ *Then Calculate* $\hat{\delta}_l = \frac{l\alpha_l}{\alpha_l - 1}$

If $\hat{\delta}_{-1} > 0$ *and* $\hat{\delta}_1 > 0$ *then set*

$m = m + \hat{\delta}_1$

otherwise

$m = m + \hat{\delta}_{-1}$

Set $\Delta = 0.1$

$Y_{-1} = Y(m-1)$, $Y_0 = Y(m)$ *and* $Y_1 = Y(m+1)$

for Q iterations do

$\Delta = \Delta/2$

if $Y_1 > Y_{-1}$

then $Y_{-1} = Y_0$ *and* $m = m + \Delta$

else $Y_1 = Y_0$ *and* $m = m - \Delta$

$$Y_0 = \left| \sum_{k=0}^{N-1} x(k) e^{-j2\pi \frac{km}{L}} \right|$$

Finally calculate

$$\hat{f} = 2\pi \frac{m}{L} f_s$$

Table 7.3 – *Guided Search of the Periodogram Peak frequency estimator.*

The initialising estimator must be computationally simple to produce computational savings and make the guided search algorithm worth while. After the initialising estimate is obtained, the starting interval Δ must be set to a value that takes into account the initialising algorithm's resolution. The worse the performance of the initialising algorithm the larger the initial value of Δ. With Quinn's first algorithm used to initialise the estimator, we found through simulations, that a value of 0.1 for Δ gives a performance comparable to the CRB in only 4 iterations. The simulations results are shown in the figure below. The standard deviation of the frequency error was obtained from 10000 simulations and is plotted against the signal to noise ratio. The results show that only 4 iterations are needed for the algorithm performance to approach the CRB curve.

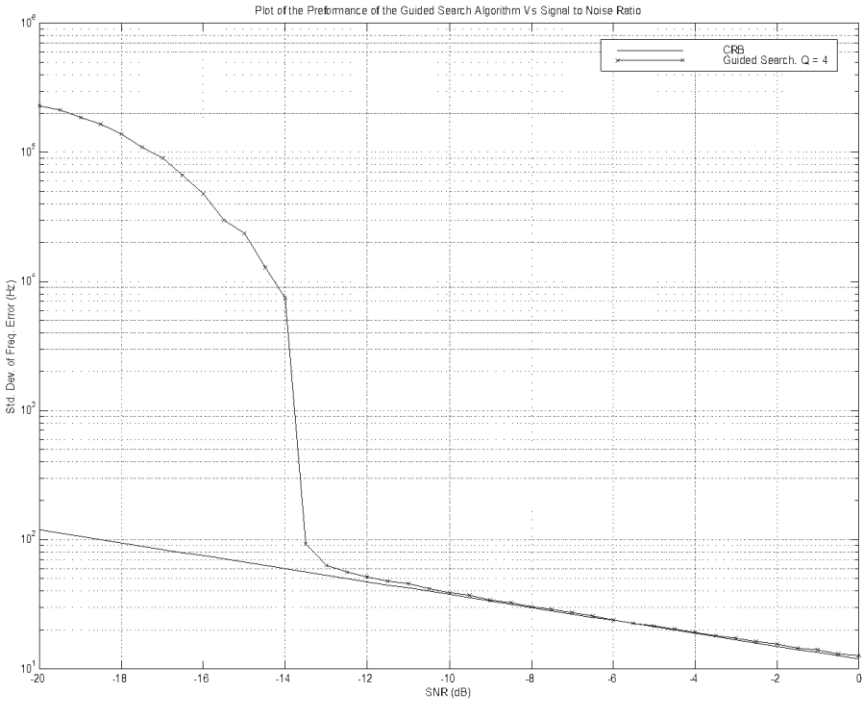

Figure 7.7 – *Plot of standard deviation of the frequency error of the Guided Search algorithm as a function of SNR. The Guided Search was run for 4 iterations. 10000 simulation runs were averaged.*

7.5 Other Hybrid Algorithms

Zakharov *et al*, in [86], employ a similar strategy to the Guided Search of the periodogram peak algorithm. They propose a number of modifications to the dichotomous search algorithm in order to improve its performance and reduce its computational complexity. The algorithms we discuss in this section assume a coarse search step is used to narrow the acquisition range and provide the initialization for the estimator. The usual form of the coarse search is the MBS algorithm. In this case the MBS is most likely obtained from a zero-padded sequence as was necessary for the Dichotomous search algorithm.

The first of the fine estimators presented in [85] was called the Parabolic Interpolation and Dichotomous Search. Equation (4.6) shows the form of the periodogram samples. Using the fact that they follow a sinc-shape, one can fit a parabola to three "closely spaced" DFT coefficients, where closely spaced means that their separation is not larger than a bin width. Although Zakharov *et al* do not acknowledge the reference, this idea was first proposed by Holm in [121] for the Cospas-Sarsat application. In the Cospas-Sarsat system, the estimated Doppler curve for a pass is analysed in order to allow for the location of the distress beacon to be determined (see section 9.2). The fine frequency estimator is of the form,

$$\hat{\delta} = \frac{Y_1^2 - Y_{-1}^2}{2\left(-Y_1^2 + 2Y_0^2 - Y_{-1}^2\right)} \tag{7.3}$$

Zakharov *et al*, however, point out that the performance of the interpolation on the magnitudes is better than that of the interpolation on the magnitudes squared. The bias is larger in the case of the magnitudes squared and the effect of the noise is worse as the lower order terms rapidly come up near the estimator problem area where the singularity occurs. The algorithm also requires an amount of zero padding to avoid the problem area around zero.

Holm discusses the estimator bias and suggests that a Gaussian fit results in a lower bias. The Gaussian fit can be implemented using logarithmic inputs in equation (7.3). The resulting bias is, according to Holm, reduced to about 2% of a bin width.

Zakharov *et al* then proposed combining the quadratic interpolation algorithm with the dichotomous search. The smaller the spacing of the three Fourier coefficients the better the quadratic fit. Therefore, this method consists of stopping the dichotomous search

when the frequency step is small enough that the quadratic interpolation provides a good fit and a small frequency error. The resulting algorithm represents a reverse strategy to the guided search algorithm where the interpolation algorithm was used to initialize the dichotomous search in order to reduce the number of iterations required to achieve a small frequency step.

The search in the Dichotomous-Parabolic interpolation hybrid algorithm requires only 4 iterations to converge as opposed to 10 iterations for the original dichotomous search algorithm.

Another variant suggested by Zakharov *et al* is the Two-rate Spectral Estimation and Dichotomous Search algorithm. This effectively consists of dividing the data into L shorter frames of length R. In the following discussion we keep as much of the terminology of [85] as is possible. A number of DFT coefficients on a finer scale are calculated for all of the R frames. The DFT coefficients from each frame that correspond to the same frequency are summed. The dichotomous search is then applied to the resulting periodogram to obtain a fine frequency estimate. The details of the procedure are given below.

Suppose that the unknown frequency is restricted to a region of width F (using a coarse search algorithm). Setting a fine frequency resolution of Δf, the new frequency region is then divided into M bins where $M = \left\lceil \frac{F}{\Delta f} \right\rceil$. Here we must note that the authors have used $M = \frac{F}{\Delta f}$, but the correct form must involve rounding up to the nearest integer. The following DFT coefficients are then calculated,

$$X(n,l) = \sum_{k=lR}^{(l+1)R-1} x(k) e^{-j2\pi kn\Delta f}, n = -\frac{M}{2} \cdots \frac{M}{2}$$

and

$$Y(n) = \left| \sum_{l=0}^{L-1} X(n,l) \right|$$

The maximum of the periodogram is found and is used to initialise the dichotomous search. The search algorithm requires a small number of iterations to converge to the required resolution.

Another hybrid estimator that is aimed at further reducing the computational load is a combination of the three techniques. It is termed the two-rate spectral search, dichotomous search and parabolic interpolation. It simply consists of implementing the estimator discussed in the previous paragraph and stopping the dichotomous search when the residual resolution is good enough for the parabolic interpolation to give a good frequency estimate.

7.6 Conclusion

In this chapter we have reviewed a number of iterative fine frequency estimation methods that are based on a binary search technique. We have presented and discussed the dichotomous search of the periodogram peak algorithm and offered an insight into the need to pad the data with zeroes in order to approach the CRB. We then suggested a modified dichotomous search algorithm that does away with the zero-padding. This was achieved using overlapping intervals in the decision step for the first iteration. Therefore, the problem in the region around zero was alleviated and consequently the modified algorithm achieves the CRB. In sections 7.4 and 7.5 we reviewed hybrid algorithms consisting of a combination of an interpolation estimator and the dichotomous search. The hybrid algorithms improve the performance of the dichotomous search while, at the same time, reducing the required number of iterations. We also proposed a new hybrid algorithm called the Guided Search of the Periodogram Peak. This algorithm was shown, through simulations, to converge to the CRB in only four iterations compared to the ten iterations needed for the zero-padded dichotomous search.

In the next chapter we present and analyse three novel iterative frequency estimation methods that are based on the interpolation algorithms of chapter 6. These iterative methods are shown to have an asymptotic frequency error variance that is only 1.0147 times the CRB.

Chapter 8

Iterative Interpolation on the Fractional Fourier Coefficients

8.1 Introduction

The frequency estimators presented in chapters 5 and 6 exhibit a frequency dependent performance. The variance is seen to be periodic with respect to the frequency bins. Whereas the performance of the estimators of chapter 5 is worst at the bin centre, that of the interpolators on the fractional Fourier coefficients is best there. The iterative implementation of an estimator aims at improving the performance by essentially making it uniform over the entire bin.

It would seem at first glance that running the estimators of chapter 5 iteratively would improve their performance. The estimator is run the first time to get an estimate of the offset which is then removed leaving a residual offset. One would then be tempted to run the estimator on the same data again in an attempt to estimate and reduce the residual further. As we will see in this chapter, however, some estimators can be implemented iteratively while others can not.

The chapter is organised as follows: In section 8.2, we look at the fixed point theorem and the conditions for the convergence of an algorithm. Quinn's first algorithm is used in section 8.3 to illustrate the point that the performance of the estimators of chapter 5 deteriorates when they are implemented iteratively. In sections 8.3, 8.5 and 8.6 we propose and analyse three new iterative algorithms based on the interpolators presented in chapter 6. The asymptotic performance of the new algorithms is derived and compared to the asymptotic CRB.

8.2 The Fixed Point Theorem and Algorithm Convergence

Consider a function $h(x)$ operating on the real line $\mathbf{R}$ and an interval $I \subset \mathbf{R}$. Starting with an initial value $x_0 \in I$, we define the sequence $\{x_i\}$ using the iterative procedure

$$x_i = h(x_{i-1}), \quad i = 0,1,2,\ldots \tag{8.1}$$

The question then becomes: does the procedure converge? The behaviour of such an iterative procedure is examined in numerical analysis texts such as Dieudonné, [122], and Atkinson, [123]. A condition for the convergence of an iterative procedure constructed using a function $h(x)$ is that $h(x)$ has a unique fixed point. The fixed point theorem then ensures the convergence of the procedure to the fixed point. In the following we review the convergence theory. We start with the following theorem.

8.2.1 Theorem

Suppose $h(x)$ is a continuous function on an interval $I \subset \mathbf{R}$ satisfying

$$x \in I \Rightarrow h(x) \in I$$

then there exists at least one point $x_0 \in I$ such that $h(x_0) = x_0$

8.2.2 Proof

The proof is simple and we include it here. Let $I = [a,b]$. Since $x \in [a,b] \Rightarrow h(x) \in [a,b]$ then we must have $h(b) \le b$ and $h(a) \ge a$. Therefore $h(b) - b \le 0$ and $h(a) - a \ge 0$. By the intermediate value theorem, [116] pp. 95, there exists a point, x_0, such that $h(x_0) - x_0 = 0$ and consequently $h(x_0) = x_0$.

The following definition is necessary.

8.2.3 Definition

A function $h(x): I \subseteq \mathbf{R} \to \mathbf{R}$ is called contractive with contractivity constant $\alpha \in [0,1)$ if

$$\|h(u) - h(v)\| \leq \alpha \|u - v\|, \qquad \forall u, v \in I \tag{8.2}$$

where $\|\bullet\|$ is the norm defined on the space (in the context of the frequency estimation problem, the space is the real line $\mathbf{R}$). Here, the norm is simply given by the absolute value. That is

$$\|u - v\| = |u - v|$$

Now, if $h(x): I \to I$ is a contractive mapping, then it converges to a fixed point. This is seen through the following argument. Firstly, given that $h(x)$ is a mapping from interval I to itself, the existence of the fixed point is assured by theorem 8.2.1. Suppose we start with an initial value of x_0 and construct the sequence $\{x_i\}$ using equation (8.1). Then we have

$$\begin{aligned} |x_i - x_{i-1}| &= |h(x_{i-1}) - h(x_{i-2})| \\ &\leq \alpha |x_{i-1} - x_{i-2}| \end{aligned}$$

We see that the distance between successive points in the sequence decreases as $i \to \infty$. This means that $\{x_i\}$ is a Cauchy sequence, [124] pp. 141 theorem 4. Therefore it converges. The convergence result is assured by the fixed point theorem stated below, [123] pp.133.

8.2.4 Fixed Point Theorem

Suppose that $h(x)$ is a contractive mapping on the interval I with contractivity constant $\alpha \in [0,1)$, then the following results hold.

1. There exists a unique $\tilde{x} \in I$ such that

$$\tilde{x} = h(\tilde{x})$$

2. For any starting point $x_0 \in I$, the sequence $\{x_i\}$ obtained by the iterative procedure defined in (8.1) converges to $\tilde{x}$.

The proof of the theorem is given in Atkinson pp. 133-134. The uniqueness property is very important as it assures that the procedure always converges to the same point, the *fixed point*.

8.2.5 Performance of Iterative Estimation and Number of Iterations

When applied to the iterative implementation of the frequency estimators, the fixed point theorem ensures that they always converge provided they constitute a contractive mapping. In chapters 5 and 6, we derived the asymptotic variances of the interpolation estimators over the estimation interval $[-0.5,0.5]$. Let the variance of an estimator that is given by the interpolation function $h(x)$ be a continuous function, $g(x)$, on the interval I. We remind the reader that additive white Gaussian noise is assumed. If $h(x)$ is a contractive mapping then

$$\lim_{i\to\infty} x_i = \tilde{x}$$

and by the continuity of g, we have that

$$\begin{aligned}\lim_{i\to\infty} \text{var}[x_i] &= \lim_{i\to\infty} \text{var}[h(x_{i-1})] \\ &= \lim_{i\to\infty} g(x_{i-1}) \\ &= g(\tilde{x})\end{aligned} \tag{8.3}$$

As the CRB gives a lower bound on the performance of an estimator, we say that the algorithm has converged if its residual error is of a lower order than the CRB. For the problem of frequency estimation, this is obtained when the residual of the frequency is $o\left(N^{-\frac{3}{2}}\right)$ (or equivalently the residual of δ_0 is $o\left(N^{-\frac{1}{2}}\right)$). Now we examine the number of iterations required for convergence. Suppose the distance of the initial estimate from the fixed point is

$$|x_0 - \tilde{x}| = O\left(N^{-v}\right)$$

for some $v > 0$, and suppose that the contractivity constant is $O\left(N^{-\kappa}\right)$, for some $\kappa > 0$ Then after iteration i,

$$\begin{aligned}\left|x_i-\tilde{x}\right| &= \left|h\left(x_{i-1}\right)-\tilde{x}\right| \\ &= O\left(N^{-(i-1)\kappa}\right)\end{aligned}$$

This implies that the convergence occurs when

$$\begin{aligned}N^{-\nu}\left|x_i-\tilde{x}\right| &= N^{-\nu}O\left(N^{-(i-1)\kappa}\right) \\ &= O\left(N^{-\nu-(i-1)\kappa}\right)\end{aligned}$$

becomes $o\left(N^{-\frac{3}{2}}\right)$. That is

$$-\nu-(i-1)\kappa+\frac{3}{2}<0$$

or

$$i>\frac{-\nu+\frac{3}{2}}{\kappa}+1$$

For instance, if the MBS is used to initialise the estimator, then $v=\frac{1}{2}$. As we will show, the interpolators of chapter 6 (with the exception of the MSI algorithm) have a contractivity constant of order $\kappa=\frac{3}{2}$. Thus, the number of iterations needed to converge is 2.

8.3 Iterative Implementation of Quinn's First Algorithm

Recall from section 5.3, table 5.1 that Quinn's first estimator consists of obtaining two independent estimates for δ_0 from the two Fourier coefficients either side of the maximum. The estimate with the higher effective signal to noise ratio is then chosen. The estimator was shown to be of the same order as the CRB, that is

$$\left|\hat{\delta}-\delta_0\right| = O\left(N^{-1/2}\right)$$

and consequently the frequency estimate is

$$\left|\hat{f}-f_0\right| = O\left(N^{-3/2}\right)$$

In this section we consider the possibility of iteratively implementing the algorithm. In particular, we present the iterative implementation and show that the resulting procedure converges but that the performance deteriorates.

Let the initial frequency estimate be given by the MBS algorithm and set $\hat{\delta}_0 = 0$. Now we construct the following iterative procedure; for each iteration i, from 1 to Q, do the following:

- Shift the maximum bin by $\hat{\delta}_i$
- Calculate the Fourier coefficients corresponding to l = -1, 0 and 1.
- Update the estimate using Quinn's algorithm, that is $\hat{\delta}_i = \hat{\delta}_{i-1} + h\left(\hat{\delta}_{i-1}\right)$ with $h(\delta)$ given by the algorithm of table 5.1.

The iterative algorithm is summarized in the table below;

Initialisation:

Get the coarse estimate

$$m = \text{MBSEstimate}$$

Initialise the error and estimate values

$$\hat{\delta}_0 = 0$$

Loop: For each i from 1 *to Q do*

Calculate the Fourier coefficients

$$X_l = \sum_{k=0}^{N-1} x(k) e^{-j2\pi k \frac{m+\hat{\delta}_{i-1}+l}{N}}, \quad l = -1,0,1$$

Estimate the residual

$$\hat{\delta}_i = \psi\left(\hat{\delta}_{i-1}\right) = \hat{\delta}_{i-1} + h\left(\hat{\delta}_{i-1}\right)$$

where $\psi(\delta)$ *is given by the algorithm in table* 5.1

Return the estimate

$$\hat{f} = \frac{m + \hat{\delta}_Q}{N} f_s$$

Table 8.1 – *Iterative Implementation of Quinn's first algorithm.*

The algorithm is run for Q iterations since we can usually predetermine the number of iterations required for convergence. A more general stopping criteria, however, would be to stop the loop when $\left|\hat{\delta}_i - \hat{\delta}_{i-1}\right|$ is below a certain tolerance.

We will now prove the convergence of the iterative algorithm. As the procedure is initialised with the Maximum Bin Search algorithm, then $\delta_0 \in [-0.5,0.5]$ almost surely. Furthermore, Quinn showed that if $\delta_0 \in [0,0.5]$, we will almost surely choose $\hat{\delta}_1$ (see table 5.1). Thus, in order to establish the convergence of the procedure, we must consider three cases:

Case 1: $\alpha_1(\delta)$ is used in two consecutive steps $i-1$ and i

Case 2: $\alpha_{-1}(\delta)$ is used in two consecutive steps $i-1$ and i

and

Case 3: $\alpha_1(\delta)$ is used in step $i-1$ and $\alpha_{-1}(\delta)$ in step i (or vice versa).

In the following we only consider the first case as the analysis of the other two cases is similar. Referring to sections 5.2.1 and 5.3, we see that

$$\begin{aligned}\alpha_1(\delta) &= \Re\left\{\frac{X_1}{X_0}\right\} \\ &= \Re\left\{\frac{\frac{1}{N}\frac{e^{j2\pi(\delta_0-\delta)}-1}{e^{\frac{j2\pi(\delta_0-\delta-1)}{N}}-1}+W_1}{\frac{1}{N}\frac{e^{j2\pi(\delta_0-\delta)}-1}{e^{\frac{j2\pi(\delta_0-\delta)}{N}}-1}+W_0}\right\}\end{aligned}$$

where the noise coefficients, W_l are $O\left(N^{-\frac{1}{2}}\sqrt{\ln N}\right)$. This implies that

$$\frac{1}{N}\frac{e^{\frac{j2\pi(\delta_0-\delta-l)}{N}}-1}{e^{j2\pi(\delta_0-\delta)}-1}W_l = O\left(N^{-\frac{1}{2}}\sqrt{\ln N}\right)$$

Now carrying out the necessary simplifications we get

$$\alpha_1(\delta)=\frac{1}{2}\left\{\frac{\cos\left(\frac{2\pi}{N}\right)-\cos\left(2\pi\frac{\delta_0-\delta}{N}\right)}{1-\cos\left(2\pi\frac{\delta_0-\delta-1}{N}\right)}+1\right\}\left[1+O\left(N^{-\frac{1}{2}}\sqrt{\ln N}\right)\right]$$

Substituting $\alpha_1(\delta)$ into the expression for $h(\delta)$ yields,

$$\begin{aligned}h(\delta)&=\frac{\alpha_1}{\alpha_1-1}\\&=\frac{\cos\left(\frac{2\pi}{N}\right)-\cos\left(2\pi\frac{\delta_0-\delta}{N}\right)+1-\cos\left(2\pi\frac{\delta_0-\delta-1}{N}\right)}{\cos\left(\frac{2\pi}{N}\right)-\cos\left(2\pi\frac{\delta_0-\delta}{N}\right)-1+\cos\left(2\pi\frac{\delta_0-\delta-1}{N}\right)}\left[1+O\left(N^{-\frac{1}{2}}\sqrt{\ln N}\right)\right]\end{aligned}\tag{8.4}$$

We now expanding $h(\delta)$ into a Taylor series about δ_0.

$$h(\delta)=h(\delta_0)+(\delta-\delta_0)h'(\delta_0)+O\left(N^{-2}\right)$$

where

$$h(\delta_0)=O\left(N^{-\frac{1}{2}}\sqrt{\ln N}\right)$$

and

$$h'(\delta_0)=\frac{2\pi}{N}\frac{\sin\left(\frac{2\pi}{N}\right)}{2\left[\cos\left(\frac{2\pi}{N}\right)-1\right]}$$

Finally, letting $\psi(\delta)=\delta+h(\delta)$, we have

$$\begin{aligned}\psi(\delta)&=\left\{\delta_0+\delta-\delta_0+(\delta-\delta_0)h'(\delta_0)\right\}\left[1+O\left(N^{-\frac{1}{2}}\sqrt{\ln N}\right)\right]\\&=\left\{\delta_0+(\delta-\delta_0)\left[1+h'(\delta_0)\right]\right\}\left[1+O\left(N^{-\frac{1}{2}}\sqrt{\ln N}\right)\right]\end{aligned}$$

Firstly, we see that $h'(\delta_0)$ is always negative and tends to -1 from above as N goes to infinity. Therefore $-1<h'(\delta_0)<0$ and $\psi(\delta)=\delta_0$ as $N\to\infty$. Now checking the conditions for convergence, we have

$$\left|\psi(\delta_1)-\psi(\delta_2)\right| = \left|1+h'(\delta_0)\right|\left|\delta_1-\delta_2\right|\left[1+O\left(N^{-\frac{1}{2}}\sqrt{\ln N}\right)\right] \tag{8.5}$$

where $\delta_1, \delta_2 \in [-0.5, 0.5]$. Since $-1 < h'(\delta_0) < 0$, we have that $\left|1+h'(\delta_0)\right| < 1$ and

$$\left|\psi(\delta_1)-\psi(\delta_2)\right| \le \alpha\left|\delta_1-\delta_2\right|$$

where $\alpha < 1$.

The same analysis, applied to the other two cases, confirms the conditions for convergence. Since $\psi(\delta_0) = \delta_0\left[1+O\left(N^{-\frac{1}{2}}\sqrt{\ln N}\right)\right]$, the fixed point of the procedure is δ_0. Using equation (5.17), the variance of the estimator for δ at the i^{th} iteration is given by

$$\begin{aligned}\mathrm{var}\left[\hat{\delta}_i\right] &= g\left(\delta_0-\hat{\delta}_{i-1}\right)\\ &= \frac{\pi^2\delta_0^2 f_s^2}{2N^3\rho\sin^2\left(\pi\left(\delta_0-\hat{\delta}_{i-1}\right)\right)}\left(1-\left|\delta_0-\hat{\delta}_{i-1}\right|\right)^2\left\{\left(\delta_0-\hat{\delta}_{i-1}\right)^2+\left(1-\left|\delta_0-\hat{\delta}_{i-1}\right|\right)^2\right\}\end{aligned}$$

Now after the first iteration the estimate is

$$\hat{\delta}_1 = -\delta_0 h'(\delta_0)\left[1+O\left(N^{-\frac{1}{2}}\sqrt{\ln N}\right)\right]$$

and the variance is

$$\begin{aligned}\mathrm{var}\left[\hat{\delta}_1\right] &= g(\delta_0)\\ &= O\left(N^{-\frac{1}{2}}\right)\end{aligned}$$

Continuing the same argument, we see that after the second iteration we have

$$\hat{\delta}_2 = \delta_0\left(1+h'(\delta_0)\right)^2\left[1+O\left(N^{-\frac{1}{2}}\sqrt{\ln N}\right)\right]$$

and the variance is

$$\begin{aligned}\mathrm{var}\left[\hat{\delta}_2\right] &= g\left(\delta_0-\hat{\delta}_1\right)\\ &= g\left(\delta_0\left[1+h'(\delta_0)\right]\right)\\ &= g\left(o\left(N^{-\frac{1}{2}}\right)\right)\end{aligned}$$

Hence it takes only two iterations for the procedure to converge in an almost sure sense. This leads us to the following theorem.

8.3.1 Theorem

Let $h(\delta)$ denote Quinn's first estimator. The iterative procedure shown in table 8.1 converges with the following properties:

- The fixed point of convergence is δ_0.
- The procedure takes 2 iterations for the residual error to become $o\left(N^{-\frac{1}{2}}\right)$

and

- The limiting ratio of the variance of the estimator to the asymptotic CRB is $\frac{\pi^2}{3}$ uniformly over the interval $[-0.5,0.5]$.

The theorem implies that the variance of the estimator when implemented iteratively worsens as $g(\delta)$ has a maximum of 3.2899 at $\delta_0 = 0$. The theoretical results were confirmed by simulations. The first plot, shown in figure 8.1 below, displays the resulting ratio of the variance to the asymptotic CRB as a function of δ_0. The graph consists of two curves obtained after the first and second iteration. We see that the curve resulting from two iterations is almost flat at the peak of the first. This confirms that the iterative algorithm converges to the fixed point at zero for all starting points in the interval $\delta_0 \in [-0.5,0.5]$. The second plot shows the performance of the iterative implementation along with the non-iterative algorithm and the CRB. The deterioration in the standard deviation of the frequency error is visible.

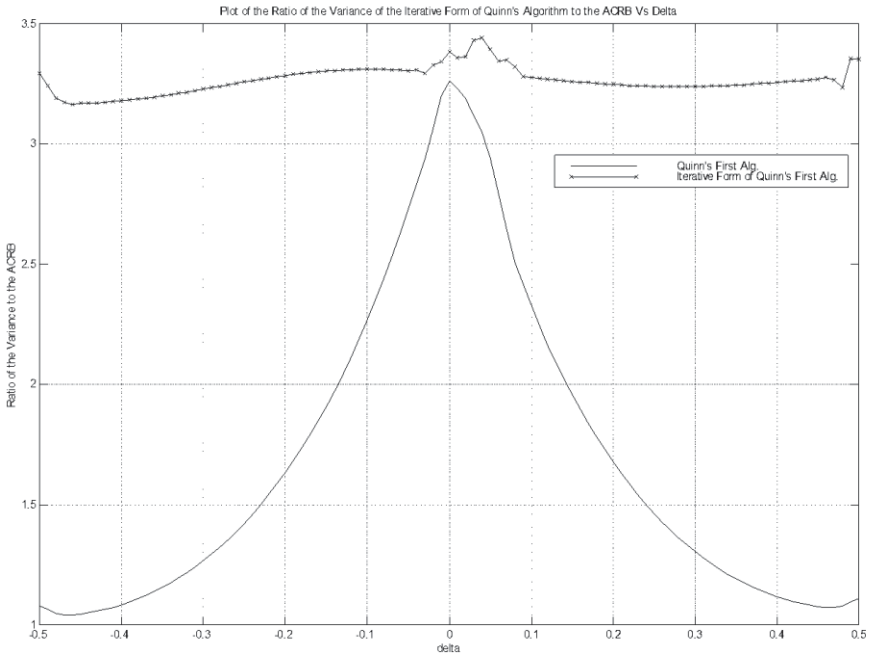

Figure 8.1 – *Plot of ratio of the variance of the iterative form of Quinn's first algorithm to the asymptotic CRB. 5000 simulation runs were averaged at an SNR = 0dB.*

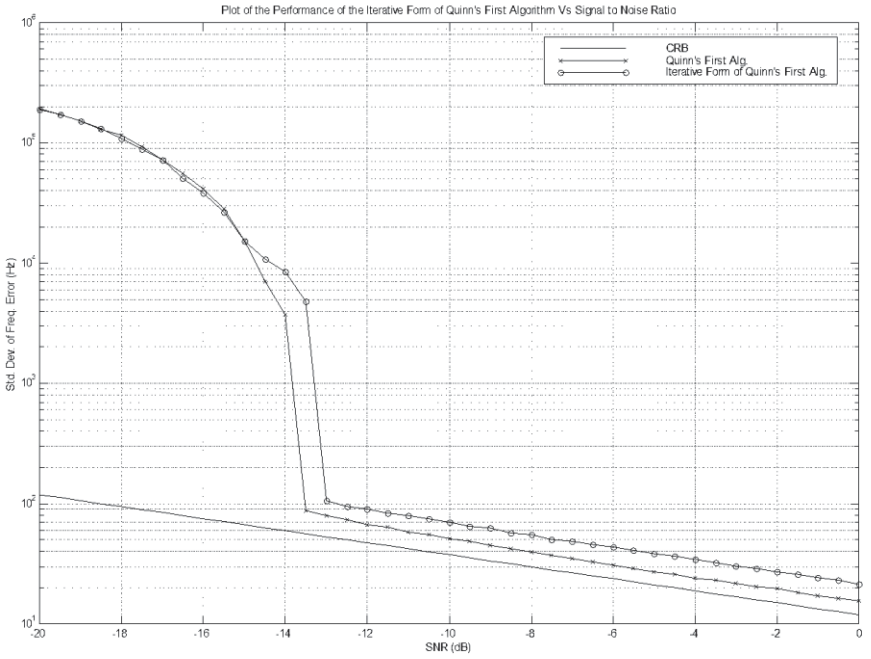

Figure 8.2 – *Plot of Standard Deviation of the Frequency Error of the iterative form of Quinn's first algorithm Vs Signal to Noise Ratio. 10000 simulation runs were averaged.*

8.4 Iterative Fractional Fourier Coefficients Interpolation

In the previous section we showed that the iterative implementation of Quinn's algorithm converges. We found, however, that the resulting performance deteriorates. This is also the case for the entire family of algorithms of chapter 5. The reason for this is that the variance of these estimators has a maximum at $\delta_0 = 0$. The interpolators of chapter 6, on the other hand, have minimum variance at zero. In this section, we consider the iterative implementation of the FFCI algorithm of section 6.3. This is shown the table below:

Initialisation:

Get the coarse estimate

$$m = \text{MBSEstimate}$$

Initialise the error and estimate values

$$\hat{\delta}_0 = 0$$

Loop: For each i from 1 *to Q do*

Calculate the Fourier coefficients

$$X_p = \sum_{k=0}^{N-1} x(k) e^{-j2\pi k \frac{m+\hat{\delta}_{i-1}+p}{N}}, \qquad p = \pm 0.5$$

Estimate the residual

$$\begin{aligned} \hat{\delta}_i &= \psi\left(\hat{\delta}_{i-1}\right) \\ &= \hat{\delta}_{i-1} + h\left(\hat{\delta}_{i-1}\right) \end{aligned}$$

where $h(\delta)$ *is given by the algorithm in table* 6.1

Return the estimate

$$\hat{f} = \frac{m + \hat{\delta}_Q}{N} f_s$$

Table 8.2 – *Iterative Implementation of the Fractional Fourier Coefficient Interpolation algorithm.*

We will, now, prove the convergence of the above algorithm and derive the asymptotic variance of the estimation error. Let us first consider the estimator interpolation function $h(\delta)$. Referring to table 6.1, $h(\delta)$ is given by

$$h(\delta)=\frac{1}{2}\Re\left\{\frac{X_{0.5}+X_{-0.5}}{X_{0.5}-X_{-0.5}}\right\}$$

where according to section 6.2,

$$X_p=-\frac{1}{N}\frac{e^{j2\pi(\delta_0-\delta)}+1}{e^{\frac{j2\pi(\delta_0-\delta-p)}{N}}-1}+W_p$$

The noise coefficients W_p are $O\left(N^{-\frac{1}{2}}\sqrt{\ln N}\right)$. Substituting the expressions for X_p, $p=\pm 0.5$, into $h(\delta)$ and carrying out the necessary simplifications yields

$$h(\delta)=\frac{\sin\left(\frac{2\pi}{N}(\delta_0-\delta)\right)}{2\sin\left(\frac{\pi}{N}\right)}\left[1+O\left(N^{-\frac{1}{2}}\sqrt{\ln N}\right)\right] \tag{8.6}$$

Now expanding the interpolation function into a Taylor series about δ_0 results in,

$$h(\delta)=h(\delta_0)+(\delta-\delta_0)h'(\delta_0)+O(N^{-2})$$

where

$$h(\delta_0)=O\left(N^{-\frac{1}{2}}\sqrt{\ln N}\right)$$

and

$$h'(\delta_0)=-\frac{\pi}{N\sin\left(\frac{\pi}{N}\right)}\left[1+O\left(N^{-\frac{1}{2}}\sqrt{\ln N}\right)\right]$$

Finally, $\psi(\delta)=\delta+h(\delta)$ becomes,

$$\psi(\delta)=\{\delta_0+(\delta-\delta_0)[1+h'(\delta_0)]\}\left[1+O\left(N^{-\frac{1}{2}}\sqrt{\ln N}\right)\right] \tag{8.7}$$

Looking at the expression for $h'(\delta_0)$ we note that, as $N \to \infty$, it tends to -1 from above. In fact we find that

$$h'(\delta_0) = \left[-1 + O\left(N^{-2}\right)\right]\left[1 + O\left(N^{-\frac{1}{2}}\sqrt{\ln N}\right)\right]$$

Therefore

$$\psi(\delta) = \left\{\delta_0 + (\delta - \delta_0)O\left(N^{-2}\right)\right\}\left[1 + O\left(N^{-\frac{1}{2}}\sqrt{\ln N}\right)\right]$$

For infinite N, we would, as expected, achieve exact estimation of δ_0. Now we check the convergence conditions as follows;

$$\begin{aligned}|\psi(\delta_1) - \psi(\delta_2)| &= |\delta_1 - \delta_2| O\left(N^{-2}\right) \\ &\leq \alpha|\delta_1 - \delta_2|\end{aligned}$$

where $\alpha < 1$. Therefore the conditions for the algorithm convergence are satisfied. The fixed point of the iterative algorithm is δ_0 as $h(\delta_0)$ is asymptotically zero and $\psi(\delta_0) = \delta_0$. Furthermore, using equation (6.5), the asymptotic variance after the i^{th} iteration is

$$\begin{aligned}\text{var}\left[\hat{\delta}_i\right] &= g\left(\delta_0 - \hat{\delta}_{i-1}\right) \\ &= \frac{f_s^2}{4N^3\rho}\frac{\pi^2\left(\left(\delta_0 - \hat{\delta}_{i-1}\right)^2 - 0.25\right)^2\left(4\left(\delta_0 - \hat{\delta}_{i-1}\right)^2 + 1\right)}{\cos^2\left(\pi\left(\delta_0 - \hat{\delta}_{i-1}\right)\right)}\end{aligned}$$

The limiting asymptotic variance is, as the number of iterations increases, given by

$$\begin{aligned}\text{var}\left[\hat{\delta}_\infty\right] &= \lim_{i\to\infty} g\left(\delta_0 - \hat{\delta}_i\right) \\ &= g(0)\end{aligned}$$

Following a similar argument to the previous section, the order of the residual after the second iteration and the resulting asymptotic variance are determined to be

$$\hat{\delta}_2 = \delta_0\left(1 + h'(\delta_0)\right)^2\left[1 + O\left(N^{-\frac{1}{2}}\sqrt{\ln N}\right)\right]$$

and

$$\begin{aligned}\mathrm{var}\left[\hat{\delta}_2\right] &= g\left(\delta_0 - \hat{\delta}_1\right) \\ &= g\left(o\left(N^{-\frac{1}{2}}\right)\right)\end{aligned}$$

respectively. Hence it takes only two iterations for the procedure to converge almost surely. Finally, we state the following theorem.

8.4.1 Theorem

Let $h(\delta)$ denote the FFCI estimator. The iterative procedure shown in table 8.2 converges with the following properties:

- The fixed point of convergence is δ_0.
- The procedure takes 2 iterations for the residual error to become $o\left(N^{-\frac{1}{2}}\right)$

and

- The limiting ratio of the variance of the estimator to the asymptotic CRB is $\frac{\pi^4}{96}$ uniformly over the interval $[-0.5,0.5]$.

The theoretical results presented above were verified through simulations. The plot in figure 8.3 shows the ratio of the variance of the estimator error to the asymptotic CRB versus the offset from the bin centre. Two curves are shown; the first was obtained after one iteration and therefore corresponds to the standard FFCI algorithm of section 6.3. The second curve shows the results of two iterations. The results show that the iterative procedure converges for all $\delta_0 \in [-0.5,0.5]$ to the fixed point δ_0. Figure 8.4 shows the resulting standard deviation of the frequency error as a function of the signal to noise ratio. The improvement of the iterative procedure over the standard procedure is clearly visible as the standard deviation curve, after two iterations, almost lies on the CRB curve. In fact, the standard deviation of the error for the IFFCI algorithm is a mere 1.0073 times the CRB.

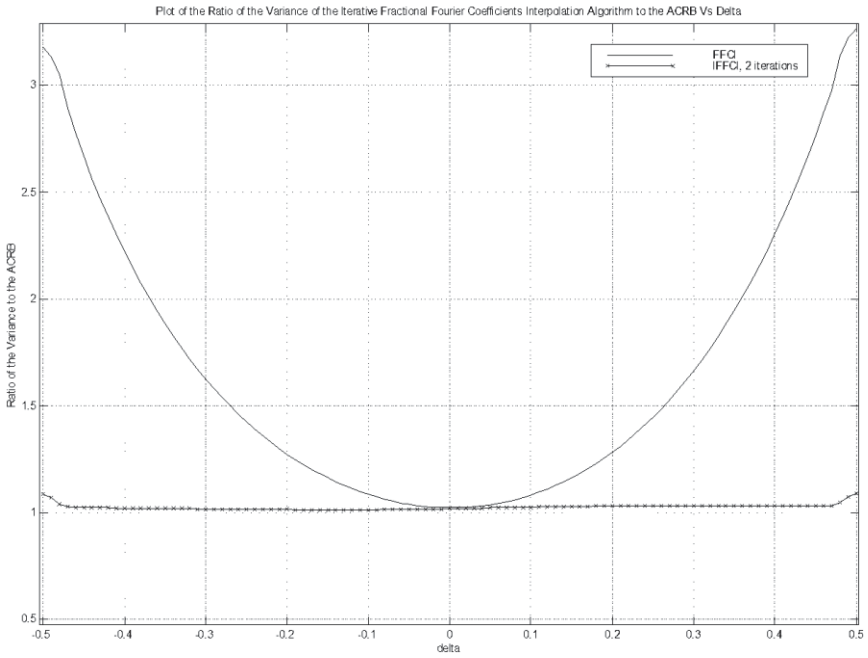

Figure 8.3 – *Plot of ratio of the variance of the iterative form of the FFCI algorithm to the asymptotic CRB. 5000 simulation runs were averaged at an SNR = 0dB.*

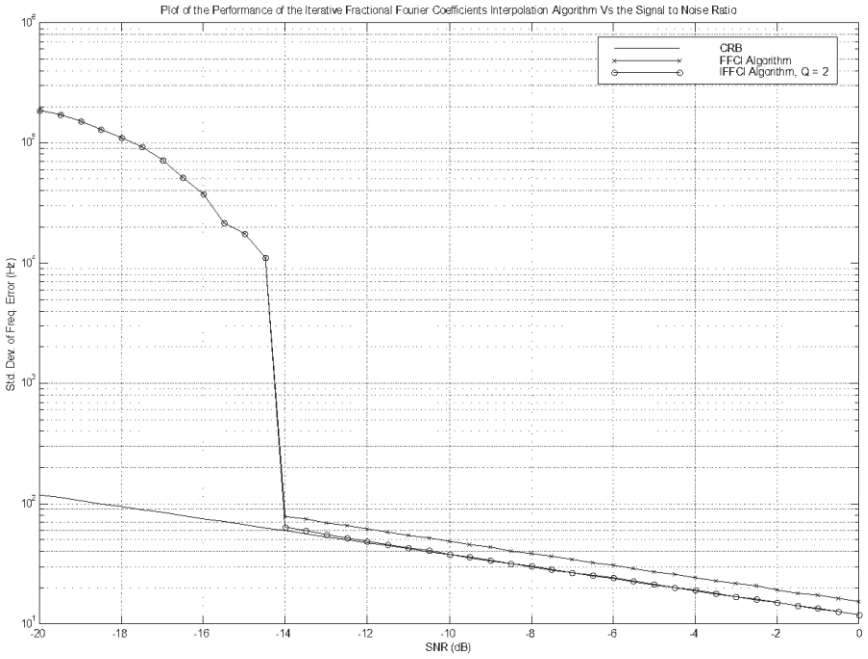

Figure 8.4 – *Plot of Standard Deviation of the Frequency Error of the iterative form of the FFCI algorithm Vs Signal to Noise Ratio. 10000 simulation runs were averaged.*

8.5 Iterative Magnitudes Only Interpolation

In this section we present and analyse the Iterative Magnitudes Only Interpolation (IMOI) algorithm. Using the same approach applied to the previous two algorithms, we show that it converges and derive the limiting ratio of the variance to the asymptotic CRB.

The IMOI algorithm is obtained by replacing $h(\delta)$, in table 8.2, by the MOI algorithm of section 6.4. That is $h(\delta)$ is now given by

$$h(\delta)=\frac{1}{2}\frac{|X_{0.5}|-|X_{-0.5}|}{|X_{0.5}|+|X_{-0.5}|}$$

where again,

$$X_p=-\frac{1}{N}\frac{e^{j2\pi(\delta_0-\delta)}+1}{e^{\frac{j2\pi(\delta_0-\delta-p)}{N}}-1}+W_p$$

and the noise coefficients are $O\left(N^{-\frac{1}{2}}\sqrt{\ln N}\right)$. In the analysis of section 6.4.2, we divided the interval $[-0.5,0.5]$ into two regions, Δ_1 and Δ_2. These regions were defined as

$$\Delta_1=\left\{\delta_0;|\delta_0|\le\frac{1}{2}-aN^{-\nu}\right\}$$

and

$$\Delta_2=\left\{\delta_0;\frac{1}{2}-aN^{-\nu}<|\delta_0|\le\frac{1}{2}\right\}$$

for some $a>0$ and $\nu>0$. We found that the behaviour of the MOI estimator in region Δ_1 was "regular". In fact, it was found to be identical to the FFCI algorithm. Thus it is straightforward to establish the convergence of the procedure in Δ_1.

Substituting the expressions for X_p into that for $h(\delta)$ and carrying out the necessary simplifications yields

$$h(\delta)=\frac{1}{2}\left\{\frac{\cos\left(\frac{2\pi}{N}(\delta_0-\delta-0.5)\right)-\cos\left(\frac{2\pi}{N}(\delta_0-\delta+0.5)\right)}{2-\cos\left(\frac{2\pi}{N}(\delta_0-\delta-0.5)\right)-\cos\left(\frac{2\pi}{N}(\delta_0-\delta+0.5)\right)}\right\}\left[1+O\left(N^{-\frac{1}{2}}\sqrt{\ln N}\right)\right] \quad (8.8)$$

Now expanding the interpolation function into a Taylor series about δ_0 results in,

$$h(\delta)=h(\delta_0)+(\delta-\delta_0)h'(\delta_0)+O(N^{-2})$$

where

$$h(\delta_0)=O\left(N^{-\frac{1}{2}}\sqrt{\ln N}\right)$$

and

$$h'(\delta_0)=-\frac{\pi}{2N}\frac{\sin\left(\frac{\pi}{N}\right)}{1-\cos\left(\frac{\pi}{N}\right)}\left[1+O\left(N^{-\frac{1}{2}}\sqrt{\ln N}\right)\right]$$

Let $\psi(\delta)=\delta+h(\delta)$, we have

$$\psi(\delta)=\{\delta_0+(\delta-\delta_0)[1+h'(\delta_0)]\}\left[1+O\left(N^{-\frac{1}{2}}\sqrt{\ln N}\right)\right] \quad (8.9)$$

Similarly to the case of the IFFCI algorithm of the previous section we find that $h'(\delta_0)$ tends to -1 from above as $N\to\infty$. In fact,

$$h'(\delta_0)=\left[-1+O(N^{-2})\right]\left[1+O\left(N^{-\frac{1}{2}}\sqrt{\ln N}\right)\right]$$

Now checking the convergence conditions,

$$\begin{aligned}|\psi(\delta_1)-\psi(\delta_2)| &= |\delta_1-\delta_2|O(N^{-2})\\ &\le \alpha|\delta_1-\delta_2|\end{aligned}$$

where $\alpha<1$. Therefore, the conditions for the convergence of the iterative procedure are satisfied in region Δ_1. The fixed point of the iterative algorithm is δ_0 as $h(\delta_0)$ is asymptotically zero. Furthermore, from theorem 6.4.2.1, the asymptotic variance after the i^{th} iteration is,

$$\begin{aligned}\mathrm{var}\left[\hat{\delta}_i\right] &= g\left(\delta_0 - \hat{\delta}_{i-1}\right) \\ &= \frac{f_s^2}{4N^3\rho}\frac{\pi^2\left(\left(\delta_0 - \hat{\delta}_{i-1}\right)^2 - 0.25\right)^2\left(4\left(\delta_0 - \hat{\delta}_{i-1}\right)^2 + 1\right)}{\cos^2\left(\pi\left(\delta_0 - \hat{\delta}_{i-1}\right)\right)}\end{aligned}$$

This is identical to that of the previous algorithm. We will not repeat the rest of the analysis as it is identical to that of the IFFCI algorithm.

So far we have proved convergence in region Δ_1. We will now consider the behaviour of the procedure for $\delta_0 \in \Delta_2$. We have determined in section 6.4.2 that the algorithm is biased. This, however, does not preclude the iterative procedure from converging. As long as the first iteration moves the estimator into region Δ_1, the conclusions obtained above continue to apply. We will now look at the case we examined in section 6.4.2, namely $\delta_0 \to 0.5$. The order of $S_{0.5}$ was found to be preserved whereas that of $S_{-0.5}$ changes. That is

$$|S_{0.5}| = O(1)$$

and

$$|S_{-0.5}| = o(1) \approx 0$$

The noise coefficients remain $O\left(N^{-\frac{1}{2}}\sqrt{\ln N}\right)$. Hence the magnitude of $X_{0.5}$ is

$$|X_{0.5}| = |S_{0.5}|\left[1 + O\left(N^{-\frac{1}{2}}\sqrt{\ln N}\right)\right]$$

whereas $X_{-0.5}$ is

$$|X_{-0.5}| = O\left(N^{-\frac{1}{2}}\sqrt{\ln N}\right)$$

Thus, we find that, for $\delta_0 \in \Delta_2$, the expression for $h(\delta)$ is

$$h(\delta) = \frac{1}{2}\left[1 + O\left(N^{-\frac{1}{2}}\sqrt{\ln N}\right)\right]$$

After the first iteration the estimate for δ_0 is

$$\begin{aligned}\hat{\delta}_1 &= \hat{\delta}_0 + h\left(\hat{\delta}_0\right) \\ &= 0 + \frac{1}{2}\left[1 + O\left(N^{-\frac{1}{2}}\sqrt{\ln N}\right)\right]\end{aligned}$$

This ensures that the residual $\delta_0 - \hat{\delta}_1$ will be $O\left(N^{-\frac{1}{2}}\sqrt{\ln N}\right)$ almost surely and the iterative procedure is driven into region Δ_1. The convergence conditions for region Δ_1 then apply. The limiting asymptotic variance, as the number of iterations increases, is given by $g(0)$. The order of the residual after the second iteration and the resulting asymptotic variance are determined to be

$$\hat{\delta}_2 = \delta_0\left(1 + h'(\delta_0)\right)^2\left[1 + O\left(N^{-\frac{1}{2}}\sqrt{\ln N}\right)\right]$$

and

$$\begin{aligned}\text{var}\left[\hat{\delta}_2\right] &= g\left(\delta_0 - \hat{\delta}_1\right) \\ &= g\left(o\left(N^{-\frac{1}{2}}\right)\right)\end{aligned}$$

respectively. Hence it takes only two iterations for the procedure to converge almost surely. We now arrive at the following theorem.

8.5.1 Theorem

Let $h(\delta)$ denote the MOI estimator. The iterative procedure shown in table 8.2 converges with the following properties:

1. The fixed point of convergence is δ_0.
2. The procedure takes 2 iterations for the residual error to become $o\left(N^{-\frac{1}{2}}\right)$

   and
3. The limiting ratio of the variance of the estimator to the asymptotic CRB is $\frac{\pi^4}{96}$

   uniformly over the interval $[-0.5, 0.5]$.

The performance of the iterative algorithm was simulated and the results are shown below. Figure 8.5 shows the ratio of the frequency error variance to the asymptotic CRB as a function of the offset from the bin centre for both the MOI and the IMOI algorithms. The IMOI algorithm was run for two iterations. The improvement resulting from the second iteration is evident as the ratio curve converges to the value of $\frac{\pi^4}{96}$.

Figure 8.6 shows the performance as a function of signal to noise ratio. The standard deviation of the frequency error is shown. The plot comprises three curves, the CRB, the performance of the MOI algorithm of section 6.4 and the IMOI algorithm. The standard deviation of the IMOI algorithm practically lies on the CRB curve for all signal to noise ratios above the threshold.

We also note here that since the performance of the MMSI algorithm of section 6.6 is identical to that of the MOI algorithm, its iterative implementation would have identical performance to that of the IMOI algorithm and the above analysis is applicable to it.

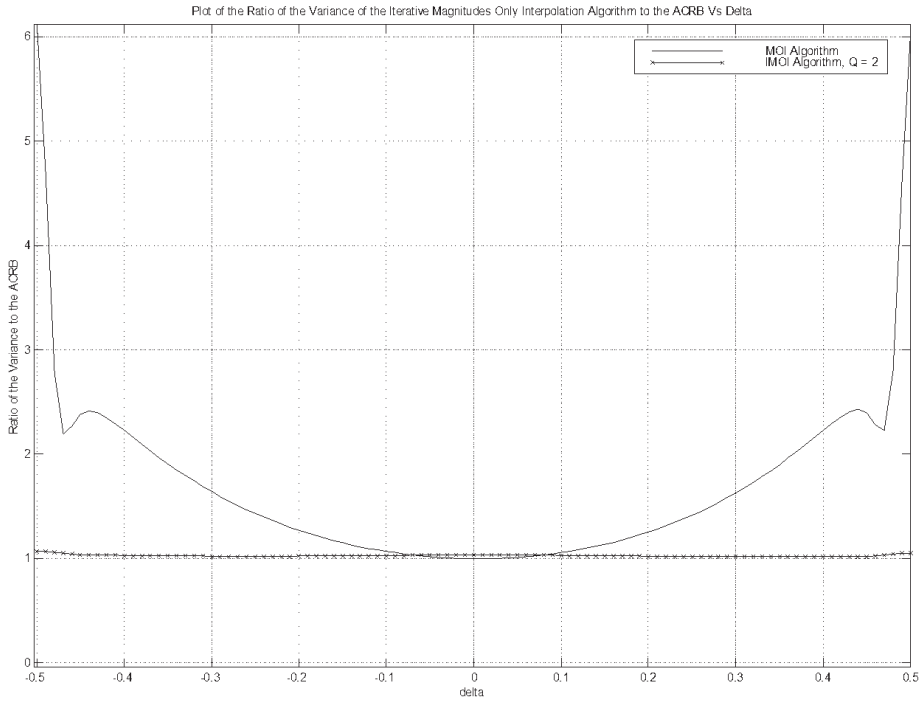

Figure 8.5 – *Plot of ratio of the variance of the iterative form of the MOI algorithm to the asymptotic CRB. 5000 simulation runs were averaged at a SNR = 0dB.*

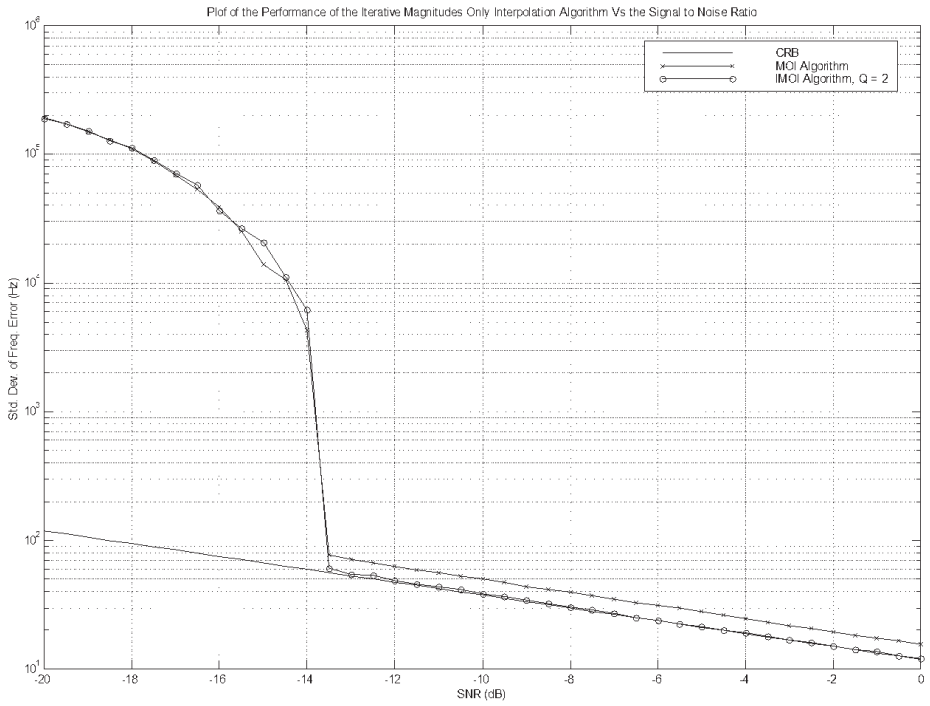

Figure 8.6 – *Plot of Standard Deviation of the Frequency Error of the iterative form of the MOI algorithm Vs Signal to Noise Ratio. 10000 simulation runs were averaged.*

8.6 Iterative Magnitudes Squared Interpolation

In section 6.5, we showed that the MSI algorithm is not an efficient estimator as it is severely biased away from zero. In this section we present the Iterative Magnitudes Squared Interpolation algorithm (IMSI), suggested in [10], and prove that it constitutes an efficient estimator. Using the same approach as the previous two algorithms, we derive the limiting ratio of the variance to the asymptotic CRB.

The iterative MSI algorithm is obtained by replacing $h(\delta)$, in table 8.2, by

$$h(\delta) = \frac{1}{4}\frac{|X_{0.5}|^2 - |X_{-0.5}|^2}{|X_{0.5}|^2 + |X_{-0.5}|^2}$$

Now let $\psi(\delta) = \delta + h(\delta)$. We must show that $\psi(\delta)$ is a contractive mapping for all $\delta_0 \in [-0.5, 0.5]$. Consider first $\delta_0 \in \Delta_1$, we can easily show that

$$h(\delta)=\frac{1}{4}\frac{|S_{0.5}|^2-|S_{-0.5}|^2}{|S_{0.5}|^2+|S_{-0.5}|^2}\left\{1+O\left(N^{-\frac{1}{2}}\sqrt{\ln N}\right)\right\}$$

This is due to the fact that $S_p=O(1)$ for both $p=\pm 0.5$, whereas the noise coefficients are $O\left(N^{-\frac{1}{2}}\sqrt{\ln N}\right)$. Substituting the expressions of S_p into that of $h(\delta)$ yields

$$h(\delta)=\frac{1}{4}\frac{\left|-\frac{1}{N}\frac{e^{j2\pi(\delta_0-\delta)}+1}{e^{\frac{j2\pi(\delta_0-\delta-0.5)}{N}}-1}\right|^2-\left|-\frac{1}{N}\frac{e^{j2\pi(\delta_0-\delta)}+1}{e^{\frac{j2\pi(\delta_0-\delta+0.5)}{N}}-1}\right|^2}{\left|-\frac{1}{N}\frac{e^{j2\pi(\delta_0-\delta)}+1}{e^{\frac{j2\pi(\delta_0-\delta-0.5)}{N}}-1}\right|^2+\left|-\frac{1}{N}\frac{e^{j2\pi(\delta_0-\delta)}+1}{e^{\frac{j2\pi(\delta_0-\delta+0.5)}{N}}-1}\right|^2}\left\{1+O\left(N^{-\frac{1}{2}}\sqrt{\ln N}\right)\right\}$$

Simplifying the above we obtain,

$$h(\delta)=\frac{1}{4}\frac{\cos\left[\frac{2\pi}{N}(\delta_0-\delta-0.5)\right]-\cos\left[\frac{2\pi}{N}(\delta_0-\delta+0.5)\right]}{2-\cos\left[\frac{2\pi}{N}(\delta_0-\delta-0.5)\right]-\cos\left[\frac{2\pi}{N}(\delta_0-\delta+0.5)\right]}\left\{1+O\left(N^{-\frac{1}{2}}\sqrt{\ln N}\right)\right\} \quad (8.10)$$

$h(\delta)$ can be expanded into a Taylor series about δ_0 giving

$$h(\delta)=h(\delta_0)+(\delta-\delta_0)h'(\delta_0)+O(N^{-2})$$

where

$$h(\delta_0)=O\left(N^{-\frac{1}{2}}\sqrt{\ln N}\right)$$

and

$$h'(\delta_0)=-\frac{\pi}{4N}\frac{\sin\left(\frac{\pi}{N}\right)}{1-\cos\left(\frac{\pi}{N}\right)}\left[1+O\left(N^{-\frac{1}{2}}\sqrt{\ln N}\right)\right]$$

Finally, $\psi(\delta)$ becomes

$$\psi(\delta)=\{\delta_0+(\delta-\delta_0)[1+h'(\delta_0)]\}\left[1+O\left(N^{-\frac{1}{2}}\sqrt{\ln N}\right)\right] \quad (8.11)$$

Upon examination of the relative orders of the terms in $h'(\delta_0)$ we see that it can be rewritten as

$$h'(\delta_0) = \left[-\frac{1}{2} + O\left(N^{-2}\right)\right]\left[1 + O\left(N^{-\frac{1}{2}}\sqrt{\ln N}\right)\right]$$

Therefore,

$$\begin{aligned} |\psi(\delta_1) - \psi(\delta_2)| &= |\delta_1 - \delta_2|\left[\frac{1}{2} + O\left(N^{-2}\right)\right]\left[1 + O\left(N^{-\frac{1}{2}}\sqrt{\ln N}\right)\right] \\ &\leq \alpha|\delta_1 - \delta_2| \end{aligned} \tag{8.12}$$

where $\alpha < 1$. Thus the conditions for the convergence of the iterative procedure in region Δ_1 are satisfied. The fixed point of the iterative algorithm is δ_0 as $h(\delta_0)$ is asymptotically zero.

Now we must consider the behaviour of the procedure for $\delta_0 \in \Delta_2$. The difference between the two regions is in the behaviour of the noise terms. The analysis follows a similar argument to that given for the IMOI algorithm. We will look at the case where $\delta_0 \to 0.5$. The order of the coefficient corresponding to $p = 0.5$ is preserved whereas that corresponding to $p = -0.5$ changes. Thus,

$$|S_{0.5}| = O(1)$$

and

$$|S_{-0.5}| = o(1) \approx 0$$

The noise coefficients remain $O\left(N^{-\frac{1}{2}}\sqrt{\ln N}\right)$. Hence $X_{0.5}$ is

$$|X_{0.5}|^2 = |S_{0.5}|^2\left[1 + O\left(N^{-1}\ln N\right)\right]$$

and $X_{-0.5}$ is

$$|X_{-0.5}| = O\left(N^{-1}\ln N\right)$$

Substituting into the expression for $h(\delta)$ yields,

$$h(\delta) \approx \frac{1}{4}\left[1 + O\left(N^{-1}\ln N\right)\right]$$

The estimate after the first iteration is $\hat{\delta}_1 = \frac{1}{4} + O\left(N^{-1} \ln N\right)$ and consequently the residual is $\left(\delta_0 - \hat{\delta}_1\right) \in \Delta_1$ almost surely. Furthermore,

$$\begin{aligned} \left|\psi(\delta_1) - \psi(\delta_2)\right| &= \left|\delta_1 - \delta_2\right| O\left(N^{-1} \ln N\right) \\ &\leq \alpha \left|\delta_1 - \delta_2\right| \end{aligned}$$

This implies that after the first iteration the algorithm moves into region Δ_1 and the analysis given above for $\delta_0 \in \Delta_1$ applies. Thus convergence requirements are satisfied and the algorithm converges to the fixed point for $\delta_0 \in \Delta_1 \cup \Delta_2 = [-0.5, 0.5]$. The limiting variance is therefore equal to that at $\delta_0 = 0$. This was found before to be the same as the other two algorithms, that is $\frac{\pi^4}{96}$.

Equation (8.12) implies that the estimate, $\hat{\delta}_1$, after the first iteration, is almost surely in the interval $[-0.25, 0.25]$. Similarly, we have that the estimate after the second iteration is $\hat{\delta}_2 = 0 + O\left(N^{-\frac{1}{2}}\right)$. Therefore, according to the convergence criteria discussed in section 8.2.5, a third iteration is needed for the algorithm to converge and the residual to become $o\left(N^{-\frac{1}{2}}\right)$. In fact, one would expect the algorithm to converge in two iterations for $\delta_0 \in \Delta_1$. In the case where $\delta_0 \in \Delta_2$, on the other hand, three iterations are required. Finally we arrive at the following theorem.

8.6.1 Theorem

Let $h(\delta)$ denote the MSI estimator. The iterative procedure shown in table 8.2 converges with the following properties:

1. The fixed point of convergence is δ_0.
2. The procedure takes 3 iterations for the residual error to become $o\left(N^{-\frac{1}{2}}\right)$ almost surely

and

3. The limiting ratio of the variance of the estimator to the asymptotic CRB is $\frac{\pi^4}{96}$ uniformly over the interval $[-0.5,0.5]$.

The performance of the iterative MSI algorithm was simulated and the results are shown in figures 8.7 and 8.8 below. The first plot shows the ratio of the frequency error variance to the asymptotic CRB as a function of the offset from the bin centre for 1, 2 and 3 iterations. After 1 iteration, the IMSI algorithm is equivalent to the MSI algorithm of section 6.5. 5000 simulation runs were averaged at each point. We see that, for $\delta_0 \in \Delta_1$, the curve after two iterations is almost flat around the value of $\frac{\pi^4}{96}$. For $\delta_0 \in \Delta_2$, on the other hand, it takes three iterations for the algorithm to converge. Figure 8.6 shows the performance as a function of signal to noise ratio. The standard deviation of the frequency error is plotted. 10000 simulation runs were averaged at each SNR value and the performance of the IMSI algorithm after 1, 2 and 3 iterations is shown. The performance after 2 iterations asymptotes out to a constant value as the SNR goes to ∞. This is expected as the analysis showed that after two iterations the estimator is still biased. It is to this bias that the curve asymptotes. The performance after the third iteration, however, is on the CRB curve indicating that the algorithm has converged uniformly in δ_0.

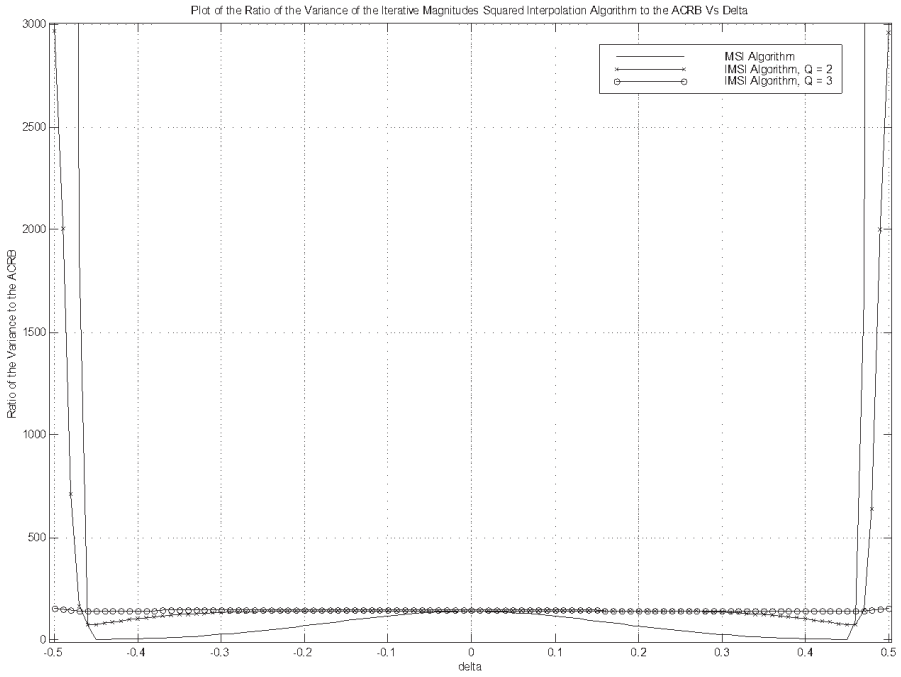

Figure 8.7 – *Plot of ratio of the variance of the iterative form of the MSI algorithm to the asymptotic CRB. 5000 simulation runs were averaged at a SNR = 0dB.*

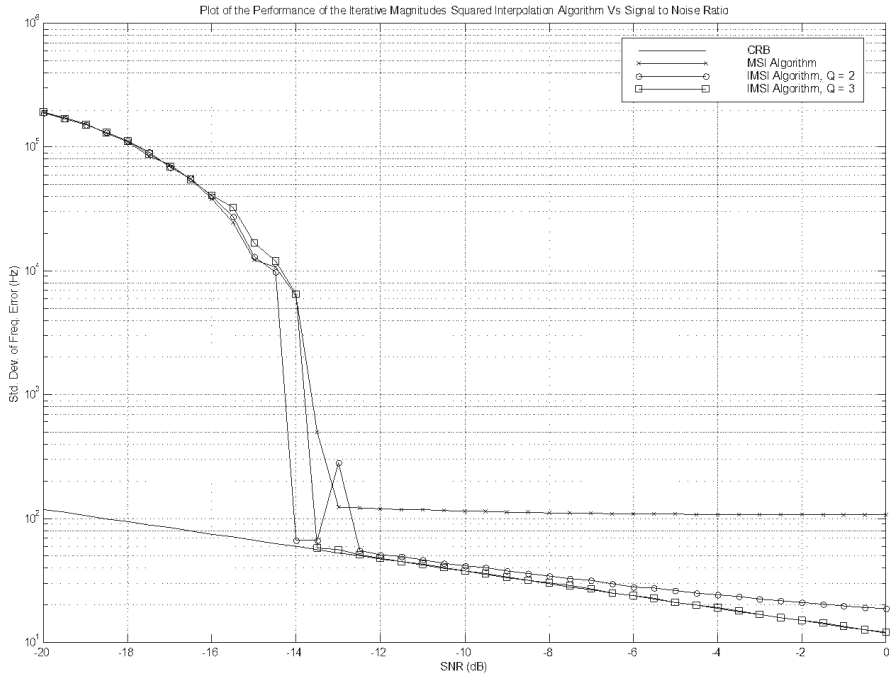

Figure 8.8 – *Plot of Standard Deviation of the Frequency Error of the iterative form of the MSI algorithm Vs Signal to Noise Ratio. 10000 simulation runs were averaged.*

8.7 Conclusion

In this chapter, we presented and analysed three new iterative frequency estimation algorithms. The algorithms all are frequency domain estimators that are based on the interpolators of chapter 6. A coarse frequency estimate is first obtained using the MBS algorithm. The interpolators are then run iteratively to refine the estimate.

We started by showing that iterative techniques based on the algorithms of chapter 5 do not converge. Quinn's first algorithm was used as an example. The new iterative algorithms, on the other hand, constitute efficient estimators. That is, they are unbiased and they achieve a frequency variance that is only $\frac{\pi^4}{96}$ or 1.0147 times the CRB. Therefore their performance practically lies on the CRB curve. The IFFCI and IMOI algorithms were shown to converge in two iterations whereas the IMSI algorithm requires three.

Chapter 9

Frequency Assisted Spatial Tracking

9.1 Introduction

As low earth orbit satellites move rapidly with respect to an earthbound observer, a spatial tracking scheme must be implemented at the earth station. The tracking requirements depend among other things on the satellite altitude, the antenna beamwidth and the maximum tolerable off-boresight pointing error, [107] pp. 2-5. Thus, the earth station needs to determine the satellite orbit and the look-angles needed to correctly point to it. The required spatial information can be obtained from many sources, such as NASA TLEs, GPS data and orbital estimation data.

NORAD, the North American Aerospace Defence Command, tracks objects and outputs the data on a NASA Bulletin Board Service (BBS). The orbital parameters are output on the NORAD website as Two Line Elements, or TLEs. For a discussion of TLEs refer to [1] Appendix C and [125]. The publicly available TLEs are updated by NORAD when their error exceeds a certain tolerance. They are used in conjunction with an orbital model such as SGP4 to predict the satellite pass. However, they have been shown to be relatively inaccurate, [126]. Therefore, TLEs may be suitable for tracking a LEO satellite when the tracking requirements are relaxed, but may not be useful, at least on their own, for tight pointing requirements.

Some satellites, such as FedSat [127], have a GPS as part of their payload. The GPS can log the satellite's position and the data is then downlinked to earth on the Tracking, Telemetry and Command (TT&C) channel. This orbital information is processed and used to predict future passes. The resulting tracking data becomes less accurate the longer the prediction interval is. The research team from the Queensland University of Technology claims that, in the case of FedSat, pointing accuracies of better than 100 m or 0.01° can be maintained for over a prediction period of 48 hours, [127].

The above methods require the earth station to have a separate communications link to the spatial information source (such as the TT&C earth station or the NASA BBS). This is undesirable in the case of remote area communications and for rapidly deployable earth stations. Therefore, it is convenient to have the earth station derive its own spatial tracking data. A number of amplitude based methods are presented in [128]. Monopulse systems utilise multiple, slightly displaced, horn feeds to create overlapping antenna patterns. An error signal is then derived and used to correct the antenna pointing. This technique, however requires very expensive and relatively large equipment and, hence, is undesirable for a low-cost rapidly deployable earth station. In order to reduce cost, sequential amplitude sensing techniques can be applied to a single feed system. These comprise the conical scanning and the step track methods. Both of these methods use time-division multiplexed, spatially distributed signal strength measurements to derive an error signal.

In this chapter we propose a method of deriving the necessary spatial tracking information of a LEO satellite at the earth station without external assistance. We consider the application of the Doppler shift information to the spatial tracking of the satellite. We call this Frequency Assisted Spatial tracking (FAST). We examine the case of LEO satellite with a circular orbit and use the orbital model derived in chapter 3, ignoring all perturbations.

9.2 Doppler Based Position Determination

The tracking of a radiating source using frequency measurements has been dealt with extensively in the literature. This is done primarily in the context of target motion analysis based on sonar Doppler measurements, [129-133]. These papers address the problem of localising a source that radiates a constant frequency tone using multiple sensor data. Other work dealt with the problem of user location using LEO satellites [4]. Position determination using a single satellite is usually considered since LEO satellite constellations are designed to have a minimum number of satellites covering the earth, [134]. Knowing the satellite's orbit precisely, the earth terminal measures the Doppler shift on the received signal for a period of time before being able to determine its own position. Perhaps the most notable example of such a system is the search and rescue Cospas-Sarsat system, [6, 7, 53, 135-138]. In the Cospas-Sarsat system, the

Emergency Locator Transmitter (ELT) of a user in distress emits an amplitude modulated signal. This signal is received by the satellite and relayed to a ground station called the Local User Terminal (LUT). The Doppler shift is measured at the LUT and the resulting data for the entire visible portion of the pass is processed to obtain the ELT location. In some cases, data from multiple passes is used to resolve the ambiguity in the ELT location. The calculated position is then transmitted to a Mission Control Centre (MCC) for search and rescue coordination.

In this work, we are concerned with the reverse problem of satellite orbit determination using frequency measurements at the earth station. This, as stated before, is necessary for the correct pointing of the earth station antenna for successful communications.

9.3 Satellite Orbit Determination

El-Mahy, in [28], applied an Iterated Extended Kalman Filter (IEKF) to measurements of the range, azimuth and elevation in order to determine the satellite orbit. He considered an arbitrary elliptical orbit that is specified by a seven element state vector which consists of the semi-major axis, the eccentricity, the inclination, the right ascension of the ascending node, the argument of the perigee, the mean anomaly and the ballistic coefficient. The first two elements relate to the ellipse and therefore specify the shape of the orbit. The next three elements relate to the relative orientation of the orbit with respect to the frame of reference. The mean anomaly is the average angular motion of the satellite on its orbit [32]. The last orbital element models the shape of the satellite and the effect of atmospheric drag on it. Several radar passes resulting in range, azimuth and elevation measurements are used with an Extended Kalman Filter algorithm to estimate the orbital elements of the satellite.

Montenbruck, in [32], addresses the problem of orbital determination in detail. He considers the various tracking system and their corresponding measurement data in chapter 6. He then linearises the different orbital models that these tracking systems utilise and derives the transitional equations and partial derivatives necessary for the orbital estimation. In chapter 8, the author looks at the weighted least squares approach and the Kalman filtering implementation for orbital estimation. He implements an Extended Kalman Filter processing range, azimuth and elevation measurements to obtain an estimate of the satellite orbit.

Brush *et al*, in [52], describe a system which uses Doppler rate to improve the spatial tracking of LEO satellites. Their method is rudimentary and they do not discuss the update of orbital elements or the satellite's position. They use the orbital elements of the satellite to derive the observed Doppler rate at the earth station. They then correlate the theoretical data to the measurements for an entire pass. The resulting timing error is printed out on the computer screen.

9.4 Frequency Assisted Spatial Tracking

The simplified orbital model derived in chapter 3 gives us some insight into the suitability of frequency and frequency rate information for the purpose of orbital determination and satellite tracking. In this thesis we don't address the problem of Doppler rate estimation. There has been some work reported in the literature on the topic. The estimation of the rate of change of the frequency of a linearly frequency modulated signal is considered in [139-141] and, in [142], Giannetti *et al* examine the Doppler rate estimation problem in the context of LEO satellite communications.

The satellite's position is, for the purpose of antenna pointing, completely specified by the azimuth and elevation pair (or X and Y rotations for an X-Y pedestal). The equations relating the Doppler shift and Doppler rate to the satellite position do not differentiate between passes of the same maximum elevation that are east or west of the earth station. A pass is said to be east of the earth station if its maximum elevation point is east of the earth station. Considering, however, the one-sided case, that is passes only east (or west of the earth station) we find a one to one mapping between a Doppler shift – Doppler rate pair and an azimuth – elevation pair. This is expressed using the following relations

$$\begin{aligned} \varphi_s &= f_1(D_s, D_r) \\ &\text{and} \\ \lambda_s &= f_2(D_s, D_r) \end{aligned} \tag{9.1}$$

This can be seen by plotting the azimuth versus Doppler shift and Doppler rate for the visibility region. The resulting surface gives a single azimuth for each D_s and D_r pair. This also holds for the elevation case. The Doppler shift and Doppler rate contours shown in figure 9.1 on a latitude-longitude plane also demonstrate this. The symmetry

of the contours about the zenith pass is clearly visible. Therefore, a Doppler shift – Doppler rate pair gives two valid satellite positions. In fact, not knowing whether the satellite pass is ascending or descending, results in another ambiguity giving four valid satellite positions. However, as will be shown in section 9.5.2, these conditions can be determined based on the previous satellite pass using simple orbital propagation. Thus, knowing which half of the latitude-longitude plane the pass is in, and whether it is ascending or descending, the earth station can uniquely determine the satellite's position from the measured Doppler shift and rate.

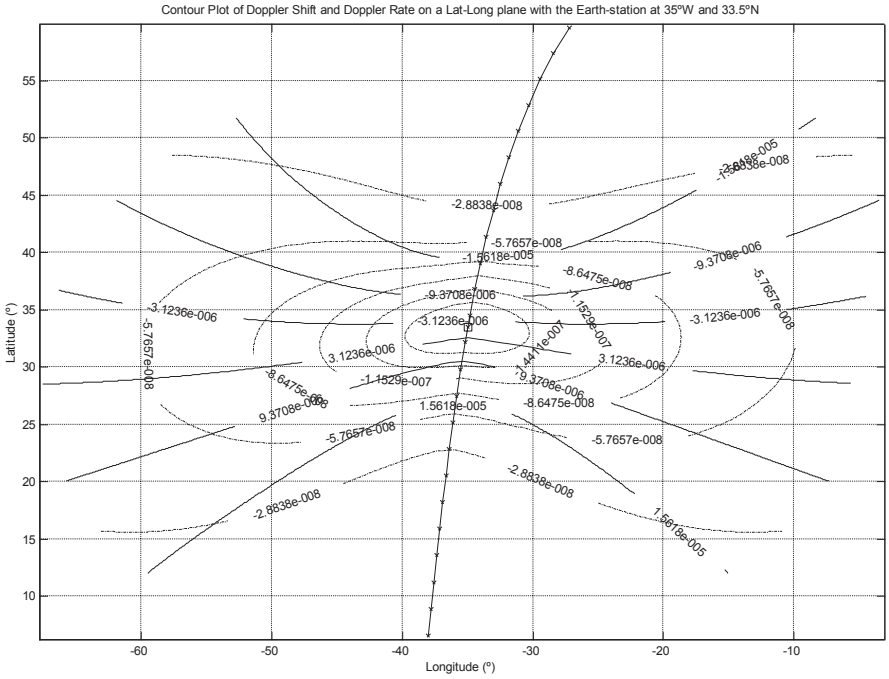

Figure 9.1 – *Doppler shift and Doppler rate contours evaluated using the approximate orbital equations developed in chapter* 3. *The full and dashed lines represent the Doppler shift and Doppler rate respectively. The earth station is marked by the square containing an x and the zenith pass is shown.*

If the rotation of the earth is taken into account, then passes of equal maximum elevation east and west of the earth station give slightly different Doppler shift and Doppler rate profiles. This is due to the fact that the Doppler shift is related to the observed angular velocity of the satellite which, as we found from equation (3.7), depends on the satellite's latitude. Thus, the observed angular velocity profile varies for

equal maximum elevation passes that are east and west of the earth station as they occur at different latitudes. A tracking system can use this fact to uniquely determine the satellite's orbit from the Doppler shift and rate measurements. The asymmetry in the Doppler shift and Doppler rate profiles can be seen in the Doppler shift and rate contours shown in figure 9.2 below.

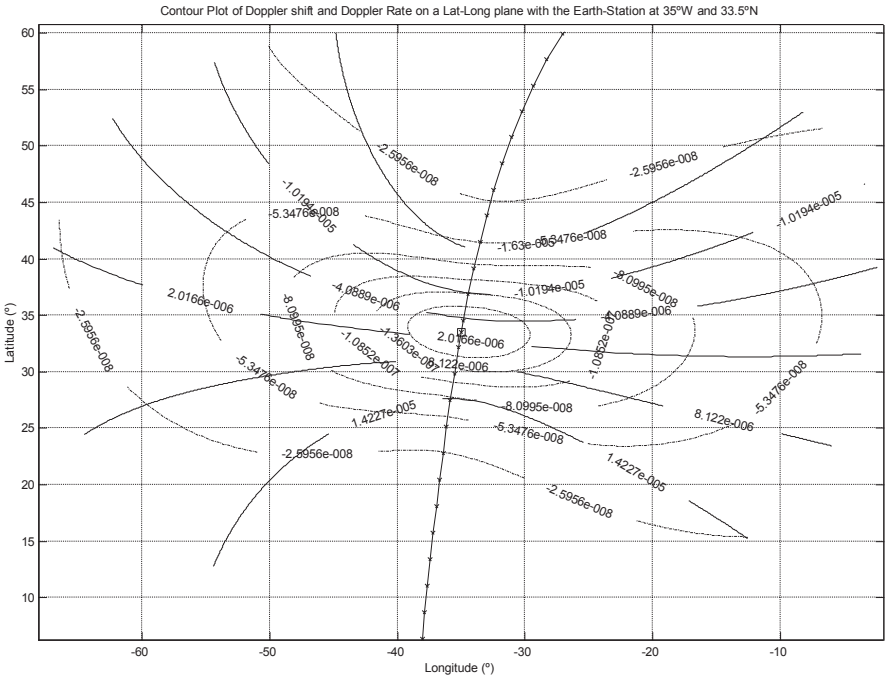

Figure 9.2 – *Doppler shift and Doppler rate contours evaluated using the orbit generation algorithm presented in chapter* 3. *The full lines represent the Doppler shift and the dashed the Doppler rate. The earth station is marked by the square containing an x and the zenith pass is shown.*

Figure 9.3 shows the Doppler shift and rate profiles of two similar maximum elevation passes that are east and west of the earth station. Since the inclination of the satellite orbit is less than 90º, the western orbit occurs at a higher latitude and the observed angular velocity of the satellite, ω_F, is slightly lower. Thus, the resulting Doppler shift and rate profiles are slightly smaller and a little skewed for the western pass with respect to the eastern one. This is clearly visible in the figure below.

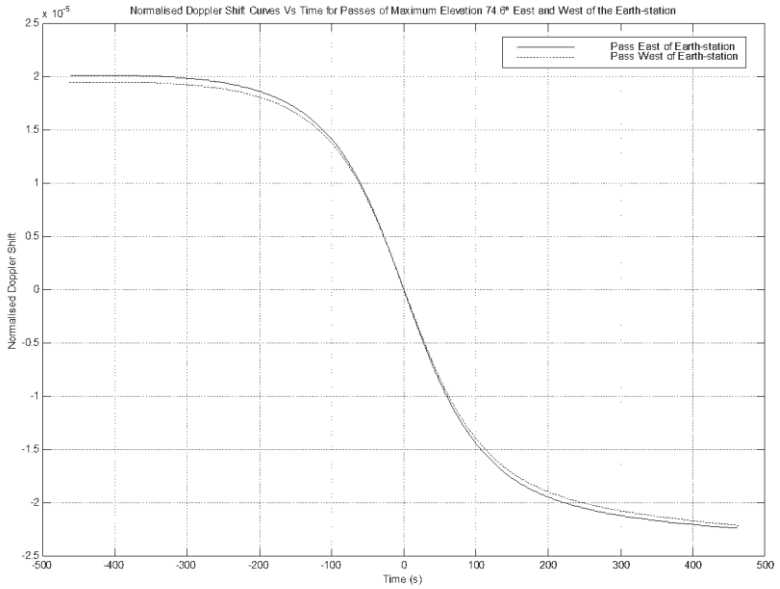

(a)

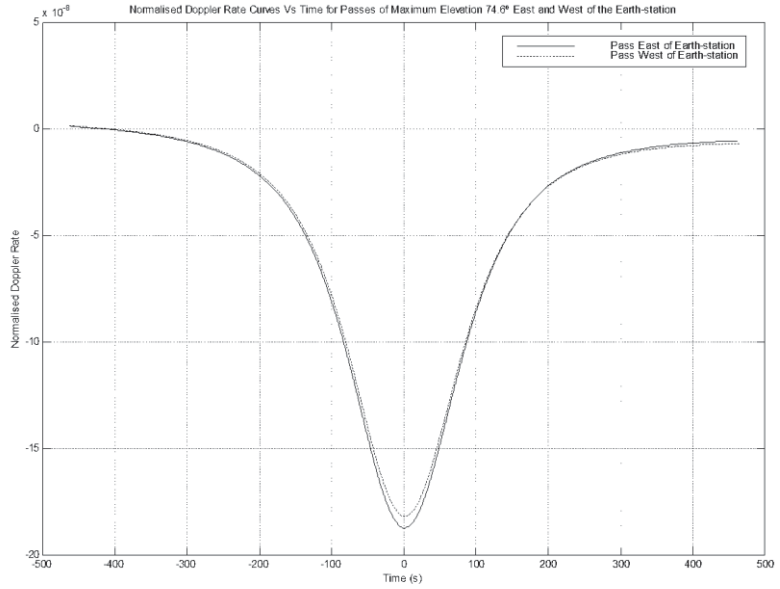

(b)

Figure 9.3 – (a) *Doppler shift and* (b) *Doppler rate curves for passes of maximum elevation 74.6º east and west of the earth station.*

9.5 FAST Implementations Based on Simplified Equations

In [51], the authors looked at the implementation of the FAST concept using a look-up table. A one-dimensional case was analysed where the maximum elevation of the pass

was assumed to be known and the Doppler shift tabulated. The frequency measurements were then used to determine the satellite's position along the orbit. The frequency data was assumed to be Gaussian distributed with a variance equal to the CRB. This gives the limit on the accuracy of the algorithm. The errors were found to be much less than 0.1. The look-up table approach, however, is not attractive due to the large amount of memory it would require to cover the entire visibility region in two dimensions at the necessary sampling rate.

In this section we consider the implementation of the FAST concept based on the simplified orbital equations presented in chapter 3. Expressions for calculating the zero-Doppler time and the maximum elevation of the pass were presented in [103]. These expressions can be used to determine the orbit based on Doppler shift and Doppler rate measurements. This approach is simple but is sensitive to noisy data, [103]. It will, however, be discussed in section 9.5.1 for the purpose of completeness. In section 9.5.2 a method for determining the maximum elevation of a pass based on that of the previous pass is presented. An Extended Kalman Filter spatial tracker is implemented in section 9.5.3 for the one-dimensional case of known maximum elevation.

9.5.1 One-sided FAST Approach

The expressions derived in [103] give the zero-Doppler time, t_0, and the maximum elevation angle, θ_0, in terms of the Doppler shift and rate measurements at two time instants t_1 and t_2. Once t_0 and θ_0 are found, the entire visible section of the pass can be calculated and the satellite tracked. As discussed in section 9.4, however, the symmetry of the equations about the zenith pass results in an ambiguity with respect to the quadrant that the satellite is in.

Given two Doppler shift and Doppler rate measurements (D_{s1}, D_{r1}) and (D_{s2}, D_{r2}) at times t_1 and t_2 respectively, with $t_2 > t_1$, the maximum elevation time is given by

$$t_0 = t_1 - \frac{\overline{\psi}_1}{\omega_F} \tag{9.2}$$

where

$$\overline{\psi}_1 = \tan^{-1}\left(\frac{D_{s1}D_{s2}^3\omega_F + D_{s1}^3 D_{r2}\sin(\omega_F \Delta t) - D_{s1}^3 D_{s2}\omega_F \cos(\omega_F \Delta t)}{D_{r1}D_{s2}^3 - D_{s1}^3 D_{r2}\cos(\omega_F \Delta t) - D_{s1}^3 D_{s2}\omega_F \sin(\omega_F \Delta t)} \right) \tag{9.3}$$

and

$$\Delta t = t_2 - t_1 = T_s$$

T_s is the spatial sampling period. Taking t_0 by convention to be the reference time, we let $t_0 = 0$. Therefore,

$$t_1 = \frac{\overline{\psi}_1}{\omega_F}$$

The central angle at the maximum elevation point, γ_0, is then calculated using

$$\gamma_0 = \cos^{-1}\left(\frac{-c^2 D_{s1}^3}{r_e r \omega_F \left[D_{r1}\sin(\overline{\psi}_1) - D_{s1}\omega_F \cos(\overline{\psi}_1) \right]} \right) \tag{9.4}$$

Substituting γ_0 into equation (3.29) gives the maximum elevation angle θ_0.

A straightforward implementation of the above expressions is very sensitive to noise. Simulations show that, even at high SNR values, the equations fail to give any meaningful result. This is mainly due to the sensitivity of γ_0 to noisy D_s and D_r measurements. This situation becomes worse as we get closer to the zenith pass due to the flatness of the cosine in expression (9.4) near the point $\gamma_0 = 0$. The authors of [103] recognised this and suggested that further research would be necessary to improve the algorithm's performance by reducing its sensitivity to noise.

An alternative to the above implementation is to use an Extended Kalman Filter (EKF) to estimate the satellite position based on the frequency information. We assume that the maximum elevation is known and derive a scalar EKF using only the Doppler shift information to filter out the satellite position. This method amounts to determining the satellite's position along the pass. As this relies on knowledge of the maximum elevation for the upcoming pass, we present in the following section a method for calculating the maximum elevation angle of the next pass based on that of the current one. The EKF is then derived in section 9.5.3.

9.5.2 Calculation of the Expected Maximum Elevation Point

In this section we present a method for predicting the maximum elevation of a pass based on observatons from the pass immediately preceding it. In [11], the authors present an algorithm for determining whether a pass is visible from a specific terminal location. They characterise the pass by the longitude of its ascending node and calculate γ, the central angle between the satellite and the earth station, at the point of closest approach. If γ is smaller than the angle corresponding to the minimum elevation for visibility, then the satellite would be visible from the terminal. In this section, we calculate the longitude of the ascending node of the available pass and propagate it to give the longitude of the ascending node of the next pass. That is we adjust it by the angle the earth rotates through in one complete satellite revolution. We then use the method of [11] to determine whether the satellite is visible from the earth terminal. If it is, we calculate the expected maximum elevation and its location.

Let the position of the satellite maximum elevation point of pass p be $\left(\lambda_0^p, \varphi_0^p\right)$ and that of pass $p+1$ be $\left(\lambda_0^{p+1}, \varphi_0^{p+1}\right)$. The following analysis refers to figure 3.5 which will be reproduced here for the reader's convenience.

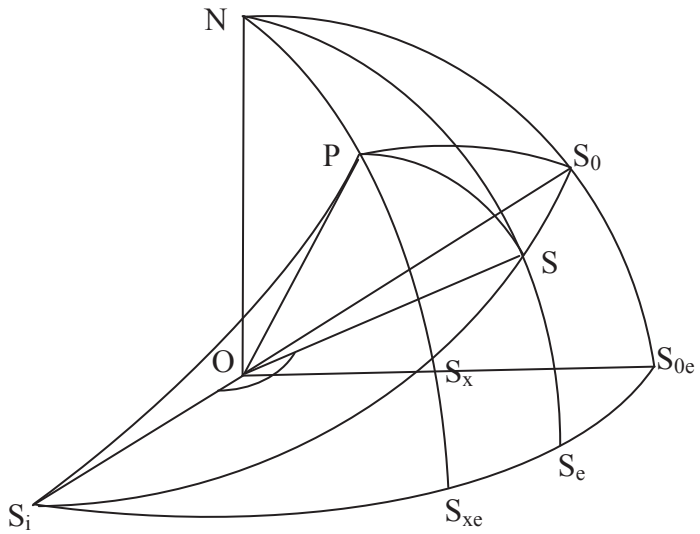

Figure 9.4– *A reprint of figure 3.5; enlarged view of sub-satellite path.*

Consider pass p. The maximum elevation point corresponds to point S_0. Applying spherical identities (A.3) and (A.6) and combining the results we obtain

$$\sin\left(\lambda_0^p - \lambda_i^p\right) = \frac{\tan\left(\varphi_0^p\right)}{\tan(i)} \tag{9.5}$$

The longitude of the ascending node of pass p is therefore given by

$$\lambda_i^p = \lambda_0^p - \sin^{-1}\left(\frac{\tan\left(\varphi_0^p\right)}{\tan(i)}\right) \tag{9.6}$$

The angular displacement of the ascending node from the maximum elevation point, ψ_i^p, is

$$\psi_i^p = \sin^{-1}\left(\frac{\sin\left(\varphi_0^p\right)}{\sin(i)}\right) \tag{9.7}$$

λ_i^p must then be modified by the angle the earth rotates in the time the satellite takes to move through ψ_i^p. Therefore we have

$$\lambda_i^p = \lambda_0^p - \sin^{-1}\left(\frac{\tan\left(\varphi_0^p\right)}{\tan(i)}\right) + \omega_e\left(\frac{\psi_i^p}{\omega_I}\right) \tag{9.8}$$

Finally λ_i^p is propagated by the angular movement of the earth during one satellite orbital period in order to get that of pass $p+1$. Thus,

$$\lambda_i^{p+1} = \lambda_i^p - \omega_e \frac{2\pi}{\omega_I} \tag{9.9}$$

If the ascending node of a pass is east of that of another pass then the maximum elevation point of the first pass will also be east of that of the other pass. Therefore, comparing the longitude of the ascending node of pass $p+1$ to that of the zenith pass, λ_{iz}, allows the terminal to determine if the pass is east or west of it. λ_{iz} can be found by substituting $\varphi_0 = \varphi_{ES}$ and $\lambda_0 = \lambda_{ES}$ in equation (9.8).

Next, the maximum elevation angle is determined from the longitude of the ascending node of the pass. Taking the ascending node to be the time reference, equations (3.23) and (3.27) are modified to give (λ, φ), the position of the satellite in the ECEF frame at time t,

$$\varphi = \sin^{-1}\left(\sin(i)\sin(\omega_I t)\right) \tag{9.10}$$

and

$$\lambda = \lambda_i + \cos^{-1}\left(\frac{\cos(\omega_I t)}{\cos(\varphi)}\right) - \omega_e t \tag{9.11}$$

As the pass in the ECEF frame is assumed to be a great circle arc, two points, S_a and S_b, given by (λ_a, φ_a) and (λ_b, φ_b), are required to define it. Let S_a and S_b be the ascending node, S_i, and the location of the satellite at time Δt from S_i. Therefore, the first point is given by $(\lambda_i^{p+1}, 0)$ and the second point is obtained from equations (9.10) and (9.11). Without loss of generality, the analysis is carried out on a unit sphere (that is the earth's sphere is taken as the unit measure). Denote the vectors originating at the earth's centre and ending at the two points S_a and S_b by $\mathbf{v}_a$ and $\mathbf{v}_b$. These are given by

$$\mathbf{v}_a = \begin{bmatrix} \cos(\lambda_i^{p+1}) \\ \sin(\lambda_i^{p+1}) \\ 0 \end{bmatrix} \tag{9.12}$$

and

$$\mathbf{v}_b = \begin{bmatrix} \cos(\varphi_b)\cos(\lambda_b) \\ \cos(\varphi_b)\sin(\lambda_b) \\ \sin(\varphi_b) \end{bmatrix} \tag{9.13}$$

where

$$\varphi = \sin^{-1}(\sin(i)\sin(\omega_I \Delta t))$$

and

$$\lambda = \lambda_i + \cos^{-1}\left(\frac{\cos(\omega_I \Delta t)}{\cos(\varphi)}\right) - \omega_e \Delta t$$

The earth station location, given by $\mathbf{v}_{ES}$ is

$$\mathbf{v}_{ES} = \begin{bmatrix} \cos(\varphi_{ES})\cos(\lambda_{ES}) \\ \cos(\varphi_{ES})\sin(\lambda_{ES}) \\ \sin(\varphi_{ES}) \end{bmatrix} \tag{9.14}$$

At the point of closest approach, the arc joining the earth station to the sub-satellite point, that is arc PS_0 in figure 9.4, is normal to the sub-satellite path. The unit normal to the plane defined by $\mathbf{v}_a$ and $\mathbf{v}_b$ is obtained from the cross product of these two vector. Hence,

$$\mathbf{n} = \frac{\mathbf{v}_a \times \mathbf{v}_b}{\left|\mathbf{v}_a \times \mathbf{v}_b\right|} \tag{9.15}$$

The perpendicular distance from the earth station to the satellite orbit, distance PS_0, is given the projection of the earth station vector $\mathbf{v}_{ES}$ onto the unit normal $\mathbf{n}$. That is, it is equal to the dot product between vectors $\mathbf{v}_{ES}$ and $\mathbf{n}$. The corresponding central angle, γ_0, given by POS_0 in the figure above, is

$$\begin{aligned} \gamma_0 &= \sin^{-1}\left(\frac{\mathrm{PS}}{\mathrm{OS}}\right) \\ &= \sin^{-1}\left(\mathbf{v}_{ES} \cdot \mathbf{n}\right) \end{aligned} \tag{9.16}$$

γ_0 can now be substituted into equation (3.29) to give the maximum elevation angle of the pass. The location of the sub-satellite point at the point of closest approach, given by vector $\mathbf{v}_0$, is

$$\mathbf{v}_0 = \frac{1}{\cos(\gamma_0)}\left(\mathbf{v}_{ES} - \left(\mathbf{v}_{ES} \cdot \mathbf{n}\right)\mathbf{n}\right) \tag{9.17}$$

The location of the maximum elevation point in the latitude-longitude coordinate system is calculated from $\mathbf{v}_0$ and the time of closest approach, t_0, is found by substituting the value of φ into equation (9.10).

As we move away from the points used to define the great circle arc, the actual orbit deviates from the approximation. Therefore, it is important to refine the estimate of the maximum elevation point by using two points closer to the instant of closest approach, say at times $t_0 - \Delta t$ and $t_0 + \Delta t$. The steps outlined above are then repeated and a refined estimate of the maximum elevation point obtained.

The algorithm presented here was simulated in Matlab. The earth station was placed at 35º west and 33.5º north. An initial longitude for the ascending node was specified and two successive passes calculated using the orbital propagation algorithm of section 3.3. The maximum elevations of passes one and two were determined using the algorithm

presented here and the data corresponding to pass one. Δt was set to 120s. That is for the first iteration in the orbit approximation, the second point was chosen to be 2 minutes after the ascending node. For the second iteration, the two points were 2 minutes either side of the maximum elevation point.

The actual and predicted maximum elevations are shown in figure 9.5. The maximum elevation of pass one was predicted by back-propagating its actual value and applying the prediction algorithm. This involved calculating the longitude of the ascending node of the pass using the actual value of the maximum elevation angle and then recalculating the maximum elevation using the great circle arc approximation. The true and predicted curves are shown by the solid line and the 'x', respectively, in figure 9.5. This method allows the assessment of the errors resulting from the great circle approximation. The dashed line and the 'o' show the results for the forward propagation and prediction of the maximum elevation of pass 2 based on the maximum elevation of pass 1 and its location. The resulting errors between the two curves for both cases of passes 1 and 2 are shown in figure 9.6. The error curve for pass 1 results solely from the great circle arc approximation whereas that for pass 2 also includes the forward propagation error of the longitude of the ascending node. We can see that the two curves are nearly identical in shape but shifted with respect to one another. This implies that the error in the propagation of the longitude of the ascending node is very small. In fact, an examination of this error reveals that it is in the order of 10^{-5} degrees.

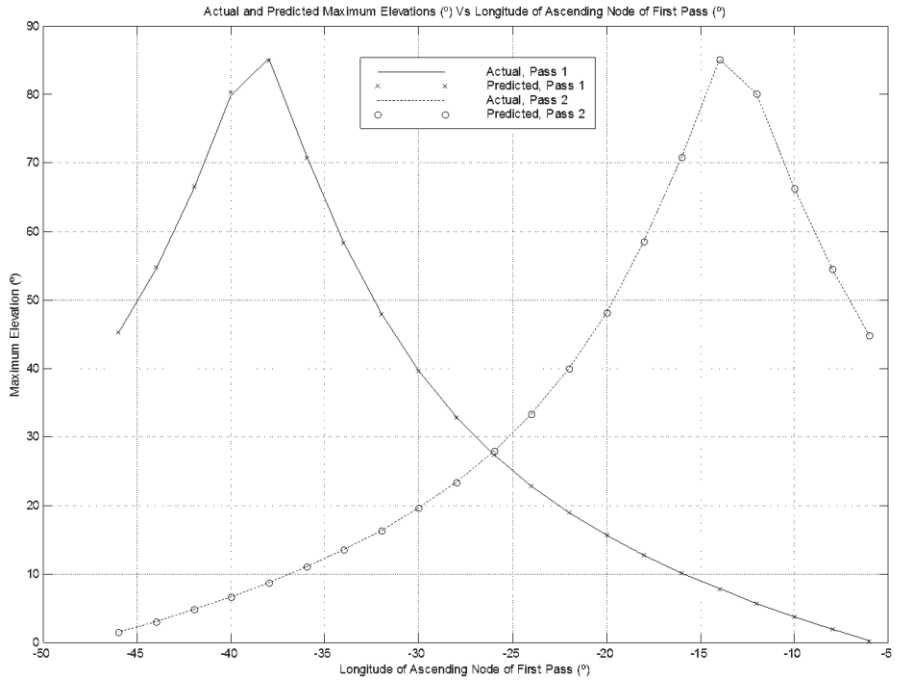

Figure 9.5 – *Actual and predicted maximum elevations for passes 1 and 2.*

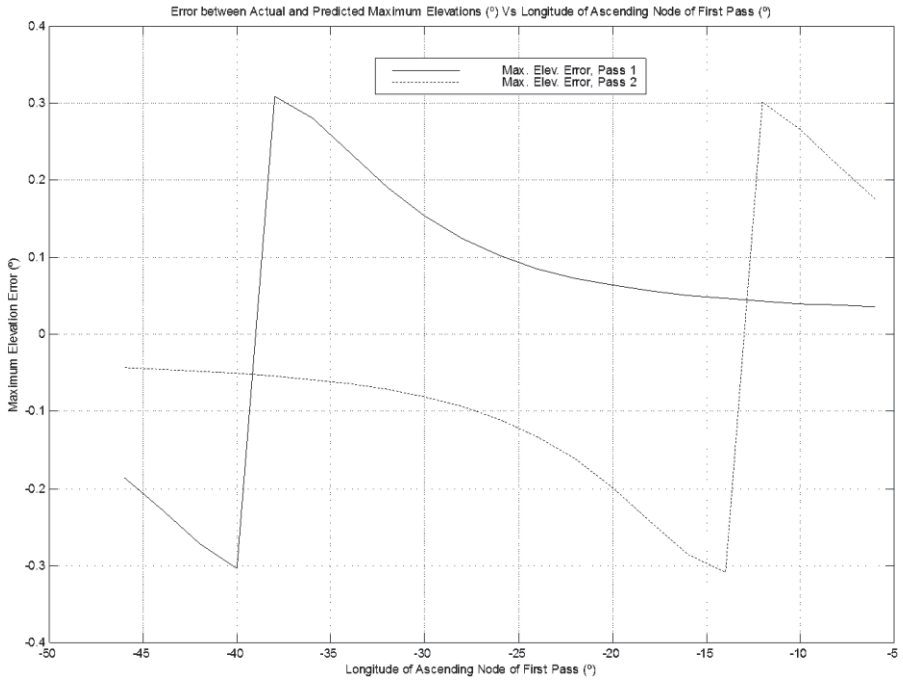

Figure 9.6 – *Errors in the predicted maximum elevations for passes 1 and 2.*

Figure 9.7 shows the errors in the longitudes and latitudes of the predicted maximum elevation positions of pass 2. The axis on the left belongs to the longitude error curve, marked with 'x', while that on the right is for the latitude error curve marked with circles. The errors are in the order of a 0.01º which validates the algorithm presented here as a method of predicting the value and location of the maximum elevation of a pass based on data from the preceding pass.

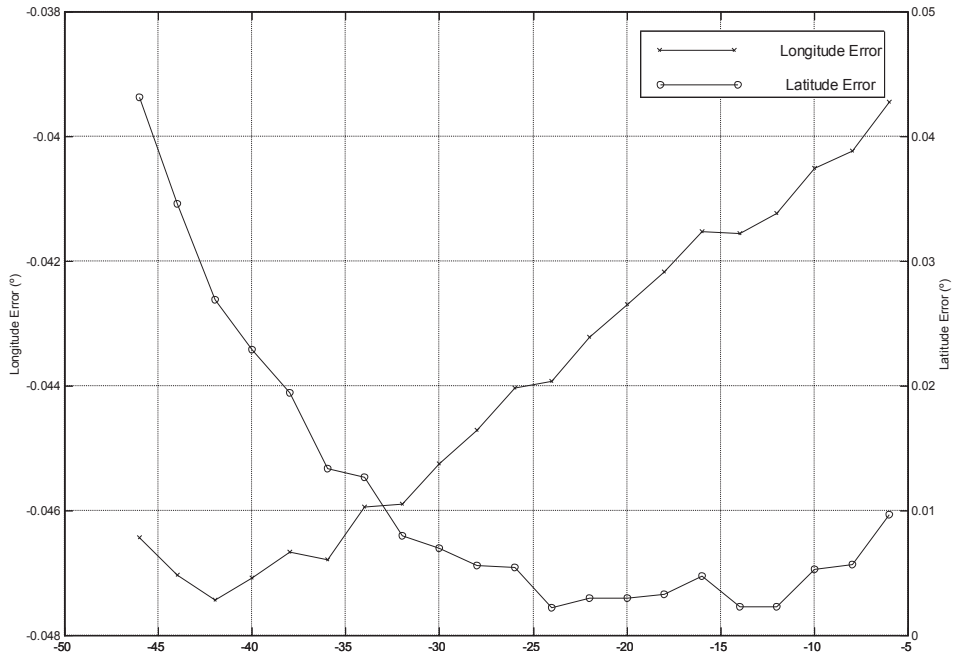

Figure 9.7 – *Error in the predicted locations of the maximum elevations for pass 2.*

9.5.3 Extended Kalman Filter for the Simplified Model

The non-linear equations presented in section 9.5.1 suffer from poor performance in the presence of noise. Therefore, a filtering scheme must be employed in order to improve the algorithm. Although a linearised Kalman filter would have also been suitable, we will in this section use an EKF to implement the FAST concept based on the simplified orbital model. For a discussion of Kalman filtering theory refer to section 2.4. We will assume the maximum elevation to be known and derive the filter and update equations.

9.5.3.1 Derivation of the EKF with the Maximum Elevation assumed known

Assuming the maximum elevation of the pass is known, the whole pass can be calculated using the simplified orbital equations of chapter 3. The tracking problem essentially reduces to the determination of the timing of the satellite along the pass. We will here derive and implement a scalar EKF that uses the Doppler shift information to estimate ψ, the angular displacement of the satellite from the maximum elevation point. The ability of a terminal to do this stems from the fact that estimating the frequency of a satellite beacon is normally achieved even with large antenna pointing error. Thus the Doppler shift information is usually available before the communications link is closed and can be used to reduce the antenna pointing error. In a practical spatial tracking system, the EKF can be combined with the maximum elevation determination algorithm presented in the previous section to characterise the pass and then locate the satellite along it. Upon the conclusion of the period of visibility, the maximum elevation prediction algorithm is used to predict the maximum elevation value of the next pass and set up the EKF for tracking the satellite.

In the following we proceed to derive and implement the scalar EKF spatial tracker. Let the state variable be ψ. The state transition equation is

$$\psi_{n+1} = \psi_n + \omega_F T_s$$

where T_s is the spatial sampling period. The measurements consist of the Doppler shift values and the measurement equation is

$$D_{sn} = f(\psi_n)$$

where f is the Doppler expression given in equation (3.45).

The state transition factor, ϕ, is 1 and the observation factor is given by the derivative of the Doppler with respect to the state variable,

$$\begin{aligned} m &= \frac{dD_s}{d\psi} \\ &= -\frac{1}{c} r_e r \omega_F \cos(\gamma_0) \frac{\left(r^2 + r_e^2\right)\cos(\psi) - r_e r \cos(\gamma_0)\left(1 + \cos^2(\psi)\right)}{s^3} \end{aligned}$$

The Kalman filtering procedure comprises the following steps:

- Set the initial value of ψ to the maximum value based on the known maximum elevation angle. That is, calculate the visibility duration, T_v, of the pass for the expected maximum elevation angle. The initial value for ψ is then given by $-\omega_F T_v / 2$.
- Initialise the variance of the measurement errors σ_f^2. The Doppler shift is usually measured at a much higher sampling rate than the spatial tracking. In the case of FedSat, for instance, the frequency measurement rate is 100 times the spatial update rate. Thus, the variance of the Doppler measurements can be calculated from the measurements themselves. This is advantageous as the quality of the frequency measurements normally improves as the elevation of the satellite increases.
- Set the initial value of p to 0.25. This accounts for the error in the initial value of ψ.
- Set the value of σ_ψ^2 to 0.1. This accounts for the model errors arising from the assumptions used.

Iterate through the following steps:

- Propagate the state variable

$$\psi_n^* = \hat{\psi}_{n-1} + \omega_F T_s$$

- Update the Kalman gain

$$K_n = \frac{p_{n-1} m_n}{\sigma_f^2 + m_n^2 p_{n-1}}$$

- Filter the state variable

$$\hat{\psi}_n = \psi_n^* + K_n \left[D_{sn} - f\left(\psi_n^*\right) \right]$$

- Update the mean square error

$$p_n = \left(1 - K_n m_n\right) p_{n-1} + \sigma_\psi^2$$

The filter was implemented in Matlab and its performance simulated. Figure 9.8, below, shows the performance in an almost noiseless case (with the signal to noise ratio set to 100 dB). The pass has a maximum elevation of 74.6º. The two curves were

obtained for each of the ECEF angular approximation strategies discussed in section 3.4. The off-boresight error has a local maximum at the point of closest approach. This is due to the fact that the observed satellite velocity in the direction perpendicular to the earth station to satellite line of sight is highest at that point. Thus, at that instant, the look-angles experience their highest rates of change.

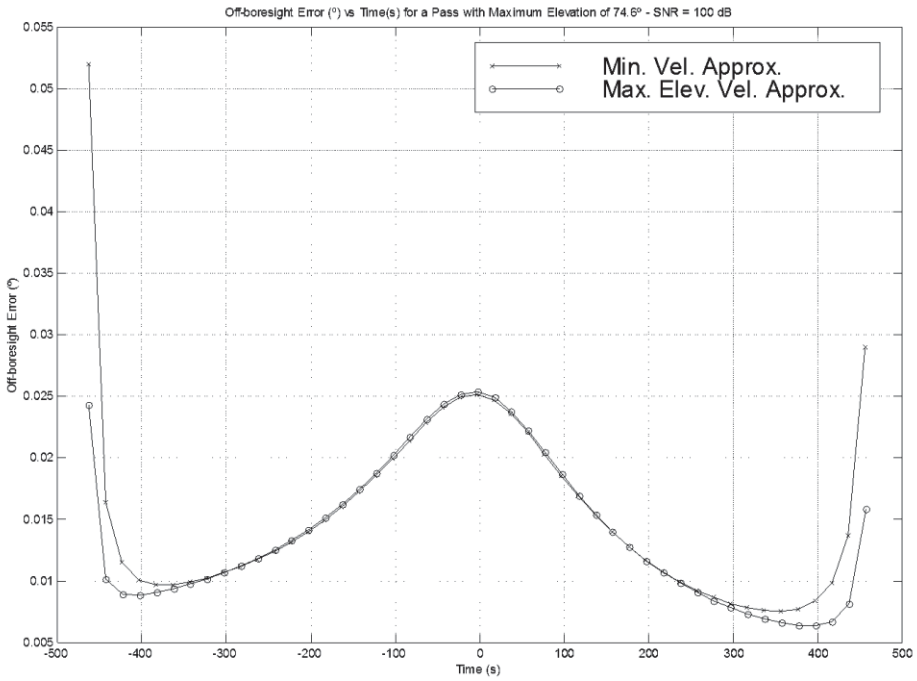

Figure 9.8 – *EKF spatial tracker performance in the noiseless case.*

Figure 9.9 shows the actual and tracked sub-satellite paths as well as the resulting off-boresight error at a SNR of 0 dB. A pass with a maximum elevation of 74.6º was chosen and the earth station placed at 35º west and 33.5º north. We can see that the two paths, shown in latitude-longitude coordinates, agree well. The off-boresight error is for the majority of the pass below 0.2º. Communications with a LEO is commonly only practical above 20º or 30º elevations, depending on the earth station environment and available link margin. The maximum tolerable off-boresight error is also dependent on the available link margin. For the FedSat Ka band communications link, for instance, the minimum visibility angle is taken to be 30º and the maximum allowable off-boresight error is 0.3º, [2]. From figure 3.6 we see that a minimum elevation angle for visibility of 30º results in a visibility duration of just over 300 seconds for a pass with a

maximum elevation of 74.6º. The lower plot in figure 9.9 shows that the off-boresight error is much less than 0.1º between -150 s and 150 s.

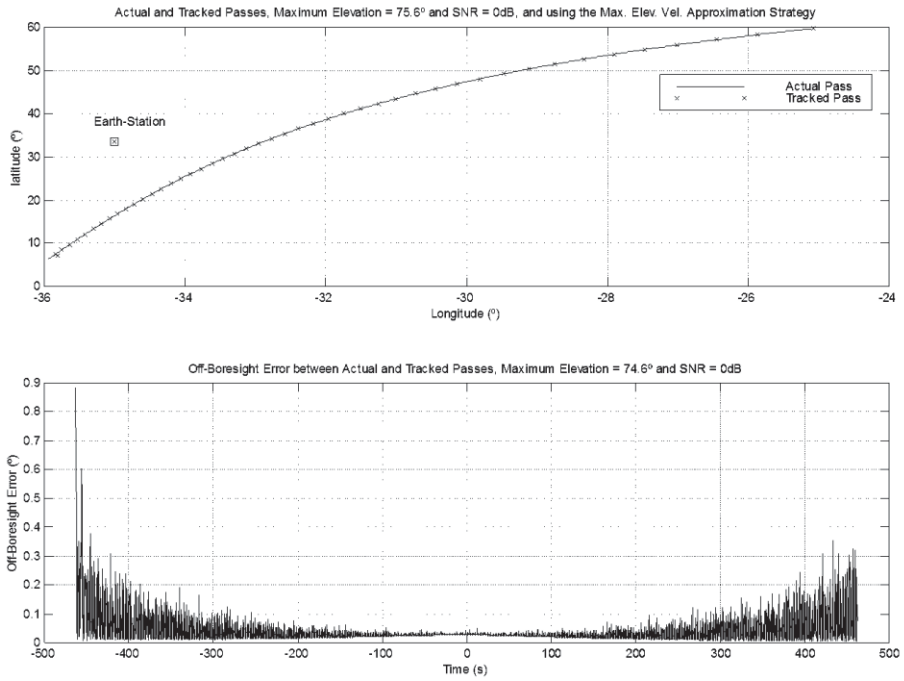

Figure 9.9 – *EKF spatial tracker performance at a SNR of 0dB.*

Figure 9.10, below, shows the filter performance for different signal to noise ratios. A Monte Carlo simulation comprising 1000 runs was performed at each SNR value. The mean off-boresight error is shown against time from the maximum elevation point. As the SNR decreases, the off-boresight error increases as expected. The central lobe at the maximum elevation point, that is, at zero time, is only visible at the higher SNR and is drowned by the effect of the noise as the SNR decreases. This is due to the fact that the noise effects bring the off-boresight error up over the entire pass and therefore obscure the modelling error. The plot also shows that the performance of the filter is very good, with an off-boresight error below 0.1º, at the low SNR of -10 dB. This SNR is close to the frequency estimation threshold for the FFCI (and IFFCI) algorithm operating on 1024 data samples, see figure 6.2. Hence, we expect that the frequency estimation threshold would form the limit of the usefulness of the frequency based tracking system proposed here.

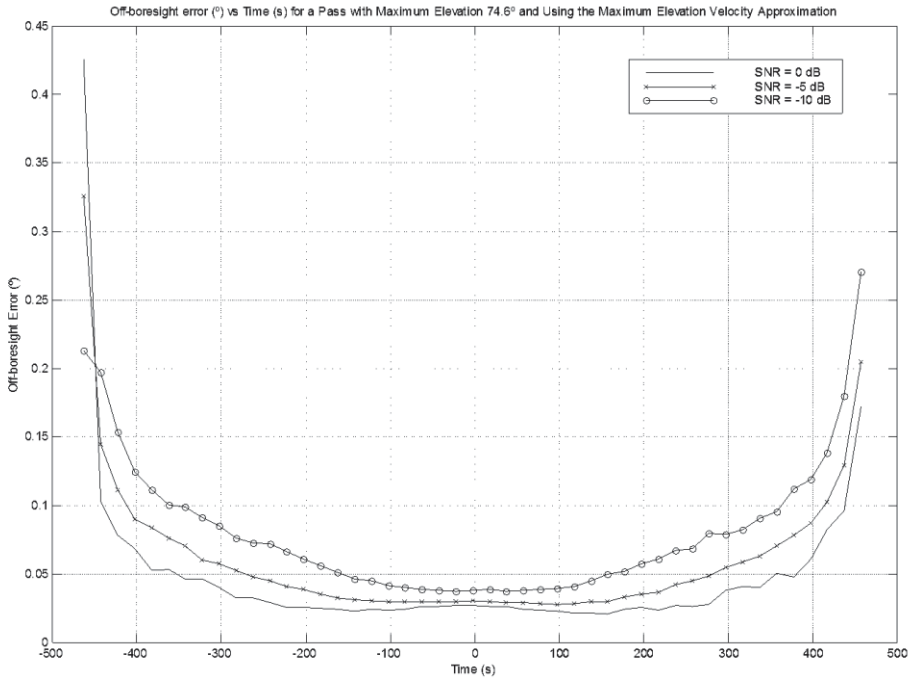

Figure 9.10 – *Off-boresight error for scalar EKF against time for different signal to noise ratios.*

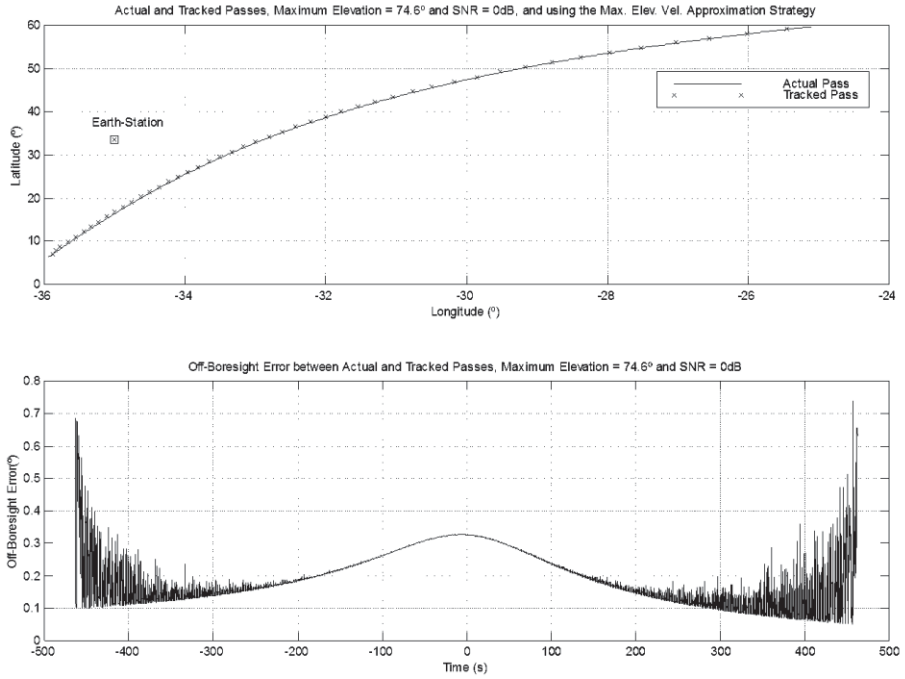

Figure 9.11 – *EKF spatial tracker performance at a SNR of 0dB with a 0.3° error in the assumed maximum elevation value.*

Figure 9.11 above shows the effect of an error in the predicted maximum elevation angle on the filter performance. We see that the off-boresight error at the point of closest approach has increased to just over 0.3º. This is much higher than the error seen as a result of the noise alone. We also see that the central lobe around the maximum elevation point reappears. This is due to the fact that the dominant error is due the orbit approximation. The filter assumes the maximum elevation angle, θ_0, is known and operates only on the corresponding pass. It is, therefore, sensitive to errors in the predicted value of θ_0. This characteristic is clearly visible in the results of the Monte Carlo simulation shown in Figure 9.12 below. The simulation consisted of 1000 runs. The maximum off-boresight error is the middle of the pass is just over 0.3º.

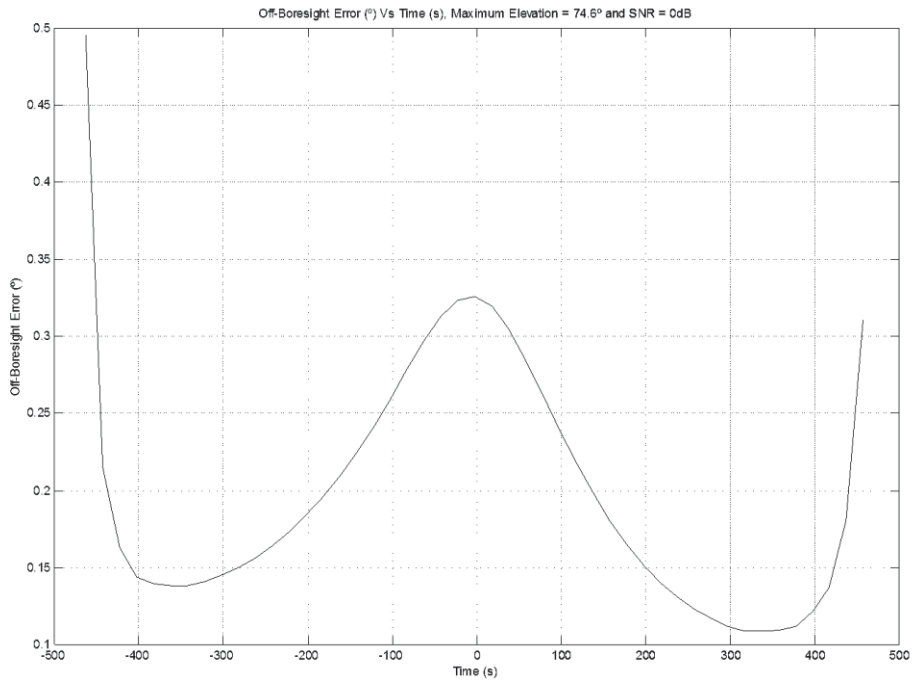

Figure 9.12 – *EKF spatial tracker performance at a SNR of 0 dB with a 0.3º error in the assumed maximum elevation value.*

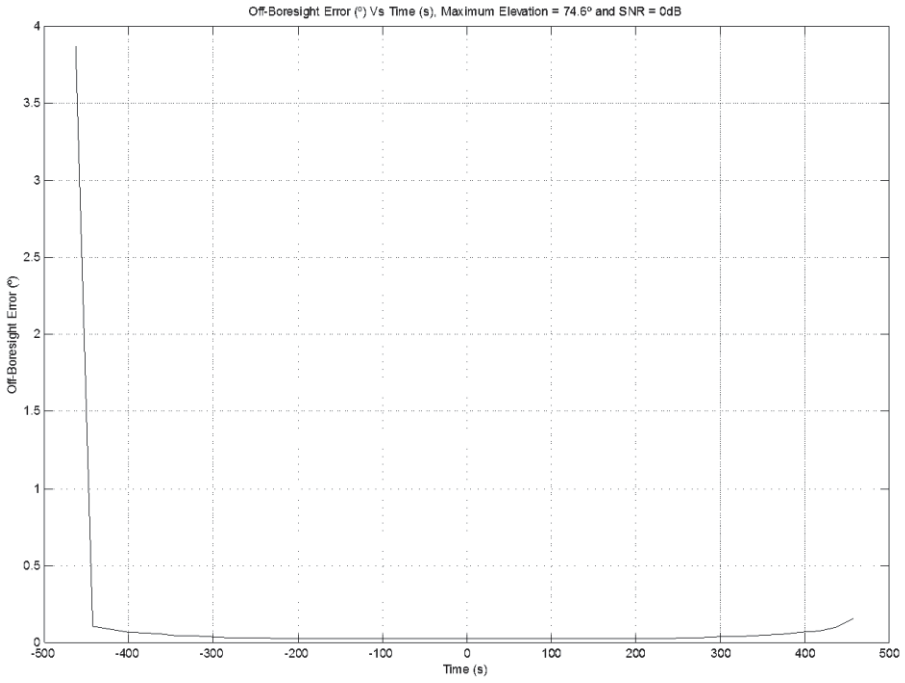

(a)

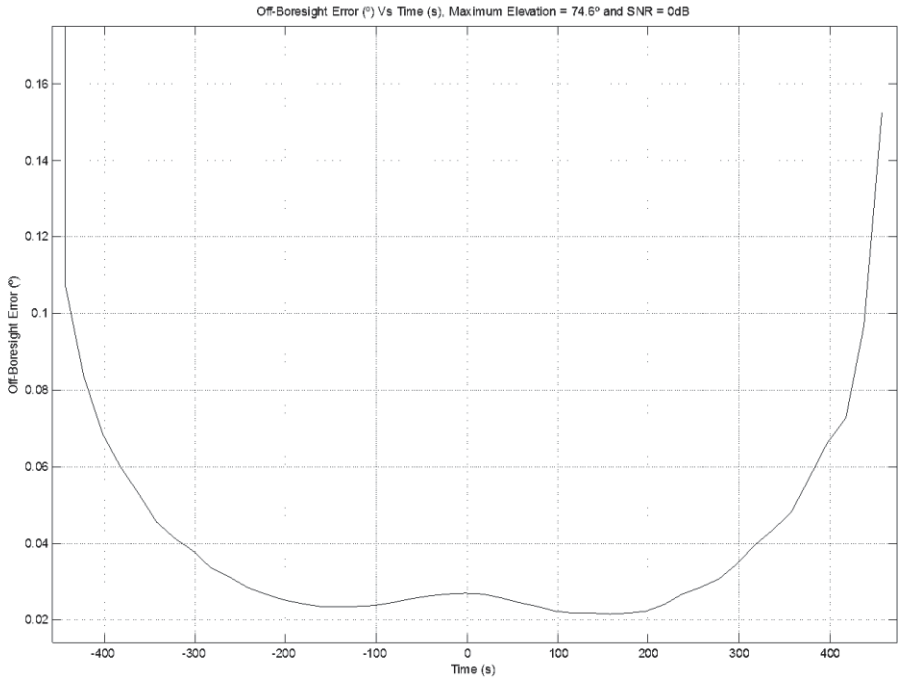

(b)

Figure 9.13 – (a) *EKF spatial tracker performance at a SNR of 0 dB. A zero-mean random (Gaussian distributed) error, with a 5° standard deviation was added to the initial value of* ψ. (b) *Zoomed version of (a).*

Figures 9.13(a) and (b) show the effect of errors in the initial conditions of ψ on the filter performance. Although the filter is sensitive to errors in the assumed value of the maximum elevation, it would be expected to be tolerant to errors in the initial conditions of the state variable. Figure 9.13 confirms this by showing a large initial off-boresight error which is then taken out by the filter and reduced to a similar order to the case reported in figure 9.8 where ψ is correctly initialised.

9.6 Conclusion

We have, in this chapter, proposed the use of the Doppler shift information to assist the spatial tracking of a LEO satellite. The Doppler shift and rate were shown to form a basis for the look-angles required to spatially track the satellite. In section 9.5.2 we presented an algorithm for predicting the maximum elevation of a pass based on the pass preceding it. The FAST concept was then implemented in the one-dimensional case by making the assumption that the maximum elevation of the orbit is known a priori. The simplified orbital model, developed in chapter 3, was used to derive the tracking and update equations of a scalar EKF spatial tracker. The filter was then simulated and its performance assessed. It was shown to have an off-boresight error in the order of 0.1°. We also examined the filter's sensitivity to the model errors, such as errors in the expected maximum elevation angle and to errors in the initialization of ψ. As was expected, the filter was found to be tolerant to errors in the initial value of ψ. It is, on the other hand, sensitive to errors in the expected maximum elevation angle, as it cannot "see" and remove these errors.

Chapter 10

Conclusion

10.1 Review of Research Results

The aim of the dissertation is twofold; firstly, the frequency estimation problem for the purpose of the Doppler compensation of a LEO satellite link is studied. Secondly, the possibility of applying the measured Doppler shift information to assist the spatial tracking of the satellite is examined. The research was motivated by the FedSat project which is run by the Cooperative Research Centre for Satellite Systems. This project will culminate in the launch of FedSat, an experimental LEO micro-satellite, into an 800 km sun-synchronous orbit. The satellite will have, as part of its payload, a Ka band communications experiment.

The relative motion between a LEO satellite and an earth station induces Doppler shifts into the transmitted signal. These shifts must be estimated and removed prior to the demodulation of the signal. In the thesis we assumed the presence of a beacon signal. Thus the research dealt with the estimation of the frequency of an unmodulated sinusoidal signal.

The highly dynamic environment of a LEO satellite link limits the available processing time and therefore dictates that the estimation algorithms be computationally simple. Furthermore, the high Ka band frequencies experience large attenuation and result in a narrower beam width for a given antenna. Therefore, the frequency estimators that are employed must perform well at low signal to noise ratios.

In chapter 2, we presented the necessary theory for the development of the ideas put forward in the thesis. We also included a review of the general literature. We then proceeded to report on the research outcomes. In the following, we will review these outcomes in the light of the stated research aims.

10.1.1 Orbital Characterisation

The low earth orbit was modeled in chapter 3. We assumed a spherical earth and used a first order model ignoring all perturbations. This served to develop a simple orbital propagator which was compared to results obtained from the program STK and found it to be accurate. We then proceeded to obtain the spatial characterisation of the orbit as a function of the observed maximum elevation angle at a particular earth station. The analysis was done in the ECEF frame of reference. We approximated the orbit by a great circle arc and assumed the observed angular velocity of the satellite to be constant. These approximations are justified by the short visibility period of a LEO satellite and by the high velocity of the satellite with respect to the earth's rotation upon its axis. Ali *et al*, [103], suggested the approximation of the angular velocity by its minimum value, which occurs at the highest latitude reached by the satellite. We, on the other hand, propose the use of the value that is observed at the maximum elevation angle. We showed that this gives better results as it spreads the error more evenly over the visibility duration. Next, we presented simplified equations for the satellite latitude, longitude, azimuth, elevation and X and Y rotations. We showed that the off-boresight error for the satellite's position, that is the angular error that is observed at the earth station, is around 0.3º. Finally, we completed the characterisation of the orbit by giving the simplified Doppler shift and Doppler rate expressions as a function of the maximum elevation angle.

10.1.2 Frequency Estimation

The material of chapter 3 is mostly relevant to the FAST concept of chapter 9. In chapters 4 to 8 we addressed the problem of estimating the frequency deviation of the received signal. The techniques we adopted in this dissertation consist of a coarse frequency search followed by a fine estimation algorithm. The coarse search was implemented using the Maximum Bin Search (MBS) algorithm. We proposed and analysed a number of novel fine frequency estimation techniques.

10.1.3 Threshold effects

The frequency estimation algorithm must perform well at low SNR and be computationally simple. The advent of digital signal processors has resulted in computationally efficient implementations of the FFT algorithm. Furthermore, frequency domain frequency estimators enjoy a better performance at low SNR values than comparable time-domain estimators. This is due to the fact that they avoid the phase unwrapping problem and achieve the best possible smoothing of the signal phase. These factors have resulted in the research effort being directed towards the FFT based frequency estimators. In chapter 4, we discussed the MBS algorithm which forms the coarse estimation stage. This consists of calculating the periodogram and choosing the frequency corresponding to the highest bin. The resulting estimate for N samples of data is $O\left(N^{-1}\right)$. This motivates the use of a fine frequency stage to achieve a resolution that is closer to the CRB. As the SNR drops, however, the probability of choosing an incorrect bin, called an outlier, increases. The expression for the outlier probability was derived by Rife and Boorstyn, in [112], under the assumption of AWGN. The expression for the outlier probability, however, is complicated and must be evaluated numerically. As the SNR decreases, a threshold effect, common to nonlinear estimators, is observed. Quinn, [9], derives an approximate expression for the threshold SNR. He obtains upper and lower bounds for the outlier probability. He then defines the onset of the threshold as the point where the total frequency MSE is equal to twice the CRB. This results in an approximate expression of the threshold SNR. We showed, however, that he made an error in the bound calculations and derived the correct form of the threshold SNR. The corrected form, however, is only of theoretical interest (and for the sake of correctness) as the difference between it and Quinn's expression is almost negligible.

10.1.4 Interpolation on the Fractional Fourier Coefficients

The fine frequency estimation stage usually consists of processing the Fourier coefficients around the maximum bin. In chapter 5 we reviewed a number of interpolation methods proposed in the literature, including the estimators of Quinn, Macleod and Rife and Vincent. These methods are computationally simple and perform

well. However, they are found to have a frequency dependent performance (periodic with period equal to a bin width). Their worst performance occurs at the centre of the bin. The methods that interpolate on the raw Fourier coefficients generally performed better than those that use the moduli. This is due to the fact that the noise is no longer white and its effect around the bin centre is exacerbated. Therefore, the decision whether the true frequency lies above or below the maximum bin fails more often. This is the reason for the problem region at the bin centre. The complete analysis of Quinn's first estimator was included in section 5.4. This is intended to serve as a template for the analysis of the new algorithms.

In chapter 6 we proposed three new algorithms that possess a similar performance to Quinn's first estimator but exhibit their best performance at the bin centre. The algorithms interpolate on two fractional Fourier coefficients. The fractional Fourier coefficients are calculated at the edges of the bins rather than the bin centre, that is, midway between two bins. This eliminates the decision step and in effect shifts the problem region to the edges of the bin. We analysed the algorithms and established their central limit theorems. We derived their asymptotic variances and found all three estimators to have a minimum asymptotic variance at the centre of the bin. This minimum value is equal to the minimum variance of Quinn's algorithms and is only 1.0147 times the asymptotic CRB. The interpolator on the raw coefficients, the FFCI algorithm, performs best as the noise is still white. The performance of the interpolator on the magnitudes of the fractional coefficients, the MOI estimator, is slightly worse midway between to bins. Finally, we found that the algorithm obtained from the magnitudes squared, that is the MSI estimator, is severely biased and has poor performance away from the bin centre. The theoretical results were all verified by simulation.

10.1.5 Iterative Estimation Using the Dichotomous Search

The dichotomous search of the periodogram peak, proposed in [86], is examined in chapter 7. It is particularly suitable for DSP implementation as it is devoid of non-linear operations and relies completely on multiply, add and compare instructions. However, it requires the data to be padded with zeroes (up to 1.5 times the number of samples) in order to obtain a performance approaching the CRB. The algorithm is essentially a

binary search for the frequency. At each iteration, the decision is directed by a comparison of the magnitudes of two DFT coefficients calculated at the edges of an interval Δ. The interval width is then halved and the frequency estimate updated. As the signal to noise ratio increases, the CRB decreases and consequently more iterations are needed for the estimator to reach it. At medium to low SNR, simulation results show that the algorithm requires 10 iterations to converge to the CRB.

Guided by the insight gained from the simulation results, we put forward an explanation for the zero-padding requirement. Similarly to the interpolators on the magnitudes of the Fourier coefficients, discussed in the previous section, we expect the dichotomous search to have a problem area around the bin centre. If the data is not padded with zeroes, the likelihood of a failure in the decision step is substantial. Furthermore, as the intervals do not overlap, this failure is not recoverable by the algorithm in subsequent iterations. Therefore, a failure in the first iteration has a significant impact on the algorithm's performance. Padding the data with enough zeroes effectively samples the DFT more densely and eliminates the problem. This led us to propose a modified algorithm, which we refer to as the modified dichotomous search. The new algorithm achieves the same performance as the original one without the zero-padding. It consequently is computationally simpler than the original algorithm. The modified estimator simply employs two overlapping intervals at the first iteration, thus allowing for the possibility of recovering an incorrect first decision.

Hybrid estimators that combine the dichotomous search with another estimator in order to reduce the computational requirements are given in [85]. We reviewed these algorithms and proposed a new hybrid estimator, termed the Guided Search of the Periodogram Peak. The Guided Search combines Quinn's first algorithm, reviewed in chapter 5, with the dichotomous search. Therefore, it converges to the CRB in four iterations without padding the data.

10.1.6 Iterative Interpolation on the Fractional Fourier Coefficients

The estimators of chapter 5 exhibit their highest estimation variance at their fixed point, that is, at the centre of the bin. Thus their performances deteriorate when they are implemented iteratively. In chapter 8 we use Quinn's first algorithm to illustrate this fact. The estimators proposed in chapter 6, on the other hand, have their lowest

variance at their fixed point (they all have the same fixed point, located at the centre of the bin). We showed that their iterative implementations converge, in an almost sure sense, to their fixed point. Thus, their asymptotic variances become uniform over the entire bin, converging, almost surely, to 1.0147 times the asymptotic CRB. The theoretical results were all verified using simulations.

The IFFCI algorithm, obtained from the FFCI estimator, converges to the asymptotic CRB in two iterations. Here convergence to the asymptotic CRB means that the residual after the second iteration is of a lower order than the CRB (in mathematical terms this implies that the residual is $o\left(N^{-\frac{3}{2}}\right)$). Similarly to the IFFCI algorithm, the iterative MOI (IMOI) estimator was shown to converge in two iterations.

The magnitudes squared interpolation, MSI, algorithm was found in chapter 6 to be severely biased close to the edges of the bin. Its iterative implementation, the IMSI algorithm, is shown to be asymptotically unbiased. The poor performance of the MSI algorithm at the edges of the bin, however, slows the convergence of the IMSI estimator. The algorithm takes three iterations for the residual to become of a lower order than the CRB. Its asymptotic variance is again 1.0147 times the asymptotic CRB.

10.1.7 Frequency Assisted Spatial Tracking

An earth station usually relies on external data from a terrestrial link in order to obtain the necessary tracking information. This data could be in the form of TLEs supplied by NASA or GPS data transmitted by the TT&C station. However, it is desirable for a remote area or rapidly deployable earth station to derive its own spatial data to track the satellite. In chapter 9, we proposed the use of the Doppler measurements to derive the satellite's position. We call this the Frequency Assisted Spatial Tracking or FAST. This minimises the earth station's reliance on external tracking data. We started the chapter by reviewing the literature on the use of frequency information for the derivation of positioning information. We then showed that the satellite position, in the two dimensions required for antenna pointing, is uniquely specified by the Doppler shift and Doppler rate pair. We assumed the maximum elevation of the pass is known and implemented the FAST concept in the one-dimensional case using a scalar EKF spatial tracker. We proposed the use of the algorithm published by Ali *et al*, [11], to predict the

maximum elevation of the upcoming pass from that of the last observed pass. Using this predicted value, the EKF uses the Doppler shift to track the satellite's position along the expected pass. We assessed the performance of the maximum elevation prediction algorithm and the EKF spatial tracker using simulations. We found the maximum elevation prediction algorithm to have a maximum error of about 0.3º at an elevation of 90º. This is due to the fact that, at this maximum elevation, the satellite's tangential velocity with respect to the earth station is highest. The corresponding rate of change of the elevation is also at its highest value. This prediction error is a model error that cannot be tracked out. Therefore, its effect was visible in the performance of the EKF tracker. The EKF off-boresight error showed, in the noiseless case, a local peak at the maximum elevation point. We also obtained simulation results of the performance of the EKF tracker in the presence of noise. We assumed an efficient frequency estimator is used to derive the Doppler shift measurements at a signal to noise ratio of 0 dB. Thus, we added to the Doppler shift measurements a zero mean Gaussian distributed frequency error with variance given by the CRB at SNR equal to 0 dB. The central peak disappeared as the modeling error was essentially drowned by the measurement noise effect. We found the EKF performance to be very good and the off-boresight error to be generally less than 0.1º for elevations above 30º.

10.2 Suggestions for Future Work

In the light of the research outcomes of the thesis, we present in this section some suggestions for future research. These include the following:

10.2.1 A Study of the Threshold Properties of the Frequency Estimators

In this work we assumed that the frequency estimators are operating above the threshold and we derived their asymptotic variances. Although their threshold performances are primarily dictated by that of the MBS algorithm, they do differ depending on the characteristics of each estimator. A detailed study of their threshold behaviour can be done and a comparison of the threshold performances of the different estimators made. More research into the extension of the threshold is also needed. This might be achieved through pre-processing the data, post-processing the frequency estimates, or

by understanding the threshold behaviour of the particular estimator and designing it to have better characteristics at low SNR.

10.2.2 Implementation of the Algorithms Recursively

It may be desirable to implement an algorithm recursively in some frequency tracking applications. The new algorithms presented of chapter 8 are suitable for recursive implementation. This would extend the iterative algorithms into a frequency tracking form, giving an updated estimate for every new data sample. The resulting recursive estimators would then require memory for N complex samples. The new sample is added to Fourier coefficients and the oldest data sample subtracted from the coefficients and shifted out of memory. The number of operations per frequency estimate would then be reduced. It is also possible to implement the algorithms using a sliding window with overlapping frames.

10.2.3 Extension of the Family of Interpolators on Fractional Fourier Coefficients

In chapter 5 we examined the family of interpolators on Fourier coefficients, including three-coefficient and five coefficient interpolators. As more coefficients are added, the performance of the interpolators was found to get closer to the asymptotic CRB. This is due to the fact that more information about the signal is used in the interpolation. In a similar way, the family of interpolators on fractional Fourier coefficients might be extended to include algorithms using any number of coefficients.

10.2.4 Rigorous Analysis of the Estimators of Chapter 7

Zakharov and Tozer, [85, 86], proposed the dichotomous search algorithms and evaluated their performances using simulations. In chapter 7, we reviewed these algorithms. We offered an insight into the necessity of padding the data with zeroes and proposed new algorithms that eliminate this need. However, we only evaluated the estimators using simulation. Further research could be done on the effect of zero-

padding the data. This would allow the rigorous analysis of these estimators to be carried out.

10.2.5 Strategies for the Doppler Shift Compensation

In this thesis we dealt with the estimation of the frequency of a sinusoidal signal for the purpose of compensating, at the earth station, for the total frequency uncertainty in the received signal of a LEO satellite link. More research is required on the efficient application of the frequency measurements to the Doppler pre-compensation of the uplink. As it is desirable to keep the satellite onboard processing to a minimum, the uplink Doppler must be pre-corrected at the earth station prior to the transmission or of the signal. The uplink Doppler can be calculated from the downlink Doppler shift. However, as the measured frequency shift also includes the LO drift, this would require the extraction of the downlink Doppler shift.

10.2.6 Development of a More Accurate Orbital Model

In chapter 3 we presented an orbital model for low earth orbits that is based on a number of simplifying assumptions. We ignored all second order influences on the satellite and assumed the earth to be spherical. Furthermore, we approximated the satellite orbit in the ECEF frame by a great circle arc and the observed angular velocity by a constant. While this is valid in many applications, for instance where the earth station antenna has a broad beam width, there are situations where a more accurate model is needed. The first step in improving the model's performance is to include second order effects such as the oblateness of the earth and the atmospheric drag. The oblateness of the earth can be accounted for by transforming the calculated geocentric latitude into its geodetic equivalent. The effect of the atmospheric drag becomes more pronounced as the altitude of the orbit decreases. Research is then needed to implementation the FAST concept using the higher accuracy model.

10.2.7 Implementation of a Two-dimensional Spatial Tracker

In chapter 9 we proposed the use of the Doppler information to assist the spatial tracking of the satellite. We assumed the maximum elevation to be predictable by propagating the last observed pass. We implemented a one-dimensional EKF spatial tracker that uses the Doppler shift to derive the satellite's position along the pass. The assumption of a known maximum elevation can, however, be discarded and a two-dimensional EKF implemented. The two-dimensional spatial tracker would then use the Doppler shift and Doppler rate information to derive the satellite's position.

10.2.8 Frequency Rate Estimation

A two dimensional frequency based spatial tracker would require the Doppler shift and Doppler rate as inputs. A limited number of publications on the estimation of the rate of change of frequency were found. Thus, research on the topic of estimation of the rate of change of frequency at low SNR is required.

10.3 Conclusion

In this dissertation we discussed the estimation of the frequency of a sinusoidal signal for the Doppler compensation of a LEO satellite link. We also proposed the use of the Doppler shift measurements for the derivation of the spatial tracking information required for antenna pointing.

The frequency estimation strategy we adopted consists of a coarse search followed by a fine estimator. The coarse estimation stage was implemented using the periodogram maximiser. The threshold effect of the periodogram maximiser was studied and an approximate expression for the threshold signal to noise ratio derived. A number of new algorithms were proposed for the fine estimation stage. The theoretical variances of the new estimators were derived. They were shown to have performances that are practically on the asymptotic CRB. The theoretical results were verified by simulations.

The low earth orbit was also completely characterised. A simplified orbital model was presented. The resulting orbital equations were used to show that the Doppler shift and Doppler rate form a basis for the satellite position in an azimuth-elevation (or X-Y)

coordinate system. This implies that the earth station can derive its own tracking information using the frequency measurements obtained from the downlink. This is called the FAST concept. A maximum elevation prediction algorithm was suggested. Finally, the FAST concept was implemented in one dimension using an extended Kalman filter.

Appendix A.

Spherical Geometry

In this appendix we present some spherical trigonometry results that are necessary for the development of the ideas of chapters 3 and 9. Consider the spherical triangle shown below:

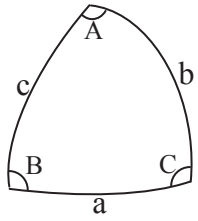

Figure A1.1 – Spherical triangle geometry

The following Spherical geometry identities hold, [143]:

$$\cos(a) = \cos(b)\cos(c) + \sin(b)\sin(c)\cos(A) \tag{A.1}$$

$$\cos(B)\sin(a) = \cos(b)\sin(c) - \sin(b)\cos(c)\cos(A) \tag{A.2}$$

$$\sin(B)\sin(a) = \sin(b)\sin(A) \tag{A.3}$$

If C is a right angle we get the following identities:

$$\cos(c) = \cos(a)\cos(b) \tag{A.4}$$

$$\sin(a) = \sin(c)\sin(A) \tag{A.5}$$

$$\cos(B) = \cos(b)\sin(A) \tag{A.6}$$

Appendix B.

Asymptotic Theory

In this appendix we present some asymptotic theory results that are necessary for the derivation of the asymptotic properties of some of the frequency estimators. Porat, in [20], presents a discussion on asymptotic theory in appendix C (pp. 421 – 428). We will, in this appendix, briefly review some asymptotic theory results that are relevant to the derivation of the asymptotic properties of the frequency estimators presented in the thesis.

B.1 The Notations o_p and O_p

Let X_n be a sequence of scalar random variables on a probability space $\{\Omega,A,P\}$. For a discussion of probability spaces and measures refer to [144] and [145]. The sequence X_n is said to *converge to zero in probability* if

$$\forall \delta > 0, \lim_{n\to\infty} P\{|X_n| \geq \delta\} = 0$$

Written another way, for all $\delta > 0$, and all $\varepsilon > 0$, there exists n_0 such that

$$P\{|X_n| \geq \delta\} < \varepsilon, \qquad \forall n > n_0$$

Such a sequence is said to be $o_p(1)$, written as $X_n = o_p(1)$.

If the sequence converges in probability to a random variable X, defined on the same probability space, we say that $X_n - X = o_p(1)$.

The sequence, X_n, is said to be *bounded in probability* if

$$\forall \varepsilon > 0, \exists \delta > 0 \text{ such that } \forall n, P\{|X_n| \geq \delta\} < \varepsilon$$

This is written as $X_n = O_p(1)$.

The notations above can be generalised as follows. Let a_n be a sequence of real positive numbers. The sequence X_n is said to be $o_p(a_n)$ if $\frac{X_n}{a_n} = o_p(1)$. We write $X_n = o_p(a_n)$. Similarly, $X_n = O_p(a_n)$ means that $\frac{X_n}{a_n} = O_p(1)$.

B.2 Properties of o_p and O_p sequences

Let X_n and Y_n be sequences of random variables defined on the same probability space $\{\Omega,A,P\}$. a is a finite real scalar, that is $|a| < \infty$. The following properties hold:

B.2.1 Lemma

1. if $X_n = o_p(1)$, then $aX_n = o_p(1)$
2. if $X_n = O_p(1)$, then
   a. $a + X_n = O_p(1)$
   b. $aX_n = O_p(1)$
3. If $X_n = o_p(1)$ and $Y_n = o_p(1)$, then
   a. $X_n + Y_n = o_p(1)$
   b. $X_n Y_n = o_p(1)$
4. If $X_n = o_p(1)$ and $Y_n = O_p(1)$, then $X_n Y_n = o_p(1)$
5. If $X_n = O_p(1)$ and $Y_n = O_p(1)$, then
   a. $X_n + Y_n = O_p(1)$
   b. $X_n Y_n = O_p(1)$

The proofs of parts 1, 2.a, 2.b, 3.a and 5.a are straightforward. We will only present proofs for 1, and 3.a. For the proofs of 3.b, 4.b and 5.b refer to ([20], pp. 422).

B.2.2 **Proof**

1. $X_n = o_p(1) \Rightarrow \forall \delta > 0, \lim_{n\to\infty} P\{|X_n| \geq \delta\} = 0$

Therefore,

$$\lim_{n\to\infty} P\{|aX_n| \geq |a|\delta\} = 0$$

Let $\delta_1 = |a|\delta$, we have that

$$\forall \delta_1 > 0, \lim_{n\to\infty} P\{|aX_n| \geq \delta_1\} = 0$$

and hence $aX_n = o_p(1)$.

3.a For all $\delta > 0$, we have

$$\begin{aligned} P\{|X_n + Y_n| \geq \delta\} &\leq P\{|X_n| + |Y_n| \geq \delta\}, \quad \text{triangle inequality} \\ &\leq P\{|X_n| \geq \delta/2\} + P\{|Y_n| \geq \delta/2\} \end{aligned}$$

This is shown in the following way:

$$P\{|X_n| + |Y_n| < \delta\} \geq P\{|X_n| < \delta/2\} P\{|Y_n| < \delta/2\}$$

Hence

$$1 - P\{|X_n| + |Y_n| < \delta\} \leq 1 - P\{|X_n| < \delta/2\} P\{|Y_n| < \delta/2\}$$

Therefore

$$\begin{aligned} P\{|X_n| + |Y_n| \geq \delta\} &\leq 1 - \left[1 - P\{|X_n| \geq \delta/2\}\right]\left[1 - P\{|Y_n| \geq \delta/2\}\right] \\ &= P\{|X_n| \geq \delta/2\} + P\{|Y_n| \geq \delta/2\} - P\{|X_n| \geq \delta/2\} P\{|Y_n| \geq \delta/2\} \\ &\leq P\{|X_n| \geq \delta/2\} + P\{|Y_n| \geq \delta/2\} \end{aligned}$$

Taking the limit as n $\to \infty$ we get

$$\begin{aligned} \lim_{n\to\infty} P\{|X_n + Y_n| \geq \delta\} &\leq \lim_{n\to\infty} P\{|X_n| > \delta/2\} + \lim_{n\to\infty} P\{|Y_n| > \delta/2\} \\ &= 0 + 0 = 0 \end{aligned}$$

Hence $X_n + Y_n = o_p(1)$.

B.2.3 Corollaries

In the following a_n and b_n are deterministic, real, sequences.

1. If $X_n = o_p(a_n)$ and $Y_n = o_p(b_n)$, then $X_n Y_n = o_p(a_n b_n)$
2. If $X_n = O_p(a_n)$ and $Y_n = o_p(b_n)$, then $X_n Y_n = o_p(a_n b_n)$
3. If $X_n = O_p(a_n)$ and $Y_n = O_p(a_n)$, then $X_n Y_n = O_p(a_n b_n)$
4. If $X_n = O_p(a_n)$ and $Y_n = O_p(a_n)$, and $a_n > b_n$ then $X_n + Y_n = O_p(a_n)$
5. If $X_n = o_p(a_n)$ then $|X_n|^m = o_p(a_n^m)$
6. If $X_n = O_p(a_n)$ then $|X_n|^m = O_p(a_n^m)$

B.3 Convergent and Bounded Deterministic Sequences

We say that a deterministic sequence, x_n, converges to zero if

$$\lim_{n\to\infty} |x_n| = 0$$

In other words, for all $\delta > 0$ and $\varepsilon > 0$, there exists n_0 such that

$$|x_n - \delta| < \varepsilon, \qquad \forall n > n_0$$

and we write $x_n = o(1)$.

For a number x, $x_n - x = o(1)$ means that x_n converges to x as n tends to ∞.

For a deterministic real sequence a_n, $x_n = o(a_n)$ means that $\frac{x_n}{a_n} = o(1)$.

A sequence, x_n, is bounded from above if for all n, there exists x such that

$$\max_{1\le n} \{x_n\} \le x$$

We write that $x_n = O_u(1)$.

A sequence, x_n, is bounded from below if for all n, there exists x such that

$$\min_{1\le n}\{x_n\} \ge x$$

We write that $x_n = O_L(1)$.

A sequence that is bounded from above and below is said to be bounded and is denoted by $O(1)$. We have that,

$$x_n = O(1) \Leftrightarrow \max_{1\le n}\{|x_n|\} \le x$$

$x_n = O(a_n)$ means that $\frac{x_n}{a_n} = O(1)$.

B.4 **Properties of Convergent and Bounded Sequences**

For the sequences x_n and y_n, and scalar a such that $|a| < \infty$, the following properties hold:

B.4.1 **Lemma**

1. if $x_n = o(1)$, then $ax_n = o(1)$
2. if $x_n = O(1)$, then
   a. $a + x_n = O(1)$
   b. $ax_n = O(1)$
3. If $x_n = o(1)$ and $y_n = o(1)$, then
   a. $x_n + y_n = o(1)$
   b. $x_n y_n = o(1)$
4. If $x_n = o(1)$ and $y_n = O(1)$, then $x_n y_n = o(1)$
5. If $x_n = O(1)$ and $y_n = O(1)$, then
   a. $x_n + y_n = O(1)$

b. $x_n y_n = O(1)$

The proofs of parts 1, 2.a, 2.b, 3.a and 5.a are analogous to those of the o_p and O_p sequences. We will therefore only present proofs for 1, and 3.a. For the proofs of 3.b, 4.b and 5.b refer to ([20], pp. 422).

B.4.2 Proof

1. $x_n = o(1) \Rightarrow \lim_{n\to\infty} |x_n| = 0$

Therefore,

$$\lim_{n\to\infty} |a x_n| = |a| \lim_{n\to\infty} |x_n| = 0$$

Hence $a x_n = o(1)$.

3.a $x_n = o(1) \Rightarrow \lim_{n\to\infty} |x_n| = 0$

and

$y_n = o(1) \Rightarrow \lim_{n\to\infty} |y_n| = 0$

Therefore
$$\begin{aligned} \lim_{n\to\infty} |x_n + y_n| &\le \lim_{n\to\infty} |x_n| + \lim_{n\to\infty} |y_n| \\ &= 0 \end{aligned}$$

and $x_n + y_n = o(1)$

3.b $x_n = o(1) \Rightarrow \lim_{n\to\infty} |x_n| = 0$

and

$y_n = o(1) \Rightarrow \lim_{n\to\infty} |y_n| = 0$

Therefore
$$\begin{aligned} \lim_{n\to\infty} |x_n y_n| &= \lim_{n\to\infty} |x_n| \cdot \lim_{n\to\infty} |y_n| \\ &= 0 \end{aligned}$$

And consequently $x_n y_n = o(1)$.

B.4.3 Corollaries

In the following a_n and b_n are deterministic, real, sequences.

1. If $x_n = o(a_n)$ and $y_n = o(b_n)$, then $x_n y_n = o(a_n b_n)$
2. If $x_n = O(a_n)$ and $y_n = o(b_n)$, then $x_n y_n = o(a_n b_n)$
3. If $x_n = O(a_n)$ and $y_n = O(b_n)$, then $x_n y_n = O(a_n b_n)$
4. If $x_n = O(a_n)$ and $y_n = O(b_n)$, and $a_n > b_n$ then $x_n + y_n = O(a_n)$
5. If $x_n = o(a_n)$ then $|x_n|^m = o(a_n^m)$
6. If $x_n = O(a_n)$ then $|x_n|^m = O(a_n^m)$

Appendix C.

Fourier Coefficients of AWGN

C.1 Properties of AWGN Fourier Coefficients

Let $w(k)$, $k = 0 \ldots N-1$, be zero-mean complex additive white Gaussian noise (AWGN) with variance σ^2. The real and imaginary parts of $w(k)$ are also independent and identically distributed (i.i.d.) with mean zero and variance equal to $\sigma^2/2$. The samples, $w(k)$, then, satisfy

$$E[w(k)] = 0 \tag{C.1}$$

and

$$E[w(k)w^*(l)] = \delta_{k,l}\sigma^2 \tag{C.2}$$

where the $(\bullet)^*$ indicates the complex conjugate of $(\bullet)$ and $\delta_{k,l}$ is the kronecker delta defined as

$$\delta_{k,l} = \begin{cases} 1, & k = l \\ 0, & \text{otherwise} \end{cases}$$

The properties of the Fourier coefficients of AWGN have been discussed quite extensively in the literature, [115] and [21], and the material here is included for the reader's convenience and for the sake of completeness. The Fourier coefficients of the noise are given by

$$W(n) = \frac{1}{N}\sum_{k=0}^{N-1} w(k)e^{-j2\pi kn/N} \tag{C.3}$$

As the Fourier transformation is a linear one, the resulting Fourier coefficients are zero-mean AWGN with variance σ^2/N. In fact we have

$$\begin{aligned} E[W(n)] &= E\left[\frac{1}{N}\sum_{k=0}^{N-1} w(k) e^{-j2\pi\frac{kn}{N}}\right] \\ &= \frac{1}{N}\sum_{k=0}^{N-1} E[w(k)] e^{-j2\pi\frac{kn}{N}} \\ &= 0 \end{aligned} \tag{C.4}$$

and

$$\begin{aligned} E\left[(W(m)-E[W(m)])(W(n)-E[W(n)])^*\right] &= E\left[\left(\frac{1}{N}\sum_{k=0}^{N-1} w(k) e^{-j2\pi\frac{km}{N}}\right)\left(\frac{1}{N}\sum_{l=0}^{N-1} w(l) e^{-j2\pi\frac{ln}{N}}\right)\right] \\ &= \frac{1}{N^2}\sum_{k=0}^{N-1}\sum_{l=0}^{N-1} E[w(k)w^*(l)] e^{-j2\pi\frac{km-ln}{N}} \\ &= \frac{1}{N^2}\sum_{k=0}^{N-1}\sum_{l=0}^{N-1} \sigma^2 \delta_{k,l} e^{-j2\pi\frac{km-ln}{N}} \\ &= \begin{cases} \frac{\sigma^2}{N}, & if\ m = n \\ 0, & otherwise \end{cases} \end{aligned} \tag{C.5}$$

It is also well known, [115] pp.101 – 103, that the magnitude and phase are independent and follow Rayleigh and uniform distributions respectively. That is, writing $W(n)$ as

$$W(n) = R_n e^{j\phi_n} \tag{C.6}$$

The distributions of R and ϕ are given by

$$p_R(r) = \frac{Nr}{\sigma^2} e^{-\frac{Nr^2}{2\sigma^2}}, \qquad r \geq 0 \tag{C.7}$$

and

$$p(\phi) = \frac{1}{2\pi}, \qquad -\pi \leq \phi \leq \pi \tag{C.8}$$

The mean and variance for the Rayleigh distributed random variable shown in equation (C.7) are, [115]:

$$\mu_R = \sigma\sqrt{\frac{\pi}{2N}} \tag{C.9}$$

and

$$Var[R] = \sigma^2 \frac{4-\pi}{2N} \tag{C.10}$$

For the expectation of a non-negative random variable R and $\delta > 0$, the following inequality holds, [144],

$$P[R \geq \delta] \leq \frac{1}{\delta} E[R]$$

Substituting the expression for the expectation, we obtain

$$P[R \geq \delta] \leq \frac{1}{\delta} \frac{\sigma}{\sqrt{N}} \sqrt{\frac{\pi}{2}} \tag{C.11}$$

From (C.11) we see that for any $\varepsilon > 0$ and $\delta > 0$, if we choose N_0 such that

$$N_0 = \left\lceil \frac{\sigma^2 \pi}{2\delta^2 \varepsilon^2} \right\rceil$$

we obtain

$$P[R \geq \delta] < \varepsilon, \qquad \forall N > N_0$$

Hence by the definition of $o_p(1)$ random sequences in B.1, we see that

$$R = o_p(1) \tag{C.12}$$

In fact it was shown in [19] (also see chapter 2, section 2.2) that

$$R = O_p\left(N^{-1/2} \sqrt{\ln N} \right)$$

C.2 Fractional Fourier Coefficients of AWGN

In the previous section we considered the standard Fourier coefficients of Additive White Gaussian Noise. This is sufficient in the majority of cases. However, in some cases, we might require to work with "Fractional Fourier Coefficients", that is Fourier coefficients obtained at non-integer indices. In this section we examine the properties of such coefficients as $W(n+p)$ for $|p| \leq 1/2$ with a particular emphasis on the special case $p = \pm 1/2$.

The fractional Fourier coefficients of the AWGN samples are given by

$$W(n+p)=\frac{1}{N}\sum_{k=0}^{N-1}w(k)e^{-j2\pi k(n+p)/N} \tag{C.13}$$

As the Fourier transformation is a linear one, we expect that the resulting Fourier coefficients are Gaussian with mean 0. In fact the mean of the $W(n+p)$ is

$$\begin{aligned} E[W(n+p)] &= E\left[\frac{1}{N}\sum_{k=0}^{N-1}w(k)e^{-j2\pi\frac{k(n+p)}{N}}\right] \\ &= \frac{1}{N}\sum_{k=0}^{N-1}E[w(k)]e^{-j2\pi\frac{k(n+p)}{N}} \\ &= 0 \end{aligned} \tag{C.14}$$

While the general form of the covariance is given by

$$\begin{aligned} E[W(m+p)W^*(n+q)] &= E\left[\left(\frac{1}{N}\sum_{k=0}^{N-1}w(k)e^{-j2\pi\frac{k(m+p)}{N}}\right)\left(\frac{1}{N}\sum_{l=0}^{N-1}w(l)e^{-j2\pi\frac{l(n+q)}{N}}\right)^*\right] \\ &= \frac{1}{N^2}\sum_{k=0}^{N-1}\sum_{l=0}^{N-1}E[w(k)w^*(l)]e^{-j2\pi\frac{k(m+p)-l(n+q)}{N}} \\ &= \frac{1}{N^2}\sum_{k=0}^{N-1}\sum_{l=0}^{N-1}\sigma^2\delta_{k,l}e^{-j2\pi\frac{k(m+p)-l(n+q)}{N}} \\ &= \frac{\sigma^2}{N^2}\frac{e^{-j2\pi(p-q)}-1}{e^{-j2\pi\frac{(m-n+p-q)}{N}}-1} \end{aligned} \tag{C.15}$$

In this thesis we are primarily concerned with the case where $p=\pm 1/2$, therefore we will use the term fractional Fourier coefficients to refer to $W\left(n\pm\frac{1}{2}\right)$. The elements of the covariance matrix, therefore, simplify to

$$E[W(m+p)W^*(n+q)]=\begin{cases}\frac{\sigma^2}{N}, & if\ m+p=n+q\\ 0, & otherwise\end{cases} \tag{C.16}$$

We observe that like the standard Fourier coefficients, the fractional Fourier coefficients are independent. That is expected as the fractional Fourier coefficients can also be obtained by shifting the signal by a frequency equal to half a bin prior to the FFT. As the shift is a linear operation which does not affect the statistical properties of the noise

samples, we expect the FFT coefficients of the shifted signal to have the same statistical properties as the original signal. In fact, we find that any two Fourier coefficients that are separated by an integer multiple of f_s/N are independent and identically distributed. It is only when any two Fourier coefficients are separated by a non-integer multiple of f_s/N that they become correlated. Also note that, like the standard coefficients, the fractional Fourier coefficients are $O_p\left(N^{-1/2}\sqrt{\ln N}\right)$.

C.3 Fourier Coefficients of Signal plus Noise

In the following we will look at the properties of the Fourier coefficients of a sinusoidal signal plus noise. Consider the signal $x(k)$, given by

$$x(k) = s(k) + w(k) \tag{C.17}$$

where $s(k)$ is the sinusoidal signal

$$s(k) = Ae^{j\left(2\pi k f/f_s + \theta\right)} \tag{C.18}$$

with f being the signal frequency, f_s the sampling frequency and θ the signal phase.

By the linearity property of the Fourier transform, the Fourier coefficients are of x are the sum of those of s and w. That is,

$$X(n) = S(n) + W(n) \tag{C.19}$$

If the signal frequency lies on a bin centre, that is, the signal frequency is equal to mf_s/N, where m is an integer, then the Fourier Transform of the signal is given by

$$S(n) = \begin{cases} Ae^{j\theta}, & n = m \\ 0, & otherwise \end{cases} \tag{C.20}$$

Thus, equation (C.20) implies that, for $n \neq m$, $|X_n|$ is Rayleigh distributed as shown in equation (C.7). $|X_m|$, on the other hand, follows the Ricean distribution shown below,

$$p_R(r) = \frac{Nr}{\sigma^2} e^{-N\frac{r^2+A^2}{2\sigma^2}} I_0\left(\frac{NAr}{\sigma^2}\right), \qquad r \geq 0 \tag{C.21}$$

where $I_0(x)$ is the modified Bessel function of the second kind, given by, [143],

$$\begin{aligned} I_0(x) &= \frac{1}{2\pi}\int_0^{2\pi} e^{x\cos\phi} d\phi \\ &= 1 + \frac{x^2}{2^2} + \frac{x^4}{2^2 \cdot 4^2} + \frac{x^6}{2^2 \cdot 4^2 \cdot 6^2} + \cdots \end{aligned}$$

For the general case, all of the X_n follow a Ricean distribution with A replaced by $B_n = |S(n)|$ in (C.21). Let $f = (m+\delta)f_s / N$, then $S(n)$ can be expressed as

$$\begin{aligned} S(n) &= \frac{Ae^{j\theta}}{N} \frac{e^{j2\pi N\left(\frac{m+\delta}{N} - \frac{n}{N}\right)} - 1}{e^{j2\pi\left(\frac{m+\delta}{N} - \frac{n}{N}\right)} - 1} \\ &= \frac{Ae^{j\theta}}{N} \frac{e^{j2\pi\delta} - 1}{e^{j2\frac{\pi}{N}(m-n+\delta)} - 1} \end{aligned} \tag{C.22}$$

Thus, B_n is given by

$$B_n = \frac{A}{N}\left|\frac{\sin(\pi\delta)}{\sin\left(\frac{\pi}{N}(m-n+\delta)\right)}\right| \tag{C.23}$$

The resulting Ricean distribution is

$$p_{R_n}(r) = \frac{Nr}{\sigma^2} e^{-N\frac{r^2+B_n^2}{2\sigma^2}} I_0\left(\frac{NB_n r}{\sigma^2}\right), \qquad r \geq 0 \tag{C.24}$$

Appendix D.

References

[1] D. Roddy, *Satellite Communications*, 2 ed: McGraw-Hill, 1996.

[2] S. Reisenfeld, E. Aboutanios, K. Willey, M. Eckert, R. Clout and A. Thoms, "The Design of the FedSat Ka Band Fast Tracking Earth Station," 8th International Aerospace Congress, Adelaide, SA, Australia, pp. 1999.

[3] M. Davidoff, *The Radio Amateur's Satellite Handbook*. Newington: The American Radio Relay League, 1998.

[4] A. Sewards, A. E. Winter and R. Mamen, "Satellites for position determination," *Canadian Aeronautics & Space Journal*, vol. 24, pp. 266-73, 1978.

[5] P. Tsakalides, R. Raspanti and C. L. Nikias, "Angle/Doppler estimation in heavy-tailed clutter backgrounds," *IEEE Transactions on Aerospace & Electronic Systems*, vol. 35, pp. 419-36, 1999.

[6] T. E. McGunigal, "COSPAS/SARSAT: an international joint venture in satellite-aided search and rescue," Wescon/80 Conference Record. Electron. Conventions, El Segundo, CA, USA, pp. 9-1/1-6, 1980.

[7] D. Levesque, "The COSPAS-SARSAT system," IEE Colloquium on 'Satellite Distress and Safety Systems', London, UK, pp. 1-4, 1993.

[8] K. Aksnes, P. H. Anderson and E. Haugen, "A precise multipass method for satellite Doppler positioning," *Celestial Mechanics*, vol. 44, pp. 317-38, 1988.

[9] B. G. Quinn and P. J. Kootsookos, "Threshold behavior of the maximum likelihood estimator of frequency," *IEEE Transactions on Signal Processing*, vol. 42, pp. 3291-4, 1994.

[10] S. Reisenfeld, "Email Communication: The Two Spectral Line Error Technique," 1998.

[11] I. Ali, N. Al-Dhahir and J. E. Hershey, "Predicting the visibility of LEO satellites," *IEEE Transactions on Aerospace & Electronic Systems*, vol. 35, pp. 1183-90, 1999.

[12] E. J. Hannan, "The Estimation of Frequency," *Journal of Applied Probability*, vol. 10, pp. 510-519, 1973.

[13] E. J. Hannan, D. Huang and B. G. Quinn, "Frequency estimation," Proceedings of the 12th Triennial World Congress of the International Federation of Automatic Control, pp. 59-62, 1993.

[14] B. G. Quinn and J. M. Fernandes, "A fast Efficient Technique for the Estimation of Frequency," *Biometrika*, vol. 78, pp. 489-497, 1991.

[15] D. Pollard, *Convergence of stochastic processes*. New York: Springer-Verlag, 1984.

[16] K. Siegrist, "The Central Limit Theorem," http://www.math.uah.edu/stat/sample/sample5.html, 2001.

[17] E. W. Weisstein, "Central Limit Theorem - From MathWorld," http://mathworld.wolfram.com/CentralLimitTheorem.html, 1999.

[18] Z.-G. Chen and E. J. Hannan, "The distribution of periodogram ordinates," *Journal of Time Series Analysis*, vol. 1, pp. 73-82, 1980.

[19] H.-Z. An, Z.-G. Chen and E. J. Hannan, "The Maximum of the Periodogram," *Journal of Multivariate Analysis*, vol. 13, pp. 383-400, 1983.

[20] B. Porat, *Digital Processing of Random Signals, Theory and Methods*: Prentice-Hall, 1993.

[21] D. C. Rife, "Digital tone parameter estimation in the presence of Gaussian noise," Polytechnic Institute of Brooklyn, 1973.

[22] E. Brookner, *Tracking and Kalman filtering made easy*. New York: Wiley, 1998.

[23] S. M. Bozic, *Digital and Kalman filtering : an introduction to discrete-time filtering and optimum linear estimation*. London: Edward Arnold, 1979.

[24] Y. T. Chan and F. L. Jardine, "Target localization and tracking from Doppler-shift measurements," *IEEE Journal of Oceanic Engineering*, vol. 15, pp. 251-7, 1990.

[25] Y. T. Chan and F. Couture, "Simple Kalman gains for filtering position and velocity measurements," *IEEE Transactions on Aerospace & Electronic Systems*, vol. 27, pp. 566-71, 1991.

[26] S.-T. Park and J. G. Lee, "Improved Kalman Filter Design for Three-Dimensional Radar Tracking," *IEEE Transactions on Aerospace & Electronic Systems*, vol. 37, pp. 727-739, 2001.

[27] Y. Asai and T. Nishimura, "Orbit determination by means of Kalman filter using Delta VLBI data," Proceedings of the 1999 IEEE International Conference on Control Applications, pp. 968-72, 1999.

[28] M. K. El-Mahy, "Efficient satellite orbit determination algorithm," Eighteenth National Radio Science Conference, Cairo, Egypt, pp. 225-32, 2001.

[29] B. F. La Scala, R. R. Bitmead and B. G. Quinn, "An extended Kalman filter frequency tracker for high-noise environments," *IEEE Transactions on Signal Processing*, vol. 44, pp. 431-4, 1996.

[30] S. Bittanti and S. M. Savaresi, "On the parameterization and design of an extended Kalman filter frequency tracker," *IEEE Transactions on Automatic Control*, vol. 45, pp. 1718-1724, 2000.

[31] S. Bittanti and S. M. Savaresi, "Frequency tracking via extended Kalman filter: parameter design," Proceedings of the American Control Conference, pp. 2225-2229, 2000.

[32] O. Montenbruck, *Satellite orbits: models, methods, and applications*. New York: Springer, 2000.

[33] J. R. Shim, "Real time frequency estimators," Ph. D., University of Missouri-Columbia, 1995.

[34] B. G. Quinn, *The estimation and tracking of frequency*. New York: Cambridge University Press, 2001.

[35] B. Boashash, "Estimating and interpreting the instantaneous frequency of a signal. I. Fundamentals," *Proceedings of the IEEE*, vol. 80, pp. 520 - 538, 1992.

[36] B. Boashash, "Estimating and interpreting the instantaneous frequency of a signal. II. Algorithms and applications," *Proceedings of the IEEE*, vol. 80, pp. 540 - 568, 1992.

[37] S. S. Haykin, *Communication systems*, 3rd ed. New York: Wiley, 1994.

[38] Y. Jun-Zhe and L. Chih-Wen, "A precise calculation of power system frequency," *IEEE Transactions on Power Delivery*, vol. 16, pp. 361-6, 2001.

[39] D. W. P. Thomas and M. S. Woolfson, "Evaluation of frequency tracking methods," *IEEE Transactions on Power Delivery*, vol. 16, pp. 367-71, 2001.

[40] M. Hilairet and F. Auger, "Frequency estimation for sensorless control of induction motors," *ICASSP, IEEE International Conference on Acoustics, Speech and Signal Processing - Proceedings*, vol. 2, pp. 925-928, 2001.

[41] O. Besson and F. Castanie, "Doppler frequency estimator performance analysis," ICASSP, IEEE International Conference on Acoustics, Speech and Signal Processing, pp. 2511-2514, 1990.

[42] W. K. M. Ahmed and P. J. McLane, "A simple method for coarse frequency acquisition through FFT," IEEE 44th Vehicular Technology Conference, Stockholm Sweden, pp. 297-301, 1994.

[43] W. K. M. Ahmed and P. J. McLane, "A method for coarse frequency acquisition for Nyquist filtered MPSK," *IEEE Transactions on Vehicular Technology*, vol. 45, pp. 720-31, 1996.

[44] S. Bellini, "Frequency estimators for M-PSK operating at one sample per symbol," Globecom '94, pp. 962-6, 1994.

[45] S. Bellini, C. Molinari and G. Tartara, "Digital frequency estimation in burst mode QPSK transmission," *IEEE Transactions on Communications*, vol. 38, pp. 959-61, 1990.

[46] W. G. Cowley, "Phase and frequency estimation for PSK packets: bounds and algorithms," *IEEE Transactions on Communications*, vol. 44, pp. 26-8, 1996.

[47] W. G. Cowley, M. Rice and A. N. McLean, "Estimation of frequency offset in mobile satellite modems," Proceedings of the Third International Mobile Satellite Conference, pp. 417-422, 1993.

[48] H. Steendam and M. Moeneclaey, "Low-SNR limit of the Cramer-Rao bound for estimating the carrier phase and frequency of a PAM, PSK, or QAM waveform," *Communications Letters*, vol. 5, pp. 218-20, 2001.

[49] G. P. Ah-Thew, "Doppler compensation for LEO satellite communication systems," UMI Dissertation Services, 2001.

[50] F. Rice, B. Cowley, B. Moran and M. Rice, "Cramer-Rao lower bounds for QAM phase and frequency estimation," *IEEE Transactions on Communications*, vol. 49, pp. 1582-1591, 2001.

[51] E. Aboutanios and S. Reisenfeld, "Analysis of Frequency Assisted Spatial Tracking For Low Earth Orbit Satellites," Sixth Ka Band Utilization Conference, Cleveland, Ohio, USA, pp. 397-403, 2000.

[52] R. J. H. Brush, P. E. Baylis and N. Tawel, "Doppler method for improving tracking accuracy of satellite receiving stations," *IEE Proceedings F (Communications, Radar and Signal Processing)*, vol. 132, pp. 539-40, 1985.

[53] H. L. Werstiuk, "COSPAS-SARSAT: a system overview," the International Electrical, Electronics Conference, Toronto, Ont., Canada, pp. 168-71, 1983.

[54] I. Ali, N. Al-Dhahir, J. E. Hershey, G. J. Saulnier and R. Nelson, "Doppler as a new dimension for multiple access in LEO satellite systems," *International Journal of Satellite Communications*, vol. 15, pp. 269-79, 1997.

[55] P. Handel, "On the performance of the weighted linear predictor frequency estimator," *IEEE Transactions on Signal Processing*, vol. 43, pp. 3070-1, 1995.

[56] V. Clarkson, P. J. Kootsookos and B. G. Quinn, "Analysis of the variance threshold of Kay's weighted linear predictor frequency estimator," *IEEE Transactions on Signal Processing*, vol. 42, pp. 2370-9, 1994.

[57] P. D. Fiore and S. W. Lang, "Efficient phase-only frequency estimation," *ICASSP, IEEE International Conference on Acoustics, Speech and Signal Processing - Proceedings*, vol. 5 1996. IEEE, pp. 2809-2812, 1996.

[58] M. P. Fitz, "Further results in the fast estimation of a single frequency," *IEEE Transactions on Communications*, vol. 42, pp. 862-864, 1994.

[59] S. Kay, "Fast and accurate single frequency estimator," *IEEE Transactions on Acoustics, Speech, & Signal Processing*, vol. 37, pp. 1987-1990, 1989.

[60] S. A. Tretter, "Estimating the Frequency of a Sinusoid by Linear Regression," *IEEE Transactions on Information Theory*, vol. IT-31, pp. 832-835, 1985.

[61] B. G. Quinn, V. I. Clarkson and P. J. Kootsookos, "Comments on "On the performance of the weighted linear predictor frequency estimator"," *IEEE Transactions on Signal Processing*, vol. 46, pp. 526-7, 1998.

[62] S. H. Leung, Y. Xiong and W. H. Lau, "Modified Kay's method with improved frequency estimation," *Electronics Letters*, vol. 36, pp. 918-920, 2000.

[63] S. W. Lang and B. R. Musicus, "Frequency estimation from phase differences," *Proceedings of the IEEE International Conference on Acoustics, Speech and Signal Processing*, vol. IV (of 4), pp. 2140-2143, 1989.

[64] M. L. Fowler and J. A. Johnson, "Extending the threshold and frequency range for phase-based frequency estimation," *IEEE Transactions on Signal Processing*, vol. 47, pp. 2857-2863, 1999.

[65] D. Bian, G. Zhang and X. Yi, "A maximum likelihood based carrier frequency estimation algorithm," 5th International Conference on Signal Processing Proceedings 16th World Computer Congress 2000, Beijing China, pp. 185-8, 2000.

[66] T. Brown and M. Wang, "An iterative frequency estimator for feedforward frequency synchronization," Vehicular Technology Conference, 2001. VTC 2001 Spring. IEEE VTS 53rd, pp. 1713-1718 vol.3, 2001.

[67] M. Luise and R. Reggiannini, "Carrier Frequency Recovery in All-Digital Modems for Burst-Mode Transmissions," *IEEE Transactions on Communications*, vol. 43, pp. 1169-1178, 1995.

[68] B. Volker and P. Handel, "Frequency estimation from proper sets of correlations," *Signal Processing, IEEE Transactions on*, vol. 50, pp. 791-802, 2002.

[69] G. W. Lank, I. S. Reed and G. E. Pollon, "A Semicoherent Detection and Doppler Estimation Statistic," *IEEE Transactions on Aerospace & Electronic Systems*, vol. AES-9, pp. 151-165, 1973.

[70] K. Barman and M. T. Arvind, "A minimum variance single frequency estimator using recursive least squares estimate of noise statistics," 1998 Midwest Symposium on Circuits and Systems, pp. 246-9, 1999.

[71] M. V. Dragosevic and S. S. Stankovic, "Generalized Least Squares method for frequency estimation," *IEEE Transactions on Acoustics, Speech, & Signal Processing*, vol. 37, pp. 805-819, 1989.

[72] R. Kumar, "Fast frequency acquisition via adaptive least-squares algorithm," *IEE Proceedings-F Radar & Signal Processing*, vol. 136, pp. 155-60, 1989.

[73] Y. T. Su and R.-C. Wu, "Frequency acquisition and tracking in high dynamic environments," *IEEE Transactions on Vehicular Technology*, vol. 49, pp. 2419-2429, 2000.

[74] H. C. So, "Adaptive algorithm for direct estimation of sinusoidal frequency," *Electronics Letters*, vol. 36, pp. 759-60, 2000.

[75] H. C. So and P. C. Ching, "Analysis of an adaptive single-tone frequency estimation algorithm," International Conference on Signal and Image Processing, pp. 465-8, 2000.

[76] B. G. Quinn, "A fast Efficient Technique for the Estimation of Frequency: Interpretation and Generalisation," *Biometrika*, vol. 86, pp. 213-220, 1999.

[77] M. McIntyre and A. Ashley, "A comparison of five algorithms for tracking frequency and frequency rate-of-change," 1990 International Conference on Acoustics, Speech, and Signal Processing, pp. 2899-2902, 1990.

[78] L. Hsu, R. Ortega and G. Damm, "A globally convergent frequency estimator," in *Automatic Control, IEEE Transactions on*, vol. 44: T, 1999, pp. 698-713.

[79] J. F. Chicharo and T. S. Ng, "Gradient-based adaptive IIR notch filtering for frequency estimation," *IEEE Transactions on Acoustics, Speech, & Signal Processing*, vol. 38, pp. 769-77, 1990.

[80] B. F. La Scala and R. R. Bitmead, "Design of an extended Kalman filter frequency tracker," *Signal Processing, IEEE Transactions on*, vol. 44, pp. 739-742, 1996.

[81] B. Boashash, P. O'Shea and B. Ristic, "Statistical/computational comparison of some estimators for instantaneous frequency," IEEE International Conference on Acoustics, Speech and Signal Processing, pp. 3193-3196, 1991.

[82] B. G. Quinn, "Estimating frequency by interpolation using Fourier coefficients," *IEEE Transactions on Signal Processing*, vol. 42, pp. 1264-8, 1994.

[83] B. G. Quinn, "Estimation of frequency, amplitude, and phase from the DFT of a time series," *IEEE Transactions on Signal Processing*, vol. 45, pp. 814-17, 1997.

[84] M. D. Macleod, "Fast nearly ML estimation of the parameters of real or complex single tones or resolved multiple tones," *IEEE Transactions on Signal Processing*, vol. 46, pp. 141-8, 1998.

[85] Y. V. Zakharov, V. M. Baronkin and T. C. Tozer, "DFT-based frequency estimators with narrow acquisition range," *IEE Proceedings-Communications*, vol. 148, pp. 1-7, 2001.

[86] Y. V. Zakharov and T. C. Tozer, "Frequency estimator with dichotomous search of periodogram peak," *Electronics Letters*, vol. 35, pp. 1608-1609, 1999.

[87] I. Djurovic, V. Katkovnik and L. Stankovic, "Instantaneous frequency estimation based on the robust spectrogram," *ICASSP, IEEE International Conference on Acoustics, Speech and Signal Processing*, vol. 6, pp. 3517-3520, 2001.

[88] H. K. Kwok and D. L. Jones, "Improved instantaneous frequency estimation using an adaptive short-time Fourier transform," *IEEE Transactions on Signal Processing*, vol. 48, pp. 2964-2972, 2000.

[89] I. Djurovic, L. J. Stankovic, S. Stankovic and R. Stojanovic, "Local frequency estimation based on the Wigner distribution," IEEE International Conference on Image Processing, pp. 736-739, 2001.

[90] B. Boashash and L. B. White, "Instantaneous frequency estimation and automatic time-varying filtering," IEEE International Conference on Acoustics, Speech and Signal Processing, pp. 1221-1224, 1990.

[91] B. Barkat and B. Boashash, "Instantaneous frequency estimation of polynomial FM signals using the peak of the PWVD: Statistical performance in the presence of additive Gaussian noise," *IEEE Transactions on Signal Processing*, vol. 47, pp. 2480-2490, 1999.

[92] B. Ristic and B. Boashash, "Instantaneous frequency estimation of quadratic and cubic FM signals using the cross polynomial Wigner-Ville distribution," *IEEE Transactions on Signal Processing*, vol. 44, pp. 1549-1553, 1996.

[93] A. Wannasarnmaytha, S. Hara and N. Morinaga, "Frequency acquisition performance of discrete wavelet transform AFC," 5th IEEE International Symposium on Personal, Indoor and Mobile Radio Communications, 1994. Wireless Networks - Catching the Mobile Future, pp. 590-594, 1994.

[94] O. Besson and P. Stoica, "Analysis of MUSIC and ESPRIT frequency estimates for sinusoidal signals with lowpass envelopes," *IEEE Transactions on Signal Processing*, vol. 44, pp. 2359-2364, 1996.

[95] J. Karhunen and J. Joutsensalo, "Sinusoidal frequency estimation by approximate MUSIC method," Fifth ASSP Workshop on Spectrum Estimation and Modeling, Rochester, NY, USA, pp. 337-41, 1990.

[96] O. Besson and P. Stoica, "Two subspace-based methods for frequency estimation of sinusoidal signals with random amplitude," *IEE Proceedings: Radar, Sonar & Navigation*, vol. 144, pp. 169-176, 1997.

[97] J. Joutsensalo and J. Karhunen, "Lowering the threshold SNR of Fourier signal subspace," EUSIPCO-92, Sixth European Signal Processing Conference, Brussels, Belgium, pp. 705-8, 1992.

[98] A. A. Beex and P. Shan, "Time-varying prony method for instantaneous frequency estimation at low SNR," *Proceedings - IEEE International Symposium on Circuits & Systems*, vol. 3, pp. III-5 - III-8, 1999.

[99] K. Kubo, "Instantaneous frequency estimation from sine wave samples," Proceedings of 39th Annual Conference of the Society of Instrument and Control Engineers, Iizuka Japan, pp. 25-30, 2000.

[100] R. Deutsch, *Orbital dynamics of space vehicles*. E. Cliffs, N.j.: Prentice-hall, 1963.

[101] V. A. Chobotov, "Orbital Mechanics," in *AIAA Education Series*, J. S. Przemieniecki, Ed., 2 ed: American Institute of Aeronautics and Astronautics, Inc., 1996.

[102] G. Maral, *Satellite communications systems*, 3rd ed. Chichester, England ; New York: Wiley, 1998.

[103] I. Ali, N. Al-Dhahir and J. E. Hershey, "Doppler characterization for LEO satellites," *IEEE Transactions on Communications*, vol. 46, pp. 309-13, 1998.

[104] I. Ali, N. Al-Dhahir and J. E. Hershey, "Accurate Doppler Characterization for LEO Satellites," GE Research and Development Center 97CRD058, May 1997.

[105] S. J. MacKo, *Satellite tracking*. N.Y.: J.f. Rider, 1962.

[106] T. S. Kelso, "Orbital Coordinate Systems, Part II," http://www.celestrak.com/columns/v02n02, 2000.

[107] K. Willey, "Pointing Error Reduction when Tracking LEO Satellites with a Low-Cost, Rapidly Deployed, Transportable Earth Station," PhD, University of Technology, Sydney, 2002.

[108] P. S. Crawford and R. J. H. Brush, "Trajectory optimisation to minimise antenna pointing error," *Computing & Control Engineering Journal*, vol. 6, pp. 61-7, 1995.

[109] "PCI/C6600 Applications Board Technical Reference Manual," Blue Wave Systems, Version 0.96, February 1999.

[110] "TMS320C6701 Floating-Point Digital Signal Processor," Texas Instruments, May 1998.

[111] Y.-T. Cheng, "Autoscaling Radix-4 FFT for TMS320C6000,". http://www-s.ti.com/sc/psheets/spra654/spra654.pdf, 2000.

[112] D. C. Rife and R. R. Boorstyn, "Single tone parameter estimation from discrete-time observations," *IEEE Transactions on Information Theory*, vol. IT-20, pp. 591-8, 1974.

[113] B. James, B. D. O. Anderson and R. C. Williamson, "Characterization of threshold for single tone maximum likelihood frequency estimation," *IEEE Transactions on Signal Processing*, vol. 43, pp. 817-21, 1995.

[114] L. Knockaert, "The Barankin bound and threshold behavior in frequency estimation," *IEEE Transactions on Signal Processing*, vol. 45, pp. 2398-401, 1997.

[115] A. D. Whalen, *Detection of signals in noise*. New York: Academic Press, 1971.

[116] S. L. Salas, *Calculus : one and several variables*, 6th ed. New York: Wiley, 1990.

[117] M. S. Bartlett, "Inference and Stochastic Processes," *Journal of the Royal Statistical Society*, vol. 130, pp. 457-477, 1967.

[118] D. C. Rife and G. A. Vincent, "Use of the discrete Fourier transform in the measurement of frequencies and levels of tones," *Bell System Technical Journal*, vol. 49, pp. 197-228, 1970.

[119] J. Kitchen and S. D. Howard, "Frequency estimation/tracking for short data windows," Fourth International Symposium on Signal Processing and its Applications, pp. 345-348, 1996.

[120] E. Aboutanios and S. Reisenfeld, "Frequency estimation and tracking for low earth orbit satellites," 2001 Spring Vehicular Technology Conference, pp. 3003-3004, 2001.

[121] S. Holm, "Optimum FFT-based frequency acquisition with application to COSPAS-SARSAT," *IEEE Transactions on Aerospace & Electronic Systems*, vol. 29, pp. 464-475, 1993.

[122] J. A. Dieudonne, *Foundations of modern analysis*. New York: Academic Press, 1960.

[123] K. E. Atkinson, *Theoretical numerical analysis : a functional analysis framework : mathematical models of science*. New York: Springer, 2000.

[124] M. R. Spiegel, *Theory and Problems of Complex Vairables*, SI (Metric) Edition ed. Singapore: McGraw-Hill, 1981.

[125] T. S. Kelso, "Orbital Estimation," http://www.celestrak.com/columns/v01n05, 2000.

[126] K. Willey, T. R. Osborn, M. Eckert, R. Liwanag and S. Reisenfeld, "The Suitability of Using NORAD TLE's to Track LEO Satellites with Ka Band Communications," Fifth Ka-Band Utilization Conference, Taormina, Sicily Island, Italy, pp. 453 - 460, 1999.

[127] Y. Feng and W. Enderle, "FedSat Real Time Orbit Solutions: Accuracy Dependences on Operation Modes," in *Publications On GPS 2001*, Y. Feng, W. Enderle and R. Walker, Eds.: Queensland University of Technology, 2002, pp. 1-14.

[128] G. J. Hawkins, D. J. Edwards and J. P. McGeehan, "Tracking systems for satellite communications," *IEE Proceedings, Part F: Communications, Radar & Signal Processing*, vol. 135-F, pp. 393-407, 1988.

[129] Y. T. Chan and S. W. Rudnicki, "Bearings-only and Doppler-bearing tracking using instrumental variables," *IEEE Transactions on Aerospace & Electronic Systems*, vol. 28, pp. 1076-83, 1992.

[130] J. P. Le Cadre and S. Laurent-Michel, "Optimizing the receiver maneuvers for bearings-only tracking," *Automatica*, vol. 35, pp. 591-606, 1999.

[131] J. M. Passerieux, D. Pillon, P. Blanc-Benon and C. Jauffret, "Target motion analysis with bearings and frequencies measurements," The Twenty-Second Asilomar Conference on Signals, Systems and Computers, San Jose, CA, USA, pp. 458-62, 1989.

[132] P. A. Rosenqvist, "Passive Doppler-bearing tracking using a pseudo-linear estimator," *IEEE Journal of Oceanic Engineering*, vol. 20, pp. 114-18, 1995.

[133] T. Xiao-Jia, Z. Cai-Rong and H. Zhen-Ya, "A generalized maximum likelihood estimation algorithm for passive Doppler-bearing tracking," the International Conference on Acoustics, Speech, and Signal Processing, pp. 3175-3178, 1995.

[134] Y. Yabumoto, M. Katayama, T. Yamazato and A. Ogawa, "Differential positioning with a single satellite," Vehicle Navigation and Information Systems Conference, pp. 579-584, 1994.

[135] B. Barstad, "COSPAS/SARSAT: a future global emergency service system," *Telektronikk*, vol. 82, pp. 46-56, 1986.

[136] P. Forsbeck, "SARSAT/COSPAS-satellite rescue system under development," *Tele (English Edition)*, vol. 89, pp. 40-2, 1983.

[137] J. V. King, "Overview of the Cospas-Sarsat satellite system for search and rescue," The International Mobile Satellite Conference Proceedings of the Sixth International Mobile Satellite Conference 1999 Canada Commun, Imsc 99, pp. 31-6, 1999.

[138] S. Kolodziej, "SARSAT-international search and rescue satellite," *Canadian Electronics Engineering*, vol. 27, pp. 30-1, 1983.

[139] P. M. Djuric and S. M. Kay, "A simple frequency rate estimator," ICASSP-89: 1989 International Conference on Acoustics, Speech and Signal Processing, Glasgow, UK, pp. 2254-7, 1989.

[140] P. Handel and P. Tichavsky, "Frequency rate estimation based on fourth order sample moments," Proceedings of the 8th IEEE Signal Processing Workshop on Statistical Signal and Array Processing, Corfu, Greece, pp. 391-394, 1996.

[141] P. Handel and P. Tichavsky, "Frequency rate estimation at high SNR," *IEEE Transactions on Signal Processing*, vol. 45, pp. 2101-5, 1997.

[142] F. Giannetti, M. Luise and R. Reggiannini, "Simple carrier frequency rate-of-change estimators," *IEEE Transactions on Communications*, vol. 47, pp. 1310-14, 1999.

[143] M. R. Spiegel and J. Liu, *Mathematical handbook of formulas and tables*, 2nd ed. New York: McGraw-Hill, 1999.

[144] P. Billingsley, *Probability and measure*, 3rd ed. New York: J. Wiley & Sons, 1995.

[145] K. L. Chung, *A course in probability theory*, 3rd ed. San Diego: Academic Press, 2001.